IMPROVED MODELING AND ANALYSIS STRATEGIES FOR PLASTIC BALL GRID ARRAY PACKAGE ASSEMBLIES SUBJECTED TO THERMAL CYCLING

by

Chienchih Chen

A Dissertation Submitted to the Graduate Faculty of
Auburn University
in Partial Fulfillment of the
Requirements for the Degree of
Doctor of Philosophy

Auburn, Alabama
December 15, 2018

Keywords: solder joint, constitutive models, fatigue models,
finite element analysis, and reliability

Copyright 2018 by Chienchih Chen

Approved by

Jeffrey C. Suhling, Chair, Quina Distinguished Professor of Mechanical Engineering
Hareesh V. Tippur, McWane Professor of Mechanical Engineering
James S. Davidson, Gottlieb Endowed Professor of Civil Engineering
Winfred A. Foster Jr., Professor of Aerospace Engineering

Abstract

Solder joint fatigue is one of the primary reliability issues in the electronic packaging area. Solder joints typically experience cyclic loading, yielding, and highly nonlinear material behavior when subjected to temperature changes. It is well-known that experimental fatigue life testing is an extremely time-consuming task. Thus, reliability predictions using the method of design for reliability (DFR) using finite element analysis can provide a more effective way for performing solder joint fatigue life studies, often reducing investigations from several months in length to a few days or weeks.

In the initial portion of this research, several different FEA approaches for Plastic Ball Grid Array (PBGA) assemblies have been compared, and their advantages and disadvantages have been discussed, especially in the areas of simulation accuracy and efficiency. The examined approaches included different types of 2D and 3D models (2D plane strain, 3D slice, and 3D quarter model), use of Multi-Point Constraints (MPCs), and use of Submodeling. The general assumptions used in all models included use of the Anand viscoplastic model for the solder constitutive behavior, and the Darveaux volume-weighted averaging energy-based fatigue criterion. For each approach, the predicted inelastic work density per cycle was calculated in the critical solder joint, and comparisons were made to distinguish the advantages and disadvantages of each of the evaluated models.

In the remainder of this work, several new approaches have been developed to improve the finite element modeling of PBGA assemblies including new techniques for (1) continuous meshing methods, (2) discontinuous meshing methods, and (3)

global/local (submodeling) methods. For the continuous meshing models, an improved fan-out meshing approach has been developed for modeling PBGA assemblies. In the investigated approach, a dome-like (hemispherical) brick element fan-out meshing scheme was used for the transitions from the circular interfaces at the top and bottom of the solder joints to the rectangular geometries found in the BT laminate and PCB substrate. This approach improved the accuracy of the simulations while simultaneously reducing the element count and simulation times up to 66%.

In the study of MPCs, a contacting element ratio was proposed for meshing mismatched contacting surfaces to adjust the balance between the required solution quality and simulation time. The master-slave relationship of the MPC technique has also been evaluated. Considering the developed master-slave relationship and the suggested location of the MPC contact pairs, the modified MPC-based analysis strategies presented great reductions in the computational times without sacrificing solution quality.

In the study of global/local submodeling approaches, it was found that the solution accuracy was dominated by the mesh quality and the step size for the local model. Furthermore, for the local model, the minimum required volumetric size has been determined for accurate simulations. Finally, the use of simplified geometry shapes for the solder joints in the global model has been studied.

In this dissertation, the most popular FE approaches for analyze the PBGA assemblies were evaluated and improved upon. Several new modeling and analysis strategies were developed to improve computational efficiency, simulation accuracy, and solution consistency between different approaches. Thus, with the proposed strategies

and guidelines, confusions can be reduced and a more reliable solution can be calculated with fewer computer resources.

Acknowledgments

I would like to thank my parents for their love and support. I would like to heartily express my gratitude to my major advisor Dr. Jeffrey C. Suhling for the support, guidance, and mentorship throughout this research. Thanks to my advisory committee members including Dr. Hareesh V. Tippur, Dr. James S. Davidson, Dr. Winfred A. Foster Jr., and Dr. Hamasha for their insightful instruction and discussion regarding this research. Thanks to my colleagues and many friends not mentioned here for their help.

Table of Contents

Abstract ii
Acknowledgments v
Table of Contents vi
List of Tables xi
List of Figures xiii
CHAPTER 1
INTRODUCTION 1
1.1 Electronic Packaging 1
1.2 Lead Free Solders in Microelectronics 3
1.3 Creep Behavior of Solder Alloy 6
1.4 Fatigue Failure of Solder Interconnection 7
1.5 Accelerated Testing Methodology 10
1.6 Design for Reliability Methodology for Reliability Prediction of Solder Joint 11
1.7 Finite Element Analysis for the DFR Methodology 13
1.8 Objectives of the Research 14
1.9 Organization of the Dissertation 16
CHAPTER 2
REVIEW OF MECHANICS OF SOLDER MATERIALS AND FATIGUE MODELS 18
2.1 Mechanics of Solder Materials 18
2.1.1 Non-Unified Constitutive Models 19
2.1.2 Unified Constitutive Models 33
2.2 Temperature Effect 46
2.3 Fatigue Models 47
2.3.1 Plastic Strain Based Fatigue Models 49
2.3.2 Creep Strain Based Fatigue Models 53
2.3.3 Energy Based Fatigue Models 55
2.3.4 Damage Based Fatigue Models 61
2.4 Design for Reliability 66
CHAPTER 3
LITERATURE REVIEW ON THE USE OF FEA APPROACHES ON ELECTRONIC PACKAGING AREA 68
3.1 Introduction 68
3.2 Nonlinear Finite Element Problems 68
3.2.1 Newton-Raphson Based Methods 69
3.2.2 Convergence Criteria 71

3.3 Finite Element Modeling Approaches in Electronic Packaging Area 73
3.3.1 2D Slice Models 73
3.3.2 3D Slice Models 76
3.3.3 3D Models 80
3.3.4 Multipoint Constraint Technique 81
3.3.5 Submodeling Technique 84
3.3.6 Substructuring Technique 86
3.3.7 Equivalent Model Technique 88
CHAPTER 4
COMPARISON OF FEA MODELING TECHNIQUES FOR PBGA ASSEMBLIES ... 90
4.1 Introduction 90
4.2 Finite Element Modeling and Simulation 92
4.3 3D Models 96
4.3.1 3D Quarter (1/4) Model 96
4.3.2 Simulation Results for 3D Quarter Model 97
4.3.3 3D Octant (1/8) Model 99
4.4 2D Slice Model 99
4.4.1 2D Slice FE Model (Diagonal Direction) 100
4.4.2 Simulation Results for 2D Slice Model (Diagonal Direction) 101
4.5 3D Slice Models 105
4.5.1 3D Slice FE Model (Diagonal Direction) 105
4.5.2 Simulation Results for 3D Slice Model (Diagonal Direction) 106
4.5.3 3D Slice Model (Diagonal Direction, Flat End) 109
4.5.4 3D Slice Model (Parallel Direction) 110
4.6 Submodeling Technique 112
4.6.1 Submodeling FE Model 112
4.6.2 Simulation Results for Submodeling Model 113
4.7 Multipoint Constraint (MPC) Technique 115
4.7.1 MPC Model 115
4.7.2 Simulation Results for MPC Model 116
4.8 Summary and Conclusions 119
CHAPTER 5
IMPROVED FINITE ELEMENT ANALYSIS STRATEGIES FOR PBGA PACKAGE ASSEMBLIES SUBJECTED TO THERMAL CYCLING 124
5.1 Introduction 124
5.2 Finite Element Modeling and Simulation 126
5.3 Example Models 127
5.4 Convergence Study on Unit Models 129

5.4.1 Effect of Element Types: Tetrahedral Element vs. Hexahedral Element 130
5.4.2 Conventional Meshing Strategy 132
5.4.3 Fan-Out Meshing Strategy 135
5.4.4 Simulation Results for Unit Models Using Conventional and Fan-Out Meshing Strategies 138
5.4.5 Adaptive Meshing Method for Two Different Meshing Strategies 141
5.4.6 Simulation Results for Unit Model Using Two Meshing Strategies with Adaptive Meshing Method 143

5.5 Determination of the Optimal Load Step Size 144

5.5.1 Optimal Determination of Required Load Step Size 145
5.5.2 Simulation Results for Models Using Optimal Load Step Sizes 147

5.6 Optimized Analysis Strategy 150

5.7 Convergence Study on Multi-Joints Package Using Quarter 8 × 8 PBGA Package Assembly 154

5.7.1 Selected Simulation Set for the Convergence Study of Multi-Joints Package Assembly 154
5.7.2 Simulation Results for Multi-Joints Package Assembly Models 154

5.8 Simulations for Quarter 15 × 15 Package Assembly Model 157

5.9 Flexibility on Design Change Using Fan-Out Meshing Strategy 162

5.10 Effect of Higher-Order Element 163

5.11 Effect of Element-Layers Used for Volume-Weighted Averaging ΔW_{avg} Calculation 166

5.12 Effect of Element-Layer for Components 167

5.13 Effect of PCB Model Size 167

5.14 Effect of Initial Temperature Range 168

5.15 Summary and Conclusions 169

CHAPTER 6
IMPROVED FINITE ELEMENT MODELING STRATEGIES WITH MULTIPOINT CONSTRAINT FOR PBGA PACKAGES SUBJECTED TO THERMAL CYCLING 172

6.1 Introduction 172

6.2 Multi-Point Constraint 173

6.3 Finite Element Modeling and Simulation 176

6.4 Example Model 177

6.5 Continuous Meshing Modeling Strategies 178

6.6 MPC Methods in the Literature 179

6.7 The Use of MPCs with Compatible Meshes 183

6.8 The Use of the MPCs with Incompatible Meshes 185

6.8.1 MPC Approach #1: MPC at the Interface between Two Different Materials 185
6.8.2 MPC Approach #2: MPC Locates within a Material 189
6.8.3 Simulation Results for Models Using Different MPC Approaches 192

6.9 Dependence of the Results on the Vertical Height of the Extruded Circular Mesh Pattern 196

6.10 The Use of Multiple MPC Contact Pair Layers (Unit Model) 198

6.11 The Use of Multiple-MPC Contact Pairs (Full Assembly Quarter Model) 201

6.12 Effect of Master-Slave Relationship on the Unit Model Results 206

6.13 Effect of Master-Slave Relationship on Package Assembly Model 209

6.14 Effect of the Hybrid Use of Multiple-MPC and the Modified Master-Slave Relationship 211

6.15 Summary and Conclusions 212

CHAPTER 7
IMPROVED SUBMODELING FINITE ELEMENT SIMULATION STRATEGIES FOR PBGA PACKAGES SUBJECTED TO THERMAL CYCLING 215

7.1 Introduction 215

7.2 Submodeling Technique 217

7.3 Finite Element Modeling and Simulations 219

7.4 Effect of Mesh Quality 222

7.4.1 Simulation Results for Different Global Models 224
7.4.2 Simulation Results for Local Models 228

7.5 Effect of Load Step Size 230

7.6 Determine the Minimum Required Volumetric Size of Local Model 231

7.7 Effect of Simplified Geometry Shapes for the Solder Joints in the Global Model 234

7.8 Effect of Hybrid Use Different Shapes of Solder Joint 239

7.9 Summary and Conclusions 241

CHAPTER 8
SUMMARY AND CONCLUSIONS 243

8.1 Comparisons of Different Popular Finite Element Approaches in Electronic Packaging Area 243

8.2 Improved Continuous Meshing Strategy 244

8.2.1 Effects of the Mesh Density and the Load Step Size 244
8.2.2 Effect of the Number of Element-Layer across the Thickness of Solder Joint 245
8.2.3 Effect of Element Types 245

8.2.4 Effect of PCB Size 246
8.3 Improved Discontinuous MPC Modeling Strategies 246
8.3.1 Effect of the Location of the MPC Contact Pair 246
8.3.2 Multiple-MPC Modeling Approach 247
8.3.3 Effect of Master-Slave Relationship 247
8.4 Improved Global-Local Modeling Strategies 248
8.4.1 Effect of the Volumetric Size of Local Model 248
8.4.2 Effect of Simplified Geometry Shapes for the Solder Joints in the Global Model 248
8.4.3 Hybrid Use of Different Simplified Joint Shapes 249
8.5 Conclusions 249
REFERENCES 251

List of Tables

Table 2.1 Summary of the Explicit Forms of $f(\sigma)$ and $g(t)$ for Creep Constitutive Equations........................ 22
Table 2.2 Popular Stead-State Creep Models for Solder Materials........................ 26
Table 2.3 Creep Model Constants for Different Solder Materials........................ 27
Table 2.4 Anand Model Constants for Common Solder Alloys........................ 40
Table 2.5 Summary of Solder Fatigue Models........................ 48
Table 4.1 Dimensions of Example PBGA Assembly........................ 93
Table 4.2 Anand Constants for SAC305 Solder........................ 94
Table 4.3 Material Properties for the Components of Example PBGA Package Assembly........................ 94
Table 4.4 Summary of Comparisons for Different FE Models........................ 123
Table 5.1 Dimensions for 8 × 8 mm^2 PBGA Package Assembly........................ 128
Table 5.2 Dimensions for 15 × 15 mm^2 PBGA Package Assembly........................ 129
Table 5.3 Model Sizes for Unit Models Using Conventional Meshing Strategy ... 135
Table 5.4 Model Sizes for Unit Models Using Fan-Out Meshing Strategy........................ 138
Table 5.5 Total Load Steps for Different Load Step Sets........................ 146
Table 5.6 Comparisons for Different Simulation Sets of Unit Model........................ 152
Table 5.7 Comparisons for Different Simulation Sets of Quarter 8 × 8 PBGA Assembly........................ 155
Table 5.8 Comparisons for Different Simulation Sets of Quarter 15 × 15 PBGA Assembly........................ 158
Table 5.9 Effect of Design Change Package Model........................ 163
Table 5.10 Effect of Element Type on Quarter 8 × 8 mm^2 Package Model........................ 165
Table 5.11 Effect of Element Type on Quarter 15 × 15 mm^2 Package Model........................ 165
Table 5.12 Effect of Initial Temperature Change........................ 169
Table 6.1 Dimensions of Example 15 × 15 PBGA Assembly........................ 178
Table 6.2 Comparison of Results for Different Unit Models........................ 184
Table 6.3 Comparison of Results for Unit Models Using MPC Approach #1 188
Table 6.4 Comparison of Results for Unit Models Using MPC Approach #2 190
Table 6.5 Comparison of Results for Unit Models Using MPC Approach #2 with Different C/R Ratios........................ 195
Table 6.6 Simulation Results for Various Unit Models........................ 200
Table 6.7 Summary of Comparisons for Multiple-MPC Package Assembly Quarter Models........................ 205
Table 6.8 Summary of Results for the Unit Model Using MPC Approach #4 with Different C/R Ratios........................ 209
Table 6.9 Summary of Results for Different Proposed MPC-Based Quarter Package Assembly Models........................ 210

Table 7.1 Dimensions of Example PBGA Assembly 220
Table 7.2 Simulation Results for Global and Local Models.................................. 223

List of Figures

Figure 1.1 Schematic of Deformation of a PBGA Package Assembly Subjected to Thermal Cycling ... 3
Figure 1.2 Typical Creep Curve ... 7
Figure 1.3 A Typical Hysteresis Loop ... 8
Figure 1.4 Different Stages of Stress Drop during Fatigue Test ... 9
Figure 1.5 Depiction of the Effects of the Accumulating Fatigue Damage in Solder Joint Structure ... 10
Figure 1.6 Schematic of Design for Reliability Methodology ... 12
Figure 2.1 Schematic of a Log-Log Plot of the Strain Rate versus the Shear Stress . 23
Figure 2.2 Schematic Plot of the Contributions from Different Mechanisms on Creep Rate versus Stress Relationship ... 25
Figure 2.3 Dwell Creep Method in Relation to Temperature Cycling Profile ... 30
Figure 2.4 Full Creep Method in Relation to Temperature Cycling Profile ... 31
Figure 2.5 Monotonic Test Simulation: Sn3.9Ag0.6Cu, at 125°C, 1.1×10^{-1} sec^{-1} Strain Rate (Left), and 4.4×10^{-4} sec^{-1} Strain Rate (Right) ... 32
Figure 2.6 Strain Energy Density History for Different Constitutive Models ... 42
Figure 2.7 Comparison of Experiments and Predictions of Modified Anand Model for Sn3.5Ag Solder: (a) Anand Model and (b) Modified Anand Model ... 44
Figure 2.8 Comparisons of Experiments and Predictions of the Bai's Modified Anand Model with Different Temperatures for (a) Sn3Ag0.5Cu and (b) Sn0.7Cu ... 45
Figure 2.9 Schematic of Total Strain versus Life Equation ... 50
Figure 3.1 Schematic of 2D Slice Model ... 74
Figure 3.2 Schematic of 3D Slice Model ... 77
Figure 3.3 The Use of GPD on Non-Perfect Diagonal Direction of a Package Assembly ... 78
Figure 3.4 FE model and Applied Boundary Conditions of a Large Die fcBGA ... 79
Figure 3.5 Schematic of 3D Models ... 80
Figure 3.6 Meshing with MPC: (a) MPC at Solder-Pad Interfaces, (b) MPC within Substrate/Board, and (c) No MPC ... 83
Figure 3.7 MPC Constraint above the Solder Joint ... 83
Figure 3.8 Scheme of Submodeling Technique ... 84
Figure 4.1 Example PBGA Package ... 92
Figure 4.2 Detail View of Example Model ... 93
Figure 4.3 Thermal Cycle Loading Curve ... 95
Figure 4.4 Volume-Weighted Averaging Regions for Simulation Result ΔW_{avg} ... 95
Figure 4.5 3D Quarter Model ... 96
Figure 4.6 Contour Plots of PLWK after Five Cycles for 3D Quarter Model ... 97

Figure 4.7 Simulation Results of ΔW_{avg} Values for 3D Quarter Model 98
Figure 4.8 History Curves of Volume Averaged PLWK for 3D Quarter Model....... 98
Figure 4.9 3D Octant Model.. 99
Figure 4.10 2D Slice Model 100
Figure 4.11 2D Plane Strain Model.. 101
Figure 4.12 Comparison of Vertical Displacements after Five Cycles for 3D Quarter Model and 2D Slice Model 102
Figure 4.13 Contour Plots of PLWK after Five Cycles for 2D Slice Model 102
Figure 4.14 Comparison of ΔW_{avg} Values for 3D Quarter Model and 2D Slice Model 103
Figure 4.15 Comparison of History Curves of Volume-Weighted Averaging PLWK for 3D Quarter Model and 2D Slice Model 104
Figure 4.16 3D Slice FE Model (Diagonal Direction) 106
Figure 4.17 Comparison of Vertical Displacements for 3D Quarter Model and 3D Slice Model 106
Figure 4.18 Contour Plots of PLWK after Five Cycles for 3D Slice Model 107
Figure 4.19 Comparison of ΔW_{avg} Values for 3D Quarter Model and 3D Slice Model (Diagonal Direction) 108
Figure 4.20 Comparison of History Curves of PLWK for 3D Quarter Model and 3D Slice Model 109
Figure 4.21 3D Slice FE Model (Diagonal Direction) Building with Simplified Flat End Surface 110
Figure 4.22 3D Slice FE Model (Parallel Direction).. 111
Figure 4.23 Comparison of ΔW_{avg} Values for 3D Quarter Model and 3D Slice Model (Parallel Direction).. 111
Figure 4.24 Submodeling FE model.. 113
Figure 4.25 Comparison of Vertical Displacements after Five Cycles for 3D Quarter and Submodeling Models 113
Figure 4.26 Comparison of PLWK after Five Cycles for 3D Quarter and Submodeling Models.. 114
Figure 4.27 Comparison of ΔW_{avg} Values for 3D Quarter and Submodeling Models 114
Figure 4.28 Comparison of History Curves of Volume-Weighted Averaging PLWK for 3D Quarter and Submodeling Models... 115
Figure 4.29 MPC Model.. 116
Figure 4.30 Comparison of Vertical Displacements after Five Cycles for 3D Quarter Model and MPC Model 117
Figure 4.31 Contour Plots of PLWK after Five Cycles for MPC Model.................. 117
Figure 4.32 Comparison of History Curves of Volume-Weighted Averaging PLWK for 3D Quarter and MPC Models... 118
Figure 4.33 Comparison of ΔW_{avg} Values for 3D Quarter and MPC Models 119

Figure 4.34 Comparison of Efficiency for Different FE Models ... 121
Figure 4.35 Comparison of Accuracy for Different FE Models ... 122
Figure 5.1 Quarter 8 × 8 mm^2 PBGA Package Assembly ... 128
Figure 5.2 Quarter 15 × 15 mm^2 PBGA Package Assembly ... 129
Figure 5.3 Detail View of Unit Model ... 130
Figure 5.4 Mesh Quality Inspection for Models Meshing via Two Different Element Types: Hexahedral (Left) and Tetrahedral (Right) Element ... 131
Figure 5.5 Geometrical Configuration of Example PBGA Package Assembly ... 132
Figure 5.6 Conventional Meshing Strategy ... 133
Figure 5.7 Unit Model Built Using Conventional Meshing Strategy with Different Mesh Qualities ... 135
Figure 5.8 Improved (Fan-Out) Meshing Strategy ... 137
Figure 5.9 Unit Model Built Using Fan-Out Meshing Strategy with Different Mesh Qualities ... 137
Figure 5.10 Variations of ΔW_{avg} with Number of Cycles ... 139
Figure 5.11 Comparisons of Simulation Results of ΔW_{avg} for Conventional and Fan-Out Meshing Strategies ... 140
Figure 5.12 Comparisons of Consistency of Simulation Results (ΔW_{avg}) and Simulation Efficiency for Two Different Meshing Strategies ... 141
Figure 5.13 Mesh Quality Inspection for Conventional and Fan-Out Models with Adaptive Meshing Method ... 142
Figure 5.14 Comparisons of Model Sizes for Models Using Fully Meshing Controlled Approach and Adaptive Meshing Approach ... 143
Figure 5.15 Comparisons of Simulation Results (ΔW_{avg}) for Models Using Fully Meshing Controlled Approach and Adaptive Meshing Approach ... 144
Figure 5.16 Divisions of Load Increments for LS 5 ... 146
Figure 5.17 Effects of Mesh Quality and Load Step Size on Simulation Results for Conventional Meshing Strategy ... 147
Figure 5.18 Effects of Mesh Quality and Load Step Size on Simulation Results for Fan-Out Meshing Strategy ... 148
Figure 5.19 Comparisons of the Effects of Mesh Quality and Load Step Size on Simulation Results for Model AR 4 ... 148
Figure 5.20 Comparisons of Simulation Result ΔW_{avg} Values and Normalized Computational Times for AR 4 Models Simulated with LS 100 ... 149
Figure 5.21 Comparisons of Simulation Result ΔW_{avg} Values and Normalized Computational Time for Different AR Models Simulating with LS 100 150
Figure 5.22 Strategy of Determination of Optimized Simulation Set ... 151
Figure 5.23 Comparisons of Simulation Result ΔW_{avg} Values and Normalized Computational Time for Different Simulation Sets ... 151
Figure 5.24 History Curves of Volume-Weighted Averaging PLWK for Different Simulation Sets ... 153

Figure 5.25 Distributions of PLWK after Five Cycles for Different Simulation Sets 153
Figure 5.26 Variations of Simulation Results with Different Solder Joint Locations for Quarter 8 × 8 PBGA Assembly 156
Figure 5.27 Comparisons of Simulation Result ΔW_{avg} Values for Critical Joints G7 and Normalized Computational Time for Different Simulation Sets 156
Figure 5.28 Two Different Meshing Quarter 15 × 15 Package Assembly Models.... 157
Figure 5.29 Vertical Displacements after Five Cycles for Different Meshing Models 158
Figure 5.30 Distributions of PLWK after Five Cycles for Quarter 15 × 15 PBGA Assembly Model Using Conventional Meshing Strategy....................... 159
Figure 5.31 Distributions of PLWK after Five Cycles for Quarter 15 × 15 PBGA Assembly Model Using Fan-Out Meshing Strategy 160
Figure 5.32 Variations of Simulation Results with Different Solder Joint Locations for Quarter 15 × 15 PBGA Assembly 161
Figure 5.33 Comparisons of Simulation Result ΔW_{avg} Values for Critical Joints M12 and Normalized Computational Time for Different Simulation Sets 162
Figure 5.34 Detailed View of Design Change Package Model................................. 163
Figure 5.35 Element-Layer Crossing 10 μm Thickness... 166
Figure 5.36 Simulation Results of PLWK Values for Models with Different Element Layers... 166
Figure 5.37 Different Element-Layers for Mold Compound and Silicon Die 167
Figure 5.38 Different PCB Size Models 168
Figure 5.39 Comparisons of the Effects of Different Modeling Setups on Simulation Results.. 168
Figure 5.40 Two Different Thermal Cycling Curves 169
Figure 6.1 Node-to-Surface Method 175
Figure 6.2 Two Different Master-Slave Relationships 176
Figure 6.3 Example 15 × 15 PBGA Assembly 178
Figure 6.4 Conventional (Left) and Fan-Out (Right) Meshing Models................... 179
Figure 6.5 Different Mesh Patterns 180
Figure 6.6 MPC FE Model 181
Figure 6.7 Comparison of Vertical Displacements after Five Cycles for Continuous Meshing Model and MPC Model 181
Figure 6.8 Comparison of History Curves of Volume-Weighted Averaging PLWK for Continuous Meshing Model and MPC Model 182
Figure 6.9 Comparison of ΔW_{avg} Values for Continuous Meshing Model and MPC Model 182
Figure 6.10 Cross-Sectional View of MPC... 184
Figure 6.11 Simulation Results of Stress and Strain for Unit Model Using Different Modeling Strategies 185
Figure 6.12 Cross-Sectional View of MPC Approach #1 186

Figure 6.13 Unit Model Built Using MPC Approach #1 with Five Different C/R Ratios 188
Figure 6.14 Cross-Sectional View of MPC Approach #2 189
Figure 6.15 Unit Model Built Using MPC Approach #2 with Five Different C/R Ratios 190
Figure 6.16 Comparison of Mesh Densities for MPC Approaches 191
Figure 6.17 Comparisons of Model Sizes for Different C/R Ratios and MPC Approaches 192
Figure 6.18 Comparisons of Simulation Results (ΔW_{avg}) for Models with Different C/R Ratios and MPC Approaches 193
Figure 6.19 The Effects of C/R Ratio on the Percentage Error in ΔW_{avg} for Different MPC Approaches 194
Figure 6.20 Comparisons of Simulation Results and Computational Times for the MPC Modeling Approaches 195
Figure 6.21 Four Different Vertical Heights for C/R = 28 Model 196
Figure 6.22 Comparisons of Simulation Results for Different Vertical Heights of the Extruded Circular Mesh Pattern 197
Figure 6.23 Dependence of the ΔW_{avg} Values on the Solder Joint Location for Different Modeling Approaches 198
Figure 6.24 Cross-Sectional View of the Multiple-MPC Model #1 199
Figure 6.25 Comparisons of Simulation Results and Computational Times for Different Models 201
Figure 6.26 Multiple-MPC Model #2 202
Figure 6.27 FE Models Built with Different Modeling Strategies 203
Figure 6.28 Dependence of the ΔW_{avg} Values on the Solder Joint Location for Different Modeling Approaches 204
Figure 6.29 Simulation Results for Package Assembly Quarter Model with Different Modeling Strategies 205
Figure 6.30 The Master-Slave Relationships for MPC Approach #1 and MPC Approach #3 207
Figure 6.31 The Master-Slave Relationships for MPC Approach #2 and MPC Approach #4 207
Figure 6.32 The Effects of C/R Ratio on the Percentage Error in ΔW_{avg} for MPC Approaches #1 and #3 208
Figure 6.33 The Effects of C/R Ratio on the Percentage Error in ΔW_{avg} for MPC Approaches #2 and #4 209
Figure 6.34 MPC Approach #5 211
Figure 6.35 General Procedure for Choosing MPC-Based Approaches 214
Figure 7.1 Scheme of Submodeling Technique 219
Figure 7.2 Engineering Drawing of Example 8 × 8 PBGA Package Assembly 220
Figure 7.3 Quarter Assembly Model 221

Figure 7.4 The Effects of Mesh Quality and Load Step Size on Simulation Results for Conventional Meshing Models ... 222
Figure 7.5 Global Models Meshed with Four Different Aspect Ratios ... 223
Figure 7.6 Simulation Results of ΔW_{avg} Values for Solder Joint Array of the Prepared Global Models ... 224
Figure 7.7 Comparisons of Simulation Results and Normalized Computational Time for the Prepared Global Models ... 225
Figure 7.8 Vertical Displacements of Point P's for the Prepared Global Models ... 226
Figure 7.9 Vertical Displacements of Point Q's for the Prepared Global Models ... 226
Figure 7.10 Contour Plots of PLWK after Five Cycles for the Prepared Global Models ... 227
Figure 7.11 History Curves of Volume-Weighted Averaging PLWK for the Prepared Global Models ... 228
Figure 7.12 History Curves of Volume-Weighted Averaging PLWK for Local Models ... 229
Figure 7.13 Simulation Results and Normalized Computational Time for Different Global-Local Model Sets ... 229
Figure 7.14 Simulation Results of ΔW_{avg} Values for Global-Local Model Sets Simulated with Different Load Step Sizes ... 231
Figure 7.15 Six Different Heights for the Vertical Cut-Boundaries of Local Model 232
Figure 7.16 Simulation Results of ΔW_{avg} Values for Local Models with Different Vertical Heights ... 234
Figure 7.17 Simplified Geometry Shapes for Solder Joints in the Global Model, Cylinder Shape ... 235
Figure 7.18 Simplified Geometry Shapes for Solder Joints in the Global Model, Brick Shape ... 235
Figure 7.19 Contour Plot of PLWK after Five Cycles for Global Model with Cylinder Shape Joints ... 236
Figure 7.20 Contour Plot of PLWK after Five Cycles for Global Model with Brick Shape Joints ... 237
Figure 7.21 Comparisons of Simulation Results for Global Models Built with Different Shapes of Solder Joint ... 238
Figure 7.22 Comparisons of Simulation Results and Computational Time for Different Global-Local Model Sets ... 239
Figure 7.23 Hybrid Use of Brick and Cylinder Shapes Joints for Global Model ... 240
Figure 7.24 Simulation Results of ΔW_{avg} for Model of the Global Model with Mixture Joint Shapes ... 240
Figure 7.25 General Procedure for Choosing Submodeling Approaches ... 242

CHAPTER 1
INTRODUCTION

1.1 Electronic Packaging

Microelectronic devices are mainly being designed and manufactured with a silicon chip, or chips, in various compact package configurations to perform their functionalities at reasonable costs. Initially, electronic components were mounted on a PCB using through-hole mount technology (THT) [1]. Through-hole components have metal leads that used to insert through-plated holes in the PCB and then soldered onto pads on the solder side. This mount technology has been gradually replaced by surface-mount technology (SMT) in the late 1980s. Compared to SMT, THT provides strong mechanical bonds but through holes take up valuable space on the PCB. The increasing space limitations gave rise to surface mount technology, the components are directly mounted onto the PCB surface, and opened a new era of more compact and portable electronic devices. SMT has several advantages including higher component density, better mechanical performance, higher real-estate rate, and certainly lower cost. A ball grid array (BGA) is a type of SMT used for integrated circuits. A BGA assembly can utilize whole bottom surface of a package to provide more interconnections; it is a solution to the problem of producing a miniature package for an integrated circuit with many I/O counts. Among different BGA types, the designs of plastic ball grid array (PBGA) are concentrated on lightweight, thin with short connections, minimizing the use of board space, and optimizing device electrical performance.

A typical PBGA assembly consists of components of different materials with different mechanical and thermal properties, and geometric configurations with existing discontinuities of material properties between the interfaces of two components. Various operating conditions and environments introducing different loading conditions (such as thermal cycling (TC), thermal shock (TS), vibration, impact, moisture etc.) during the manufacturing and the service life often induce these materials and components to various failure modes. The failure modes can be categorized as: metal line voiding, passivation cracking, process die cracking, fine metal line smearing, package swelling, warpage, and delamination, and these failure mods may cause performance degradation or failure before the designed service life. With the emergence of the modern electronic packaging technology over the last few decades, solder alloys have been become the primary interconnect material used in electronic packaging. According to Yeh's report [2], the main cause for failure of electronic package is temperature fatigue (55 %) and the other causes are vibration fatigue (20 %), humidity (19 %), and dust (6 %). Due to mismatch in the thermal expansion coefficient (CTE), electronic package assembly experiences high stress/strain fluctuations while undergoing temperature changes [3]. Figure 1.1 illustrates the schematic of deformation of PBGA package assembly subjected to thermal cycling; along with the CTE mismatch between various package components, temperature changes result in high stress/strain concentration and the accumulation of stress and strain may induce fatigue crack in a packages assembly, especially in solder interconnection/joint, and as such solder interconnection is often the most vulnerable component in a package assembly. Thus, the reliability of solder interconnection is the main crucial issue in electronic packaging community.

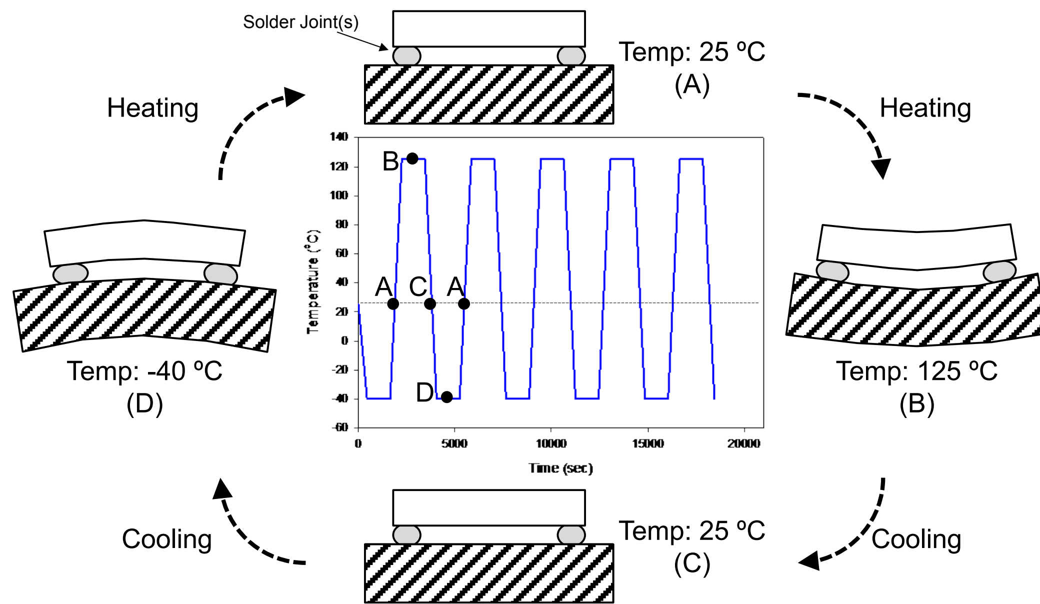

Figure 1.1 Schematic of Deformation of a PBGA Package Assembly Subjected to Thermal Cycling

1.2 Lead Free Solders in Microelectronics

In the past, eutectic Sn-37Pb has been the most extensively used soldering alloy in the packaging industries. The eutectic Sn-Pb solders were very attractive due to their relative low melting temperature (183 °C) and excellent ductility and good reliability and for their superior wettability and compatibility with most substrates and devices [4]. In order to minimize harmful effects of dangerous substances to people and the environment, EU legislation has restricted the use of certain hazardous substances in electrical and electronic equipment (EEE) and promoted the collection and recycling of such equipment since 2003. Two major directives have been adopted, they are the waste of electrical and electronic equipment (WEEE) and the directive of the restriction of the use of certain hazardous substances (RoHS) [5]. The WEEE directive requires that lead has to be removed from any end-of-life electrical or electronic components. The RoHS specifically bans lead from electrical and electronic components manufactured after July

2006, had a major impact on the electronics manufacturing industry where cooperative efforts have seen the industry made a smooth transition from Sn-Pb alloys to lead free SnAg-u, SAC, alloys. Due to great efforts have been achieved to restrict the use of Pb-based solders and replace it with Pb free solders in consumer electronic products, the conversion to lead free solders in the global electronic market appears imminent [6] [7]. In the United States, the lead free solder project headed by the NCMS initiated research and development of lead free solder in a database program [8]. The results of the project have been made available in a database and offer information on such matters as modifying equipment and processes for selecting alternative materials. The database on lead free solder includes (1) recommended applications for lead free solder, (2) alloy composition guidelines reflecting price and availability, (3) database of the seven selected alloys and comparison with eutectic Sn-Pb alloy, (4) data on the characteristics of the other 70 eliminated alloys, (5) optimal process conditions using various test PCBs, (6) strength evaluation and metallurgical reaction analysis for the selected alloys and various surface mounting process reactions, (7) predicted life (using NCMS project proprietary life prediction software) and thermal fatigue evaluation for four of the selected alloys, and (8) assessment of nontoxicity and alloy composition.

In selecting suitable alternative of SnPb soldering materials, it is important to take into consideration that the properties of the alternative solders are comparable or superior to SnPb solders. Compatible candidates must have the following behaviors [9]:

- Physical behaviors similar to eutectic SnPb
- Adequate wettability for the metallization used in the electronics industry
- Good fatigue resistance, electrical performance and reliability

- Compatibility with existing liquid flux systems
- Adequate shelf life and performance as a solder paste
- Low cost and easier manufacturability

Among various alloy systems that are considered as lead free solder candidates, SAC alloys have been recognized as the most promising because of their relatively low melting temperature (compared to the binary eutectic SnAg solder alloys), superior mechanical properties, and good compatibility with other components [10] [11] [12] [13]. SAC alloys have widely been used as lead free solutions of interconnections for BGA as solder joints and pastes [14]. Typical SAC alloys contain 3 - 4 % Ag, 0.5 - 0.7% Cu, and the balance 95+ % Sn; some popular representatives of SAC family solders are listed as follows [15].

1. SAC305 (Sn3.0Ag0.5Cu): The most popular SAC solder alloy, especially in auto and consumable electronics industries. It has the advantage of low cost, excellent fatigue resistance, and good mechanical characteristics.
2. SAC105 (Sn1.0Ag0.5Cu): Popular in cellphone industry, because of superior drop and vibration resistance.
3. SAC405 (Sn4.0Ag0.5Cu): Perform a better fatigue performance than SAC305 due to contain more silver. As a result, it is more expensive than SAC305.

There are some major challenges for the current series of lead free solders. SAC series alloys have a higher melting temperature compared to 183 $^{\circ}$C for the eutectic SnPb solders. They require higher reflow temperature during the manufacturing process, which may cause reliability problems. The excessive buildup of intermetallic formed at

the interface between the solder joint and the copper pad can also cause reliability problems. In addition, high costs are another issue for lead free solders.

1.3 Creep Behavior of Solder Alloy

Solder alloys experience both phenomena of creep and viscoplasticity at high homologous temperature $T_h = T/T_m$, (where T is the process temperature and T_m is the melting temperature). Creep refers to the redistribution of stresses and strains with time in the material under constant stress levels, while viscoplasticity is time-dependent plastic deformation. Creep and viscoplastic deformation are physically indistinguishable; the separate description of each phenomenon is for analytical convenience. Creep deformation becomes significant above a homologous temperature of 0.5. This significant contribution is a result of the low solidus temperature of solder alloys. Even room temperature (T = 25 $^{\circ}$C) represents an elevated temperature for the lead free alloys, as indicated by a high homologous temperature for these and nearly all electronic solders. For the eutectic Sn-Pb solder, T_m is 183 $^{\circ}$C and the T_h is 0.65 T_m at room temperature. For the lead free solders T_h is 0.61 T_m (where T_m = 217 $^{\circ}$C) at room temperature. The typical test temperature range of accelerated thermal cycling test is considered as between -40 and +125 $^{\circ}$C, then the lead free solder T_h is between 0.48 - 0.81 T_m and this is in the range of creep deformation. Thus, creep is not negligible for most solder materials even at room temperature.

Figure 1.2 shows a typical creep curve, which generally consists of three stages after the initial instantaneous elastic strain when a constant load is applied [16]. In every creep tests there is an initial strain which is due to the elastic jump and/or plastic

deformation for application of the load. The strain rate starts with a very high magnitude and decreases rapidly over time in the first stage of creep test. This is caused by work hardening, which restricts the deformation. The second stage is called as the secondary creep, or steady-state creep stage, in which the strain rate becomes approximately constant. The steady state creep rate is due to the dynamic balance of strain hardening and recrystallization and mostly the region of plastic deformation. It is very important because so many researchers use the steady state creep rate for the finite element simulation to predict the responses of solder alloys. The tertiary creep region occurs when rupture is imminent, and typically features an abrupt change to a nearly constant but significantly increased creep rate.

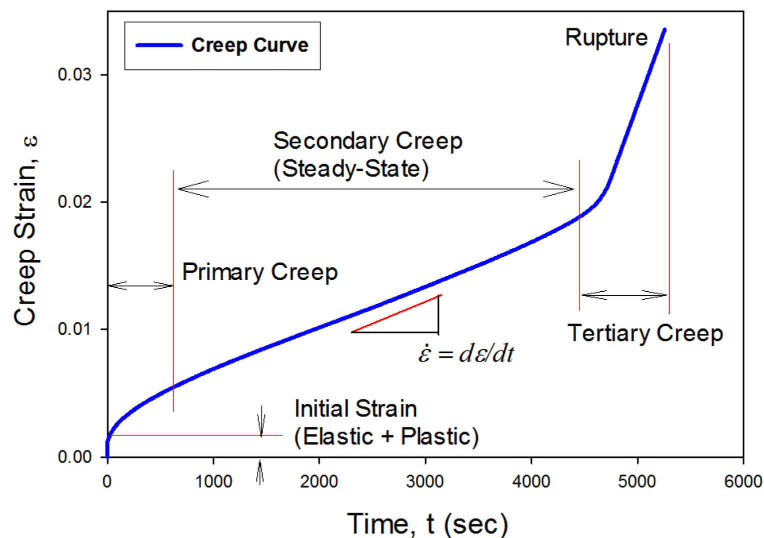

Figure 1.2 Typical Creep Curve

1.4 Fatigue Failure of Solder Interconnection

Electronics device experiences fluctuating or cyclic stresses in operating conditions that often result in fatigue failure. The process involves the initiation and gradual propagation of a crack until the remaining section of the structure can no longer

support the applied load. Due to mismatch in the CTE between different components, stresses concentration and accumulation occur when a package assembly subjected to temperature changes. Since solder interconnection connecting different components (such as PCB, BT substrate, silicon chip/die), cyclic temperature changes can lead to substantial alternating stresses within a solder joint. During cyclic loading, micro cracks form within the solder material followed by macro cracks which leads to damage and ultimately to fatigue failure.

A hysteresis loop as shown in Figure 1.3 is a convenient means of depicting stress-strain relationships during fatigue. The width of the loop is equal to the inelastic strain range, $\Delta\varepsilon_{in}$, and the elastic strain range, $\Delta\varepsilon_e$, which is given by the difference between the total strain range, ε, and the plastic strain range. For solder materials, the extent of elastic strain is small so that in most cases, $\Delta\varepsilon_{in} \gg \Delta\varepsilon_e$. The area enclosed by the loop is a measure of the inelastic strain energy required to produce the observed deformation.

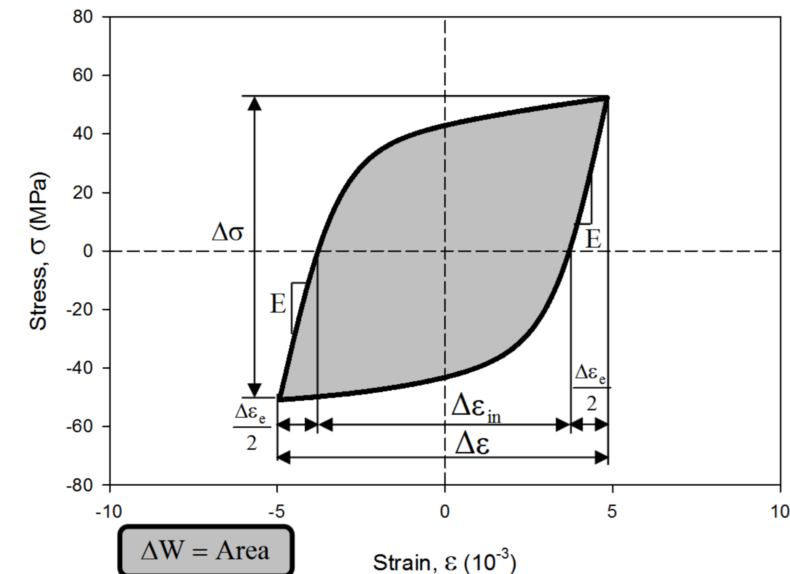

Figure 1.3 A Typical Hysteresis Loop

It has been observed that for a strain-controlled fatigue test, cyclic tension-compression loading causes damage accumulation eventually resulting in crack initiation. Different stages of peak stress drop during a fatigue test are shown in Figure 1.4. It is seen that the stress drops rapidly during the initial cycles due to damage accumulation and material softening. A steady state stage is then attained where grain growth progresses, re-crystallization occurs in the microstructure, and micro-voids forms.

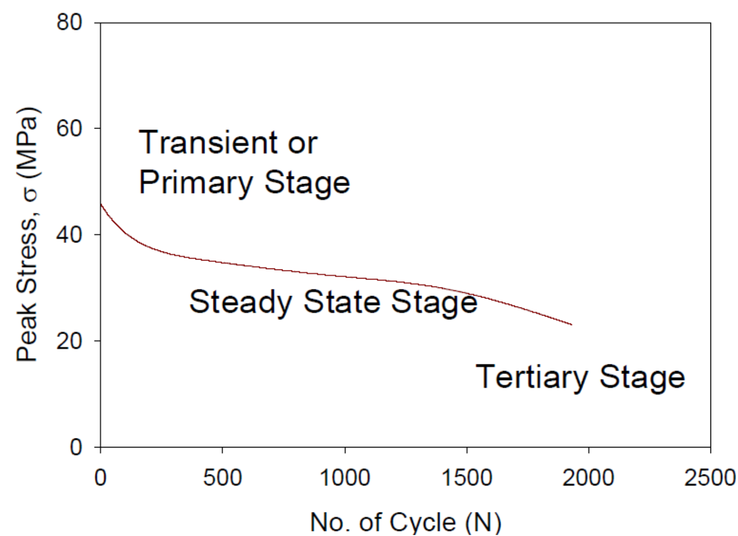

Figure 1.4 Different Stages of Stress Drop during Fatigue Test

The grain structure of solder is inherently unstable; the grains grow in size over time as the grain structure reduces the internal energy of a fine-grained structure (as illustrated in Figure 1.5 [17] [18]). This grain growth process is enhanced by elevated temperatures as well as strain energy input during cyclic loading. The grain growth process is thus an indication of the accumulating fatigue damage. At the grain boundaries contaminants like lead oxides are concentrated; as the grains grow these contaminants are further concentrated at the grain boundaries, weakening these

boundaries. After the consumption of ~25% of the fatigue life micro-voids can be found at the grain boundary intersections; these micro-voids grow into micro-cracks after ~40% of the fatigue life; these micro-cracks grow and coalesce into macro-cracks leading to fracture. The number of cycles until fracture is commonly defined as the fatigue life of for material. Generally the number of cycles at 50% drop of the tensile load is taken to be the fatigue life as recommended by ASTM [19].

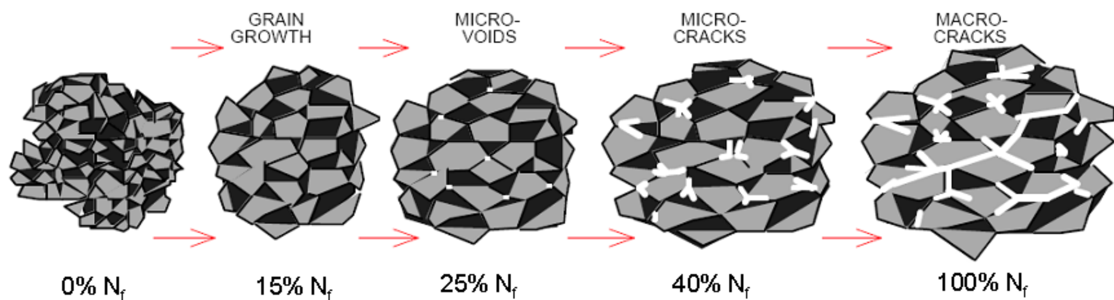

Figure 1.5 Depiction of the Effects of the Accumulating Fatigue Damage in Solder Joint Structure [17]

1.5 Accelerated Testing Methodology

Accelerated tests use much harsher conditions, such as elevated loading levels and higher cycling frequency, to assess the reliability in a short time. Accelerated tests are targeted to produce identical failure mechanisms to those found during service conditions for the specific package design and generate relevant information for understanding the physics of package failures [20]. In addition, accelerated test data are collected to represent the statistics of failures [21] which determines the mean time of failure for the package when subjected to a specified accelerated test condition.

Accelerated thermal cycling (ATC) tests are used to evaluate the reliability of electronic package subjected to extreme temperatures [22]. The ATC test standards can

be found on JEDEC where two common ATC tests used for solder joint reliability are the thermal cycling (TC, JESD22-A104, [23]) and thermal shock (TS, JESD22-A106, [24]) tests. TC has a ramp rate varying from 8 $^{\circ}$C/min to 33 $^{\circ}$C/min and TS has a ramp rate between 33 $^{\circ}$C/min and 55 $^{\circ}$C/min.

In the JEDEC stands, the temperature levels that vary from -40 to +125 $^{\circ}$C correspond to the temperature range $\Delta T = 165$ $^{\circ}$C that has significant temperature ramp rates. The high/low temperature at the dwell time activates creep deformation and the fast temperature ramp rates induce viscoplastic deformation [25]. The samples will be monitored for electrical resistance/continuity during ACT tests, if the resistance shows a very large increase this indicates that a crack has grown completely through the solder joint and the sample is considered to have failed. The average number of cycles to failure is used as a measure of the reliability of a package assembly.

However, the drawbacks of accelerated tests are that they are still time- and cost-consuming elaborate tasks and it is very difficult to study the physical mechanisms and fatigue phenomena of solder joint due to the small physical dimensions of solder joint compared to a PBGA package assembly. It yields the use of the design for reliability has become more popular today.

1.6 Design for Reliability Methodology for Reliability Prediction of Solder Joint

Numerical simulation by using finite element analysis (FEA) is an efficient and systematic approach to evaluate the internal states values (e.g. displacements, stresses, strains, energy, etc.) of interest, such as solder joint, subjected to various loading conditions. FEA provides an understanding of physical mechanisms and fatigue

phenomena of solder joint. In addition, it prevents excessive and time-consuming experimental tests of the package assemblies that have similar material properties, package configurations, and loading conditions. Thus, design for reliability (DFR) integrating the FEA simulation results, experimental data, and fatigue models for reliability prediction of solder joint has been widely accepted and utilized in electronic package society. The schematic of DFR is shown in Figure 1.6 and can be summarized as following steps [26] [27] [28] [29]:

1. Establish a constitutive model to describe the complex behaviors of the interest material in electronic package assembly.
2. Build a FE model implemented with the established constitutive model and apply the boundary conditions and the loading condition on the FE model.
3. Apply an appropriate fatigue model to predict the thermo-mechanical reliability of the assembly.
4. Verify the results using thermal-mechanical cycling test data.

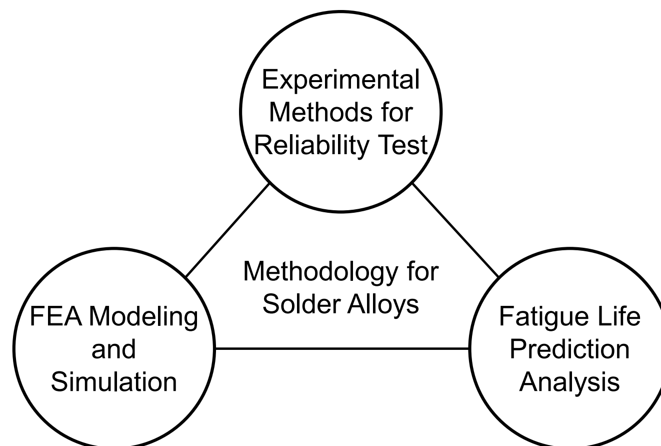

Figure 1.6 Schematic of Design for Reliability Methodology [29]

1.7 Finite Element Analysis for the DFR Methodology

FEA developed from the discretization of continuous problem advances in computational mechanics. The idea of FEA is to discretize a structure domain into a number of simple domains called elements that using mathematical shape functions to approximate the variation of the displacements over finite elements. FE model is a representation of an assembly of finite elements that are connected at nodes. The variational principle of mechanics, such as the principle of minimum potential energy, is often used to obtain the governing equations of the continuum FE model. A system of equilibrium equations that obtained by assembling the equations for the individual elements represents the relationship of stiffness matrix, unknown displacements, and boundary conditions. After the unknown displacements are solved from the system of equilibrium equations, the strains and stresses can be calculated. General FEA procedure involves the following steps:

(1) Modeling elements to fit the body of the structure or assembly.

(2) Specify the loading and boundary displacement conditions.

(3) Derivation of each element type stiffness matrix.

(4) Assembly of equations for the overall FE model stiffness matrix.

(5) Iterative solutions for all unknown nodal displacements.

(6) Calculation of the element strains/stresses from the nodal displacements.

For the DFR methodology, important guide lines have been summarized in literature [3] [30], they are:

(1) The modeling methodology is able to accommodate different types of loading conditions induced by thermal cycling and power cycling as well

as vibration. Thermal gradients associated with thermal/power cycling and frequencies/mode shapes associated with vibration loading are needed to be determined.

(2) Representing the structural and thermal contribution of solder joint is critical as well as detailed modeling of solder geometry.

(3) Loading conditions, symmetry and other assumptions are needed to be carefully addressed in the model.

(4) Use appropriate material behaviors (such as elastic, plastic, creep, viscoplastic, etc.) to account for solder deformation mechanism.

(5) Calculating accumulated damage metric induced by different loading conditions is required, e.g. inelastic strain range, inelastic strain energy density range.

(6) Applying appropriate fatigue law, the required parameters such as the range of inelastic strain or inelastic strain energy needs to be extracted from the FEA simulation results, for fatigue life prediction.

However, these guide lines are still not sufficient for analyst to calculate a converged, accurate solution in an efficient way, and still lack of solution consistency between different approaches.

1.8 Objectives of the Research

The motivation of this research is to systematically study the effects of the use of modern FEA approaches on the simulation results of PBGA package assemblies and to develop improved modeling and analysis strategies that include continuous meshing and

advanced FE approaches to predict solder joint reliability in microelectronic packaging. The following objectives will be achieved in this research:

I. Improved continuous meshing models

1. Perform convergence study that understands the effects of mesh quality for the package assembly model and load step size for simulation on the solution accuracy and simulation efficiency;
2. Develop optimal analysis strategy for PBGA assemblies when subjected to thermal cycling;
3. Develop improved modeling approaches to further simply PBGA assembly models and save simulation times without sacrificing the accuracy of simulation.

II. Improved discontinuous MPC models

1. Study the effect of location of MPC setup;
2. Investigate the effect of the ratio of mesh densities between two contacting surfaces;
3. Investigate the master-slave relationship of two contacting surfaces;
4. Develop improved MPC-based modeling strategy for the PBGA assemblies with complex configurations, high-density components, and high I/O counts.

III. Improved global and local models

1. Validate the use of submodeling in electronic packaging area;
2. Investigate the effects of mesh quality and load step size on the use of submodeling technique;

3. Develop improved submodeling-based modeling strategy to identify the most critical solder joint of a PBGA assembly and calculate accurate detail responses of the critical joint;
4. Perform the solution consistent between different proposed approaches;
5. Provide improved guide lines to reduce modeling confusions.

1.9 Organization of the Dissertation

This dissertation mainly focuses on studying the procedures for reliability prediction with aging effects for lead free solder materials, and the application of aging aware constitutive models for solders. The study is presented in the following chapters:

Chapter 1: Introduction to electronic packaging, lead free solders alloys, failure modes, testing methodology, reliability study, and numerical analysis approaches.

Chapter 2: Literature review on different constitutive equations for describing behavior of solder alloys. And, four different types of fatigue models for reliability prediction were reviewed.

Chapter 3: Review of nonlinear finite element method and the convergence criteria for iteration in FE calculation. The popular FEA approaches used in electronic packaging area, including 2D slice model, 3D slice model, full/symmetric 3D model, MPC model, submodeling model, and substructure model, were also reviewed.

Chapter 4: Comparison of different FE approaches to understand their own advantages and disadvantages.

Chapter 5: Develop improved modeling and analysis strategies for continuous meshing models of PBGA assemblies.

Chapter 6: Develop improved MPC-based analysis strategies for reducing modeling difficulty, improve simulation efficiency and accuracy.

Chapter 7: Develop improved submodeling-based analysis strategies for further reducing modeling difficulty, and improving simulation efficiency and accuracy.

Chapter 8: Summary and conclusions.

CHAPTER 2
REVIEW OF MECHANICS OF SOLDER MATERIALS AND FATIGUE MODELS

As the DFR method has become the most widely acceptable approach for reliability prediction of solder interconnection, a reliable prediction is relied on an accurate constitutive model, an appropriate fatigue model, and a reasonable FEA simulation [31]. In this chapter, the review of constitutive models and fatigue models for solder material are addressed.

2.1 Mechanics of Solder Materials

A constitutive model for a material governs its thermal/mechanical behavior when subjected to different loading conditions at different temperatures. The constitutive models used by the electronic packaging area for describing nonlinear material behaviors of solder alloys can be broadly categorized into two families: non-unified (uncoupled) model and unified model [32] [33]. The non-unified models consider the plastic strain and creep strain separately, whereas the unified models consider the plastic and creep strains as an inelastic strain. A notable feature of the unified models is the use of a complicated flow rule for describing the rate- and temperature- dependences of solder materials [27]. In non-unified constitutive models, the inelastic deformation is separated into two main groups: plastic and creep deformations [32]. In the following sections, important constitutive models for solder alloys were reviewed.

2.1.1 Non-Unified Constitutive Models

The plastic deformation occurring over a very short time scale (e.g. due to dislocation slip) is treated as instantaneous and independent of the loading rate [32]. For deformation occurring over a longer time scale is termed as creep deformation. Therefore, in non-unified models, the total strain can be constructed as a combination from three separate deformation mechanisms: time-independent elastic strain, time-independent plastic strain, time-dependent creep strain, and as such the non-unified constitutive models can be subdivided into (1) elastic-plastic , (2) elastic-creep , (3) elastic-plastic-creep categories [34].

2.1.1.1 Plastic Based Constitutive Models

Elastic-plastic (EP) model [35] treats the total strain as the summation of the components of elastic strain and plastic strain as shown in eq. (2.1):

$$\varepsilon = \varepsilon_e + \varepsilon_p \tag{2.1}$$

where ε, ε_e, and ε_p are total, elastic, plastic strains, respectively. Ramberg-Osgood model [36] can be used to describe the stress-strain curve of solder materials given by:

$$\varepsilon = \frac{\sigma}{E} + \alpha \left(\frac{\sigma}{\sigma_0} \right)^n \tag{2.2}$$

where n is the hardening exponent, α and σ_0 are material constants. This version of Ramberg-Osgood model, however, does not describe the effects of temperature and strain

rate what solder alloys are highly dependent on. A modified Ramberg-Osgood model has been developed to include the temperature and strain-rate dependences [37], given as:

$$\varepsilon(T,\dot{\varepsilon}) = \frac{\sigma}{E} + \alpha\left(\frac{\sigma}{\sigma_0(T,\dot{\varepsilon})}\right)^{n(T,\dot{\varepsilon})} \tag{2.3}$$

where $\sigma_0(T,\dot{\varepsilon})$ and $n(T,\dot{\varepsilon})$ are temperature and strain rate dependent. The plastic properties for four different tin-based solder alloys were determined by Darveaux et al. [38].

It is a critical issue for solder materials to define the plastic curves from the experimental data. The time-independent plasticity can be obtained a specific temperature at a low strain rate (1×10^{-10} sec^{-1}), which may not be feasible for test machine. One expedient definition of plasticity can be the tensile strain/stress curve at a relatively high strain rate (e.g. 0.1 sec^{-1}) [39]. Solder joints, however, of an electronic package experience continuous strain rate changes while temperature changes. There is always, in fact, the time-dependent deformation involved. Any particular choice from a specific strain rate may not suitable for determine the plasticity of solder materials. Thus, the EP model is a suitable model for the problem when mechanical loading (e.g. bending) with shorter cyclic time is encountered due to the inelastic deformation is induced by plastic effect but not creep effect [34].

2.1.1.2 Creep Models

Creep deformation becomes significant and cannot be ignored while the homologous temperature is higher than 0.5. For the eutectic SnPb solder, T_m is 183 $^{\circ}$C

and the T_h is 0.65 T_m at room temperature while for the lead free solders T_h is 0.61 T_m, where T_m = 217 $^{\circ}$C. The typical test temperature range of ATC test is considered as between -40 and +125 $^{\circ}$C, then the lead free solder T_h is between 0.48 - 0.81 T_m and this is in the range of creep deformation. A typical time-dependent creep deformation curve is composed of primary, secondary, and tertiary stages. The creep behavior of a solder material is often characterized by its steady-state creep strain rate ($\dot{\varepsilon}_c$). In the broadest sense, creep strain, ε_c, can be expressed as a function of time, applied stress, and temperature [40]:

$$\varepsilon_c = f(\sigma)\, g(t)\, e^{(-Q/RT)} \tag{2.4}$$

and

$$\dot{\varepsilon}_c = f(\sigma)\left[\frac{dg(t)}{dt}\right] e^{(-Q/RT)} \tag{2.5}$$

where Q is creep activation energy, R is the universal gas constant, and T is absolute temperature. The explicit forms of the stress dependence term, $f(\sigma)$, and the time dependence term, $g(t)$, were summarized in Table 2.1 [40] [41].

Table 2.1 Summary of the Explicit Forms of $f(\sigma)$ and $g(t)$ for Creep Constitutive Equations [40] [41]

$f(\sigma)$		$g(t)$	
$f(\sigma) = A\sigma^n$	Norton	$g(t) = \left(1 + \eta t^{1/3}\right) e^{kt}$	Andrade (Primary Creep)
$f(\sigma) = B\left(\sinh(\beta\sigma)\right)^m$	Garofalo		
$f(\sigma) = C\, e^{c\sigma}$	Dorn	$g(t) = t$	Stead-State (Secondary Creep)
$f(\sigma) = D \sinh(d\sigma)$	Prandtl	$g(t) = \eta\, t^n$	Bailey (Tertiary Creep)

where A, B, C, D, β, c, d, m, n η are constants, t is time, and k is reproductive factor

Two common regression types, power law and hyperbolic law, used for creep model are discussed here. The Norton power law [27] [42] [43], given by:

$$\dot{\varepsilon}_c = A\sigma^n\, e^{(-Q/RT)} \tag{2.6}$$

where A is material constant, σ is applied stress, and n is stress exponent. The activation energy, Q, and the stress exponent, n, change with creep mechanism and can be interpreted as functions of temperature and applied stress. This type of power law model works well with steady creep rate, but has application limitation in high-stress region [27] where a breakdown in the creep rate-stress relationship can be observed due to the creep strain rate is an exponential function of stress rather than a power law function [38] [44]. The creep strain rate in high-stress region can be expressed as:

$$\dot{\varepsilon}_c = C\, e^{(c\sigma)} \tag{2.7}$$

The steady-state creep deformation of solder materials at high homologous temperature generally exhibits different characteristic behavior at different stress levels [45]. As shown in Figure 2.1, four distinct straight-line segments can be observed where

the dominant deformation mechanisms can be categorized as [46]: (1) Nabarro-Herring matrix-diffusion creep (region 1), (2) superplasticity caused by grain boundary sliding (region 2), and, (3) climb-controlled dislocation creep (region 3), and (4) power-law breakdown creep (region 4). The first three mechanisms occur at low- and medium-stress level regions while the fourth mechanism occurs at high-stress level region that having a more rapid increment in shear stresses, and where the power law breaks down. It was reported in Shine et al.'s work [47], the exponent, *n*, for Sn37Pb has a value of 1.6 to 2 for low-stress level dominated by grain boundary and a value of 5 to 12.5 for high-stress level dominated by matrix deformation. For lead free solder alloys, Song et al. [48] concluded the steady-state creep rates can be separated into two regimes with different stress exponents by their investigation from three lead free solder joints: Sn3.5Ag, Sn3Ag0.5Cu, and Sn0.7Cu solders. The low-stress exponents range from 3.5 to 6.6 while the high-stress exponents range from 8.9 to 10.7. Similar reports of two regimes exponents can be found in literature [49] [50] [51].

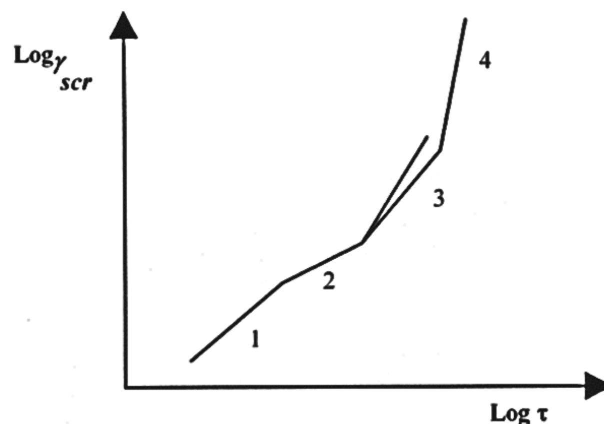

Figure 2.1 Schematic of a Log-Log Plot of the Strain Rate versus the Shear Stress

One of the solutions for power law breakdown is describing the relationship of creep strain rate-shear stress, alternatively, by a hyperbolic sine (sinh) law (Garofalo model [52]), given by:

$$\dot{\varepsilon}_c = B\left(\sinh(\beta\sigma)\right)^m e^{(-Q/RT)} \tag{2.8}$$

where B and m are material constants, and β prescribes the stress level at which the power law dependence breaks down. Darveaux et al. [38] have published a set of sine law constants for four different alloys including Sn40Pb, Sn36Pb2Ag, Pb2.5Sn, and Sn3.5Ag. By comparing the creep deformation predicted by the hyperbolic sine model with the experimental results, the model was found to be able to predict the creep deformation at the intermediate temperature regime for the entire stress range, but slightly misestimate at low and high temperatures [38] [53]. As listed in Table 2.3, many researchers have successfully applied hyperbolic sine model on both eutectic SnPb solder and lead free solder.

Another model for improving the inadaptability of power law at high stress level is the double power law model. Two regimes model of steady-state creep assumes the dominant creep mechanisms at low-stress and high-stress levels are grain boundary (sliding) and matrix deformation (dislocation movement), respectively [47] [50] [54] [55] [56]. Both grain boundary creep and matrix creep can be represented by a power law expression. As the equation of double power law given in eq. (2.9) and as illustrated in Figure 2.2, the first term corresponds to the grain boundary creep while the second term corresponds to the matrix creep.

$$\dot{\varepsilon}_c = A_{GB}\sigma^{n_{GB}} e^{(-Q_{GB}/RT)} + A_{MC}\sigma^{n_{MC}} e^{(-Q_{MC}/RT)} \tag{2.9}$$

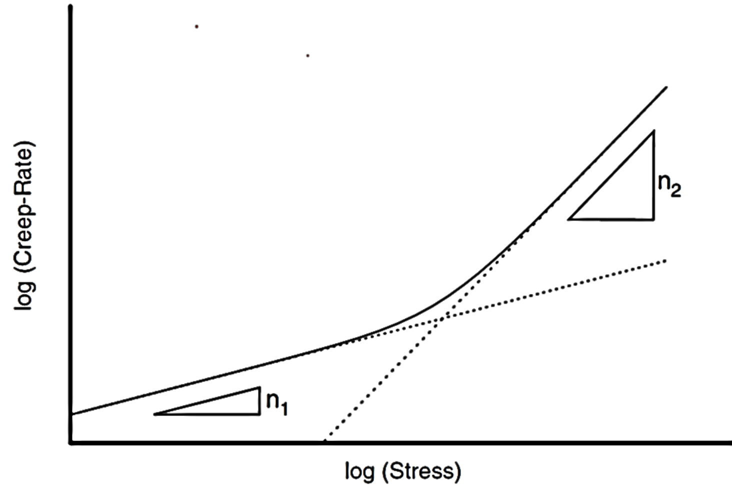

Figure 2.2 Schematic Plot of the Contributions from Different Mechanisms on Creep Rate versus Stress Relationship

In a similar framework, Shi et al. [53] derived a new unified dislocation-controlled creep constitutive model based on hyperbolic sine model, eq. (2.8) as:

$$\frac{d\gamma}{dt} = B_l \frac{G}{T}\left(\sinh\left(\beta_d \frac{\tau}{G}\right)\right)^{m_l} e^{(-Q_l/RT)} + B_h\left(\sinh\left(\beta_d \frac{\tau}{G}\right)\right)^{m_h} e^{(-Q_h/RT)} \tag{2.10}$$

where B_l and B_h are constants, β_d is a parameter related to power law breakdown, m_l and m_h are the stress exponents, and the term *G*/*T* is introduced to take into account the temperature effect. This model was found to have a better description of the creep deformation at different temperatures over a wide stress range.

Since creep is one of the most important material behaviors of solder materials, many creep models have been proposed and modified as seen in literature [38] [53] [57]. The current popular stead-state creep models for solder materials have been summarized

in Table 2.2 [58]. Based on above steady-state constitutive models, material parameters can be determined directly from the experimental data and numerical fitting. As listed in Table 2.3, some studies [25] [44] [59] [60] have summarized the material parameters of these major types of creep models for both leaded and lead free solder alloys. It is worth mentioning these phenomenological/empirical constitutive models have geometry dependent constants [26], which values may differ for the same solder alloy from different experimental setups.

Table 2.2 Popular Stead-State Creep Models for Solder Materials [58]

Classification (Type)	Model	Equations
Exponential dependence on temperature; Power-law dependence on stress	Norton [42]	$\dot{\varepsilon}_c = A\sigma^n e^{(-Q/RT)}$
Power-exponential dependence on temperature; Power-law dependence on grain size and on stress	Modified Norton [61]	$\dot{\varepsilon}_c = \frac{AGb}{RT}\left(\frac{b}{d}\right)^p\left(\frac{\tau}{G}\right)^n D_0 e^{(-Q/RT)}$
Two terms model with exponential dependence on temperature; Power law dependence on stress (different dependencies at low and high stresses)	Modified Norton [54] [62]	$\dot{\varepsilon}_c = A_{GB}\sigma^{n_{GB}} e^{(-Q_{GB}/RT)} + A_{MC}\sigma^{n_{MC}} e^{(-Q_{MC}/RT)}$
Exponential dependence on both temperature and stress	Modified Dorn [63]	$\dot{\varepsilon}_c = Ae^{(c\sigma)}\, e^{(-Q/RT)}$
Exponential dependence on Temperature; Hyperbolic sine dependence on stress	Garofalo [52]	$\dot{\varepsilon}_c = B(\sinh(\beta\sigma))^m e^{(-Q/RT)}$

Table 2.3 Creep Model Constants for Different Solder Materials

Constitutive Model	Solder Alloy	A (s^{-1})	n	Q (kJ/mol)	References
Norton Power Law	Sn40Pb	1.1×10^{-12}	6.3	20	Mei [64]
	Sn3.5Ag	5×10^{-6}	11	79.8	Wiese [62]
		2×10^{-6}	11	73.2	Wiese [65]
		6×10^{-25}	20	74.9	Wiese [65]
		9.44×10^{-5}	6.05	61.1	Clech [66]
		9.3×10^{-5}	6.05	61.2	Frear [67]
		6.62×10^{-5}	12	108.5	Mavoori [68]
	Sn3.8Ag0.7Cu	6×10^{-23}	19	84.2	Wiese [65]
		1×10^{-12}	13	75.2	Wiese [65]
		2.6×10^{-5}	3.69	36	Frear [67]
	Sn4.0Ag0.5Cu	2×10^{-21}	18	83.1	Wiese [62]
		8×10^{-11}	12	74.8	Wiese [65]

Constitutive Model	Solder Alloy	B (s^{-1})	β (MPa^{-1})	m	Q (kJ/mol)	References
Garofalo Hyperbolic Sine Law	Sn37Pb	0.158	0.406	1.38	50	Xiao [57]
		10	0.2	2	44.9	Wiese [69]
		1999.4	0.2	2.1	54.1	Zhang [70]
		131.9	0.118	3.11	52.9	Pang [71]
		1.09×10^{7}	0.07	3.16	78.3	Amagai [72]
		1.15×10^{4}	0.2	2.2	59.3	Zhang [32]
	Sn40Pb	2.48×10^{4}	0.0793	3.04	56.9	Stephens [73]
		2.78×10^{5}	0.116	3.3	67	Darveaux [74]
	Sn3.5Ag	178.6	0.115	4.75	57.1	Wiese [62]
		1044	0.0615	4.89	57	Clech [66]
		8.18×10^{11}	0.0266	8.67	77.4	Clech [66]
		3.77×10^{5}	0.0983	5.55	74.5	Clech [66]
		9.84×10^{4}	0.103	6.65	79.5	Hong [75]
		2.46×10^{5}	0.0914	5.5	72	Darveaux [74]
	Sn3.0Ag0.5Cu					
	Sn3.9Ag0.6Cu	0.184	0.221	2.89	62.0	Xiao [57]
		4.41×10^{5}	0.005	4.2	45	Vianco [76]
		248.4	0.188	3.79	62.9	Zhang [70]
		1.5×10^{3}	0.19	4.0	71.3	Zhang [32]
	Sn3.8Ag0.7Cu	3.2×10^{4}	0.037	5.1	54.3	Pang [43]
		501.3	0.0316	4.96	45.2	Pang [71]
	Sn3.8Ag1Cu	2.6×10^{-3}	0.185	3.0	38.7	Wiese [62]
	Sn3.5Ag0.75Cu	4.61×10^{6}	0.038	6.17	70	Amagai [72]

	Sn2Ag0.5Cu	2.42×10^{7}	0.043	5.95	70	Amagai [72]
	Combining Sn3.8Ag0.7Cu, Sn3.0Ag0.5Cu, Sn2.5Ag0.8Cu 0.5Sb	2631	0.0453	5.0	59	Vianco [51]
	Combining Sn3.8Ag0.7Cu, Sn3.5Ag0.75Cu, Sn0.5Ag0.5Cu, Castin™	2.78×10^{5}	0.0245	6.41	52	Schubert [77]

Constitutive Model	Solder Alloy	Constants						References
Double Power Law		A_{GB} (s^{-1})	n_{GB}	Q_{GB} (kJ/ mol)	A_{MC} (s^{-1})	n_{MC}	Q_{MC} (kJ/ mol)	
	Sn3.5Ag	1.5×10^{-4}	3.5	53.1	7×10^{-5}	11	92.4	Wiese [55]
	Sn4.0Ag0.5Cu	1×10^{-4}	3	34.6	1×10^{-12}	12	61.1	Wiese [55]
	SnPb	1.4×10^{-6}	1.96	46.0	2.4×10^{3}	7.1	77.6	Shi [53]

Constitutive Model	Solder Alloy	B_l	m_l	Q_l	B_h	m_h	Q_h	β_d	References
Double Sine Law	SnPb	2×10^{-5}	5	48.5	0.25	3	81.5	1289	Shi [53]

2.1.1.3 Elastic-Creep Based Constitutive Models

Similar to elastic-plastic model, the creep models still need to work with elastic deformation to describe the inelastic deformation of solder materials. There are two categories of creep-based constitutive models: (1) elastic-creep model and (2) elastic-plastic-creep model. Elastic-creep (Creep) model considering inelastic deformation is caused by creep phenomena only and the total strain can be written as:

$$\varepsilon = \varepsilon_e + \varepsilon_c \tag{2.11}$$

For the problem regarding slow rate loading and lower stress, it is reasonable to consider creep behavior as dominant effect while the effect of plastic is not significant [34].

Elastic-plastic-creep (EPC) model combines time-independent elastic-plastic model and time-dependent creep model as a more accurate and realistic constitutive model for solder materials. The total strain of EPC model can be expressed by following eq. (2.12).

$$\varepsilon = \varepsilon_e + \varepsilon_p + \varepsilon_c \tag{2.12}$$

and the secant modulus can be expressed as:

$$\frac{1}{E_{\sec}} = \frac{\varepsilon_e}{\sigma} + \frac{\varepsilon_p}{\sigma} + \frac{\varepsilon_c}{\sigma} \tag{2.13}$$

Pang [78] mentioned that the contribution of the time-dependent creep strain decreases as increasing the strain rate. Similarly, the contribution of the time-

independent plastic strain decreases as decreasing the stress level of taking the slope on the stress-strain curve for calculating secant modulus.

In separate works, Pang et al. [79] [80] have proposed two simulation methods: (1) dwell creep method, and (2) full creep method, utilizing EPC model to analyze the inelastic behavior of solder material subjected to thermal cycling. These two methods are illustrated as follows:

1. Dwell creep method: Time-independent EP model was implemented at temperature ramp while creep model is only used at dwell period. The dwell creep method in relation to temperature cycling profile is shown in Figure 2.3

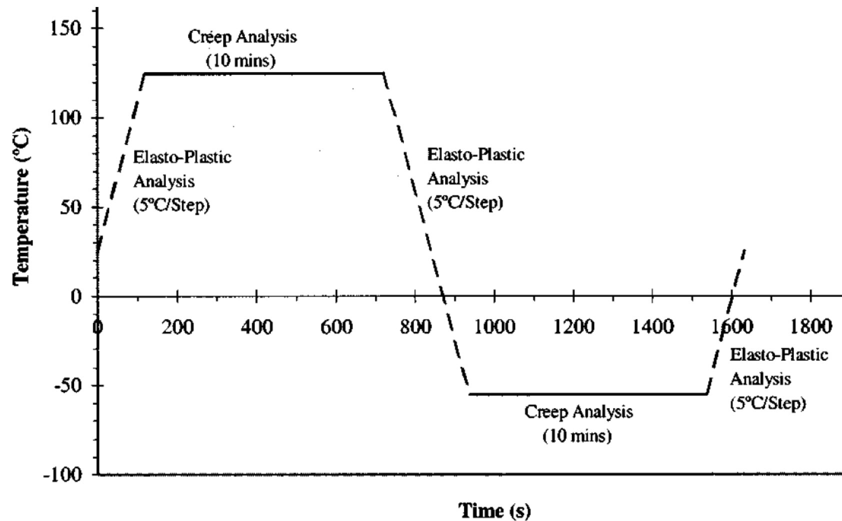

Figure 2.3 Dwell Creep Method in Relation to Temperature Cycling Profile [80]

2. Full creep method: Time-independent EP model and time-dependent creep model are implemented at temperature ramp by using alternate increments. The alternate increments, shown in Figure 2.4, can be described as: in a

small temperature-time range, the temperature-time profile was transformed as a step function. Thus, analysis for a ramp can be divided as two analyses alternately between a small temperature step for elastic-plastic analysis and then a time step for creep analysis.

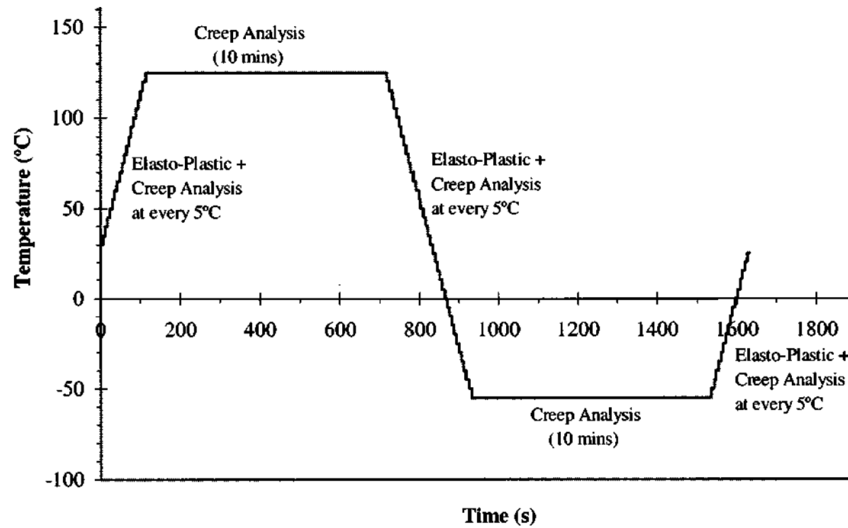

Figure 2.4 Full Creep Method in Relation to Temperature Cycling Profile [80]

In their comparisons [79] [80], the fatigue lives predicted by dwell creep method were much longer than by the full creep method. Hence, they recommended to use the full creep method for thermal cycling analysis and chose EPC model for describing solder material property. In another work, Zhang et al. [45] presented a similar analysis on Sn3.9Ag0.6Cu solder at 125 $^{\circ}$C with two strain rates (1.1×10^{-1} and 4.4×10^{-4} sec^{-1}). Figure 2.5 shows the EPC model performed better agreements correlated to the experimental data than other models in both low and high strain rates.

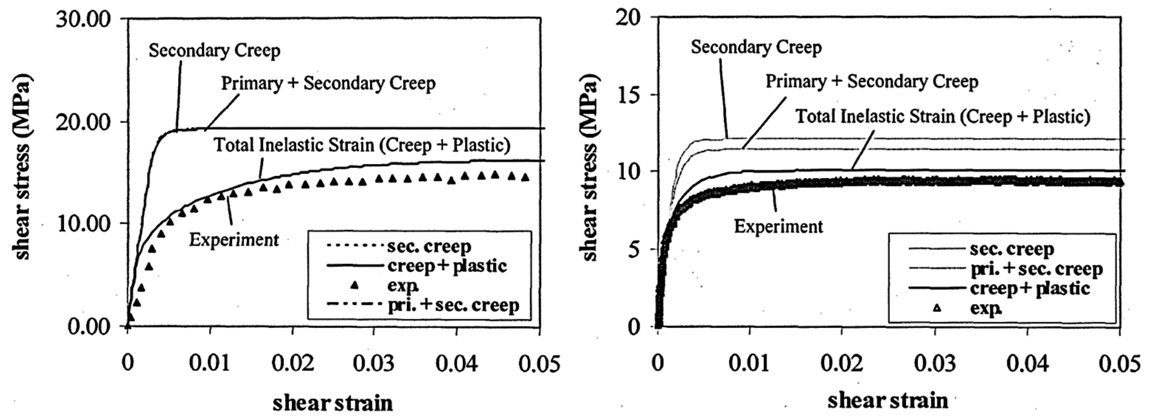

Figure 2.5 Monotonic Test Simulation: Sn3.9Ag0.6Cu, at 125°C, 1.1×10^{-1} sec^{-1} Strain Rate (Left), and 4.4×10^{-4} sec^{-1} Strain Rate (Right) [45]

The methods of determining the plastic strain component consider the resultant of the subtraction of the total strain and the creep strain, no matter using experimental approach [54] or hybrid numerical and experimental approach [45]. However, since creep deformation is temperature- and time- dependent and it can be developed in any stress level for solder materials, it is difficult to separate time-independent plastic strain and time-dependent creep strain [25] [27] [34] [81]. In addition, it has been reported in literature [82] that creep behavior is intimately linked to prior and concurrent plasticity and vice versa in the regime of viscous deformation. Thus, classical decoupled creep and plasticity models, even modeled with temperature-dependent parameters, often yield unsatisfactory strain magnitude due to they cannot capture the interaction effect [26] [83]. Alternately, unified inelastic strain model has emerged and become more popular than other models in this era.

2.1.2 Unified Constitutive Models

In the unified inelastic strain model, the total strain can be expressed as the summation of elastic and inelastic strain terms:

$$\varepsilon = \varepsilon_e + \varepsilon_{in} \tag{2.14}$$

The unified constitutive model still differentiates between elastic and inelastic strains, but integrates creep and plastic deformations into a single inelastic term which is expressed in terms of internal state variables [32]. Several unified inelastic strain models have been introduced [84] [85] [86] [87]. Among all, the Anand Model is the most widely accepted unified constitutive model in the electronic packaging area.

2.1.2.1 Anand Model

The Anand model [84] [88], introduced for modeling the deformation of metals under high homologous temperatures, has been widely used to represent the deformation of solder joints during reflow and subsequent reliability temperature cycles. An averaged isotropic resistance to plastic flow (such as dislocation density, solid solution hardening, grain size effects, etc.) can be represented by an internal variable s. It unifies the creep and rate-independent plastic behavior of the solder by making use of a stress equation, a flow equation, and an evolution equation. The model needs no explicit yield condition and no loading/unloading criterion. The deformation resistance is proportional to the equivalent stress.

$$\sigma = c\,s, c < 1 \tag{2.15}$$

where σ is the equivalent stress for the steady plastic flow, s is the deformation resistance which has the dimensions of stress and c is a function of strain rate and temperature expressed as:

$$c = c(\dot{\varepsilon}_{in}, T) = \frac{1}{\xi} \sinh^{-1}\left(\left[\frac{\dot{\varepsilon}_{in}}{A} e^{(Q/RT)} \right]^m \right) \tag{2.16}$$

where $\dot{\varepsilon}_{in}$ is the inelastic strain rate, A is the pre-exponential factor, ξ is the multiplier of stress, m is the strain rate sensitivity, Q is the activation energy, R is the universal gas constant, and T is the absolute temperature, respectively. Substitution of eq. (2.16) into (2.15) gives the equivalent stress as:

$$\sigma = \frac{s}{\xi} \sinh^{-1}\left(\left[\frac{\dot{\varepsilon}_{in}}{A} e^{(Q/RT)} \right]^m \right) \tag{2.17}$$

Rearranging eq. (2.17) and solving for the strain rate yields the flow equation of the Anand model:

$$\dot{\varepsilon}_{in} = A e^{(-Q/RT)} \left[\sinh\left(\xi \frac{\sigma}{s} \right) \right]^{1/m} \tag{2.18}$$

The differential form of the evolution equation for the internal variable s is assumed to be of the form:

$$\dot{s} = h(\sigma, s, T)\dot{\varepsilon}_{in} - \dot{r}(s, T) \tag{2.19}$$

where $h(\sigma, s, T)$ is associated with strain hardening and recovery processes, while static recovery is accommodated through the function $\dot{r}(s, T)$. However, results from loading test on solder materials showed that the contribution of the static recovery can be neglected. Then, the evolution eq. (2.19) is represented as

$$\dot{s} = h(\sigma, s, T)\,\dot{\varepsilon}_{in} \tag{2.20}$$

The hardening function $h(\sigma, s, T)$ has the following form:

$$h = h_0 \left| 1 - \frac{s}{s^*} \right|^a \mathrm{sign}\left(\left| 1 - \frac{s}{s^*} \right| \right), a > 1 \tag{2.21}$$

where h_0 the hardening constant and a is the strain rate sensitivity of the hardening process, s^* is the saturation value of s. From eqs. (2.20) and (2.21), $\dot{s}$ can be rewritten as:

$$\dot{s} = \left[h_0 \left| 1 - \frac{s}{s^*} \right|^a \mathrm{sign}\left(\left| 1 - \frac{s}{s^*} \right| \right) \right] \dot{\varepsilon}_{in} \quad , a > 1 \tag{2.22}$$

where

$$s^* = \hat{s} \left[\frac{\dot{\varepsilon}_{in}}{A} e^{(Q/RT)} \right]^n \tag{2.23}$$

where $\hat{s}$ is a coefficient and n is the strain rate sensitivity of the saturation value of the deformation resistance. From eqs. (2.17) and (2.23), saturation stress can be written as:

$$\sigma^* = \frac{\hat{s}}{\xi}\left[\frac{\dot{\varepsilon}_{in}}{A}e^{(Q/RT)}\right]^n \sinh^{-1}\left(\left[\frac{\dot{\varepsilon}_{in}}{A}e^{(Q/RT)}\right]^m\right) \tag{2.24}$$

The above equation relates to the saturation stress, temperature, and plastic strain rate. For isothermal, and $s^* > s$ conditions, eqs. (2.15) and (2.21) given by:

$$\frac{d\sigma}{d\varepsilon_{in}} = c\,h_0\left|1-\frac{\sigma}{\sigma^*}\right|^a \text{sign}\left(1-\frac{\sigma}{\sigma^*}\right), a > 1 \tag{2.25}$$

The integrated form of (2.25) is:

$$\sigma = \sigma^* - \left[(\sigma^* - \sigma_0)^{(1-a)} + (a-1)\,c\,h_0(\sigma^*)^{-a}\,\varepsilon_{in}\right]^{1/(1-a)}, a \neq 1 \tag{2.26}$$

or

$$s = s^* - \left[(s^* - s_0)^{(1-a)} + (a-1)h_0(s^*)^{-a}\,\varepsilon_{in}\right]^{1/(1-a)}, a \neq 1 \tag{2.27}$$

where $\sigma_0 = c \cdot s_0$ and s_0 is the initial value of s.

Combining eqs. (2.23) and (2.27) results in an evolution equation for the internal variable s in terms of the plastic strain and plastic strain rate:

$$s = \hat{s}\left[\frac{\dot{\varepsilon}_{in}}{A}e^{(Q/RT)}\right]^n - \left[\begin{array}{l}\left(\hat{s}\left[\frac{\dot{\varepsilon}_{in}}{A}e^{(Q/RT)}\right]^n - s_0\right)^{(1-a)} \\ +(a-1)h_0\left(\left[\hat{s}\,(\frac{\dot{\varepsilon}_{in}}{A}e^{(Q/RT)}\right]^n\right)^{-a}\varepsilon_{in}\end{array}\right]^{1/(1-a)} \tag{2.28}$$

or

$$s = s\left(\dot{\varepsilon}_{in}, \varepsilon_{in}\right) \tag{2.29}$$

The final versions of the Anand model equations are the stress equation in eq. (2.17), the flow equation in eq. (2.18), and the integrated evolution equation in eq. (2.28). These expressions include nine material parameters: A, ξ, Q/R, m in eqs. (2.17), (2.18), and constants h_0, a, s_0, s, and n in eq. (2.28).

The post yield uniaxial stress-strain relations predicted by the Anand model are obtained by substituting the expression for internal variable 's' from eq. (2.28) into the stress equation in eq. (2.17). This calculation results in [89]:

$$\sigma = \frac{1}{\xi}\sinh^{-1}\left(\left[\frac{\dot{\varepsilon}_{in}}{A}e^{(Q/RT)}\right]^m\right) \cdot \left\{\begin{array}{l}\hat{s}\left[\frac{\dot{\varepsilon}_{in}}{A}e^{(Q/RT)}\right]^n - \\ \left[\left(\hat{s}\left[\frac{\dot{\varepsilon}_{in}}{A}e^{(Q/RT)}\right]^n - s_0\right)^{1-a} + (a-1)\varepsilon_{in}\left(h_0\left(\hat{s}\left[\frac{\dot{\varepsilon}_{in}}{A}e^{(Q/RT)}\right]^n\right)^{-a}\right)\right]^{1/(1-a)}\end{array}\right\} \tag{2.30}$$

or

$$\sigma = \sigma\left(\dot{\varepsilon}_{in}, \varepsilon_{in}\right) \tag{2.31}$$

For a uniaxial tensile test performed at fixed (constant) strain rate and constant temperature T, this expression represents highly nonlinear stress-strain behavior (power law type function) after yielding:

$$\sigma = \sigma\left(\varepsilon_{in}\right) \tag{2.32}$$

Anand model predictions for the yield stress, σ_Y, and the UTS, Ultimate Tensile Strength = maximum/saturation stress, can be obtained by considering limiting cases of eq. (2.30). The UTS is given by the limit as ε_{in} goes to ∞:

$$UTS = \sigma\Big|_{\varepsilon_{in}\to\infty} = \frac{\hat{s}}{\xi}\left[\frac{\dot{\varepsilon}_{in}}{A}e^{(Q/RT)}\right]^{n}\sinh^{-1}\left(\left[\frac{\dot{\varepsilon}_{in}}{A}e^{(Q/RT)}\right]^{m}\right) \equiv \sigma^{*} \tag{2.33}$$

while the yield stress is given by the limit as ε_{in} goes to 0:

$$\sigma_Y = \sigma\Big|_{\varepsilon_{in}\to\infty} = c\, s_0 = \frac{1}{\xi}\sinh^{-1}\left(\left[\frac{\dot{\varepsilon}_{in}}{A}e^{(Q/RT)}\right]^{m}\right)\cdot s_0 \equiv \sigma_0 \tag{2.34}$$

Using the saturation stress (σ^{*} = UTS) relation in eq. (2.33), the post yield stress-strain response (power law) in eq. (2.30) can be rewritten as:

$$\sigma = \sigma^* - \left[\left(\sigma^* - c\, s_0 \right)^{1-a} + (a-1)\varepsilon_{in} \left(c\, h_0 \left(\sigma^* \right)^{-a} \right) \right]^{1/(1-a)} \tag{2.35}$$

One method to obtain the values of these parameters for a specific material is to perform a series of stress-strain tests over a wide range of temperatures and strain rates. From the measured data, the value of the saturation stress can be obtained for several strain rates and temperatures. In addition, the stress-strain (σ, ε) data for each temperature and strain rate can be recast as stress vs. plastic strain data $(\sigma, \varepsilon_{in})$ by using:

$$\varepsilon_{in} = \varepsilon - \frac{\sigma}{E} \tag{2.36}$$

where E is the initial elastic modulus of the material at the specific temperature and strain rate being considered. The Anand model parameters can be obtained by following procedure:

(1) Determine the values of the parameters $\hat{s}$, ξ, A, Q/R, n and m by nonlinear regression fitting of eq. (2.33) to the saturation stress vs. strain rate and temperature data.

(2) Determine the values of parameters s_0, h_0, and a by nonlinear regression fitting of eq. (2.35) to the stress vs. plastic strain data at several strain rates and temperatures.

The Anand model constants for common solder materials are listed in Table 2.4.

Table 2.4 Anand Model Constants for Common Solder Alloys

Anand Constant	s_0	Q/R	A	ξ	m	h_0	$\hat{s}$	n	a	Reference
Units	MPa	K	sec^{-1}	-	-	MPa	MPa	-	-	
SAC105	7.5	8,850	6,900	4	0.215	137,500	25.1	0.0062	1.96	[90]
SAC205	16.5	9,090	4,300	4	0.238	169,000	29	0.0087	1.84	[90]
SAC305	21	9,320	3,501	4	0.25	180,000	30.2	0.01	1.78	[90]
SAC405	23.65	9,580	3,175	4	0.263	183,000	31.3	0.011	1.77	[90]
Sn3.5Ag†	-0.0673T +28.6	10,255	1.77×10^3	7	0.207	T and $\dot{\varepsilon}_{in}$ dependent	52.4	0.0177	1.6	[91]
Sn3.5Ag	0.65	6,523	344	3	0.143	23,241	26	0.0447	1.46	[92]
Sn0.7Cu†	4.43	5,824	764	2	0.123	11,656	26.4	0.043	2.33	[92]
SAC305	2.45	6,053	717	2	0.13	14,560	29	0.0436	2.22	[92]
Sn92.5Pb2.5Ag	33.07	11,010	105200	7	0.241	1,432	41.63	0.002	1.3	[93]
Sn40Pb	56.33	10,830	1.49×10^7	11	0.303	2,640.75	80.42	0.0231	1.34	[93]
Sn3.5Ag	39.09	8,900	2.23×10^4	6	0.182	3,321.15	73.81	0.018	1.82	[93]
Sn3.8Ag0.7Cu	3.299	9,883	15.77	1.067	0.3686	1,076.9	3.15	0.035	1.68	[94]
Sn3.8Ag0.7Cu	22.64	7,619	107.65	59.36	4.03	9,002	86.28	0.0046	1.3	[95]
SAC105	2.348	8,076	3.77	0.995	0.4454	4,507.5	3.58	0.012	2.17	[94]
Sn37Pb	37.9	5,797	26	10	0.256	92,148	83.12	0.043	1.24	[35]
Sn36Pb2Ag	42.32	11,262	2.3e7	11	0.303	4,121.3	80.79	0.0212	1.38	[93]
SAC405	20	10,561	325	10	0.32	8×10^5	42.1	0.02	2.57	[96]
Sn3.8Ag0.7Cu	37.1	6,656	65.92	8	0.346	86,442.8	80.8	0.0002	1.29	[78]
Sn0.7Cu	33.8	5,276	9875	2	0.176	61,987.3	65.2	0.003	1.03	[78]
Sn37Pb	N/A	9,400	1.09×10^7	0.07	0.316	2,884	0.998	1.37×10^{-5}	1.26	[72]
Sn36Pb2Ag	N/A	9,400	8.49×10^6	0.065	0.322	2,951	0.99	6.71×10^{-4}	1.33	[72]

† Modified Anand model constants

Anand Constant	s_0	Q/R	A	ξ	m	h_0	$\hat{s}$	n	a	Reference
Units	MPa	K	sec^{-1}	-	-	MPa	MPa	-	-	
Sn3.5Ag0.75Cu	N/A	8,400	4.61×10^{6}	0.038	0.162	3,090	1.04	4.6×10^{-3}	1.56	[72]
SAC205	N/A	8,400	2.42×10^{7}	0.043	0.168	3,162	1.005	8.1×10^{-4}	1.59	[72]
Sn2Ag0.5Cu	6.6	8,500	500	4.3	0.16	6,100	28.7	0.04	1.3	[97]
Sn3.38Ag0.84Cu	1.3	9,000	500	7.1	0.3	5,900	39.4	0.03	1.4	[97]
Sn3.8Ag0.7Cu	3.3	9,883	15.77	1.067	0.369	1,076.9	3.15	0.0352	1.683	[94]
SAC105	2.3	8,076	3.77	0.995	0.445	4,507.5	3.58	0.012	2.167	[94]
Sn3.5Ag	7.17	29,800	0.0034	2.48	0.03	2,080	5.8	0.0068	1.41	[98]
Sn3.5Ag†	12.92+ 0.004T	11449+ 21.5T	4×10^{6}- 2e4T	1.98- 0.0038T	0.314- 0.0015T	114.4- 0.295T	7.55+ 0.005T	0.04- 1.7×10^{-5}T	0.035+ 3.9×10^{-4}T	[98]
Sn3.8Ag0.7Cu†	9.19+ 0.039T	6955+ 38.8T	1.37×10^{8} -7.6×10^{5}T	0.98- 5×10^{-4}T	0.073- $3\times10^{--4}$T	-3.4e5+ 1.5×10^{4}	64.91- 0.328T	-0.015+ 5.6×10^{-4}T	0.48+ 0.028T	[98]

† Modified Anand model constants

Che et al. [34] [99] have compared four different constitutive models, including EP model, Creep model, EPC model, and the Anand model, in the area of representing the material behaviors of the Sn3.8Ag0.7Cu solder. In their simulation results (Figure 2.6), the strain energy density calculated from EP model is lower than that from the other models due to the creep behavior was not considered in EP model. In contrast with other models, the strain energy density curve for EP model represents flat lines without increment in strain energy density at temperature dwell period. They concluded that the Creep, EPC, Anand models are suitable constitutive models for solder material undergoing thermal cycling loading.

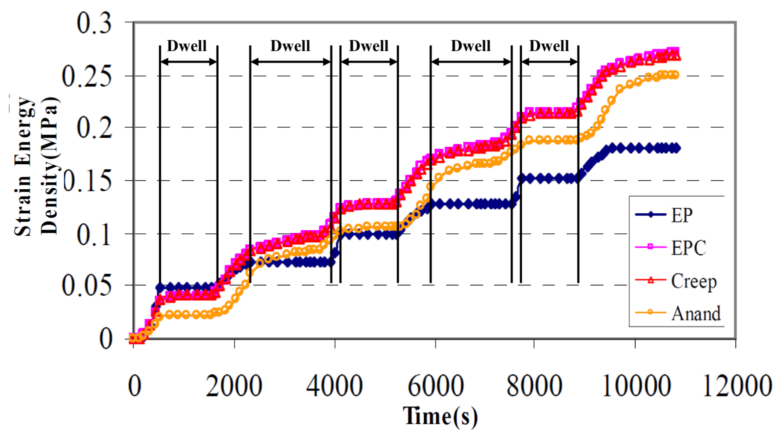

Figure 2.6 Strain Energy Density History for Different Constitutive Models [34]

Unlike the constitutive model involving time-independent plasticity term (e.g. EPC model), the Anand model does not rely on an explicit yield condition and loading/unloading criterion and an internal state variable, *s*, was used to present the resistance to inelastic deformations [72]. Thus, it makes researcher more convenient to utilize the Anand model to describe the material nonlinear behavior of solder alloy after nine required parameters are determined.

2.1.2.2 Modified Anand Models

Although the Anand Model has been widely used, one of drawbacks of Anand model has captured researcher's attention. Due to the Anand model uses only a single scalar as internal variable to describe the strain hardening, that lacks the definition of dynamic hardening rule to represent the Bauschinger effect and multi-axial stress-strain response, it is not feasible to apply the Anand model for the complex loading conditions (e.g. multi-axial or cyclic mechanical loading conditions) [27].

Chen et al. [91] [100] have developed a modified Anand model that involved using temperature and strain dependent strain hardening parameter h_0. They pointed out that the effect of work hardening has an intimate relation with constant parameter h_0, which assumed to be a constant in the original Anand model. They proposed using a function of strain rates and temperature instead of a constant to describe h_0 given as:

$$h_0 = a_0 + a_1 T + a_2 T^2 + a_3 \dot{\varepsilon}_{in} + a_4 \left(\dot{\varepsilon}_{in}\right)^2 \tag{2.37}$$

where T is temperature and a_0, a_1, a_2, a_3, a_4 are constants. They also found the relation of initial value of deformation resistance and temperature for Sn3.5Ag alloy can be quantitatively described as: $s_0 = -0.0673T + 28.6$. Note that the original methods to calculate the other parameters for the Anand model were not changed in this modified model. As shown in Figure 2.7, the modified performed a better agreement with experimental data of Sn3.5Ag solder at different temperatures. A similar study based on Chen's work has been done by Pei et al. [98]. They introduced linear temperature dependent variables for all Anand constants and elastic modulus, whereas there are twenty constants been used totally in Pei's modified Anand model.

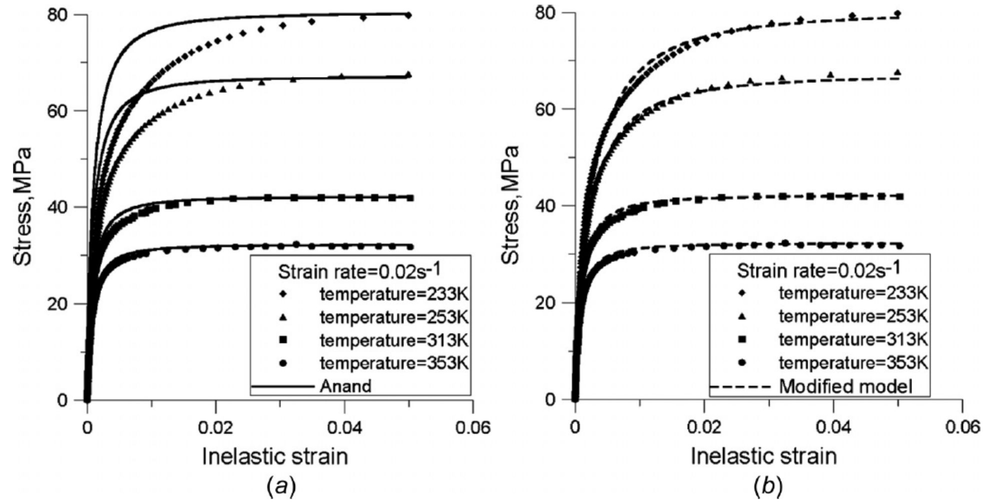

Figure 2.7 Comparison of Experiments and Predictions of Modified Anand Model for Sn3.5Ag Solder: (a) Anand Model and (b) Modified Anand Model [91]

Bai et al. [92] also proposed a modified Anand model where h_0 was set to be a function of strain rate:

$$h_0 = a_h \left(\frac{\dot{\varepsilon}_{in}}{A} \right)^{n_1} \left[e^{(Q/RT)} \right]^{n_2} \tag{2.38}$$

where a_h, n_1, and n_2 are material constants. Unlike Chen's model, the h_0 of the Bai's model can be expressed as a constant after calculation but the comparison between experiments and predictions for the Bai's modified Anand model shows somewhat away from experimental data at some temperature regions as shown in Figure 2.8.

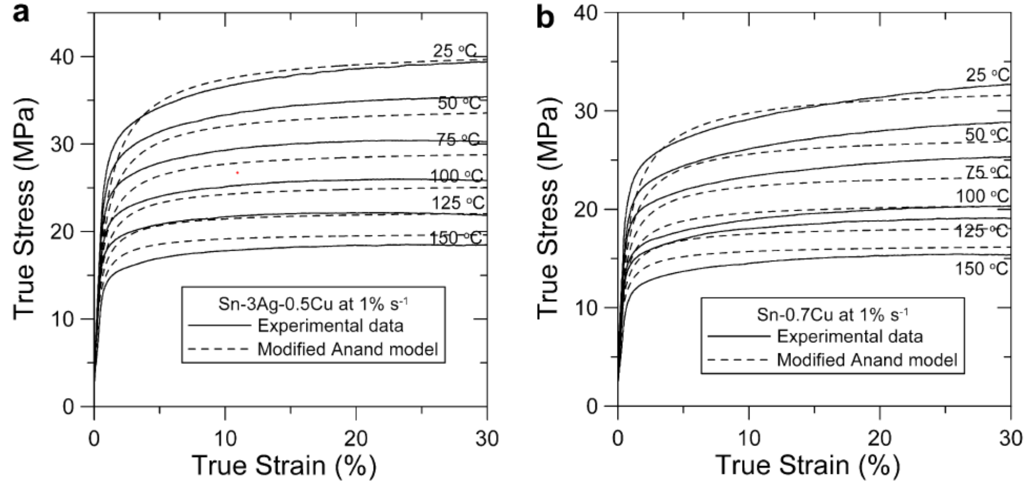

Figure 2.8 Comparisons of Experiments and Predictions of the Bai's Modified Anand Model with Different Temperatures for (a) Sn3Ag0.5Cu and (b) Sn0.7Cu [92]

2.1.2.3 Other Unified Inelastic Strain Models

In contract to Anand model, the Chaboche's model [101] [102] uses a power term without introducing explicitly temperature-dependent terms to describe inelastic strain rate given in eq. (2.39). In Chaboche's model, all the model parameters are temperature-dependent and must be identified in each temperature range.

$$\dot{\varepsilon}_{in} = \left\langle \frac{|\sigma - X| - r - y}{D} \right\rangle^n \tag{2.39}$$

and

$$r = q(1 - e^{-bp}) \tag{2.40}$$

where $\langle G \rangle = \max(G,0)$ is the Macauley brackets, D is drag stress, p is accumulated plastic strain, b and q being two coefficients depending on the material and on the

temperature, and y is the initial yield stress. Variable X represents the evolution law of the kinematic hardening. Therefore, the Chaboche's model can to take into account the influence of both kinematic and isotropic hardening effects.

The McDowell's model considers the dislocation motion mechanisms, the thermal effects, and kinematic hardening evolution equation [82] [101] given as:

$$\dot{\varepsilon}_{in} = \sqrt{\frac{3}{2}} A\,\Theta \left(\frac{\langle S_v \rangle}{D} \right)^n e^{B \frac{\langle S_v \rangle^{n+1}}{D}} N \tag{2.41}$$

$$\begin{cases} \Theta = e^{-Q/(RT)} & \text{for } T \geq T_m/2 \\ \Theta = e^{\frac{-2Q}{RT_m}\left(\ln\left(\frac{T_m}{2T}\right)+1\right)} & \text{for } T < T_m/2 \end{cases} \tag{2.42}$$

where Θ is a diffusivity parameter, T_m is melting temperature, N is the unit vector in the direct hardening direction, and A, B are material parameters. Variable S_v is the viscous overstress including both kinematic and isotropic hardening effects. The McDowell's model presents sixteen parameters to be determined while only six are temperature-independent parameters. Msolli et al. [101] have shown using these two viscoplastic models for describing Sn36Pb2Ag solder alloy had performed better results than Anand model in the areas of strain controlled cyclic response, jump test, and stress relaxation.

2.2 Temperature Effect

A temperature rise of ΔT results in a strain that depends on the coefficient of thermal expansion (CTE), α, of the material. A temperature change does not cause shear strains; thus contribute only to normal strain components.

$$\varepsilon_T = \begin{bmatrix} \varepsilon_x \\ \varepsilon_y \\ \varepsilon_z \\ \gamma_{xy} \\ \gamma_{xz} \\ \gamma_{yz} \end{bmatrix} = \begin{bmatrix} \alpha(T - T_0) - \alpha(T_i - T_0) \\ \alpha(T - T_0) - \alpha(T_i - T_0) \\ \alpha(T - T_0) - \alpha(T_i - T_0) \\ 0 \\ 0 \\ 0 \end{bmatrix} \tag{2.43}$$

where T_0 is a reference temperature and the terms T and T_i are the current and initial temperatures, respectively. The stress-strain equation, accounting for the thermal effect, can then be expressed as:

$$\sigma = C\varepsilon + C\varepsilon_T \tag{2.44}$$

2.3 Fatigue Models

Many efforts have been made for developing and applying the fatigue models to the fatigue life predictions of solder materials. Proposed models in the literature can be divided into four major categories, they are: (1) plastic strain based, (2) creep strain based, (3) energy based, and (4) damage based fatigue models [26] [30] [33] [44]. A remarkable work made by Lee et al. [26] have identified fourteen models in the literature, as listed in Table 2.5 which were developed based upon various assumptions, including the manner in which the physical and metallurgical aspects of fatigue are taken into account. Lee also pointed out that stress based model is based on the application of a force or stress to a component, causing a resultant strain. As a result, stress based model can be applied to vibration, physically shocked or stressed component but lack of prediction of fatigue life [103]. The objective of this section is to provide a

comprehensive review and the fundamental studies of the fatigue models used in low-cycle fatigue area for solder materials.

Table 2.5 Summary of Solder Fatigue Models [26]

Fatigue Model	Model Class	Parameters	Coverage	Applicability
Coffin-Manson	Plastic Strain	Plastic Strain	Low-Cycle Fatigue	All
Total Strain	Plastic + Elastic Strain	Strain Range	High- and Low-Cycle Fatigue	All
Solomon	Plastic Shear Strain	Plastic Shear Strain	Low-Cycle Fatigue	All
Engelmaier	Total Shear Strain	Total Shear Strain	Low-Cycle Fatigue	Leaded and Leadless, TSOP
Miner	Superposition (Plastic and Creep)	Plastic Failure and Creep Failure	Plastic Shear and Matrix Creep	PQFP, FCOB
Knecht and Fox	Matrix Creep	Matrix Creep Shear Strain	Matrix Creep Only	All
Syed	Accumulation of Creep Strain Energy	GBS Energy and MC Energy	Implies All Coverage	PBGA, SMD, NSMD
Dasgupta	Total Strain Energy	Energy	Joint Geometry Accounted For	LLCC, TSOP
Liang	Stress/Strain Energy Density	Energy	Constants from Isothermal Low-Cycle Fatigue Tests	BGA and Leadless Joints
Heinrich	Energy Density	Energy	Hysteresis Curve	BGA
Darveaux	Energy Density	Damage and Energy	Hysteresis Curve	PBGA, Leadless
Pan	Strain Energy Density	Strain Energy Density and Plastic Energy Density	Hysteresis Curve	LCCC
Stolkarts	Damage Accumulation	Damage	Hysteresis Curve & Damage Evolution	All
Norris and Landzberg	Temperature and Frequency	Temperature Frequency	Test Condition vs. Use Conditions	All

2.3.1 Plastic Strain Based Fatigue Models

The irreversible inelastic deformation, including the time-independent plastic strain and time-dependent creep strain, is the original of strain-based fatigue model [104]. The Coffin-Manson low-cycle fatigue model ($N_f < 10^4$ - 10^5 cycles) is the most widely used plastic strain fatigue model [105] [106]:

$$\frac{\Delta\varepsilon_p}{2} = \varepsilon'_f (2N_f)^k \text{ or } N_f = \frac{1}{2}\left(\frac{\Delta\varepsilon_p}{2\varepsilon'_f}\right)^{1/k} \tag{2.45}$$

where $\Delta\varepsilon_p$ is the plastic strain range, ε'_f is the fatigue ductility coefficient, N_f is the total number of cycles to failure, and k is the fatigue ductility exponent. In the same framework, Solomon [85] proposed another version of plastic strain fatigue model in terms of plastic shear strain, given by:

$$\Delta\gamma_p N_f^{\alpha} = \theta \tag{2.46}$$

where α and θ are constants, $\Delta\gamma_p$ is the plastic shear strain. Pang et al. [107] indicated that the creep deformation is negligible in eq. (2.46) and the constants are mainly due to the effects of plastic deformation only. Yang et al. [108] also mentioned that the Coffin-Manson model is useful for evaluating crack initiation, but it lacks ability to predict crack propagation.

The original version of plastic strain based fatigue model assumes that plastic deformation is dominant the fatigue failure and the elastic strains contribute only a small portion to fatigue failure. However, considering the high cycle fatigue, the magnitudes of

elastic strains are greater than plastic strains [109]. It is difficult to use plastic strain range for plastic strain based fatigue model although the damage still induced by plastic deformation. In this case, the total strain equation, as shown in eq. (2.47) , has the advantage of combining both high- and low-cycle fatigue life predictions into a single equation (Figure 2.9).

$$\frac{\Delta\varepsilon}{2} = \frac{\sigma'_f}{E}\left(2N_f\right)^b + \varepsilon'_f(2N_f)^k \tag{2.47}$$

where $\Delta\varepsilon$ is the total strain range, σ'_f is the fatigue strength coefficient, and E is the elastic modulus. Note that although the plastic strains cause fatigue damage, the amplitudes of plastic strains are much less than elastic strains in high cycle fatigue; the elastic strains are used to estimate fatigue life [109].

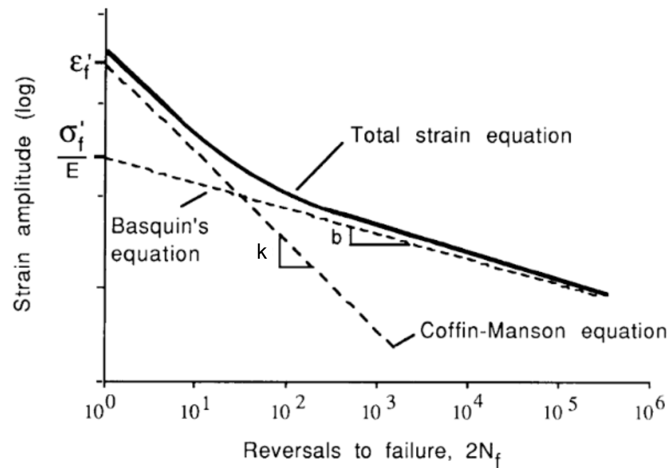

Figure 2.9 Schematic of Total Strain versus Life Equation [109]

The modified Coffin-Manson relation relating elastic and inelastic strains and lives can be applied for each of strain ranges where [110]:

$$\Delta\varepsilon_p = A'_p \left(N_p\right)^{c_p} \tag{2.48}$$

$$\Delta\varepsilon_c = A'_c \left(N_c\right)^{c_c} \tag{2.49}$$

$$\Delta\varepsilon_{in} = \Delta\varepsilon_p + \Delta\varepsilon_c \tag{2.50}$$

and fatigue life:

$$\frac{1}{N_f} = \frac{\Delta\varepsilon_p}{\Delta\varepsilon_{in}}\frac{1}{N_p} + \frac{\Delta\varepsilon_c}{\Delta\varepsilon_{in}}\frac{1}{N_c} \tag{2.51}$$

where A' and c are material constant, subscript *p,* c, and *in* stand for plastic, creep, and inelastic, respectively.

To consider the effect of cycling frequency, Coffin [111] has shown a modified Coffin-Masson model as below:

$$N_f = \frac{1}{\nu^{m-1}}\left(\frac{C}{\Delta\varepsilon_p}\right)^{1/k} \tag{2.52}$$

where ν is frequency and m is a frequency exponent. For $m = 1$, there is no dependence of the fatigue life with frequency variations. And when $m = 0$, the number of cycles to failure is halved when the frequency is halved due to a constant time to failure [112]. Shi et al. [113] showed the Sn37Pb bulk specimen is slightly frequency-dependent in the frequency range 10^{-3} to 1 Hz, but is strongly frequency-dependent in the lower frequency

range 10^{-4} to 10^{-3} Hz. It is also reported that the fatigue exponent, k, is independent of temperature, however, the ductility coefficient, C, is temperature dependent parameter while Shi examined the eq. (2.52) with experimental data. Shi also mentioned the approach that assumes C is an averaged value over a temperature range may result in a large error in fatigue life prediction.

In a separate work, Engelmaier [114] introduced a cyclic strain range, $\Delta\gamma$, (it extended to cyclic energy range in the later version) and the temperature- and cyclic frequency- dependent fatigue ductility exponent, k, to improve the Coffin-Manson model [115]. This original version of Engelmaier model can be expressed as:

$$N_f = \frac{1}{2}\left(\frac{\Delta\gamma}{2\varepsilon'_f}\right)^{1/k} \tag{2.53}$$

Engelmaier determined constants of eq. (2.53) for Sn37Pb solder using the correlations between the fatigue ductility exponent and both the solder joint temperature and the cyclic frequency. Thus, $2\varepsilon'_f \approx 0.65$

and

$$k = -0.442 - 6\cdot 10^{-4}\overline{T}_s + 1.74\cdot 10^{-2}\ln(1+f) \tag{2.54}$$

where $\overline{T}_s$ means cyclic solder joint temperature, f is cyclic frequency where $1 \le f \le 1000$ cycles/day.

2.3.2 Creep Strain Based Fatigue Models

It is commonly accepted that creep can be separated into two possible mechanisms, matrix creep and grain boundary creep, due to dislocation movement and grain boundary sliding, respectively [26]. Shine et al. [47] [116] have proposed a simple matrix creep fatigue model relating the solder microstructure and the matrix creep shear strain range as shown in eq. (2.55).

$$N_f = \frac{C}{\Delta\gamma_{mc}} \tag{2.55}$$

where N_f is the number of cycles to failure, C is a constant dependent on failure criteria and solder microstructure, and $\Delta\gamma_{mc}$ is the total integrated matrix creep per cycle. In [47], C is given as 125% for Sn37Pb, which may be interpreted as the creep exhaustion value or creep fatigue ductility of the samples.

Another important creep fatigue model was proposed by Syed [117] [118] [119] [120], he developed a fatigue model incorporating grain boundary sliding with matrix creep given in eq. (2.56),

$$C = N_f(Y_{GBS}\,\varepsilon_c^{I} + Y_{MC}\,\varepsilon_c^{II}) \tag{2.56}$$

where C is a constant, ε_c^{I} and ε_c^{II} are the accumulated equivalent creep strain per cycle for grain boundary sliding and the matrix creep, respectively. The constants Y_{GBS} and Y_{MC} can be determined from two data points if the ε_c^{I} and ε_c^{II} and the cycle to failure are

known for these data point. Syed also gave the constants of eq. (2.56) for SnPb and SAC solder alloys as follows [119] [120]:

$$N_f = \left(0.022\,\varepsilon_c^{I} + 0.06\,\varepsilon_c^{II}\right)^{-1} \quad \text{for SnPb solder}$$
$$N_f = \left(0.013\,\varepsilon_c^{I} + 0.036\,\varepsilon_c^{II}\right)^{-1} \quad \text{for SAC solder} \tag{2.57}$$

It can be seen in eqs. (2.55) and (2.56), the Shine's and Syed's fatigue models considered creep deformation only while Solomon's fatigue model only considered plastic deformation. When considering the resultant fatigue life due to both plastic and creep deformations, it is necessary to consider the interaction between plastic and creep deformations. Dasgupta et al. [121] utilized Palmgren-Miner's linear superposition relation to computer the total energy dissipation per cycle, W_t, is given by:

$$W_t = W_e + W_p + W_c \tag{2.58}$$

where W_e, W_p, and W_c are energy dissipations per cycle for elastic, plastic, and creep, respectively. The estimated fatigue life, N_f, for constant amplitude cycle loading is given by:

$$\frac{1}{N_f} = \frac{1}{N_e} + \frac{1}{N_p} + \frac{1}{N_c} \tag{2.59}$$

where N_e, N_p, N_c are the fatigue lives calculated from elastic, plastic, and creep energies per cycle, respectively. In a similar framework, Pang et al. [107] have demonstrated

another resultant fatigue model combining the Solomon's equation and the Shine's equation. This fatigue model, eq. (2.60), can be expressed as follows:

$$\frac{1}{N_f} = \frac{1}{N_p} + \frac{1}{N_c} \tag{2.60}$$

where N_p is the fatigue life estimated using eq. (2.46) and N_c is the creep life estimated using eq. (2.55). The comparison [107] between plastic strain based (Solomon and Engelmaier fatigue models) and creep strain based (Shine and Pang fatigue models) showed the results for plastic strain based models have a significant different than for creep strain based models.

2.3.3 Energy Based Fatigue Models

Similar to strain-based fatigue models, Morrow [122] has shown that the energy-based fatigue model can be expressed as:

$$\Delta W = W_f' \,(2N_f)^{b+c} \text{, or } N_f = \frac{1}{2}\left(\frac{\Delta W}{W_f'}\right)^{1/(b+k)} \tag{2.61}$$

where b is fatigue strength exponent, k is fatigue ductility, ΔW is plastic strain energy density per cycle, and W_f' is the intercept energy term. Che et al. [31] have compared fatigue lives computed by the Coffin-Manson strain-based and Morrow energy-based fatigue models for Sn3.8Ag0.7Cu solder joints mounted on a PBGA assembly. They showed the Morrow model predicted a more accurate solder joint fatigue life than Coffin-

Manson model compared to experimental test results. Similar report can be found in Darveaux et al.'s work [74].

In order to capture the effects of frequency and temperature, Solomon et al. [123] proposed a frequency-modified energy model as shown below:

$$N_f = \frac{1}{\nu^{m-1}}\left(\frac{\nu^q C}{\Delta W_p}\right)^{1/k} \tag{2.62}$$

where ν is frequency, m is a frequency exponent which is determined from the relationship between fatigue life and frequency, q is another frequency exponent, C is material ductility coefficient, and k is fatigue exponent. ΔW_p is the area of stress-strain hysteresis loop. Shi [113] argued the C value in eq. (2.52) is more dependent on the temperature than that in Coffin-Manson model (eq. (2.62)). Shi introduced a temperature-dependent material parameter, X, which decreases with increasing temperature. Then eq.(2.62) can be rewritten as:

$$N_f = \frac{1}{\nu^{m-1}}\left(\frac{X\,C}{\Delta W_p}\right)^{1/k} \tag{2.63}$$

Shi also showed that flow stress of the material, σ_f, decreases with increasing temperature. Therefore, the suggested X can be described as flow stress and eq.(2.63) can be modified as:

$$N_f = \frac{1}{\nu^{m-1}}\left(\frac{2\sigma_f C}{\Delta W_p}\right)^{1/k} \tag{2.64}$$

where $W_p / 2\sigma_f$ has a dimension of strain, may referred as equivalent strain. The average values of constants for Sn37Pb were found to be: k = 0.7, C = 1.69, (1 - m) = 0.1 for $\nu > 10^{-3}$ Hz or (1 - m) = 0.59 for $\nu < 10^{-3}$ Hz. This frequency-modified fatigue life, presented as a function of the flow stress-modified strain energy density, fitted well with the experimental data at different temperatures (20 – 50 °C).

2.3.3.1 Volume-Weighted Averaging Technique

It was reported by Akay et al. [124] that the creep based fatigue model considering the point with highest value of stress or strain [75] [125] may not be appropriate for predicting the fatigue life of crack initiation and propagation. The authors mentioned that the crack initiates at the point of highest stress-strain while propagates along the high strain band that extends from this location. In addition, it has been studied that about 70 - 80 % of the total fatigue life is consumed for the crack propagation [126]. Hence, a volume-weighted averaging technique was proposed by Akay et al. [124] for predicting the complete failure life of solder instead of using a single extreme high stress-strain at the critical location. The creep based fatigue model can be rewrite in term of the volume-weighted average effective creep shear strain, $\Delta\bar{\gamma}_{avg}$, given by:

$$N_f = \frac{1}{2}\left(\frac{\Delta\bar{\gamma}_{avg}}{\varepsilon'_f}\right)^{1/k} \tag{2.65}$$

$$\bar{\gamma}_{avg} = \left(2\,\varepsilon_{avg}\,\varepsilon_{avg}\right)^{1/2} \tag{2.66}$$

where ε'_f is fatigue ductility coefficient, ε_{avg} is the average strain components. This average creep based fatigue model was used to calculate fatigue life with comparison to the experimental data. It is observed that the prediction quality was not quite satisfactory although the accuracy was reasonable. Therefore, the authors argued that the strain based fatigue model was not very reliable for prediction. In the same work, Akay et al. proposed a volume-weighted averaging total strain energy fatigue model as given by:

$$N_f = \left(\frac{\Delta\overline{W}}{W_0}\right)^{1/p} \tag{2.67}$$

where $\Delta\overline{W}$ is the total strain energy density calculated from the volume weighted averages over a cycle, and W_0 and p are load-independent material constants. This average total strain energy density fatigue model performed a better prediction than the creep based fatigue model (eq. (2.65)) and additionally includes the effects of geometry and volume of the solder joint. Thus, the authors concluded the average energy density fatigue model as a more reliable model for fatigue life prediction.

2.3.3.2 Volume-Weighted Averaging Inelastic Strain Energy Density Model

A volume-weighted averaging inelastic strain energy-based fatigue model coupling the initiation and propagation of crack was proposed by Darveaux [127] [128] and it has been subsequently accepted in industry. This model assumes the number of cycles to crack initiation N_0, and the crack propagation rate da/dN are dependent on the

volume averaged inelastic strain energy density dissipation per cycle ΔW_{avg} and can be expressed as follows:

$$N_0 = K_1 \ \Delta W_{avg}^{K_2} \tag{2.68}$$

$$\frac{da}{dN} = K_3 \ \Delta W_{avg}^{K_4} \tag{2.69}$$

and

$$\Delta W_{avg} = \frac{\sum \Delta W \ V}{\Sigma V} \tag{2.70}$$

where K_1, K_2, K_3, and K_4 are the empirical constants. The ΔW_{avg} value of interested region not only calculates the crack propagation but prevents the extreme simulated result in certain element overestimating the effort of ΔW. This energy based fatigue model predicts the accumulated energy required to initiate a crack; it does not predict when fatigue failure will occur, only that a crack will form. The characteristic life is given by:

$$N_f = N_0 + \frac{a_c}{da/dN} \tag{2.71}$$

where a_c is the joint diameter at the interface (final crack length). The Darveaux fatigue model utilizing volume-weighted averaging technique, can predict the entire fatigue life including the initiation and propagation of a crack, has the advantage over the Akay's fatigue model (eq. (2.67)) that lacks the information about crack initiation. It is also

shown in Darveaux et al.'s work [74], the maximum crack length in the population was approximately 2X the characteristic length. Hence, the failure free life, N_{ff}, approximately equivalents to one half of the characteristic life:

$$N_{ff} = N_f / 2 \tag{2.72}$$

Darveaux summarized the procedure to calculate fatigue life as follows:

(1) Calculate inelastic strain energy density per cycle using FEA approaches.

(2) Calculate number of cycles to crack initiation using eq. (2.68) and crack growth correlation constants K_1 and K_2.

(3) Calculate crack growth rate using eq. (2.69) and crack growth correlation constants K_3 and K_4.

(4) Calculate characteristic life based on eq. (2.71).

(5) Calculate failure free life based on eq. (2.72).

Although there is still no conclusion about which fatigue model is the best energy-based fatigue model, Pang et al. [129] have demonstrated that the fatigue lives of solder joints of a flip chip assembly computed by Darveaux model is more closed to the predictions by strain-based models while Shi's model predicted a higher fatigue life. In a different work, Chong et al. [130] compared the fatigue lives of one-piece lid HP-fcBGA subjected to thermal cycling and thermal shock computed by the Shi and Darveaux models. They have showed both Shi and Darveaux models predicted similar fatigue life for solder joint subjected to thermal shock. However, Shi's model performed a more conservative for the thermal cycling loading. Thus, Darveaux model has become a more popular model over other energy-based fatigue models.

2.3.4 Damage Based Fatigue Models

Fatigue-fracture propagation has been modeled to yield the number of cycles to failure despite where the crack initiates. Since the failure of a solder joint usually involves the growth of a major crack, the synergistic effects of all various damage processes can be represented by the propagation rate of the major crack [131]. Thus, the description of the fatigue crack propagation rate can be phenomenologically expressed in terms of stress intensity factor *K* given by [40] [131]:

$$\frac{da}{dN} = B(\Delta K)^m = B(\pi a)^{m/2}(\Delta\sigma)^m \tag{2.73}$$

where *B* and *m* are constants derived from experiment. The stress intensity *K* is given by $K = (\pi a)^{m/2}\sigma$ and $\Delta\sigma$ is the difference between the maximum and minimum applied stresses. Solomon has deduced the parameters of eq.(2.73) from isothermal fatigue data for SnPb solder joint [132]. If the initial crack size is a_0 and the final length is a_f , then the number of cycles N_f can be calculated by using integration:

$$N_f = \int_{a_0}^{a_f} \left[B\left(\Delta\sigma(\pi a)^{m/2}\right)\right]^{-1} da = \frac{2\left(a_0^{-(m-2)/2} - a_f^{-(m-2)/2}\right)}{(m-2)B\pi^{m/2}(\Delta\sigma)^m}, m \neq 2 \tag{2.74}$$

The crack growth-rate data for eutectic SnPb solder at 300 °K can be found in [133] [134]. Instead of using eq. (2.73), Satoh et al. [135] proposed the crack propagation rate can be approximated in terms of crack by a simple equation:

$$\frac{da}{dN} = Aa + B \tag{2.75}$$

where A is a parameter of crack propagation resistance and B is a parameter of crack initiation. And the fatigue life N_f can be determined as:

$$N_f = \int_{a_0}^{a_f} \frac{da}{(Aa + B)} = A^{-1} \ln\left(\frac{Aa_f + B}{Aa_0 + B}\right) \tag{2.76}$$

where a fit of using this relation for the crack striations in QFP SnPb solder joints indicates that $A = 1.48 \cdot 10^{-3}$ and $B = 0.18$, respectively.

Damage integral approaches using fracture mechanics provide a framework to account for the complexities of loading history, such as the load and crack length are as a function of cycles N. However, it is argued in [136] that the applicability of fracture mechanics becomes questionable when the crack length is physically short; the growth rate of short crack is higher than those predicted by the conventional theory of fracture mechanics.

In another damage based fatigue model, damage is treated as a material internal state variable (damage variable) that causes degradation of the strength properties of the material with loading conditions. A crack in a sufficiently large specimen represents material damage in the macroscale while microscale accounts for discontinuities, such as microcavities and microcracks, in the material [25]. The fatigue model considering the damage metric emphasizes describing the fatigue mechanisms and damage evolution processes that induce the failure of solder interconnection [26] [44] [108] [136] [137]. Hence, a parameter is used to evaluate the material degradation over loading history/time

[44]. Stolkarts et al. [137] utilized a damage variable, d, (representing a reduction in stiffness of the representative volume element) that defined between 0 and 1 where $d = 0$ corresponds to undamaged material and $d = 1$ to computer the fracture of the representative volume element. Then the amount of damage at any given time is given by:

$$d = 1 - \left[1 - (k+1) \int_0^t f dt \right]^{\frac{1}{k+1}} \tag{2.77}$$

where f is a function of all of the state variables except d, and k is a material constant. In the case of cycling loading, when $L = \int f dt \approx \text{constant}$, the damage after N cycles is given by:

$$d = 1 - [1 - (k+1) N L]^{\frac{1}{k+1}} \tag{2.78}$$

And, the number of cycle to failure is given by:

$$N_f = \frac{1 - (1 - d_f)^{k+1}}{(k+1) L} \tag{2.79}$$

where d_f is the amount of damage at failure where for solder d_f is usually taken to be about 0.5. This model has been simulated the inelastic behavior of SnAg eutectic solder.

In the microscale, the number of cycles to macrocrack growth, N_{mf} given in eq.(2.80), used to present the damage evolution changing from microcrack nucleation to a macrocrack growth governed process, was proposed by: Stolkarts et al. [138] [139].

$$N_{mf} = \frac{\overline{\omega}_c}{(\Delta\gamma)^{\chi}} \tag{2.80}$$

where $\overline{\omega}_c$ is the critical microcrack density, χ is material constant, and $\Delta\gamma$ is an increase in shear strain per cycle. For relatively large Sn37Pb specimens under continuous uniaxial cyclic loading eq. (2.80) was determined as:

$$N_{mf} = \frac{0.0007}{(\Delta\varepsilon)^{3}} \tag{2.81}$$

The hybrid micro-macro damage approach can be found in Chow et al.'s work [136]. One of the challenges of describing the damage evolution in a solder material is it requires a great number of material constants to capture reasonable actuary [27] [108]. It is reported that more than ten parameters are required for Stolkarts's and Chow's models [26] [136]. In addition, these models typically collaborate with numerical analysis (e.g. FEA) to account for the information of inelastic strain range, or hysteresis loop of the stress-strain per cycle. It is, however, is impractical to perform a full cycles simulation; only the first few cycles are simulated. Thus, the costs of determining the numerous parameters and cycling effects are extreme high.

The cohesive zone method (CZM) considers the fracture as a gradual process in which separation between incipient material surfaces resisted by cohesive tractions (e.g.

cohesive strength, cohesive energy) [140]. It utilizes the cohesive strength and critical separation displacement as intrinsic values for predicting crack initiation and propagation where the cohesive parameters for different fracture modes (mode I, mode II, and mode III) can be determined by simple fracture tests [108]. In addition, the fracture characteristics of the material such as fracture energy and fracture strength are included in a typical cohesive zone constitutive relation [140]. Cohesive zone has easy adaptability to material nonlinearity compared to fracture mechanics [141]. And, the cohesive zone method can be used to model cracking at interfaces between dissimilar materials compared to continuum damage mechanics.

Yang et al. [108] have shown that the damage accumulation is an intrinsic function of accumulated plastic shear strain (model II) for the model of Sn40Pb thin solder layer (where the shear strain across the joint thickness direction is close to uniform) under high frequency fixed strain range cycling. The damage evolution law, $\dot{D}_{cyc}$, can be defined in terms of accumulated plastic shear strain under cyclic, γ_p, and fitted in a form of a power law as [112]:

$$\dot{D}_{cyc} = 0.067(\gamma_p)^{-0.543} \tag{2.82}$$

However, this model lacks the applicability for other solder joint configurations such as solder joints in BGAs or on flip chip. Abdul-Baqi et al. [140] have demonstrated a method of embedding CZM at the physical interfaces, i.e., grain boundaries, phase boundaries and colony boundaries of a eutectic SnPb solder joint. The state of damage is incorporated into the cohesive zone constitutive law by an elasticity-based damage formulation. Although, in the comparison of the fatigue lives of bulk specimen, Abdul-

Baqi's method showed a good agreement with experimental results [142], this method is still questionable due to the bulk solder material was not characterized as a viscoplastic material.

2.4 Design for Reliability

As mentioned in Chapter 1.6, the DFR methodology combing empirical data, and FEA simulation results involves four main steps: (1) Establish a constitutive model, (2) Build a FE model with the established constitutive model to simulate the stress, strain, and energy response data, (3) Apply an appropriate fatigue model to predict the reliability of the assembly, (4) Verify the results. Early fatigue data was collected experimentally using strain gauges or the optical techniques (such as: shadow moiré, moiré interferometry, holographic, etc.). However, with the decreasing size of the electronic package assemblies, experimental collection of stress-strain data has become a very difficult job. And, actual fatigue tests are very time-consuming and often require significant experimental efforts and testing instruments. In addition, the experimental results usually applicable only to the specific configuration of the package assembly and the specific geometry of the solder joint. Knowledge of the inelastic strain or energy range, related to the specific geometry, is required for calculating fatigue life. The use of FEA providing an effective and efficient way to determine the required information eliminates the restriction of the geometrical specific problem. Moreover, FEA is also used for providing deeper information (e.g. the hysteretic loop of stress/strain/energy) for building more accurate fatigue models (volume-weighted averaging energy/strain based

models) and constructing damage based fatigue models. Thus, a reliable fatigue life prediction is based on constitutive model, fatigue model, and FEA model.

CHAPTER 3
LITERATURE REVIEW ON THE USE OF FEA APPROACHES ON ELECTRONIC PACKAGING AREA

3.1 Introduction

FEA is widely used to study the responds of interest component in an electronic package. Due to the material behavior of solder alloys show high nonlinearity, the use of nonlinear finite element methods must be taken into consideration. In this chapter, the review of general nonlinear FEM was addressed firstly. Newton-Raphson method for solving nonlinear problem and the convergence criteria were introduced. Then, several popular FEA approaches used in electronic packaging area were illustrated. These FEA approaches include 3D models, 2D slice model, 3D slice model, and advanced modeling techniques: multipoint constraint, submodeling, and substructure. Each approach has its own assumption/simplification on modeling and analysis procedures. Some approaches focus on simulation efficiency while some concentrate on the result accuracy. In this chapter, the advantages and disadvantages of different FEA approaches in available literature were reviewed and compared.

3.2 Nonlinear Finite Element Problems

For problem involving large displacement that the deformed configuration of the body may be very different than the initial configuration, and thus the configuration in which various equations are written must be treated very carefully. Due to it is very

difficult to obtain an analytical solution, the numerical approximation utilizing Newton-Raphson based methods were commonly used for solving nonlinear problem.

3.2.1 Newton-Raphson Based Methods

Assume the global system of nonlinear equations is written as [143] [144] [145] [146]:

$$K \cdot d = f_E \tag{3.1}$$

where $d = (u_1\ u_2\ \ldots\ u_n)$ is the vector of unknown, $K \cdot d$ is the vector of nonlinear functions of d, and f_E is the vector of known quantities. The Newton-Raphson-based method starts by assuming a solution which is then improved iteratively until a specified convergence criterion is satisfied. Suppose that an approximate solution at the ith iteration is known and is designated by d^i. The solution at the next iteration can be approximated using the Taylor series as follows.

$$K \cdot d^{i+1} \approx K \cdot d^i + K_T^i \Delta d^i = f_E \tag{3.2}$$

$$K_T^i \Delta d^i = f_E - K \cdot d^i \tag{3.3}$$

where Δd^i is the solution increment and K_T^i is the global tangent matrix at the ith iteration. After solving this system of equations for the solution increment Δd^i, a new approximate solution is obtained:

$$d^{i+1} = d^i + \Delta d^i \tag{3.4}$$

In structure applications the terms in the linearized system of equations are commonly referred to as follows: Δd is the displacement increment, K_T is the tangent stiffness matrix, f_E is the external load vector, $K \cdot d \equiv f_I$ is the internal force vector, and $f = f_E - f_I$ is defined as the unbalanced force vector. The tangent stiffness matrix and unbalanced force vector can also be expressed as (detail derives can be found in [144] [145] [146]):

$$K_T = K_c + K_s \tag{3.5}$$

and

$$f = r_i + r_q + r_b \tag{3.6}$$

where K_c is the current stiffness matrix, K_s is geometric stiffness matrix, r_i is the equivalent nodal load vector due to stresses in the current known configuration, r_q is the equivalent nodal load vector due to surface forces and r_b is the equivalent nodal load vector due to body forces.

The scheme of Newton-Raphson method can be described as follows:

1. Calculate stiffness matrix K_T based on d = 0 and initial material tensor, calculate external forces f_E, set internal forces f_I to 0

2. Solve $K_T \cdot \Delta d^i = f_E - f_I$ for Δd^i, and $d^{i+1} = d^i + \Delta d^i$

3. Calculate the total strain ε_{tot}

4. Local iteration at each integration point

5. Calculate stress σ from total strain ε_{tot}

6. Update history variables

7. Form the consistent material tangent $\partial\sigma/\partial\varepsilon_{tot}$

8. Calculate the internal forces f_I based on the stress σ and the tangential stiffness matrix K_T based on the material tangent $\partial\sigma/\partial\varepsilon_{tot}$

9. Go to 2 until convergence is achieved.

3.2.2 Convergence Criteria

As stated above a Newton-Raphson scheme converges in the vicinity of the solution [143]. In the FEM of structural mechanics, *df* is the difference between internal and external forces, f_I and f_E:

$$df = f_I - f_E \tag{3.7}$$

The goal is to reduce the load imbalance *df* to zero, or at least a very small number in each iteration. Thus a measure for convergence is how far this has been achieved. Since *df* has many components, a vector norm must be calculated:

$$\|df\| = \sqrt{\sum_{i=1}^{n} df_i^2} \tag{3.8}$$

The next step is to find a criterion in which order of magnitude this length can be considered as approximately zero. This must be a relative value obtained from the comparison with quantities contributing to d.

The force convergence criterion can be expressed as:

$$\frac{\|df\|}{\|f\|} < \lambda \tag{3.9}$$

where λ denotes a small number chosen beforehand and influencing the accuracy; and f either the internal or the external nodal forces. Furthermore, $df = 0$ means that the increment of the primary variables, Δd, becomes 0, too. Thus,

$$\frac{\|\Delta d\|}{\|d\|} < \lambda \tag{3.10}$$

can also be used as the displacement convergence criterion. Here Δd is the actual increment of the iteration step and d can be the total displacement or its portion in the actual load step. It happens that the two criteria do not indicate convergence at the same time. It is on the safe side to consider the two criteria at the same time. An improvement can be an energy criterion:

$$\frac{\sqrt{\Delta d^T df}}{\sqrt{\Delta d^T f}} < \lambda \text{ or } \frac{\Delta d^T df}{d^T df} < \lambda^2 \tag{3.11}$$

3.3 Finite Element Modeling Approaches in Electronic Packaging Area

In this section, FE modeling approaches for obtaining the responses of solder interconnections were reviewed; they are 2D slice model, 3D slice model, 3D model, MPC model, submodeling model, substructuring model and equivalent model.

In FEA, different modeling and analysis approaches have their own simplifications and assumptions to execute the simulations for calculating the best approximated solutions. Some assumptions improve the simulation efficiency and some are concentrated on improving modeling flexibility. Among all models, a full detailed 3D model is considered as the most acceptable and reliable modeling approach. Due to the simulation costs for a full refined 3D model are too high and computer resources are always limited, the tradeoff between solution quality and simulation efficiency must be taken into consideration while chose choosing a FE modeling approach for analysis.

3.3.1 2D Slice Models

2D model is a simple and easy-to-build model, and it can be meshed with fewer elements/DOF's compared to a full 3D model. In this approach, the 2D slice model, cutting along the direction of interest where the most critical joint located, captures the details through top-to-bottom sides of a package assembly as shown in Figure 3.1 [147]. In the out-of-plane direction, it can be considered as an assumption of plane stress or plane strain.

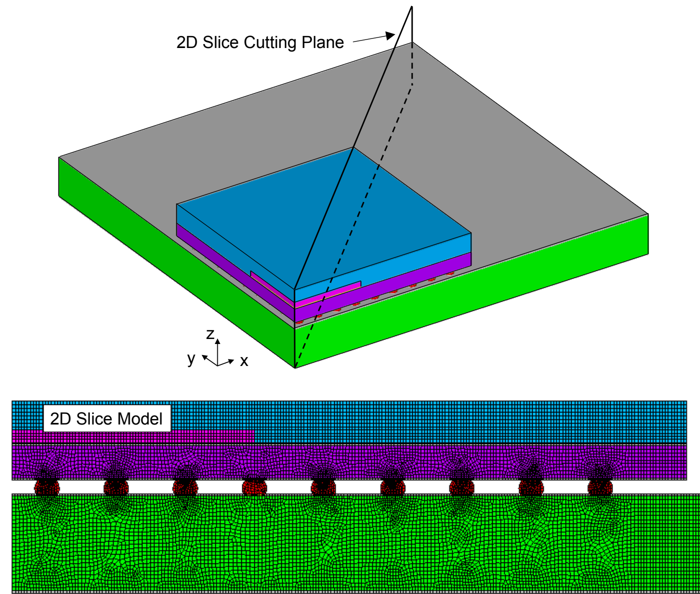

Figure 3.1 Schematic of 2D Slice Model

Pang et al. [129] have studied the effects of 2D models on the performances of the solder joint reliability prediction in a flip chip on board (FCOB) assembly. They pointed out that due to the thickness of out-of-cutting plane of the package assembly is always large compared to its top-to-bottom thickness, the 2D electronic packaging problems are usually represented by a 2D plane strain setup. The simulation results showed the 2D plane stress and 2D plane strain usually bound the 3D model results. In a similar work, Che et al. [99] have used a PBGA package with Sn3.8Ag0.7Cu solder joints to compare the effects of different 2D models. The results showed similar trends to Pang et al.'s work: the 2D plane stress model result in the highest inelastic strain energy density. Hence, the authors concluded 2D plane strain and 2D plane stress models gave the highest and lowest solder joint strains, respectively. Similar result has been reported by Dudek et al. [148].

Although plain strain assumption has been found in several literature [149] [150] [151], Paydar et al. [125] reported that the plane stress results in creep strain were closer to the 3D model than plane strain model. In a separate work, Akay et al. [152] presented a 2D modeling method combining plane strain and plane stress assumptions. In their 2D PBGA model, plane stress element with thickness is always used for solder joints and calculating energy dissipation. For the packages in which the solder joints are positioned along four sides of chip carrier, plane strain element is used for chip carrier and PCB board, because the solder joints resist the expansion of chip carrier and PCB board in four directions. It is found that the 2D plane stress model gave a different total creep dissipation energy compared to the 3D octant FE model, but can give approximately the same distribution trend of total creep dissipation energy on solder joints and predict the same position for critical solder joints as the 3D octant FE model.

In general, 2D plane models provide a good understanding of the qualitative behavior of a package assembly. However, plane models do not capture the geometrical shape of the solder joint accurately and they lack of ability to describe the out-of-plane variation of material properties. Michaelides et al. [153] have shown the plane strain assumption is approximately valid at a cross section parallel to the die edge. The plane strain assumption becomes invalid as one moves toward the corner of the assembly where the constraint diminishes and three dimensional edge effects become more pronounced. Consequently, plane models do not provide quantitatively accurate results [124] [154] [155] [156] [157]. It also has been reported in the literature [149] [150] that 2D plane strain model gives a consistent result compared to the result obtained from complex 3D model. In summary, 2D model can be still used to compare qualitatively the effects of

various geometrical and material parameters, such as: a flip chip with underfill material [158] [159] [160], without underfill [161] , and copper core solder joints [162].

3.3.2 3D Slice Models

3D slide model considers a diagonal slice from the center of a package assembly to a corner that has a width covering solder joints and passes through top-to-bottom sides of the package assembly as shown in Figure 3.2. Typically, at least one row of solder joints in the chosen direction is included in a 3D slice model. 3D slide model actually simulates a package assembly that is of infinite extension in the out-of-plane directions. Therefore, the constraints of generalized plane deformation are needed to be considered as the boundary conditions for the slicing planes [44] [79] [128] [147] [163]. The generalized plane deformation (GPD) constraint states as follows: the nodal deformations of the nodes on the cutting plane are identical in the out-of-plane direction of the cutting plane. Not that the GPD constraint was applied on the two cutting planes as not representing symmetric nor free planes.

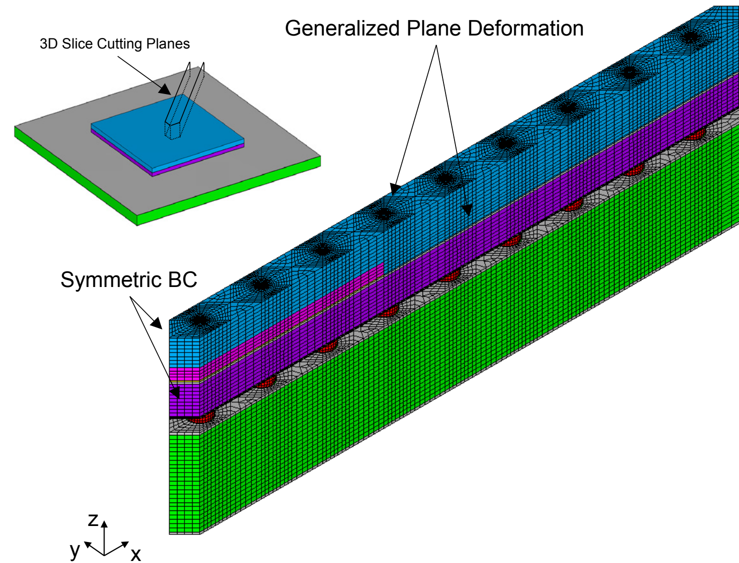

Figure 3.2 Schematic of 3D Slice Model

Gustafsson et al. [164] mentioned the advantages of using 3D slice model include: (1) the 3D slice model captures all major components and a full set of solder joints, (2) the temperature-dependent material properties and viscoplastic solder behaviors are included in the three-dimensional nonlinear analysis. However, simulation results yielded to an underestimation of the warpage of the package and overestimate the shear loading on the solder joints due to the assumption of infinitely dimensions in the directions perpendicular to the slice planes. In Dauksher et al.'s work [165], the 3D slice model, constructing with hexahedral eight node elements, easily captures the physical construction and stiffness of both large and small packages in a computationally efficient model. The authors also pointed out that this approach allows full geometric description of the solder joints, resulting in accurate definitions of BGA stress and strain, while maintaining much of the computational simplicity of a 2D model. Similar approaches have been found in literature [75] [79] [166] [167] [168] [169] [170] [171]. It is worth

mentioning that the use of GPD constraints on a non-perfect diagonal direction of a package assembly can also be found in Zahn's work (Figure 3.3, [172]).

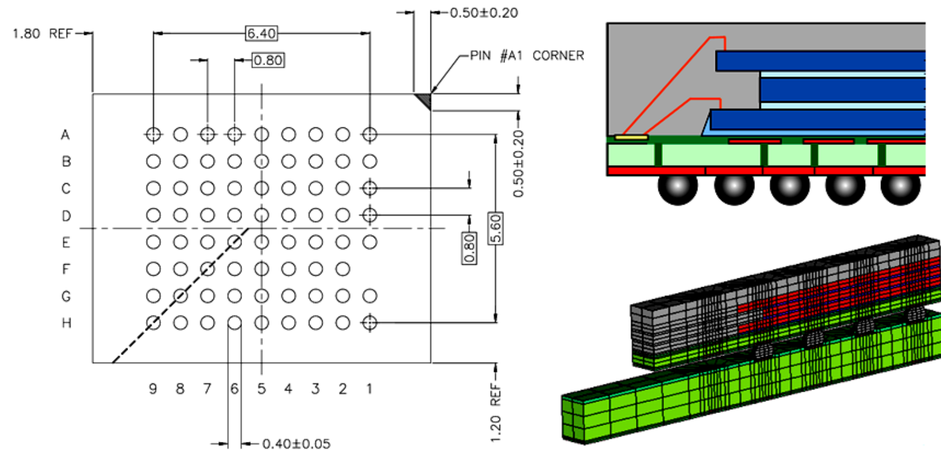

Figure 3.3 The Use of GPD on Non-Perfect Diagonal Direction of a Package Assembly [172]

Hsieh et al. [166] have demonstrated using a 3D slice model, that the all geometrical details of underfill, under-bump-metallurgy (UBM), and intermetallic compounds (IMC) were addressed, to build a 28-nm extreme low-k (ELK) large die flip chip ball grid array (fcBGA) assembly. As shown in Figure 3.4, the major advantage of 3D slice model was illustrated: more elements were used to build the details of interest and the effects of global geometry of the package assembly were also considered. In their work, not only were the critical factors that comprehend ELK, UBM, and bump stresses were illustrated, but the significant factors to warpage were determined. As a result, it provides a better reliability prediction of large die fcBGA.

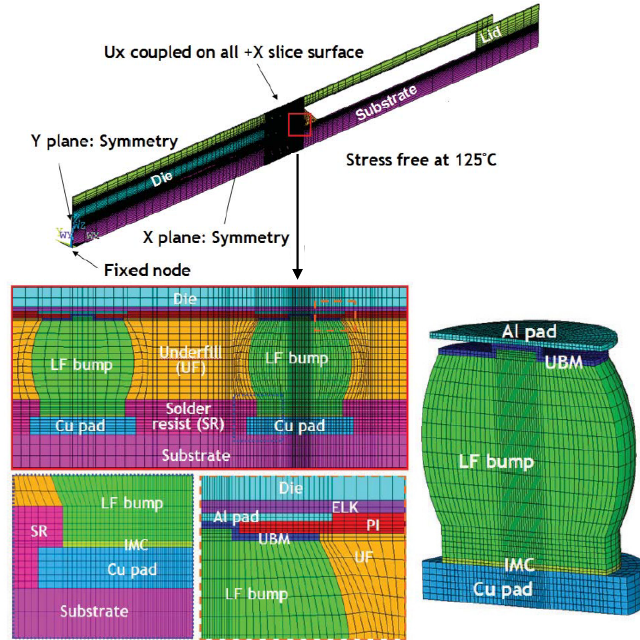

Figure 3.4 FE model and Applied Boundary Conditions of a Large Die fcBGA [166]

The 3D slice approach has a number of advantages over competing approaches, such as 2D models or full 3D models [165]. While 2D models are computationally efficient, their plane stress or plane strain assumption approximates the package as being of infinite extent in the out-of-plane dimensions, hence results in an inaccurate prediction of solder joint stresses and strains. Although the GPD assumption still influents the simulation result accuracy of the 3D slice model, 3D slice model captures a complete description of the solder joints, leading to a more accurate definition of the stress and strain state within the joints. Zhu et al. [173] pointed out that when calculation time becomes very critical, the 3D slice model is an option which can sustain most geometrical details of the packages and at the same time have high simulation efficiency. Hence, this efficiency can be evidenced in a fast solution time and provides a more reasonable result as the location of solder joint more closed to the package canter. In

order to avoid the assumptions of boundary conditions as used for 2D and 3D slice models, a full 3D model may be constructed.

3.3.3 3D Models

It is widely accepted that 3D model can produce the most accurate results and 3D model is the only reasonable modeling solution for certain geometry of the component, such as a rectangular silicon chip with large aspect ratio, precluding the use of a 3D slice model [147]. For larger package or in the case of fine mesh, a full 3D model can have a very large number of elements. And, the solder materials have nonlinear material properties. These reasons induce the computation with a full 3D model may be impractical. Quarter (1/4) or octant (1/8) model comes from the full model by considering the symmetry of the geometry of a package assembly (Figure 3.5), and is expected to has the same solution quality in a more reasonable time compared to the full 3D model.

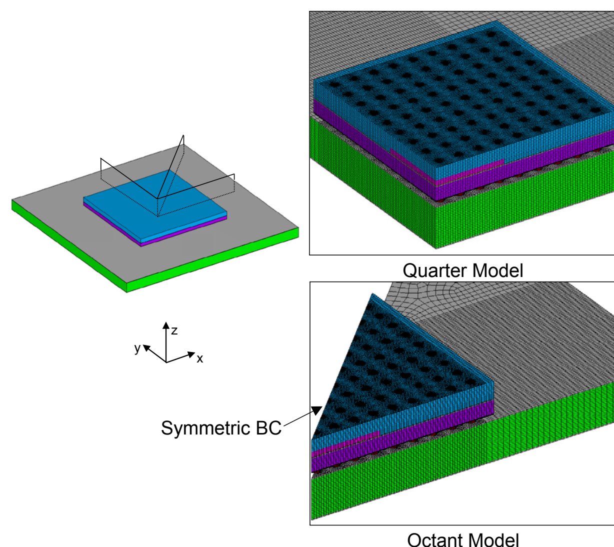

Figure 3.5 Schematic of 3D Models

Yao et al. [174] have compared the effects of 2D and 3D models on the simulation results of stress distribution and deflection of the flip chip assembly under thermal loading. It is found that the results of 3D model were compared favorably with experimental measurements, while the 2D results consistently overestimated both stresses and deflection. Therefore, results from the 3D model can better explain the observed failure modes in the flip chip assemblies, such as cracks in silicon die and encapsulant, delamination in the silicon underfill interface, and cracks in the silicon-solder interfaces. Yeo et al. [171] has studied solder joints of a FCOB assembly with Sn37Pb and Sn3.5Ag solder joints. The solder joint fatigue lives predicted by the 2D axisymmetric model, 3D slice model, and 3D octant model fall within the predicted life of the plane stress model and plane strain model.

3D models, which take advantage of quadrant or octant symmetry, avoid boundary condition approximations made with the 3D slice. However, these full 3D models require significant analyst time in model construction and computer resources for computing.

3.3.4 Multipoint Constraint Technique

It is not always an easy task to achieve mesh continuity between different components of a package assembly model. Multiple geometric partitions are required for dividing a model into several regular shaped partitions to improve mesh transition. In this paper, the use of MPCs is limited to the use of tie constraints to connect two regions with incompatible meshes. Syed [175] has presented a FEA modeling based study that aims to maximize the simulation efficiency without sacrificing the accuracy using several

advance FE modeling and analysis techniques, such as MPC and substructure. In this study, constraint equations are employed in joining the fine-mesh model containing the critical joint with the coarse-mesh model of the rest components of the package assembly. The author indicated that the constraint equations do not result in strain continuity and the stress/strain results of fine mesh at the interface are inaccurate. Syed proposed a solution to avoid the inaccurate results by including a very thin layer (2 microns) of Cu or intermetallic at the interface in between the solder and PCB elements.

In his following study [176], MPC was used in the substructure model to bound the fine-mesh critical joint together with the coarse-mesh other sections. In order to compare the effect of MPC, models with three different bonding setups were built as shown in Figure 3.6. The first model used MPC at the interfaces between solder, package , and board pads referred as Type 1 MPC. In the second model, the MPC were moved to within the package and board, Type 2 MPC. The mesh is continuous in z-direction (thickness) but discontinuous in x and y direction (interface of blue and gray elements). The third model did not use any MPC, No MPC, and mesh continuity was maintained across coarse-to-fine model interface. The simulation results showed that when all joints had nonlinear property, Type 1 MPC model resulted in 25% higher accumulated energy density, Type 2 MPC model resulted in the same accumulated energy density as No MPC model. This is because the responses of the joints with nonlinear material property affect the responses of both package components and the PCB which connected by these solder joints. However, this effect is not captured completely when MPC are located very close to the critical solder joint (such as Type 1 MPC), thus over-stiffening the system. Syed

concluded that when MPC is located far away from critical joint model, Type 2 MPC, they work as expected and do not cause a difference in the responses.

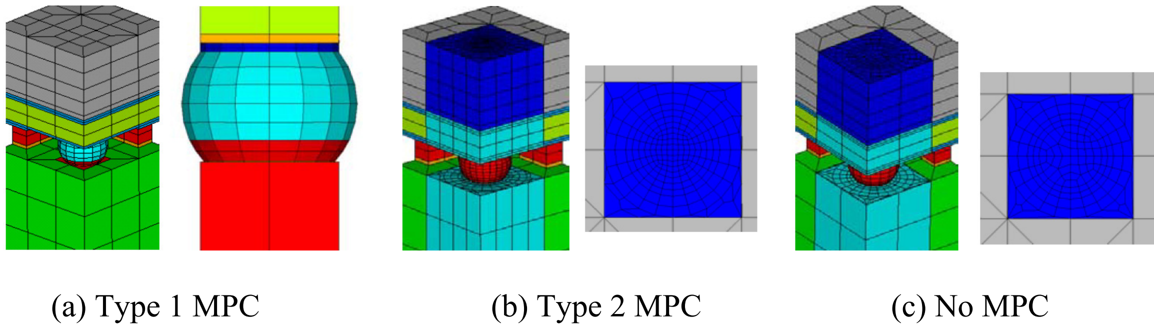

(a) Type 1 MPC (b) Type 2 MPC (c) No MPC

Figure 3.6 Meshing with MPC [176]:
(a) MPC at Solder-Pad Interfaces, (b) MPC within Substrate/Board, and (c) No MPC

Similar conclusion has been reported in Fan et al.'s study [28]. It is recommended that MPC must be placed away from the location of interest (e.g. solder-copper pad interface). Figure 3.7 shows the MPC constraints were placed above and below the solder joint at the interfaces between the copper pads and the substrate/PCB. In their simulation results, however, this MPC setup introduced about 40% error in the averaged accumulated creep strain.

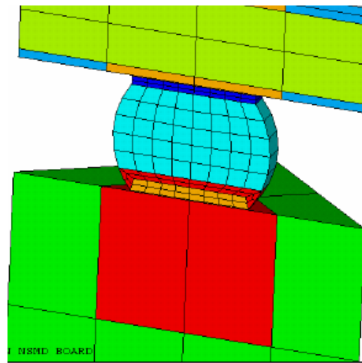

Figure 3.7 MPC Constraint above the Solder Joint [28]

3.3.5 Submodeling Technique

Submodeling is a finite element based technique to study the local behavior which is relatively smaller than overall behavior of the entire model. The submodeling technique can be applied on the problem that the size of full 3D model is too large for detailed simulation and the solution of the potential critical region is required. In submodeling, the behavior of the entire model, also called global model, is analyzed at first. A coarse mesh is preferred for global model by the reason of saving computational costs. Displacements information calculated on the cutting boundaries of the global model are interpolated and applied as boundary conditions for the local model as shown in Figure 3.8

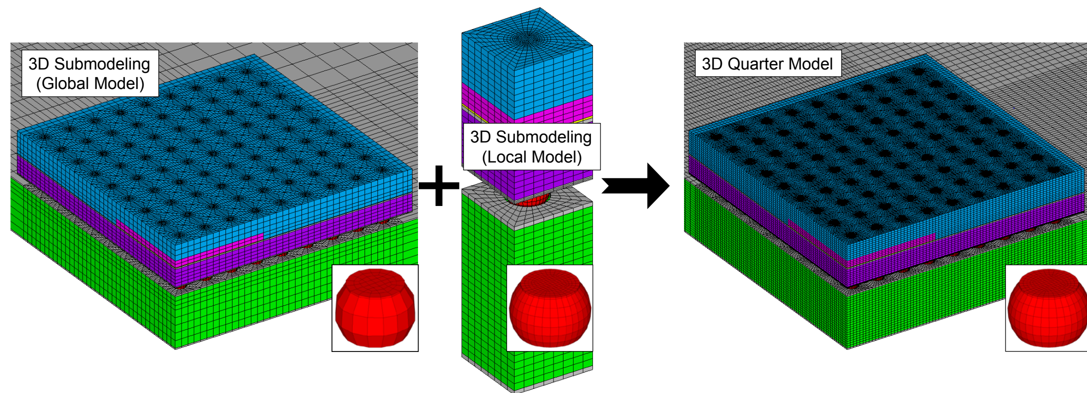

Figure 3.8 Scheme of Submodeling Technique

Gustafsson et al. [164] have categorized four common submodeling-based methods, they are: (1) Linear global model with nonlinear local model, (2) Nonlinear global and local models, (3) Nonlinear global model with fine-meshing critical joint and a nonlinear local model, and (4) Nonlinear global model with linear superelements. These four methods were discussed here.

Linear global model with nonlinear local model: A linear model of the substrate and board and all of the solder balls using 3D elements in order to identify the critical solder joint for a subsequent nonlinear submodeling. The global model includes only the linear material properties, whereas the local model includes nonlinear material behavior. The linear global model is subjected to a one-degree temperature change, providing displacement fields on a per-degree basis [177]. The displacement fields in accordance with the thermal cycling become the boundary conditions for the submodel of the critical joint. This permits the simulation of any thermal cycle using only one set of global model results.

Nonlinear global model with a nonlinear local model: The nonlinear global model, meshed with a very coarse-mesh for the substrate, PCB, and solder joints, provides the critical joint for the subsequent nonlinear submodeling of the critical solder joint [178]. Mesh refinement in the local model is the same as that in the previous model. As in the preceding approach, the displacement information becomes the additional boundary conditions for the nonlinear local model containing the critical joint(s) in accordance with the thermal cycling. The global and local models include temperature-dependent and the viscoplastic material behavior.

Nonlinear global model with fine-meshing critical joint and a nonlinear local model: This model includes temperature-dependent and the viscoplastic behaviors of the solder joints for the both global and local models. The global model employs a relatively coarse mesh for all of the components of a package except for the critical solder joint(s). The fine-mesh associated with the critical solder joint(s) has higher mesh density than the remaining coarse-mesh components. In the aspect of mesh generation for this approach,

therefore, mesh continuity becomes a time-consuming task due to high incompatible mesh patterns. If the package consists of a large number of solder joints, it is not feasible to model all of the solder joint(s) with a refined mesh.

Nonlinear global model with linear superelements [28]: This approach is related to the substructure technology. The package and board are modeled as two super-elements and all of the solder balls as 3D finite elements. Except for the critical joint(s), the solder balls are modeled with a coarse mesh. The critical solder joint identified a priori is modeled with a highly refined mesh. The superelements include only the linear material properties and all of the solder joints with nonlinear material behavior. The global model in which the package and the board are represented by the super elements is subjected to the appropriate thermal cycles.

Methods (2) and (3) are most used in the literature; the major difference is: refined meshes are used in the interested solder joints of the global model in the third approach. Recently, several analysts have utilized the advantages of submodeling technique to analysis the complicated problems, such as complex geometry, large packaging, and detailed local behaviors including the effect of IMC.

3.3.6 Substructuring Technique

Substructuring uses a smaller matrix system, called substructure or superelement, which is condensed by eliminating the interior nodes and keeping only exterior or boundary nodes of the portion of a structure, to reduce computational cost [179]. During the analysis, the size of the matrix system of equations becomes the number of unknown DOF's of the main structure. Superelements are attached to the main structure through

the Master DOF's. Once the solution is obtained, all degrees of freedom belonging to the nodes of the main structure are known. Finally, the solution for the superelement sections is obtained by using the known Master DOF's as the boundary conditions. In electronic packaging area, the procedures of the use of substructuring can be summarized as follows [64]:

1. Create linear superelements out of the PCB and the package.
2. Consider the solder balls as main structure and introduce superelements into the main structure. And then the solution for the main structure is obtained including the solution for the master degrees of freedom of each superelement.
3. Complete solutions for the superelements can be obtained by expanding the master degree of freedom solution.

The advantage of the substructuring technique is that it allows for calculating a problem at relatively low computational costs. The main disadvantage of substructuring is that it is computer-intensive to form superelements and Master DOF's while the problem involves a various of nonlinear components.

Syed [175] [176] has pointed out that the fundamental limitation of substructuring is that all the elements constituting the superelement must have linear, time- and temperature- independent material properties. In order to use the full potential of substructuring for solder joint response simulation, all non-critical solder joints are assumed to have linear, time and temperature independent properties. Thus, the response of package assembly can not be captured accurately due to the interconnections lack of ability to represent the nonlinear behaviors subjected to loading conditions.

In Syed's works, the use of substructuring was limited on a certain solder joints, typically on the critical joint. It is because the effort of forming the matrix of main structure requires huge computer resources. Furthermore, for temperature-variant problem, it is crucial to determine when to update the main structure matrix and the superelement information. Liu et al. [180] have developed an improved substructure-based approach allowing ANSYS to update the data of superelements and main structure matrix. However, the use of substructure approach was still only applied on a pre-identified critical solder joint, not used on the package level problem.

3.3.7 Equivalent Model Technique

Cheng et al. [181] have studied the use of equivalent beam model for incorporating use with submodeling approach. The first step is to construct an equivalent beam model to simulate the solder joint in both elastic and plastic characteristics when subjected to the same axial/shear forces and moments. The one-dimensional beam theory was first derived by virtue of the general Mindlin plate theory where the effects of shear are taken into account. In addition, two types of equivalent beams with different cross sections were considered and investigated: (1) a solid round beam and (2) a thin-walled round pipe with a uniform thickness [182]. Results show that this methodology and assumptions that were made in the mathematical derivations of the equivalent beam model were valid and rational. The equivalent beam model can significantly reduce the analysis CPU time, and more importantly, make the full-scaled packaging analysis possible and effective. Similar approach can be found in literature [183].

Zhang et al. [184] have presented another improved a global-local methodology: (1) the global deformation analysis includes a formulation for determining an optimal geometry of equivalent solder joints derived from nonlinear load-deformation response and (2) the local critical solder joint analysis involves rigorous application of nonlinear submodeling technique. This developed methodology was applied to fine pitch ball grid array (fpBGA) and super ball grid array (SBGA) packages. A good agreement was obtained between the simulated deformation results and experimental observations. Based on proposed modeling and simulation results and package designs studied, the SBGA package is more durable than the fpBGA package.

CHAPTER 4
COMPARISON OF FEA MODELING TECHNIQUES FOR PBGA ASSEMBLIES

4.1 Introduction

Solder joint provides both electrical and mechanical connections between silicon chip and subtract/PCB. Solder joint is also the most fragile component of an electronic assembly undergoing mechanical or thermal loading. The prime failure mode of the solder joint is caused by high stress/strain concentration due to the mismatches in thermal expansions of various different materials while temperature changes during service operations. In addition, damage accumulates with cyclic loadings and ultimately causes the solder joint to fail. Thus, solder joint reliability, refers to the ability of the solder joint to retain functionality during its designed service life, is a major concern in the electronic package industry.

The fatigue life of solder joint can be predicted using FEA results associated with appropriate fatigue models. For FE analysis of a package assembly subjected to thermal loadings, a full 3D model is the most trustful model due to fewer assumptions and simplifications are made. However, model size of a package assembly model involves many considerations, such as geometric shapes of components, total amounts of I/O counts, configuration of package. Furthermore, effects of nonlinear material property and cycling loading conditions make a high-density meshing model, huge computer resources, and significant simulation time are required to obtain a solution. Hence, a full detailed 3D model is an expensive model for thermal cycling simulation. Besides

modeling and computer resources, inappropriate analysis setups by inexperience analyst may result in an inaccurate simulation. Thus, the FEA for electronic package area still faces several challenges to achieve the balance between efficiency and accuracy, and also maintain the consistency of the simulation results.

Several FEA techniques using 2D and 3D models have been employed to study the behaviors of interconnections of an electronic package assembly [28] [71] [125] [128] [129] [152] [175] [176] [185] [186]. The choice of analysis model depends on the solution accuracy needed and time-limit of the task. 2D model is a simple and easy-to-build model, and it can be meshed with fewer elements/DOF's comparing with a full 3D model; hence, less computer resources and simulation time are required. But, restrict to the assumptions of plane problem, 2D model lacks of ability to describe the out-of-plane variations of geometry and material properties. A full 3D model can simultaneously simulate the responses of solder joint array influenced by the configuration of the package assembly undergoing mechanical or thermal loading. In the most of time, however, a detailed 3D model is not practical due to several restrictions, such as generating an extreme high-density mesh model, limited computer resources, and the capability of software. Advanced FEA techniques [28] [175] [176] [187] have been developed to reduce modeling difficulty and improve simulation efficiency. However, comparisons of using these advanced techniques have the assumption of the critical joint had been identified. For the package level problem, there are still no comparisons addressed on the simulation accuracy and efficiency from identifying critical joint to final simulation results.

In this chapter, an example PBGA model was built using different FE approaches, including 2D slice model, 3D slice model [163] [165], 3D quarter model, submodeling, and MPC [28] approaches, and simulated with Anand constitutive model. Energy-based fatigue model was chosen to identify the most critical joint and estimate the fatigue life. Comparisons of different types of approaches were addressed, advantages and disadvantages of different approaches were discussed, and then suggestions were made.

4.2 Finite Element Modeling and Simulation

An example model for a PBGA configuration composed of a chip (center red box in Figure 4.1) and an area array of 324 solder joints. Figure 4.2 shows the details of the package components. Dimensions of the example package are listed in Table 4.1. The solder joint pitch in the model was 0.8 mm.

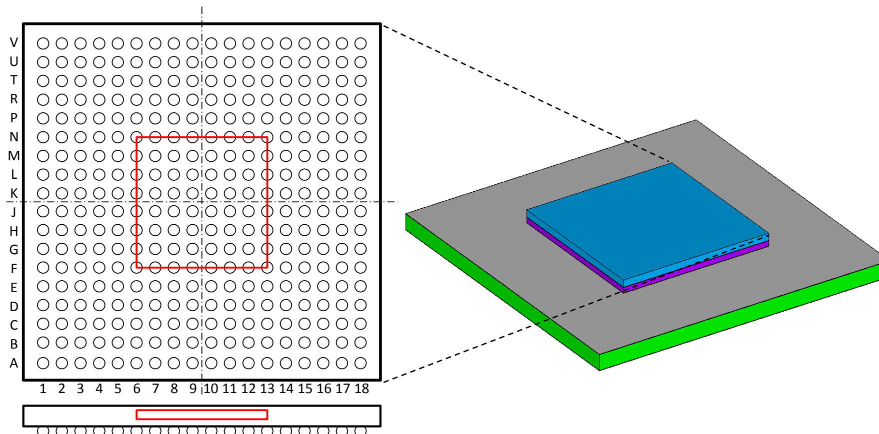

Figure 4.1 Example PBGA Package

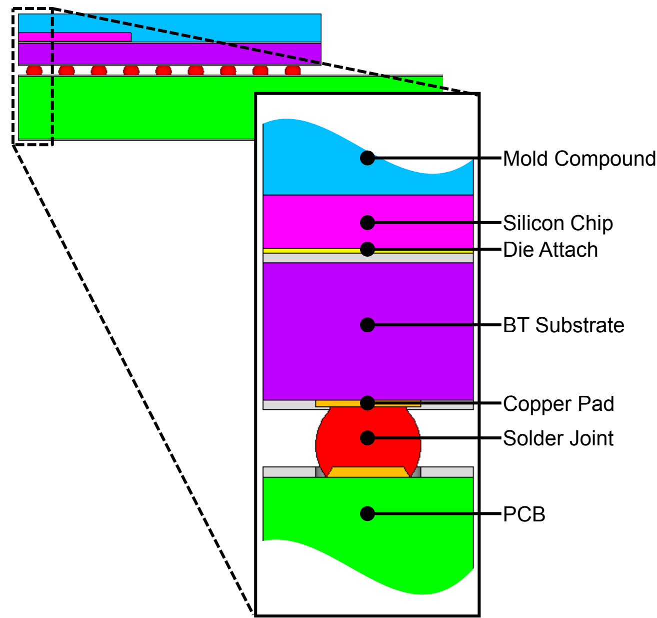

Figure 4.2 Detail View of Example Model

Table 4.1 Dimensions of Example PBGA Assembly

Component	Dimensions (mm^2)
PCB	30 × 30
Solder Mask	30 × 30
BT Laminate	15 × 15
Die Attach	5.6 × 5.6
Silicon	5.6 × 5.6
Mold Compound	15 × 15

SAC305 lead free alloy [62] was chosen as the material of the solder joints, and the Anand model was utilized as the constitutive model for describing material behavior of the solder alloy (the nine Anand parameters are listed in Table 4.2 [188]). The PBGA pads at the substrate side were modeled as Solder Mask-Defined (SMD) and Non-Solder Mask-Defined (NSMD) at the PCB side. The material properties were listed in Table 4.3. The computer used for all simulations in this research was equipped a Intel Core i7-4790K Processor (4 GHz) and 32 GB RAM.

Table 4.2 Anand Constants for SAC305 Solder

Anand Constant	Definition	Units	SAC 305
s_0	Initial Value of Deformation Resistance	MPa	21.0
Q/R	Activation Energy / Boltzmann's Constant	K	9,320
A	Pre-Exponential Factor	sec^{-1}	3,501
ξ	Multiplier of Stress	-	4
m	Stain Rate Sensitivity of Stress	-	0.25
h_0	hardening constant	MPa	180,000
$\hat{s}$	Coefficient for Deformation Resistance Saturation Value	MPa	30.2
n	Strain Rate Sensitivity of Saturation (Deformation Resistance) Value	-	0.01
a	Strain Rate Sensitivity of Hardening	-	1.78

Table 4.3 Material Properties for the Components of Example PBGA Package Assembly

Component	Elastic Modulus (GPa)	Poisson's Ratio	CTE (ppm/°C)
PCB	$E_x = 16.90$, $G_{xy} = 7.62$ $E_y = 16.90$, $G_{xz} = 3.33$ $E_z = 7.44$, $G_{yz} = 3.33$	$\nu_{xy} = 0.11$ $\nu_{xz} = 0.39$ $\nu_{yz} = 0.39$	$\alpha_x = 14.5$ $\alpha_y = 14.5$ $\alpha_z = 67.2$
Solder Mask	3.1	0.3	16.3
Copper Pad	128	0.34	17
BT Laminate	$E_x = 17.90$, $G_{xy} = 8.06$ $E_y = 17.90$, $G_{xz} = 2.82$ $E_z = 7.84$, $G_{yz} = 2.82$	$\nu_{xy} = 0.11$ $\nu_{xz} = 0.39$ $\nu_{yz} = 0.39$	$\alpha_x = 12.4$ $\alpha_y = 12.4$ $\alpha_z = 57.0$
Die Attach	Temperature Dependent		
Silicon	162.7	0.28	2.54
Mold Compound	25.0	0.3	Temp Dependent

The thermal cycling loading curve (Figure 4.3) varies between -40 and 125 °C, with 10-min ramp-up/down, and dwell times of 20-min at the maximum and minimum temperatures. The reference (stress-free) temperature was chosen to be 25 °C.

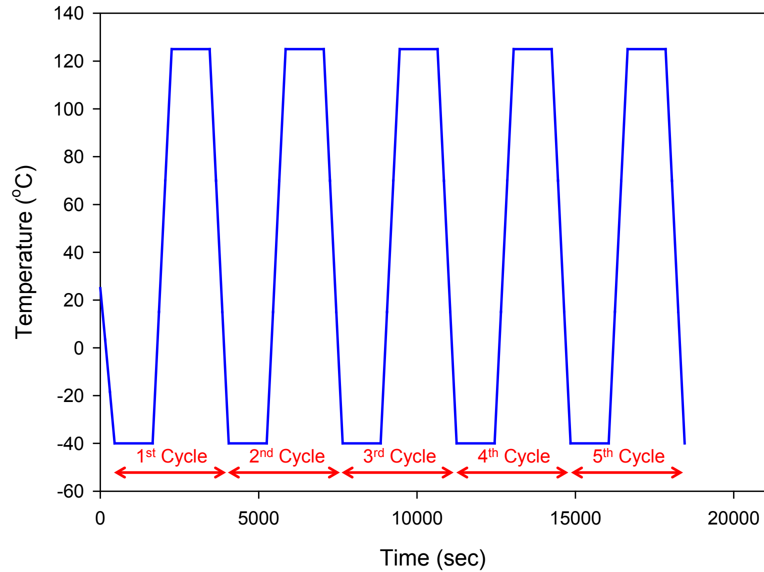

Figure 4.3 Thermal Cycle Loading Curve

The energy-based fatigue model coupling the initiation and propagation of crack proposed by Darveaux (Chapter 2.1.2) has been subsequently used in many literatures. In our previous work [189], simulation result of ΔW_{avg} was stabilized after five cycles and the critical region was located at the top region of solder joint as shown in Figure 4.4. In this study, similar approach was followed; five thermal cycles were simulated and ΔW_{avg} value of top side of solder joint was present.

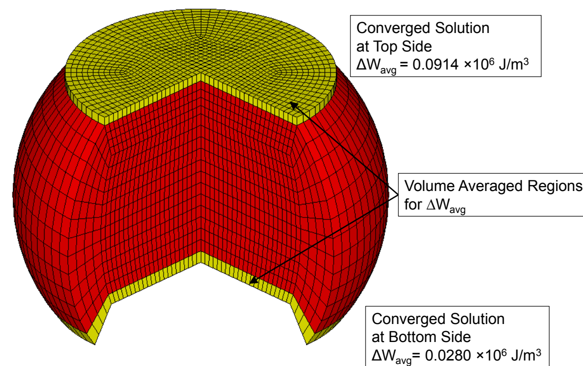

Figure 4.4 Volume-Weighted Averaging Regions for Simulation Result ΔW_{avg}

4.3 3D Models

A full 3D package model requires large computer resources and calculation time. Even given infinite amount of computational time, the oversize model would still crash the computer system. 3D quarter and octant models are used to replace full size model for reducing overall size of the model while a geometric symmetric pattern can be found from the full model.

4.3.1 3D Quarter (1/4) Model

The boundary conditions in 3D quarter and octant models are either structure exterior surfaces or symmetry planes. This makes the 3D quarter and octant models are most accurate, since no simplified assumptions are made to the boundary conditions. Due to the symmetry of the example package, a one quarter model with symmetric boundary conditions was taken for demonstration (Figure 4.5). In order to calculate a good solution quality, the 3D quarter model was meshed with 2,065,644 hexahedral elements.

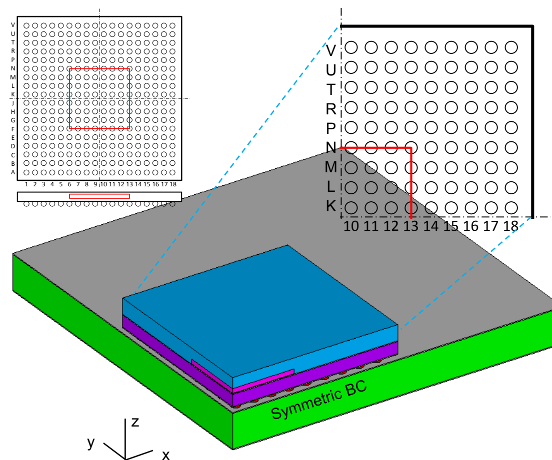

Figure 4.5 3D Quarter Model

4.3.2 Simulation Results for 3D Quarter Model

After five cycles, the most critical region was identified at the top region of solder joint M12 (under the corner of die shadow). The contour plots of volume averaged inelastic strain energy density (PLWK) for the solder joints locating along diagonal direction of the package assembly were plotted in Figure 4.6 (presented in the cross-sectional view A-A). High PLWK values concentrated (circled in red) at the top corners of all joints, where are the potential regions for crack initiation. Comparing the distributions of PLWK for the solder joints, it can be seen greater distributions of PLWK were observed at the joint V18.

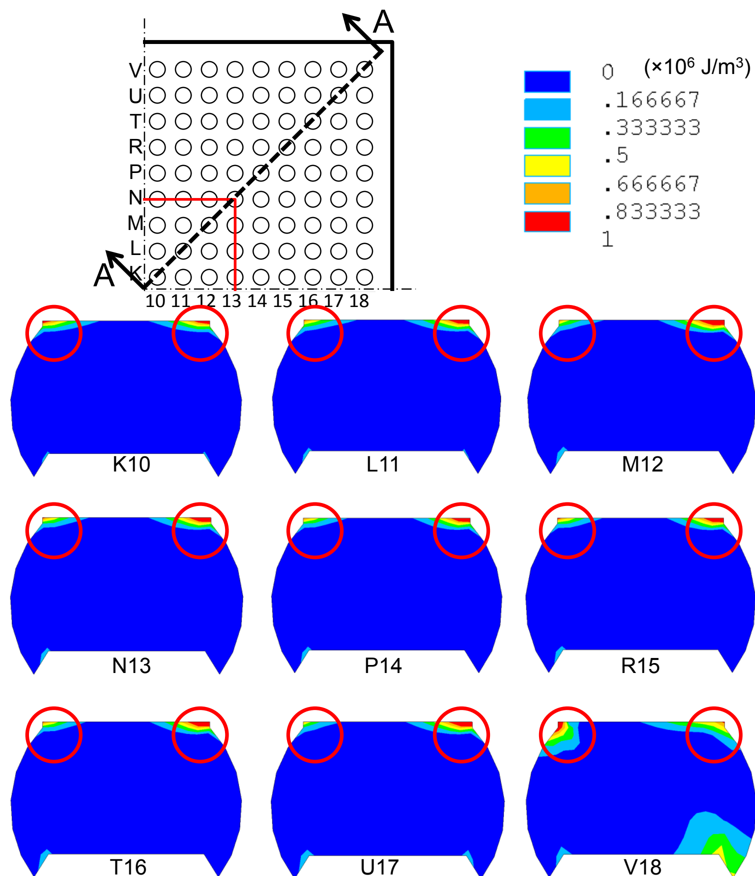

Figure 4.6 Contour Plots of PLWK after Five Cycles for 3D Quarter Model

However, ΔW_{avg} value for joint V18 showed only 65% of joint M12 (as shown in Figure 4.7) while considering volume averaged energy-based fatigue model which preventing extreme high ΔW value of single element. It also can be validated on the history curves of volume averaged PLWK (Figure 4.8), joint M12 experienced higher volume averaged PLWK over other joints during thermal cycles.

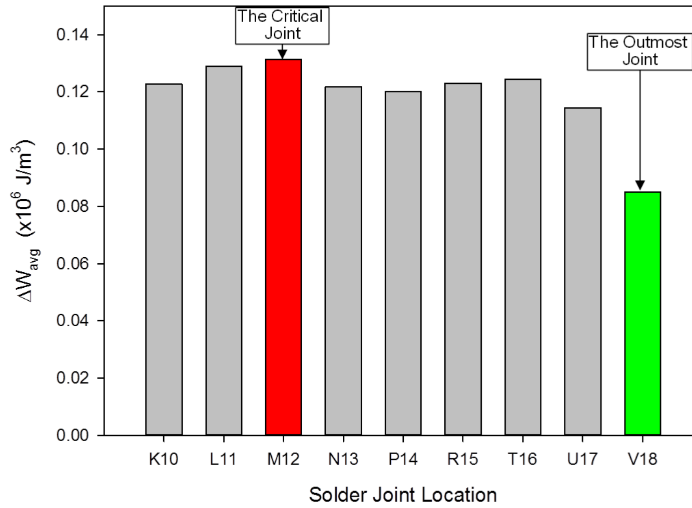

Figure 4.7 Simulation Results of ΔW_{avg} Values for 3D Quarter Model

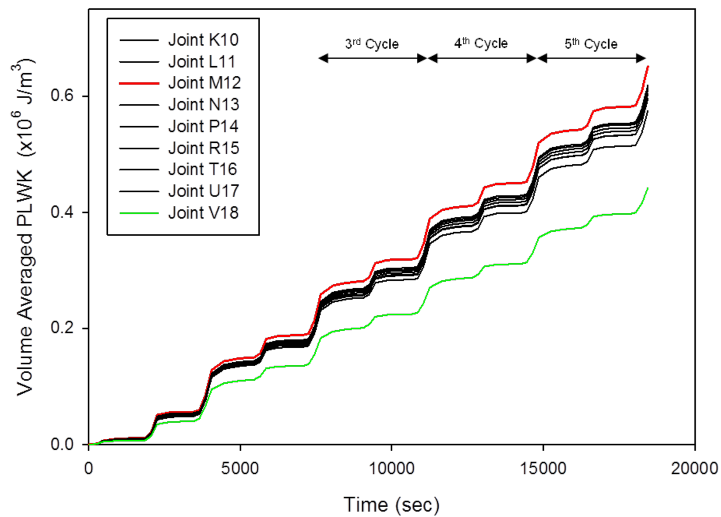

Figure 4.8 History Curves of Volume Averaged PLWK for 3D Quarter Model

4.3.3 3D Octant (1/8) Model

The geometry of octant model has triangular prisms along the diagonal cutting plane of the package assembly (Figure 4.9) that do not allow using unique array pattern to build solder joint array (in this example is area array). Separate modeling and meshing for theses triangular are required, and thus increase modeling difficulty. It is still recommended while the packaging includes high I/O's counts due to a octant model only have half mesh density compared to the quarter model under the same controlled mesh quality.

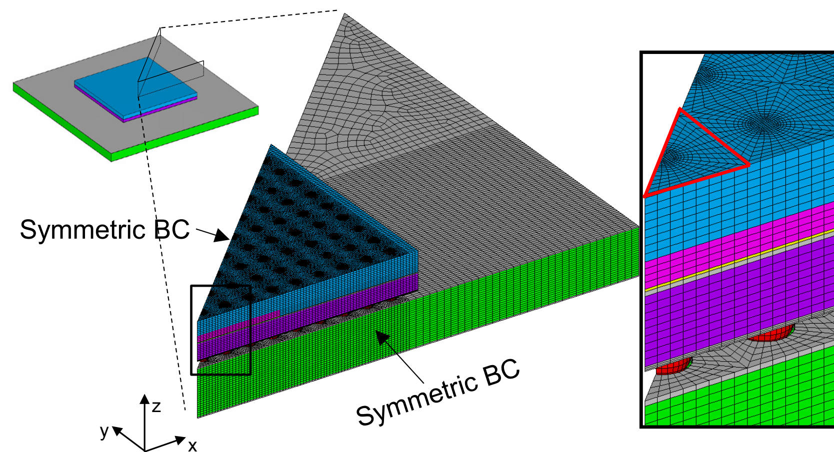

Figure 4.9 3D Octant Model

4.4 2D Slice Model

2D slice model was cut along the diagonal direction from the center to the corner of the package assembly. The details of configurations were captured as shown in Figure 4.10. 2D problem can be assumed as a plane strain or plane stress problem. In the literature [129], the electronic packaging problem is usually considered as a 2D plane

strain problem due to the dimensions along the out-of-plane directions become very large as compared with its in-plane dimensions.

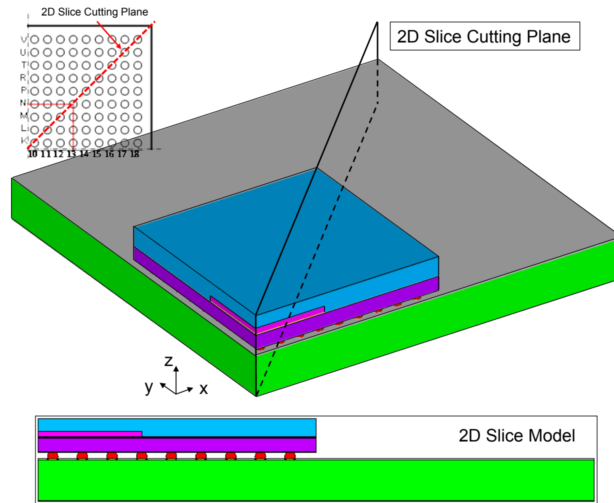

Figure 4.10 2D Slice Model

4.4.1 2D Slice FE Model (Diagonal Direction)

In Figure 4.11, the 2D model was mapped onto the x-y plane and then meshed with four node plane strain quadrilateral elements using auto-meshing approach with 26,058 nodes and 25,136 elements. The orthogonal material properties were also transformed to x-y plane. Boundary conditions for 2D slice model were described as follows: (1) symmetry setup applied at the center line describing geometric symmetry, and (2) a fixed point at the bottom left point of the package assembly to prevent rigid body motion of the model.

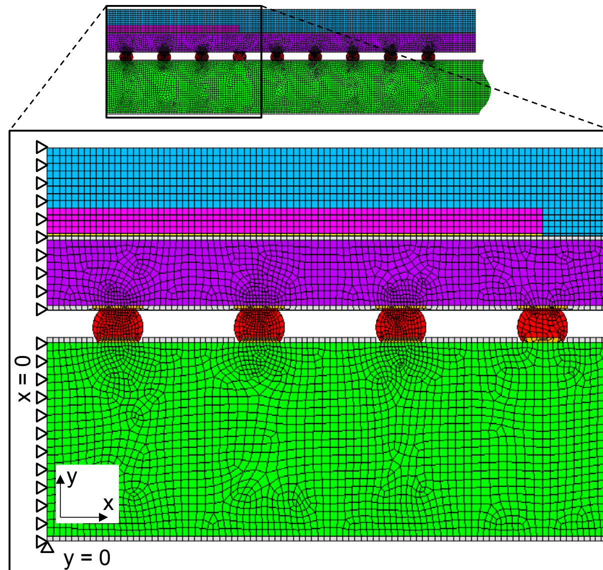

Figure 4.11 2D Plane Strain Model

4.4.2 Simulation Results for 2D Slice Model (Diagonal Direction)

The vertical displacements for 2D slice and 3D quarter models were compared in Figure 4.12. 2D model performed greater vertical deformation than 3D quarter model as a factor of 2.4 at point P locating at the top corner of mold compound. The distribution of the contour range of vertical displacement for 2D slice model was also denser than for 3D Quarter model; thus, 2D slice model using plane strain element overestimated package level simulation results. Similar observations were noted in PLWK contour plots (Figure 4.13); 2D model overestimated PLWK values and performed greater distribution of high PLWK than 3D quarter model among all solder joints.

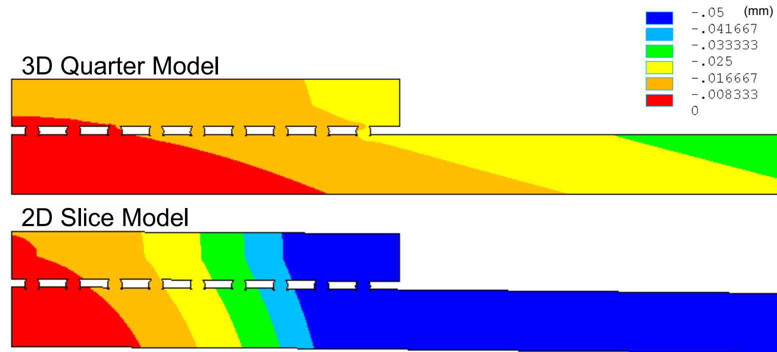

Figure 4.12 Comparison of Vertical Displacements after Five Cycles for 3D Quarter Model and 2D Slice Model

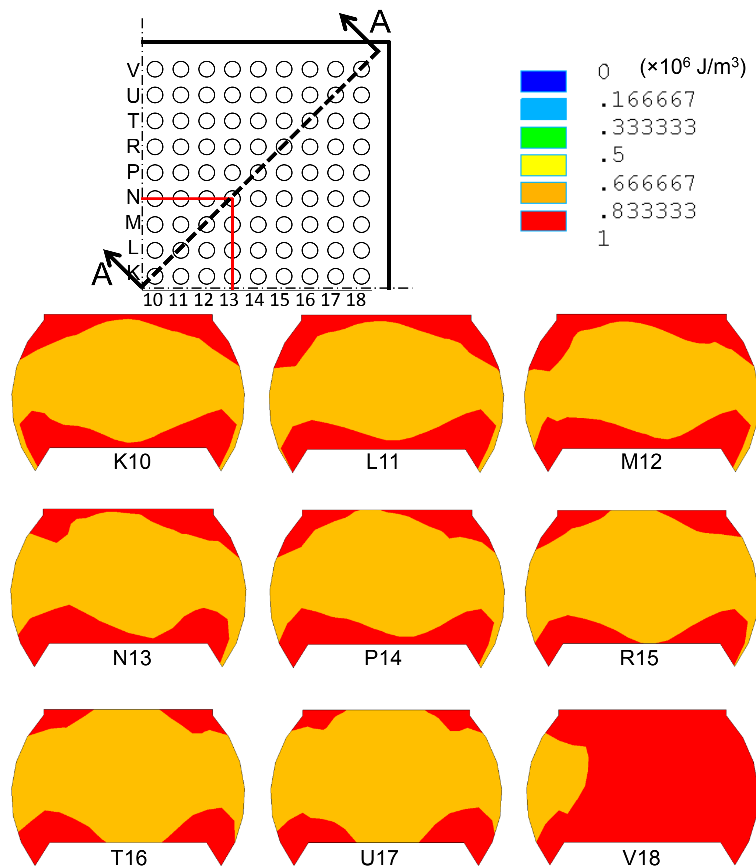

Figure 4.13 Contour Plots of PLWK after Five Cycles for 2D Slice Model

After ΔW_{avg} values were calculated, the most critical region was found at the top region of joint M12. It can be seen in Figure 4.14 that ΔW_{avg} values for joints K10 to

U17 of 2D slice model were always about 50% higher comparing with 3D quarter model due to plane strain element having an infinite thickness. The ΔW_{avg} value for the joint V18 (outmost joint of the package assembly) obtained by 2D model was about 115% higher than 3D quarter model. This can be explained by the plane strain assumption and the die size of this example was small, the effort of DNP (distance from neutral point) acts as major influence on the outmost joint V18 of 2D slice model. The joint V18 of 3D quarter model, by contrast, was not been fully surrounded by other joints resulted in a less restriction while deformation occurred and less PLWK accumulation undergo cyclical thermal loading. Thus, mechanism of response for solder joints of 3D quarter model was more dominated by the configuration of the package assembly.

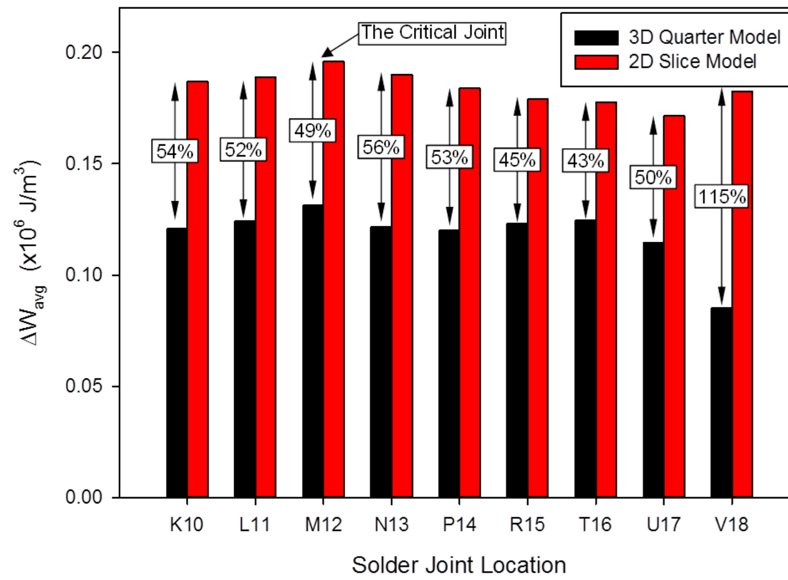

Figure 4.14 Comparison of ΔW_{avg} Values for 3D Quarter Model and 2D Slice Model

As history curves of volume averaged PLWK (shown in Figure 4.15) for both joints M12 and V18 of two different models, joint M12 of 2D model has the highest PLWK responses while joint V18 of 3D quarter has least.

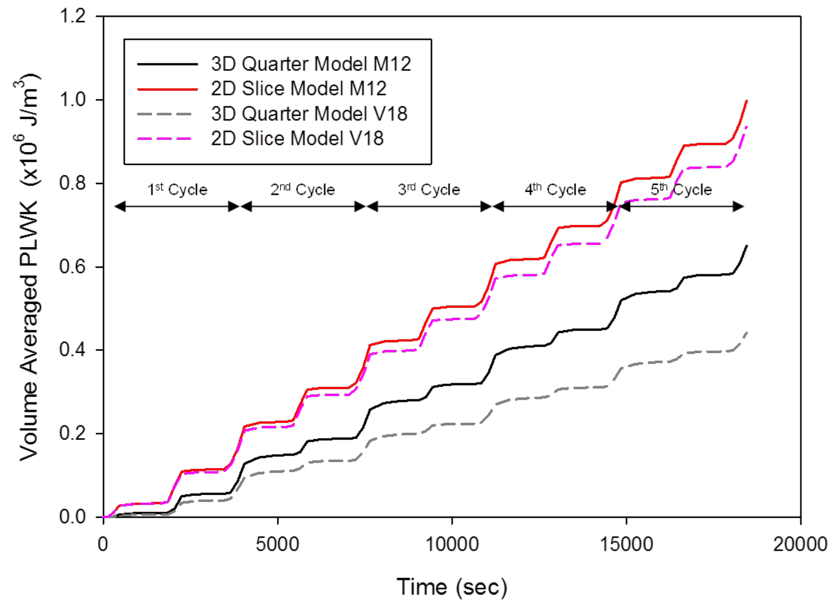

Figure 4.15 Comparison of History Curves of Volume-Weighted Averaging PLWK for 3D Quarter Model and 2D Slice Model

2D model provides an understanding of the qualitative behavior of a package assembly in a very short time. But, the geometry shapes and configuration of package assembly cannot be accurately captured by a plane model in out-of-plane directions, as only a particular sectional shape can be present. Also, the material property was restricted to the plane element which cannot describe the out-of-plane variation of material behaviors. As such, 2D slice model predicts inaccurate quantitatively solution for solder joint of electronic package assembly.

4.5 3D Slice Models

3D slide model considers a slice model along the direction of interest that has a width covering solder joint and passes through top-to-bottom sides of the package assembly. Typically, at least one row of solder joints in a chosen direction is included in a 3D slice model. In this example, the assumption is the maximum ΔW_{avg} occurs at the diagonal direction of the package assembly.

4.5.1 3D Slice FE Model (Diagonal Direction)

The most common 3D slide model is considering a slice from the center of the package to a corner (along diagonal direction). For the convenience of FE modeling, the 3D slice model was rotated 45° about z axis after FE model was built, and then its cutting planes were paralleled with x-z plane. The orthogonal material properties were also transferred to the new coordinate system. As shown in Figure 4.16, there were five boundary conditions were applied including two symmetric planes, two generalized plane deformation planes, and one fix point. The generalized plane deformation (GPD) constraint states as follows: the nodal deformations of nodes on the cutting plane are identical in the out-of-plane direction of the cutting plane. The GPD constraints were separately applied on the two cutting planes as not representing symmetric nor free planes. In this 3D slice model, the cutting planes are free to move in the ±y directions, but the planes are required to remain planar subjected to loading conditions. Similar to 3D quarter model, 3D slice model was meshed with hexahedral element using 225,404 elements.

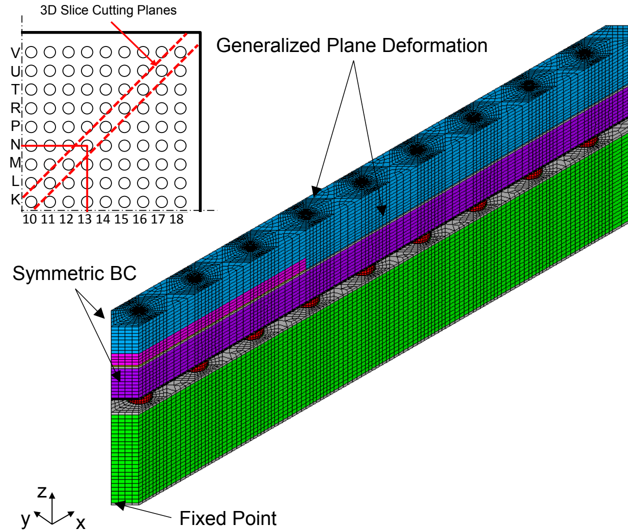

Figure 4.16 3D Slice FE Model (Diagonal Direction)

4.5.2 Simulation Results for 3D Slice Model (Diagonal Direction)

As shown in Figure 4.17, the vertical displacement contours for two models still not matched well, but the difference of vertical displacement at point P was reduced to 36%. The distribution of vertical displacement was also more closed to 3D quarter model than 2D slice model. In Figure 4.18, PLWK contour plots showed the distributions of PLWK for 3D slice model have a better agreement with 3D quarter model.

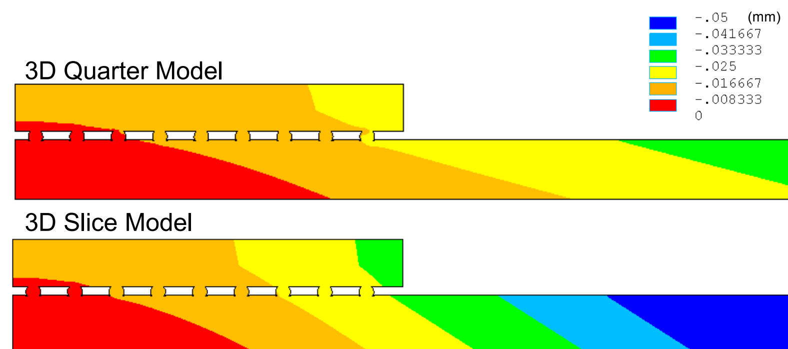

Figure 4.17 Comparison of Vertical Displacements for 3D Quarter Model and 3D Slice Model

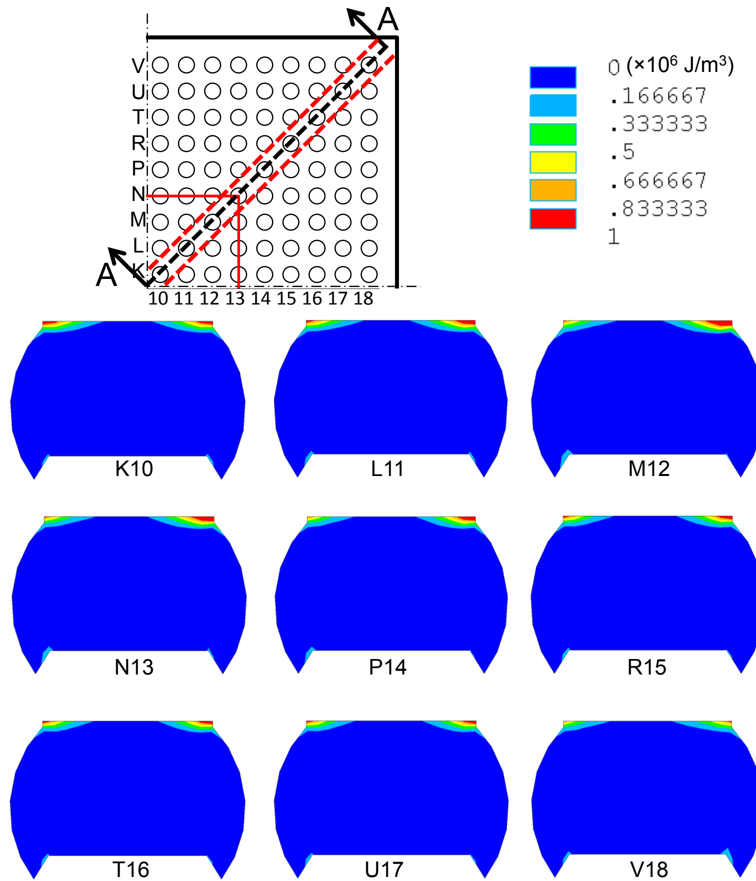

Figure 4.18 Contour Plots of PLWK after Five Cycles for 3D Slice Model

After ΔW_{avg} values were evaluated, the differences were only around 5% for joints K10 to U17 (Figure 4.19). Although the PLWK and ΔW_{avg} for joint V18 of 3D slice model were still higher than 3D quarter model, their values have reduced to a more reasonable range where no extreme solutions as 2D model have been shown.

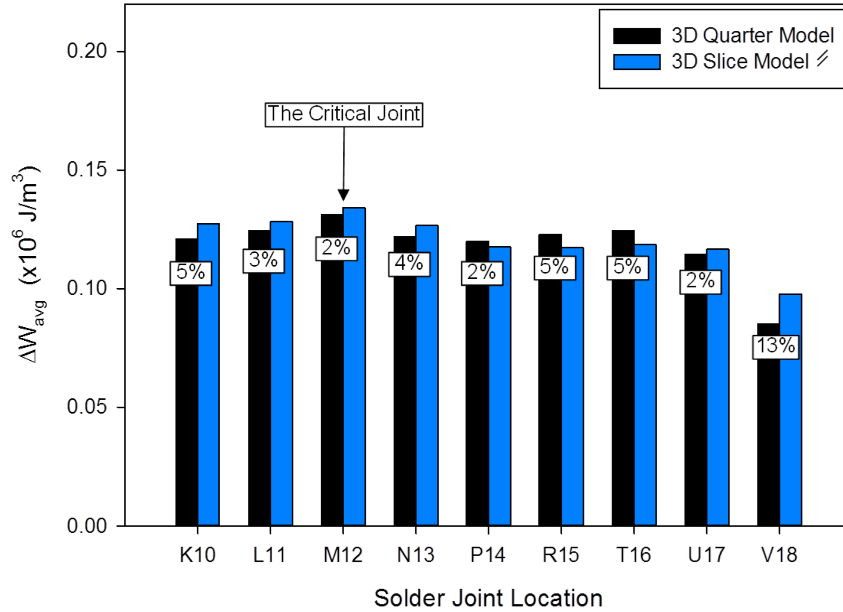

Figure 4.19 Comparison of ΔW_{avg} Values for 3D Quarter Model and 3D Slice Model (Diagonal Direction)

The same trend can be observed on the history curves of volume-weighted averaging PLWK for joints M12 (Figure 4.20), a good match showed that both models can predict closed results subjected to thermal cycles. As a result, the simulation of 3D slice model preformed a better improvement than 2D slice model. Both assumptions of plane strain for 2D and GPD for 3D yielded the solution more valid as the joint more closed to the package center, but become invalid as away from the center where 3D effect becomes more pronounced [165] [190].

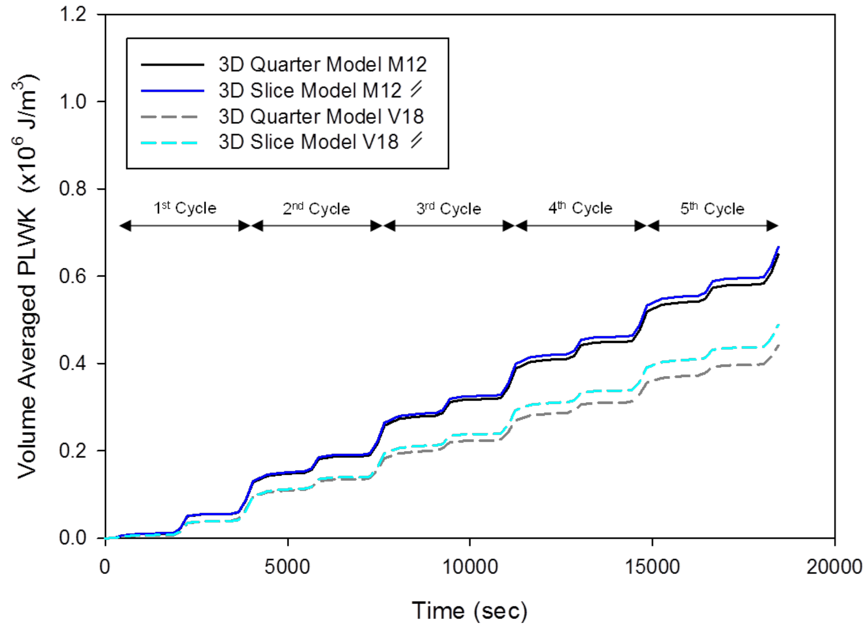

Figure 4.20 Comparison of History Curves of PLWK for 3D Quarter Model and 3D Slice Model

4.5.3 3D Slice Model (Diagonal Direction, Flat End)

We also noticed there is another modeling approach for 3D diagonal slice model. The right angle at the package corner was simplified as a flat end surface as show and BCs were also modified as a symmetric plane and a fixed point as shown in Figure 4.21. Simulation results of ΔW_{avg} values for the most critical joint M12 were 0.1341 and 0.1344 $\times 10^6$ J/m^3 for right angle and flat end models, respectively. Thus, geometric simplification and BC assumption at the center corner of quarter package model have a very minor effect on simulation result.

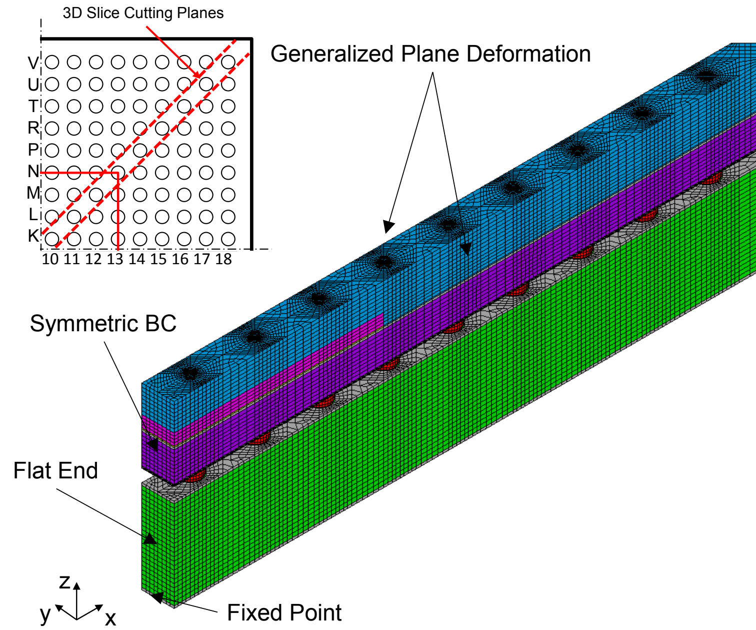

Figure 4.21 3D Slice FE Model (Diagonal Direction) Building with Simplified Flat End Surface

4.5.4 3D Slice Model (Parallel Direction)

Next, we consider a 3D slice model, its cutting planes were paralleled to natural boundary of the package, contains the solder joints locating at row L as illustrated in Figure 4.22. Boundary conditions were also shown in the figure. As the comparison shown in Figure 4.23, the ΔW_{avg} values for joints on row L of two different models have very close simulation results. However, the assumptions of the BC's in this example did not consider the distance to center in y direction. Both rows M and L simulated exact the same solutions, and this phenomenon would also true for rows P to V. Thus, misidentify the critical joint occurs while using 3D slice model without proper considering deformation in out-of-plane directions.

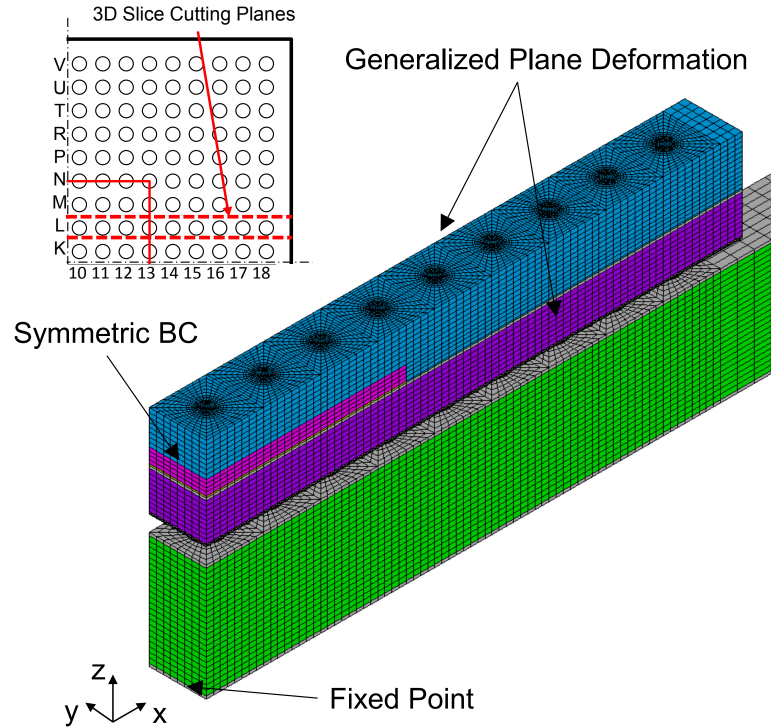

Figure 4.22 3D Slice FE Model (Parallel Direction)

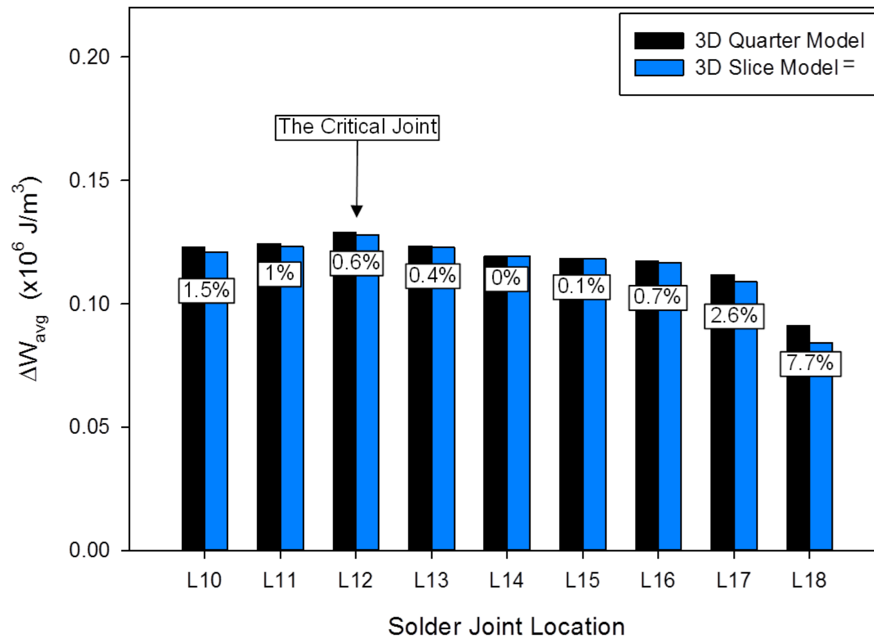

Figure 4.23 Comparison of ΔW_{avg} Values for 3D Quarter Model and 3D Slice Model (Parallel Direction)

3D slice model captures the top-through-bottom configuration of package assembly and also has a width dimension that provides geometric definition of the solder joint. 3D element type can be used to better describe the out-of-plane nonlinear material behaviors. As a result, the 3D slide model simulated an accurate solution for the solder joints along diagonal direction of package assembly. It provides computationally efficient due to only selected solder joint row is calculated. For a time and computer resources intensive analysis, 3D slice model is still a better option than 2D slice model.

4.6 Submodeling Technique

As the technique of submodeling has been introduced in Chapter 3.3.5, in this section, we used the method of nonlinear global model and local model. Initially, the coarse-mesh global model was used to identify critical joint and then a better local solution was calculated by a fine-mesh local model.

4.6.1 Submodeling FE Model

The example model was initially built with a coarse mesh using 259,104 hexahedral elements as the global model. As shown in the Figure 4.24, the coarse-mesh solder joint of the global model has lost geometry accuracy, only a barely sphere shape can be observed. Note that a single solder joint for 3D quarter model and 3D global model was built using 2,496 and 288 nonlinear hexahedral elements, respectively, and the local model, containing the most critical joint, shared the exact same meshing as the 3D quarter model.

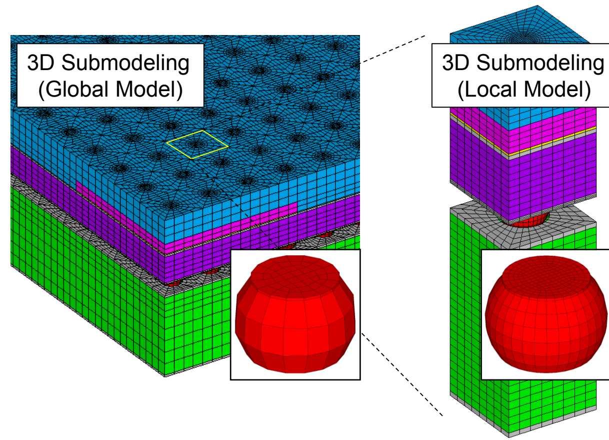

Figure 4.24 Submodeling FE model

4.6.2 Simulation Results for Submodeling Model

Figure 4.25 showed the results of vertical displacement for global and 3D quarter models were matched well. As a result, the 3D global model captured the package level responses as 3D quarter model does. The critical joint M12 was also identified by the global model. Then, the local model was built from a unit model (through the top-to-bottom of the package assembly) contains the most critical joint M12. Displacement information corresponding to load step was interpolated into the simulation of local model as additional local BC's for local model simulation.

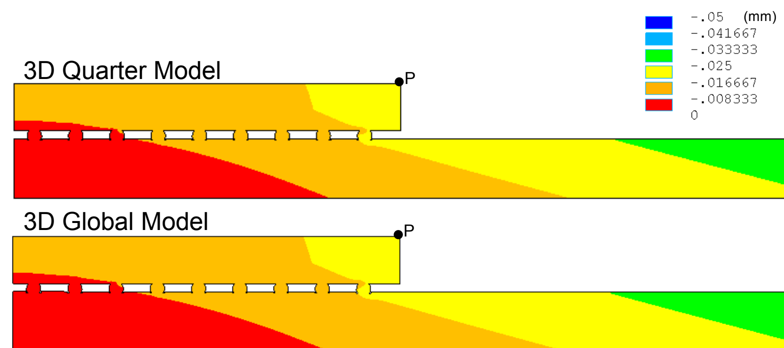

Figure 4.25 Comparison of Vertical Displacements after Five Cycles for 3D Quarter and Submodeling Models

In Figure 4.26, distribution of PLWK contours for the local model was identical to 3D quarter model. As shown in Figure 4.27 and Figure 4.28, the local model showed very good agreements of ΔW_{avg} and history curve of volume-weighted averaging PLWK as 3D quarter model. Similar accumulations of PLWK's at temperature ramps and dwells were presented on the local model and 3D quarter model, despite the large difference of global model.

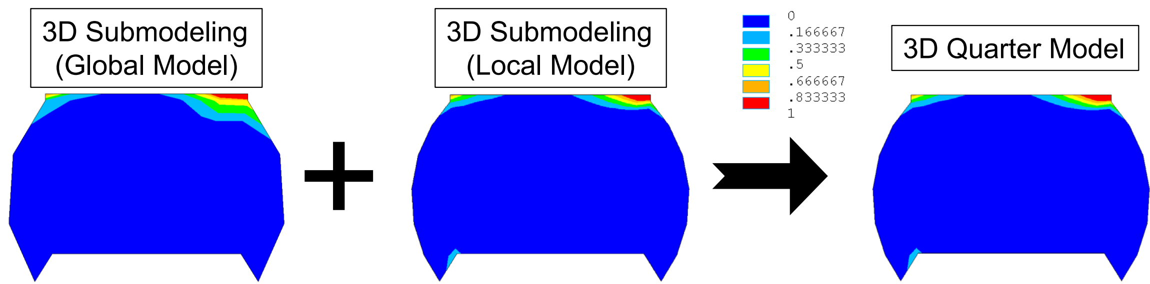

Figure 4.26 Comparison of PLWK after Five Cycles for 3D Quarter and Submodeling Models

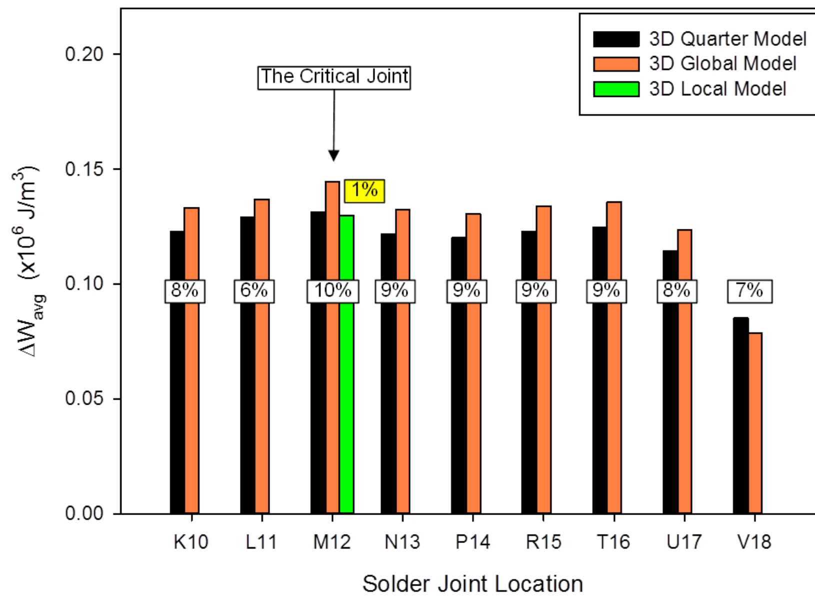

Figure 4.27 Comparison of ΔW_{avg} Values for 3D Quarter and Submodeling Models

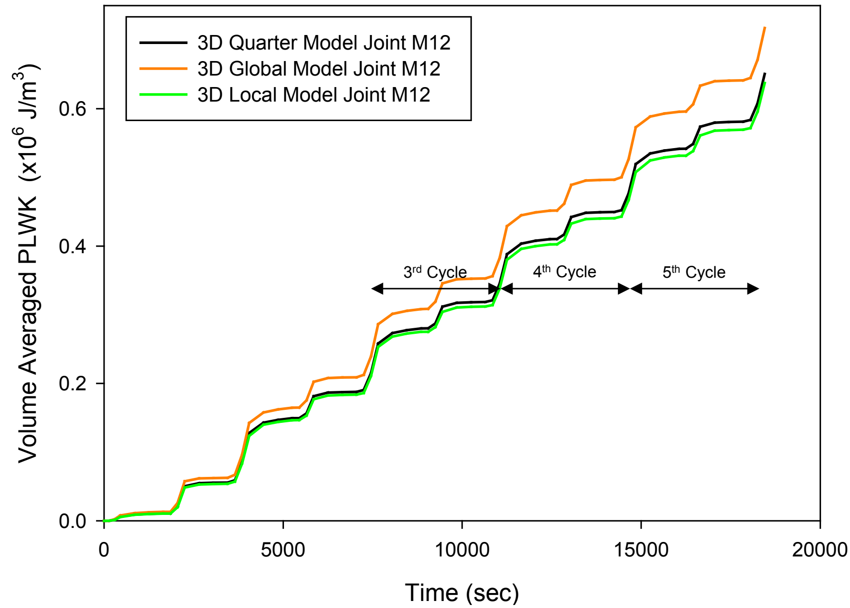

Figure 4.28 Comparison of History Curves of Volume-Weighted Averaging PLWK for 3D Quarter and Submodeling Models

4.7 Multipoint Constraint (MPC) Technique

MPC is a technique to establish a relation of contact compatibility to prevent interpenetration using extra elements (including contact and target elements) deployed along the contacting interfaces after the model was meshed with traditional elements. Although the constraint equations eliminate some of DOF's of the FE model, overall computational time may increase as forming MPC equations, and updating MPC relations of large deformation analysis.

4.7.1 MPC Model

The example model was meshed separately and yielded to two different mesh patterns, described as follows: (1) the solder joints, copper pads and solder mask were meshed using a fine mesh as the corner region where a circular mesh pattern was presented as shown in Figure 4.29, and (2) the rest components of the package were

meshed using a coarse mesh. Instead of circular mesh pattern, a more regular rectangular mesh pattern can be observed from the top/bottom view of MPC model. The mesh density was hugely reduced at the rectangular meshing region where low interest was taken. Then, MPC setup was added at the interface of these two different mesh patterns to establish constraint relation. Figure 4.29 showed the incompatible meshing patterns at the top of copper pad (orange) and the substrate (purple).

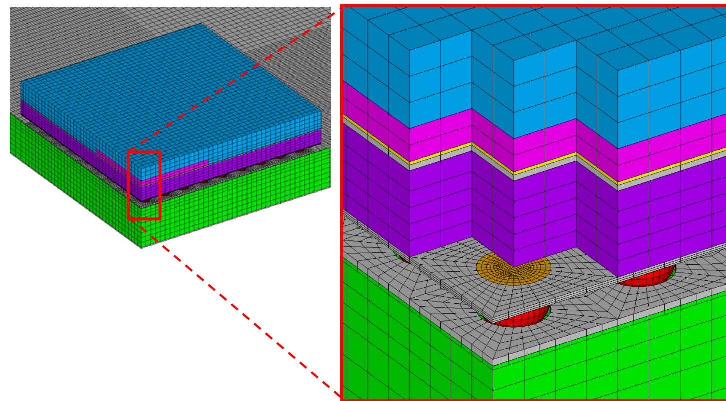

Figure 4.29 MPC Model

4.7.2 Simulation Results for MPC Model

As the vertical displacement contours plotted in Figure 4.30, the overall displacement distribution for MPC model matched well with 3D quarter model. However, the PLWK contour plot (Figure 4.31) showed that MPC preformed larger distribution of high PLWK than 3D quarter model on all joints. It can be explained by the behavior of package assembly captured by coarse rectangular meshing model was accurate, but the detailed response of displacement above the solder joint interpolating by MPC was lack of accuracy. Due to the inaccurate interpolation of the displacement, the

distribution of high PLWK presented larger areas than the results for the 3D quarter model on all solder joints.

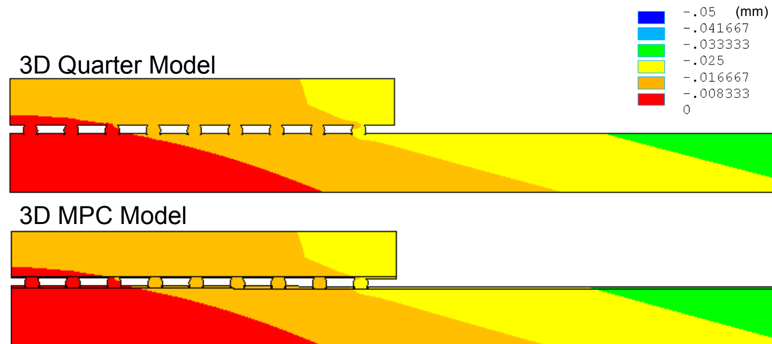

Figure 4.30 Comparison of Vertical Displacements after Five Cycles for 3D Quarter Model and MPC Model

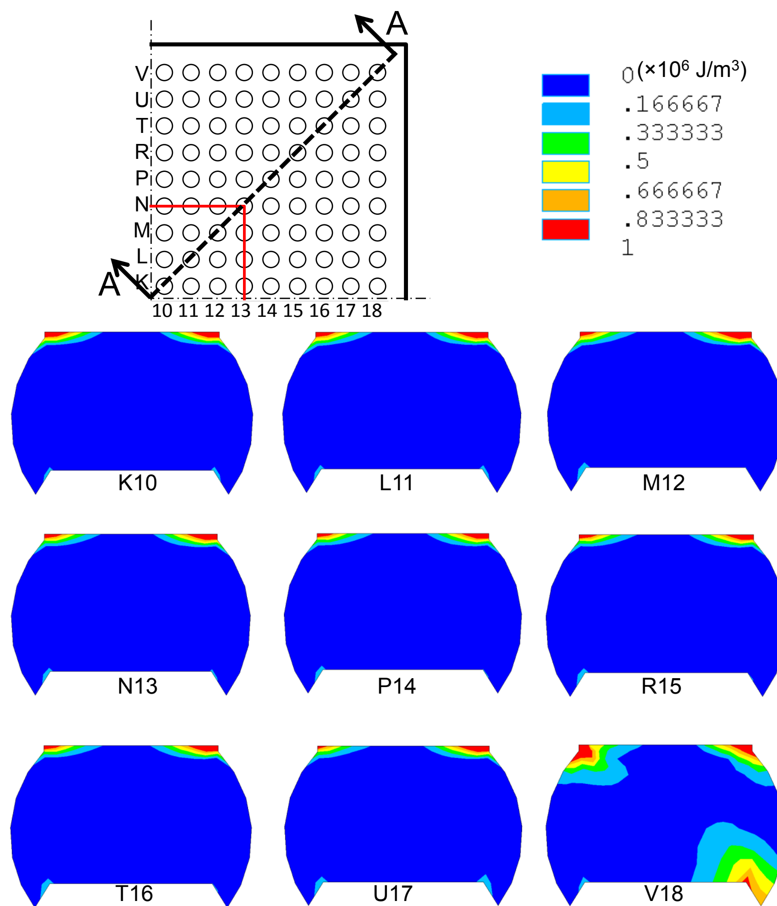

Figure 4.31 Contour Plots of PLWK after Five Cycles for MPC Model

In Figure 4.32, it can be seen that MPC model overestimate the PLWK over thermal cycles. The ΔW_{avg} values for MPC model were also greater than for 3D quarter model; this MPC setup introduced 24 – 42 % differences of ΔW_{avg} as shown in Figure 4.33.

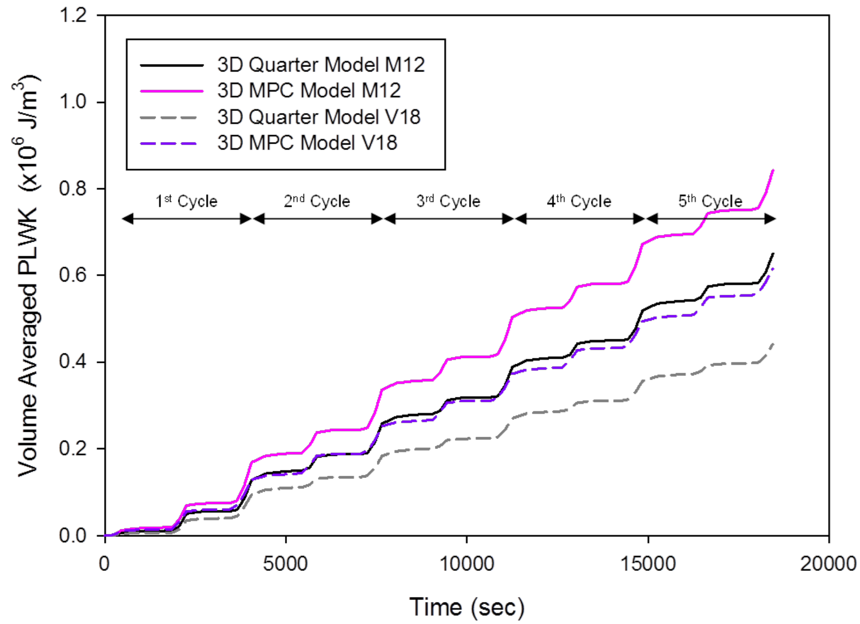

Figure 4.32 Comparison of History Curves of Volume-Weighted Averaging PLWK for 3D Quarter and MPC Models

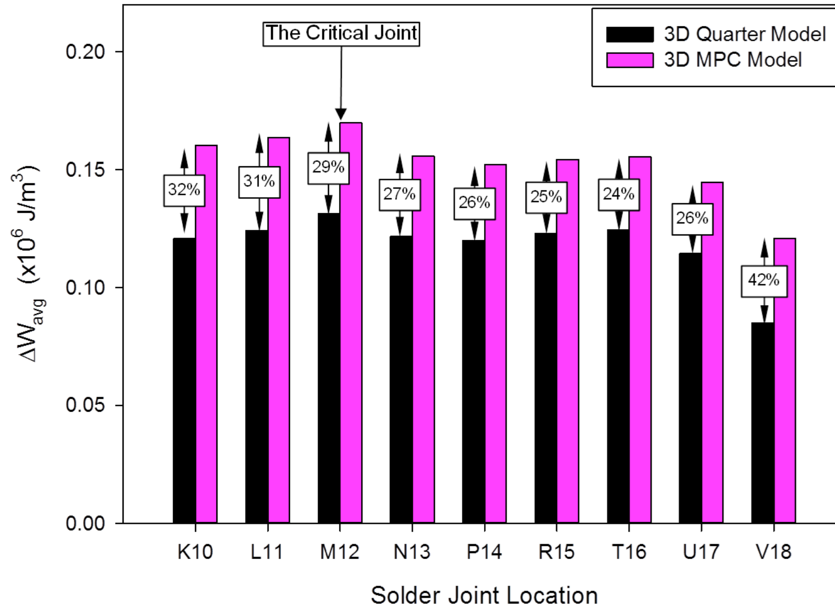

Figure 4.33 Comparison of ΔW_{avg} Values for 3D Quarter and MPC Models

The MPC technique provides an effective approach for bonding two components together without considering mesh continuity. It improves modeling convenience using less geometric partitions, and reduces overall mesh density of the FE model. In addition, similar to 3D quarter model, the analysis using MPC calculates the responses for all solder joints of a package assembly in a simulation; unlike submodeling technique that an extra simulation local simulation is needed. Caution must be taken while using MPC to bond incompatible mesh pattern [176] [191] [192] [193]. Bonding over coarse mesh with refine meshing may lose the accuracy of simulation.

4.8 Summary and Conclusions

The efficiency and accuracy for five different approaches were compared in Figure 4.34 and Figure 4.35, respectively.

2D model performed the fastest simulation and yield a quick result over other models but sacrificing the accuracy. It also showed a most different trend of ΔW_{avg} values than other models and overestimated the values of ΔW_{avg} for all joints.

3D slice model improved the solution quality over 2D slice model and still performed an efficient simulation. Similar to plane strain setup for 2D slice model, the use of GPD made the solution more accurate as closed to the center of the package assembly. For the joint row paralleled to edge surface, deformation in out-of-plane must be proper treated or different row of joints may yields in the same simulation result.

Submodeling performed an efficient simulation as 3D slice model in this study. The global model captured the package level responses and identified the correct critical joint. Then, detailed local model simulated an improved result. Combined global and local model simulations, the balance between efficiency and accuracy of simulation can be achieved. It is worth mentioning the trend of simulation result for submodeling model is correct, but the simulation efficiency maybe lost while detailed solutions for all joints are required. An improved submodeling approach has been proposed [194] to achieve a large reduction in computational time, better detailed modeling for local model, and improved simulation accuracy.

MPC, a powerful modeling technique requires no meshing continuity, simulated a large difference compared to the 3D quarter model. Mesh incompatibility is still an issue affecting the simulation accuracy. Syed [176] has proposed a solution by moving MPC away from the critical region to reduce the difference form the MPC interpolation. An improved MPC analysis approach can be applied on the package level problem utilizing

multiple-MPC to improve simulation efficiency without losing accuracy has been proposed [193].

The comparisons of different modeling approaches were summarized in Table 4.4. 3D-based approaches have their own advantages on capturing accurate responds in 3D space (such as package level deformation), but more DOF's and elements consume more computer resources. Considering the common configurations of PBGA assembly in the market, submodeling has its advantage on the balance between accuracy and efficiency. For more complex configurations, MPC provides more flexibility on modeling but accuracy may lose without appropriate treatments.

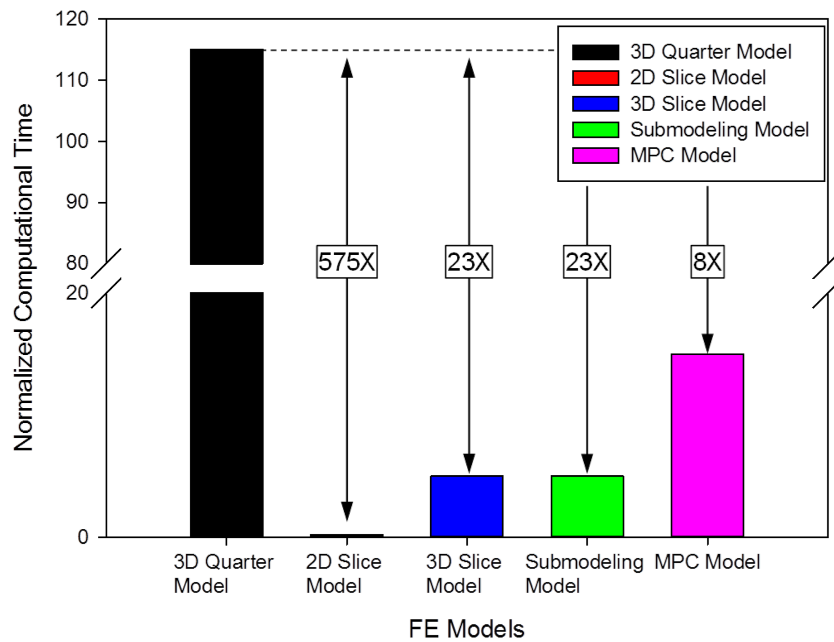

Figure 4.34 Comparison of Efficiency for Different FE Models

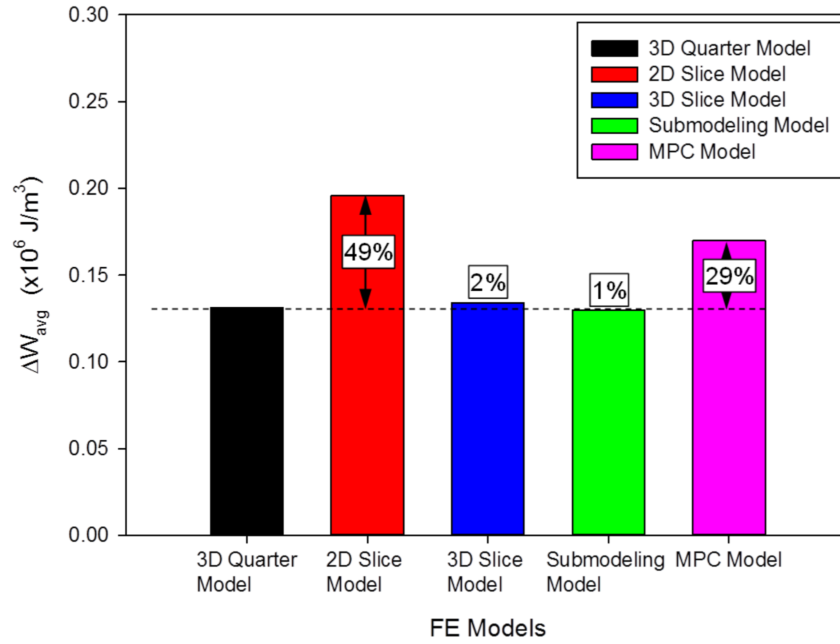

Figure 4.35 Comparison of Accuracy for Different FE Models

Table 4.4 Summary of Comparisons for Different FE Models

FE Model Types	3D Quarter Model	2D Slice Model	3D Slice Model	Submodeling Model	MPC Model
Modeling Difficulty	Fair	Easy Auto-Mesh	Easy	Advanced	Advanced
Mesh Density	High	Low	Fair	Low	High
Modeling Assumption	Symmetric BC	Plane Strain	GPD	Cutting Plane	MPC
Vertical Displacement at Point P (mm)	-0.0215	-0.0738	-0.0293	-0.0215	-0.0217
Result Accuracy for Package Level	(Reference)	Poor	Fair	Good	Good
Solution of Joints	All	Sliced Row	Sliced Row	Selected Joints	All
ΔW_{avg} for Critical Joint ($\times 10^6$ J/m^3)	0.1313	0.1959	0.1341	0.1297	0.1699
Result Accuracy for Critical Joint	(Reference)	Poor	Fair	Good	Poor
Efficiency	Poor	Very Fast	Fast	Fast	Fair
Modeling Difficulty	Difficult	Easy	Fair	Fair	Easy

CHAPTER 5
IMPROVED FINITE ELEMENT ANALYSIS STRATEGIES FOR PBGA PACKAGE ASSEMBLIES SUBJECTED TO THERMAL CYCLING

5.1 Introduction

Most of the PBGA designs are the choices for optimizing device electrical performance. They are lightweight, thin with short connections, and they minimize the use of board space. The solder joints of PBGA have been deployed on the bottom surface and have distinct advantage over other package in that can be placed on much closer centers. A typical PBGA is fabricated with many different components which in turn are fabricated from many different materials which exhibit different material properties (e.g. modulus of elasticity, Poisson's ratio, CTE etc.). Differential thermal expansions are induced in each component when the temperature changes in service life.

Solder interconnection is often the weakest component in a PBGA package assembly. Large strain/stress and energy accumulated per loading cycles lead to the crack initiation and subsequent propagation within solder interconnection [25] [78] [195]. In additions, the operating temperatures are relatively close to the low melting temperatures of solder alloys, solder joints undergo server fluctuations during the service life and may result in an unacceptable short service life [125]. Thus, the reliability of a package depends on the reliability of the solder joint and the reliability analysis of solder interconnection has become a serious concern in electronic package designs.

In order to understand the responses of solder joint and make a better fatigue life prediction, realistic constitutive relations for solder alloys are needed. Constitutive models of separating inelastic strain into time independent plasticity, time dependent viscoplasticity, and creep approaches often lead to over predicting the strain magnitude and inconsistencies in the final results [25] [26] [78]. A set of constitutive equations for viscoplastic, isotropic resistance to inelastic flow, rate-dependent deformations model proposed by Anand and Brown [84] [88] has been widely used in industry to illustrate the nonlinear material behavior of lead free solders.

In finite element modeling, mesh continuity is always a challenge task while building a model containing several different geometrical shapes of components. Besides geometric modeling, the constitutive models used for solder alloys introduce material nonlinearity into the analysis [196]. These factors increase simulation difficulty to another higher level; hence, it can be seen in many literature [71] [99] [164] [197] that high-density mesh models and computer-intensive tasks were required for package assembly simulations. In additions, the guidelines for simulating a consistence and convergence solution still have not been completely studied. In order to prevent using unreasonable model size/DOF's and unlimited computer resources, guidelines for an efficient simulation without sacrificing solution accuracy are in urgent [3] [187].

In this chapter, modeling approaches were focused on the continuous meshing models. An improved FE modeling approach was developed that utilizes a transition region of hexahedral meshing to reduce model size/total elements/DOF's while the mesh quality of the FE model was still under controlled in a high-quality mesh. Then the convergence studies studying the effects of the mesh quality and the load step size on

both unit and package models were investigated to develop the optimal analysis strategy. This optimal analysis strategy can achieve the best balance between simulation accuracy, efficiency, as well as solution consistency.

5.2 Finite Element Modeling and Simulation

The procedures of using FE-based approaches to study the reliability of solder joints undergoing thermal cycling loading are extracting simulation results and then incorporating with proper failure criteria to predict the fatigue life of the solder joint. A reliable simulation result is the key of these procedures. Considering the material nonlinearity of solder alloy and the mismatch of CTE for components in a package assembly, the analysis can be categorized as a material nonlinear problem. In additions, the loading condition in this type of problem is a thermal cycling loading; several cycles must be simulated to better understand the responses of all components of a package assembly. High-density meshing model is preferred for material nonlinear problem but not an ideal option for a cycling loading condition; resources and capabilities of computer are always limited. Oversize meshing model even crashes computer environment before analysis start. Combined above considerations, an efficient FE simulation for electronic package assembly subjected to thermal cycling without losing simulation accuracy is still a challenge job. Advanced FEA techniques (such as constraint relationship, submodeling, substructure techniques, etc.) may improve simulation efficiency [28] [99] [125] [129] [148] [152] [175] [176] [173] [193] [194] [198]. But, caution must be taken that inappropriate use of advanced FEA techniques easily introduces significant simulation error while incautious setup made by inexperienced analyst.

In this chapter, FE modeling methods were focused on continuous meshing model; less assumptions and simplifications were made to reduce unexpected numerical issue in the analysis. Start from the convergence study of unit model, we have investigated the effects of mesh quality and load step size on the solution quality and simulate efficiency. An improved meshing strategy was proposed to reduce mesh density of the FE model, improve simulation efficiency and also maintain simulation accuracy. And then similar approach was extended to a small 8 × 8 mm^2 package assembly to understand the effects of mesh quality and load step size are still valid on a package size model. Thus, an improved FE analysis strategy for package level problem subjected to thermal cycling was developed and validated utilizing a 3D unit model and quarter package assembly model.

5.3 Example Models

Two different sizes of PBGA assembly packages were used as example models. The first model is an 8 × 8 mm^2 PBGA configuration composed of a 4 × 4 mm^2 chip (center red box in Figure 5.1) and 100 solder joints. This package mounted on a PCB board was used to study convergence and develop the improved analysis strategy. Dimensions of the example package are listed in Table 5.1. The second model is a 15 × 15 mm^2 PBGA configuration composed of a 5.6 × 5.6 mm^2 chip and 324 solder joints (Figure 5.2 and Table 5.2) for demonstrating the efficiency and flexibility of the optimized simulation strategy. Both solder joint pitches in the example models were 0.8 mm. Due to the symmetry of the example packages, two one quarter 3D models with symmetric boundary conditions were taken for demonstration (Figure 5.1 and Figure 5.2).

The material properties, loading condition, and fatigue model used in this chapter can be found in Chapter 4.2.

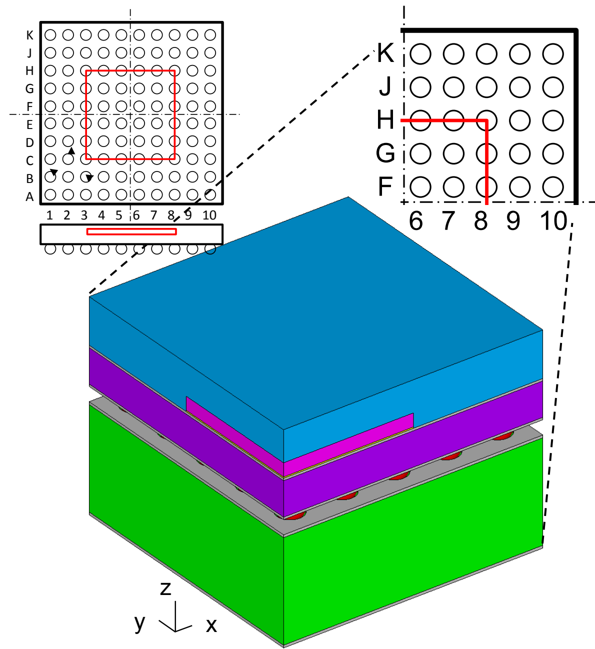

Figure 5.1 Quarter 8 × 8 mm^2 PBGA Package Assembly

Table 5.1 Dimensions for 8 × 8 mm^2 PBGA Package Assembly

Component	Dimensions (mm^2)
PCB	8 × 8
Solder Mask	8 × 8
BT Laminate	8 × 8
Die Attach	4 × 4
Silicon	4 × 4
Mold Compound	8 × 8

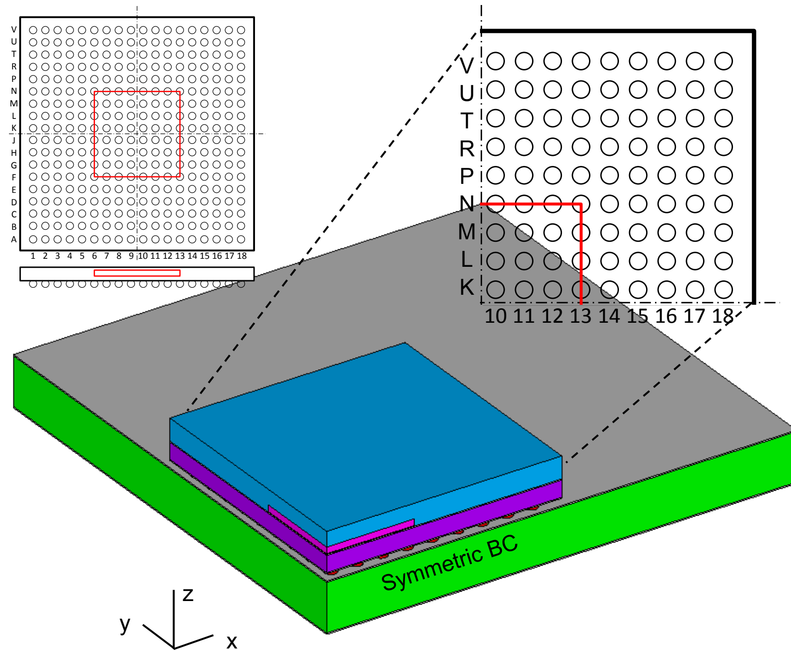

Figure 5.2 Quarter 15 × 15 mm^2 PBGA Package Assembly

Table 5.2 Dimensions for 15 × 15 mm^2 PBGA Package Assembly

Component	Dimensions (mm^2)
PCB	30 × 30
Solder Mask	30 × 30
BT Laminate	15 × 15
Die Attach	5.6 × 5.6
Silicon	5.6 × 5.6
Mold Compound	15 × 15

5.4 Convergence Study on Unit Models

A unit model, contains one solder joint, was utilized for a convergence study before a package simulation. By the use of a unit model containing all the component-layers and different material properties, it would help us understand the response trends of the configuration within the package assembly subjected to thermal cycling in an efficient way. As shown in Figure 5.3, the unit model was separated from the center of quarter package in order to capture all details of the example models.

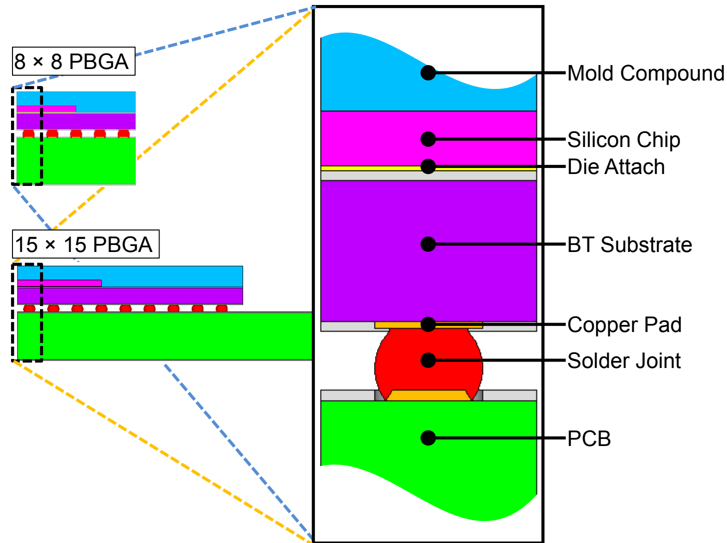

Figure 5.3 Detail View of Unit Model

5.4.1 Effect of Element Types: Tetrahedral Element vs. Hexahedral Element

In a 3D FE analysis, two most common used element types are tetrahedral and hexahedral (brick) elements [144]. Several robust algorithms [199] have been developed to make it possible for auto-meshing via tetrahedral element on an arbitrary geometry without mesh continuity trouble. Unfortunately, literature [25] [200] [201] [202] [203] [204] have showed that there are convergence and accuracy concerns about the application using tetrahedron in nonlinear material having plasticity behavior. Hexahedral element performs better accuracy over tetrahedral element in the problems related to plasticity, contact, and distortion [203], and less elements and computer resources are required in a general problem while a model is meshed with hexahedral elements. Hexahedral element has becomes a more popular element type for the simulation encountering large deformation, contact, plasticity, etc. However, the mesh generation solver for fully auto-meshing via hexahedral element is still under developing; especially for algorithm of generating an all hex model with a reasonable element size

[205]. Process of decomposition/partition for complex geometric is still required to generate and perform high quality hexahedral mesh. In this study, all models were partitioned interactively while necessary and meshing with hexahedral elements.

As an example of mesh quality inspection shown in Figure 5.4, two models were partitioned in the same way and then meshed using two different element types. It can be seen high-density mesh was used but poor mesh quality was detected on the model meshing with tetrahedral element via auto-meshing approach.

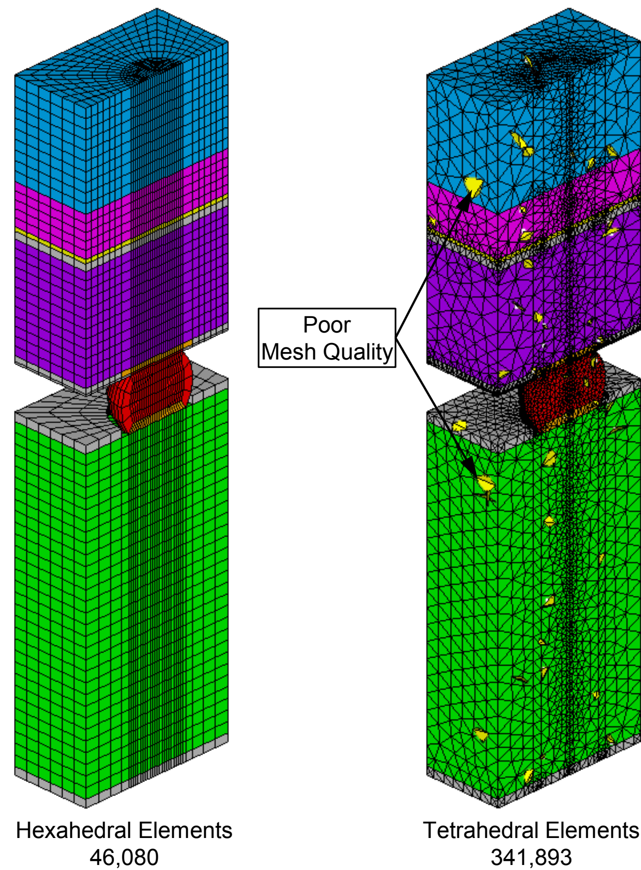

Figure 5.4 Mesh Quality Inspection for Models Meshing via Two Different Element Types: Hexahedral (Left) and Tetrahedral (Right) Element

5.4.2 Conventional Meshing Strategy

Mesh generation is one of the most important steps in FEA since the decision made at this point affects the efficiency and accuracy of simulation. Take advantage of fast simulation from a low-density meshing model is preferred by analyst, but the solution quality cannot be guaranteed; a poor solution can be expected. In the most cases of nonlinear analyses, the tradeoff must be made between solution quality and simulation efficiency. Thus, the choice of meshing strategy for analysis is crucial.

There are various geometrical shapes of the components of a package assembly, such as solder joint has a shape of sphere, and silicon die has shape of rectangular block. Hence, mesh continuity between different components is always the first challenge for FE modeling. In the perspective of FE modeling of building example PBGA assembly, the major challenge is the mesh continuity between the interfaces of solder joints/copper pads and PCB/BT substrate as illustrated in Figure 5.5.

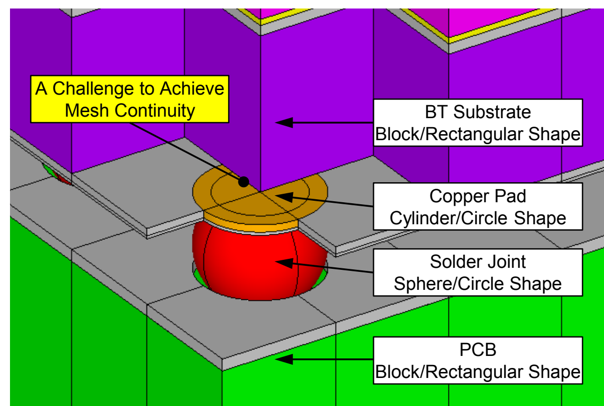

Figure 5.5 Geometrical Configuration of Example PBGA Package Assembly

Most analysts start meshing from the solder joint and then extrude the elements at the top and bottom of the joint to create the copper pad meshes after geometrical

parameters and partitions have been specified. Once meshes of the solder joint and copper pads have been created, the mesh regions related to the PCB, BT substrate, silicon die, and mold compound are generated with the same approach as the copper pad mesh. In meshes using this strategy, a circular mesh pattern can be observed in its top/bottom view as seen in the literature. We named this approach as the conventional meshing strategy (Figure 5.6).

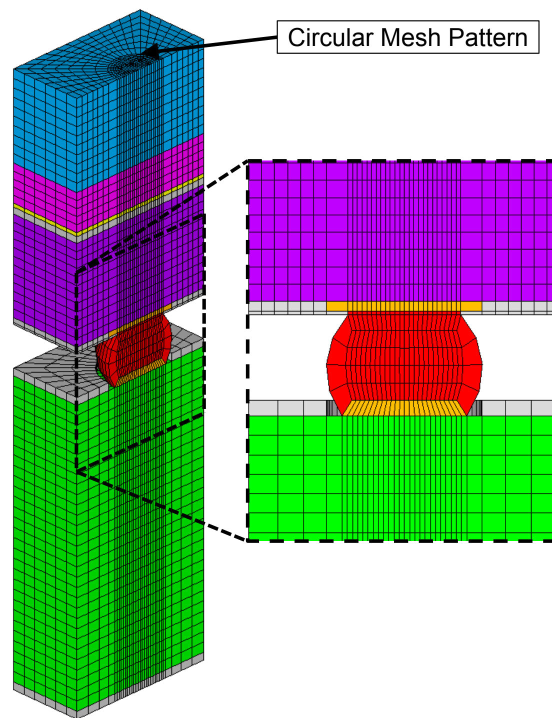

Figure 5.6 Conventional Meshing Strategy

The geometrical shapes of components in an electronic package assembly are relative in regular shapes; there are no freeform surfaces or irregular shapes need to be considered while modeling in proceeding. As a result, the shape of element can be easily kept as a regular shape and the mesh quality can be maintained by controlling the maximum aspect ratio of element shape. The aspect ratio is defined as the ratio of the

longest dimension to the shortest dimension of an element. Typically, decreasing the aspect ratio improves the mesh quality as well as accuracy of the solution of the analysis.

In this study, the maximum aspect ratio of the element shape was controlled in a range of fine meshes (between 4 and 7); and then applied to different meshing strategies. Meshing of unit model was started with an aspect ratio of 7 (AR 7), and then the aspect ratio was reduced to regenerate a new meshing model for results comparison. It should be noted that in the region of the example model where the solder mask was a very thin coating, the controlled maximum aspect ratio can be only reduced to a number of 4 (AR 4). The unit model was meshed with the maximum aspect ratio of 7, 6, 5, 4.5 and 4 (as shown in Figure 5.7); and the total number of elements dramatically increased as the maximum ratio decreased as listed in Table 5.3. In this study, different aspect ratio models shared the same geometrical partitions and the element shapes in most partitions were close to an aspect ratio of 2, except some tiny partition regions in the solder mask. We categorized these sets of different AR models as fully meshing controlled approach. It is worth mentioning that this approach can avoid the confusion of how many element-layers should be used for a layer of component in a package assembly model.

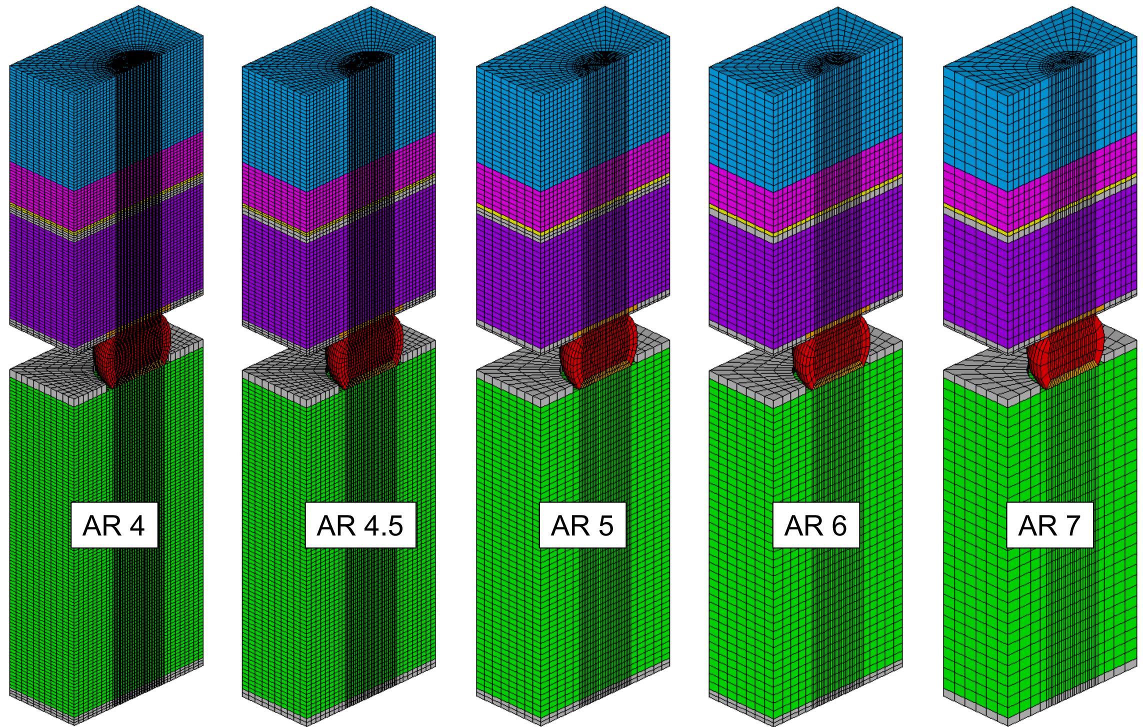

Figure 5.7 Unit Model Built Using Conventional Meshing Strategy with Different Mesh Qualities

Table 5.3 Model Sizes for Unit Models Using Conventional Meshing Strategy

Conventional Meshing Strategy		
Mesh Quality Max. Aspect Ratio	No. of Nodes	No. of Elements
AR 4	504,451	491,832
AR 4.5	342,650	332,960
AR 5	151,738	146,048
AR 6	90,925	86,912
AR 7	48,765	46,080
AR 6_10	24,719	23,104

5.4.3 Fan-Out Meshing Strategy

Meshing transition region has been supported by commercial FEA packages [206] [207] [208] to achieve mesh continuity between a map-meshable volume part and a geometrical complex part. Hexahedral elements are suggested to fill the map-meshable

regions of a volume, and tetrahedral elements to fill the remainder. Unfortunately, use of a mix of hexahedral and tetrahedral elements leads to nonconformities in a mesh. Although, using pyramid elements [209] at the interface can maintain mathematical continuity between hexahedral and tetrahedral elements, it is still not easy to generate a reasonable model size [210]; the total elements of this type of model still cannot compete with full hexahedral model.

An improved (fan-out) meshing strategy was developed that utilizes geometrical partitions as a transitional region for hexahedral meshing to fan out forming circular mesh pattern into regular rectangular shape after the solder and copper pads were meshed [189]. The unit model was still meshed with full hexahedral elements and with controlled aspect ratios of specific numerical values as mentioned earlier. Unlike the conventional meshing strategy, this improved meshing strategy fanned out the element shapes not only to rectangular shape but gradually increased the element size using a hemispherical (dorm-like) transition region (Figure 5.8), which means large size elements can be incorporated within a geometrical partition while mesh quality was still under control. Comparing to conventional meshing models (plotted in Figure 5.7), lower mesh densities were observed from the models built with fan-out meshing approach (shown in Figure 5.9 and listed in Table 5.4).

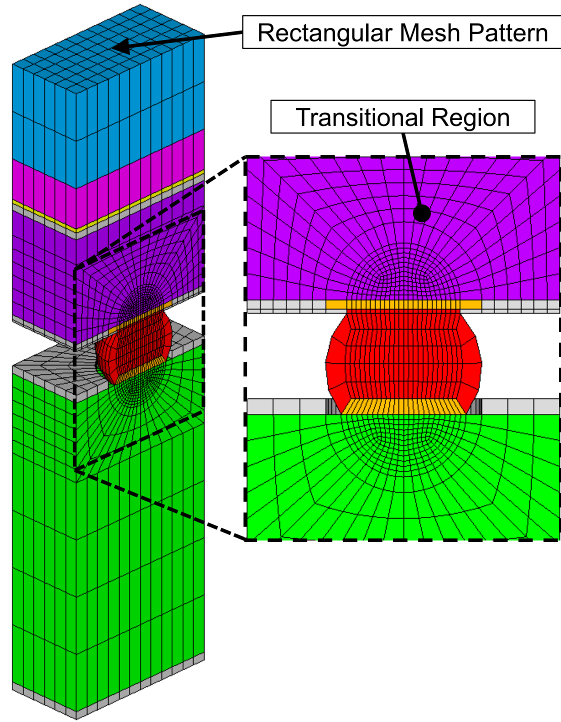

Figure 5.8 Improved (Fan-Out) Meshing Strategy

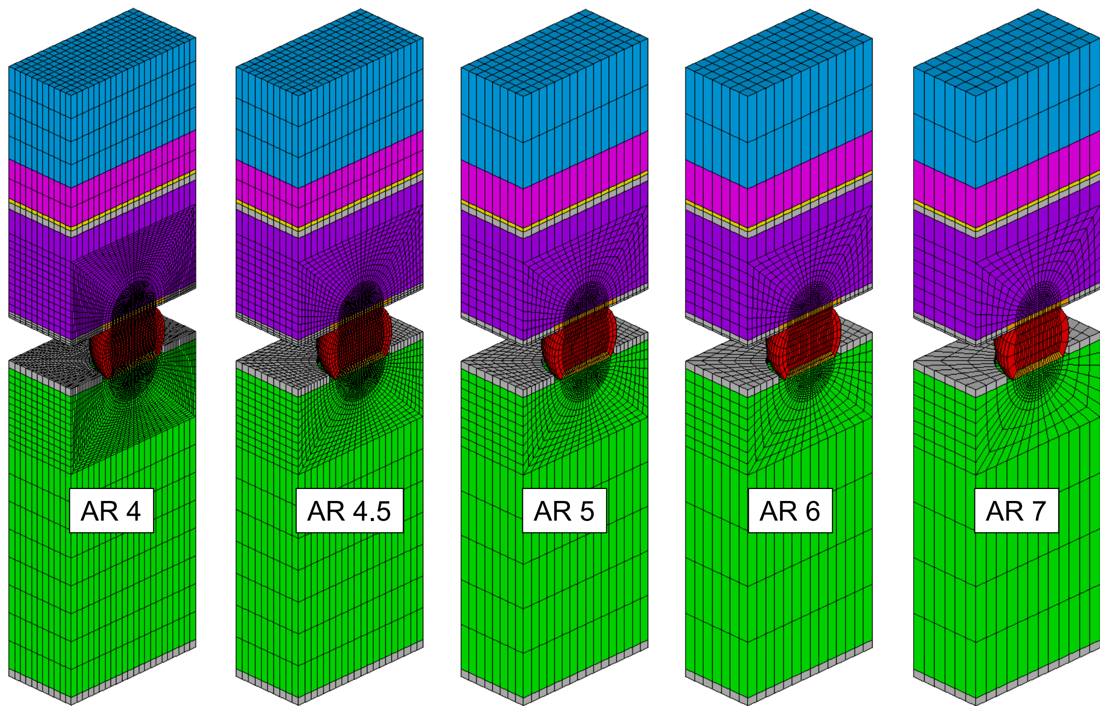

Figure 5.9 Unit Model Built Using Fan-Out Meshing Strategy with Different Mesh Qualities

Table 5.4 Model Sizes for Unit Models Using Fan-Out Meshing Strategy

Fan-Out Meshing Strategy		
Mesh Quality Max. Aspect Ratio	No. of Nodes	No. of Elements
AR 4	170,589	165,352
AR 4.5	101,101	97,520
AR 5	49,870	47,616
AR 6	32,659	30,968
AR 7	18,943	17,712
AR 6_10	10,181	9,408

As comparisons of the model sizes for different meshing models listed in Table 5.3 and Table 5.4, the fan-out meshing strategy resulted in a great reduction in model size compared to conventional meshing strategy. Taking AR 7 (maximum aspect ratio of 7) models as an example, the model sizes are 46,080 and 17,712 elements for conventional and fan-out meshing models, respectively. As a result, the use of fan-out meshing strategy saving about 67% of elements in different AR set models was realized.

5.4.4 Simulation Results for Unit Models Using Conventional and Fan-Out Meshing Strategies

In the initial stage of the convergence study for unit model, we used a relative small load step set LS 5, each duration of a thermal cycle was divided evenly into five load steps, as the thermal loading condition. ΔW_{avg} values were stabilized after three cycles of all simulations (Figure 5.10). The simulation results of ΔW_{avg} were converged to the solutions for AR 4.5 and AR 4 models. As comparing with the same mesh quality models (same color dots at the same cycle) in Figure 5.10, the maximum difference of the ΔW_{avg} values for models using two different meshing strategies was less than 0.5%. it stated the fan-out model can simulate a very close solution to conventional model.

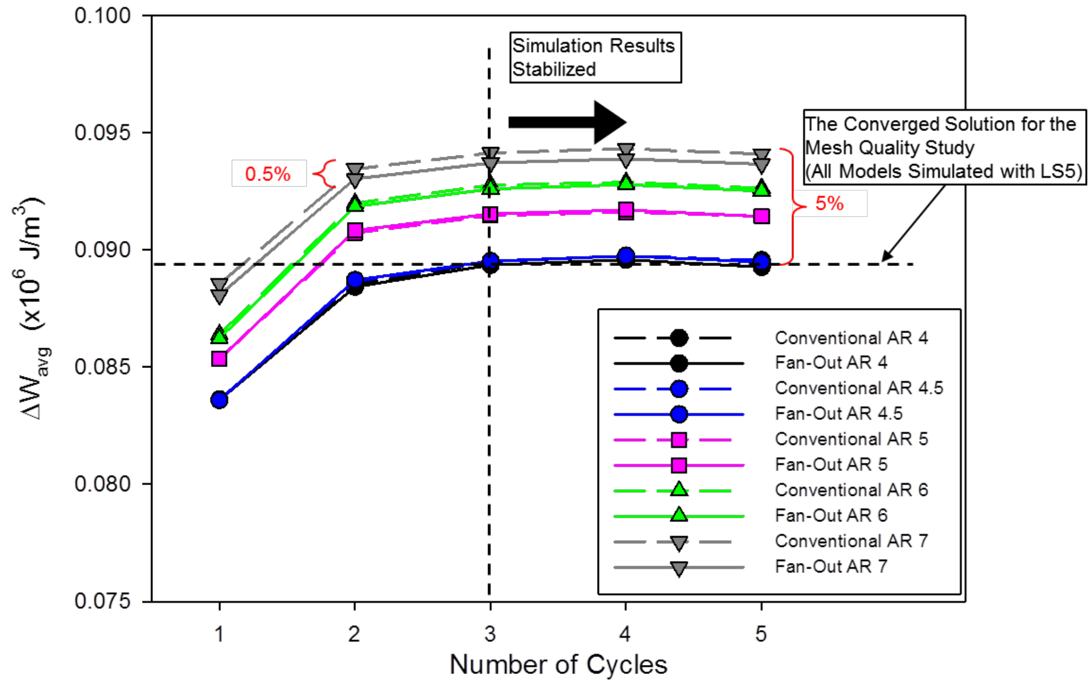

Figure 5.10 Variations of ΔW_{avg} with Number of Cycles

The maximum differences of the ΔW_{avg} values for different mesh quality models in two different meshing strategies were less than 5% (Figure 5.11). In this convergence study, the mesh quality does not show great impacts to the simulation results due to the chosen aspect ratios of element shape were in a good range (AR 4 to 7), and the load step size is also small enough (LS 5) for analyses.

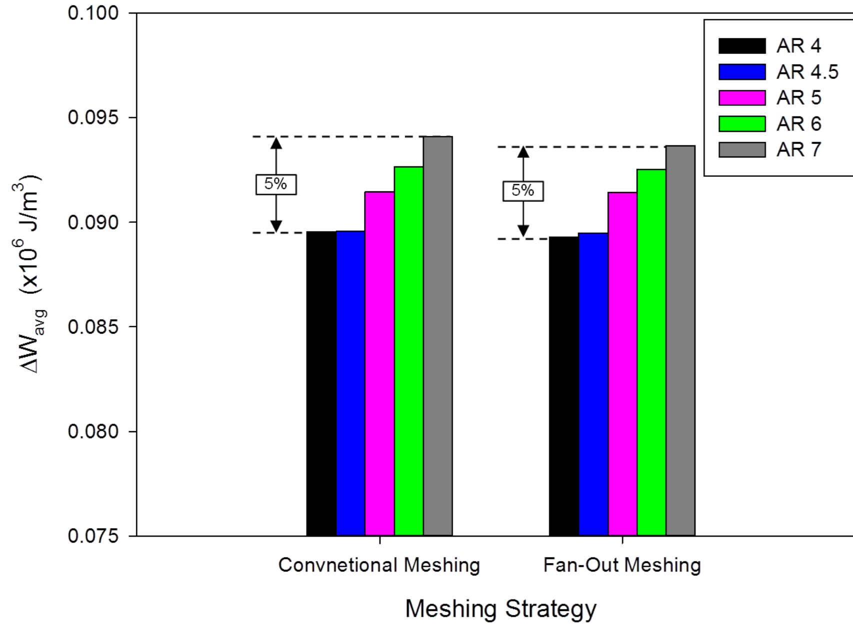

Figure 5.11 Comparisons of Simulation Results of ΔW_{avg} for Conventional and Fan-Out Meshing Strategies

In Figure 5.12, however, it can be observed that the computational time dramatically increased as the max aspect ratio decreased (finer mesh quality was used). In contrast to the maximum difference of simulation results was 5%, the ratio of the longest simulation time (conventional AR 4) over the shortest simulation time (fan-out AR 7) reached to 27X. Simulation using fan-out meshing strategy preformed much more efficiently, and obtained good consistent simulation results relative to the conventional meshing strategy.

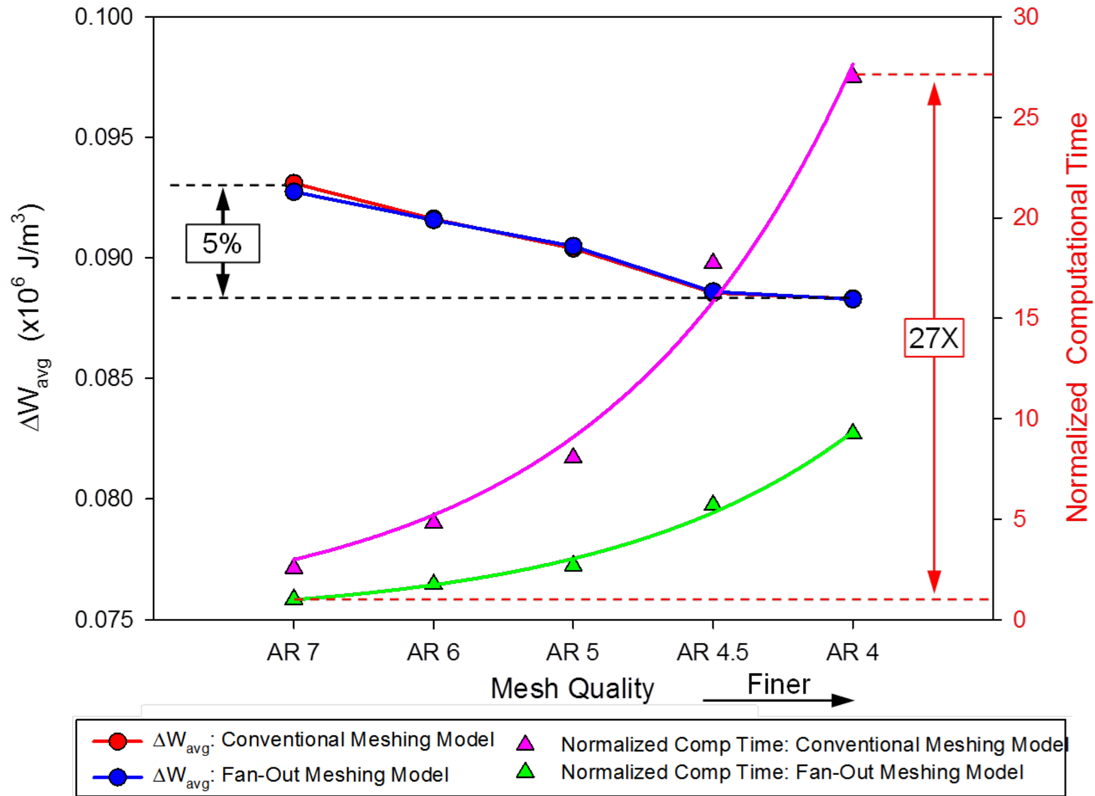

Figure 5.12 Comparisons of Consistency of Simulation Results (ΔW_{avg}) and Simulation Efficiency for Two Different Meshing Strategies

5.4.5 Adaptive Meshing Method for Two Different Meshing Strategies

Even the use of the AR 7 model with the fan-out meshing strategy, the model size of a unit model reached 17,712 elements, which was still too many for a package assembly model. An adaptive meshing method further relaxing mesh density was developed as follows:

(1) Instead of full meshing (aspect ratio) control of entire unit model, the controlled maximum aspect ratio for tiny uninteresting partition was increased for a balance between geometrical fitting and mesh density.

(2) This adaptive meshing method can be introduced into prior two meshing strategies.

(3) The size of element is also relaxed, larger element size can be used while element-extrusion for components other than solder joint and copper pad.

The maximum aspect ratio of AR 6_10 was used in this example; most partitions of unit model were modeled with a maximum aspect ratio of 6, while the thin solder mask layer was modeled with an increased maximum aspect ratio of 10. Figure 5.13 showed the mesh inspection result for the unit model, the aspect ratios of blue elements are less than a factor of 6 while the yellow elements are between 6 and 10. In Figure 5.14, the model sizes of conventional and fan-out models using adaptive meshing method (AR 6_10) are 23,104 and 9,408 elements, respectively, which were the smallest model sizes among all models.

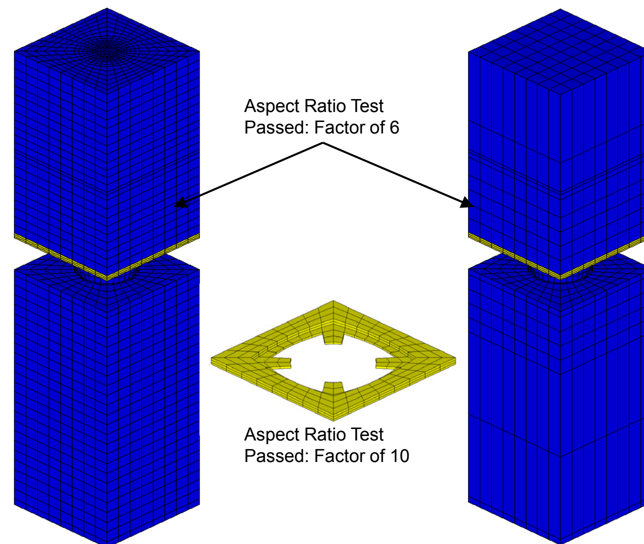

Figure 5.13 Mesh Quality Inspection for Conventional and Fan-Out Models with Adaptive Meshing Method

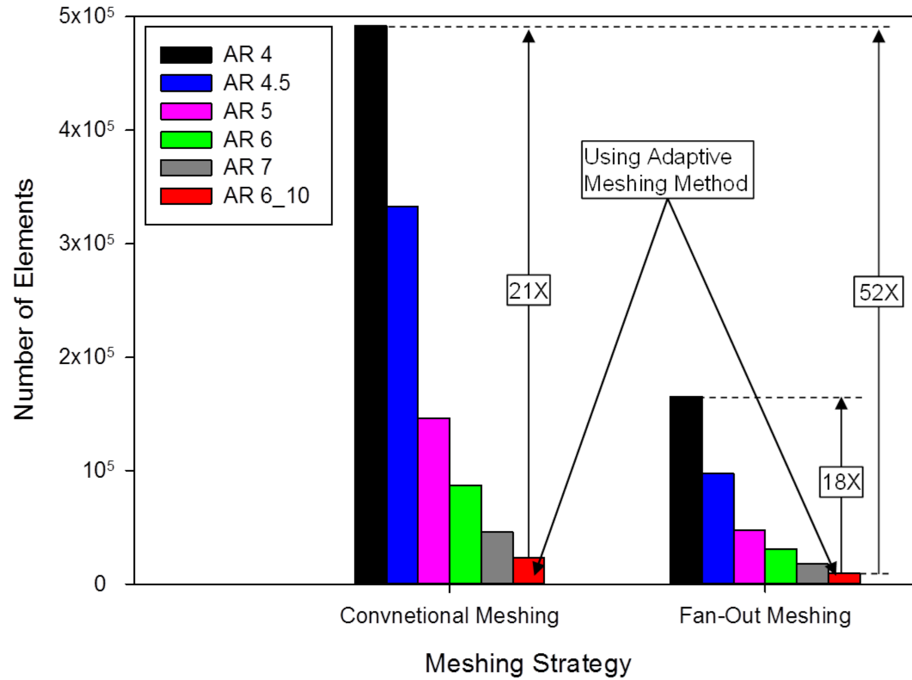

Figure 5.14 Comparisons of Model Sizes for Models
Using Fully Meshing Controlled Approach and Adaptive Meshing Approach

5.4.6 Simulation Results for Unit Model Using Two Meshing Strategies with Adaptive Meshing Method

Figure 5.15 showed that the simulation results of ΔW_{avg} for using adaptive meshing method were always fall between the ΔW_{avg} values for models AR 6 and AR 7; their differences were less than 5% comparing to AR 4 models. The great reduction on mesh density and the good solution quality make it a promising approach for an efficient package simulation without sacrificing accuracy.

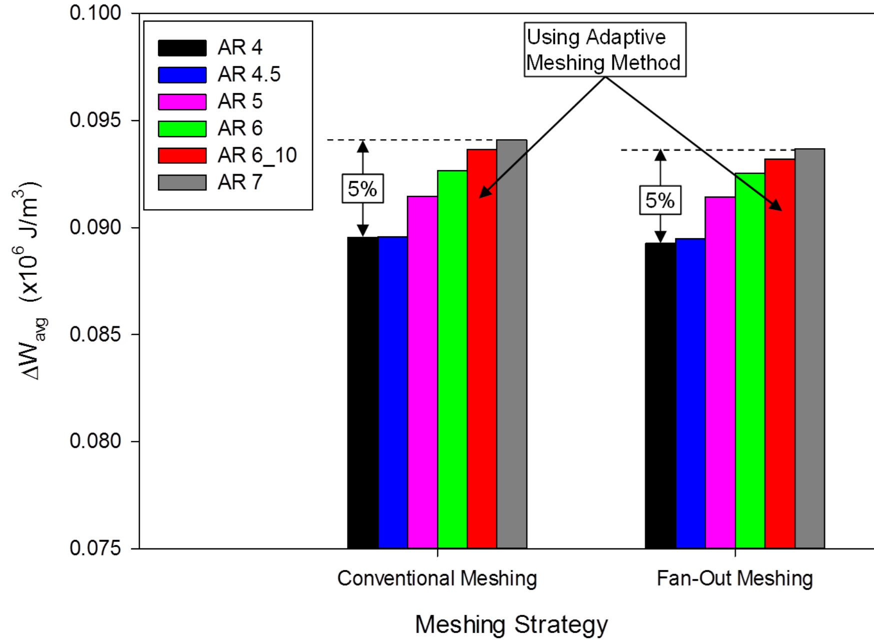

Figure 5.15 Comparisons of Simulation Results (ΔW_{avg}) for Models Using Fully Meshing Controlled Approach and Adaptive Meshing Approach

5.5 Determination of the Optimal Load Step Size

Since the material behavior of solder alloy is highly nonlinearity, nonlinear analysis focuses on solving problems accurately and effectively. Once the problem is well posed, there is no guarantee that a nonlinear problem setup has a unique solution. In general, a solution of a nonlinear problem can be obtained by solving a system of linearized equations iteratively. Starting from an initial estimate and increment, convergence criteria are checked to prevent a deviated solution in iteration. The loading curve of a nonlinear problem using the Newton-Raphson based method is subdivided into a series of load increments (e.g. durations of ramp and dwell) [143] [145] [146] [179] [211] [212] [213]. The load increments can be over several load steps. During each iteration, Newton-Raphson method checks residuals of the system for comparing with convergence criteria. The convergence criteria can be force criterion, energy criterion, or

displacement criterion. If the convergence criteria are not satisfied, a new stiffness matrix is updated and the iterative procedure continues until the problem converges. The optimal load step size was chosen based on a balance of the solution quality required and the available time for calculation. It should be note that (1) the external loads and boundary conditions were applied at each load step, and (2) multiple substeps were performed to apply the load gradually in a load step. Convergence was obtained at each substep [207]. (3) Oversize of load step may results in a non-convergence calculation; small load step size helps convergence speed but costs more computer resources.

An ideal load step size is infinitesimally small, but more load steps would consume more computer resources, calculate too much information, and eventually reach to an unacceptable long time calculation and huge storage spaces. In contrast to small load step size, large or arbitrary load step sizes were used in many literatures for the purpose of saving overall simulation time while cycling loading conditions were required. The lack of the study relating to the influences of simulation results between different load step sizes makes the choice of the load step still confused researchers. Thus, a guideline of required load step size is in urgent for an efficient, accurate, and consistent nonlinear simulation.

5.5.1 Optimal Determination of Required Load Step Size

An optimal determination of required load step size was developed as follows. Temperature change curve was gradually divided into a series of increments for adjusting the stiffness matrix at the end of each increment and reducing accumulation of numerical errors. Each duration of a thermal cycle was divided evenly into a set of number (e.g. 1,

2, 3, 4, 5, 10, 15, 25 50 and 100) (Figure 5.16), and the total numbers of load steps for each choice are listed in Table 5.5. Converged and consistent result of ΔW_{avg} for the unit model can be obtained by simulated two meshing strategies with these ten loading conditions.

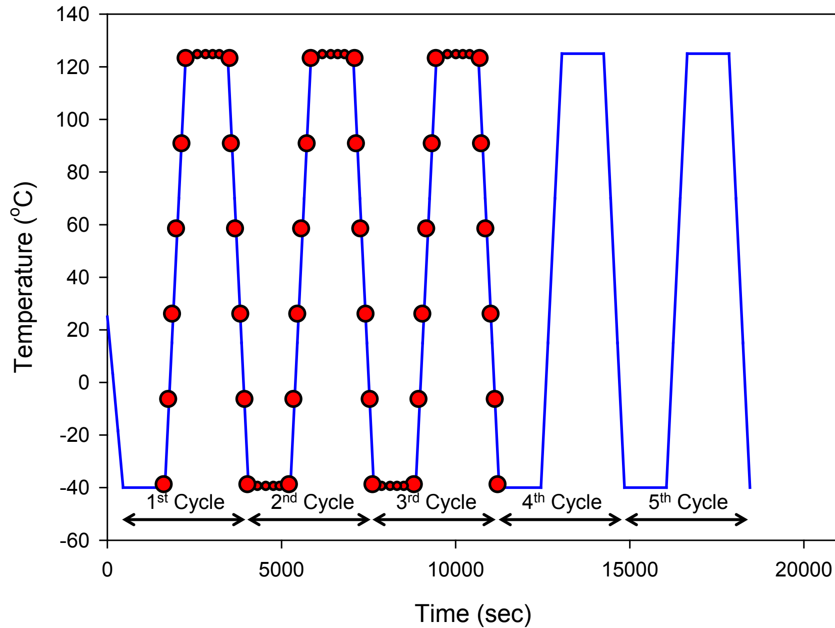

Figure 5.16 Divisions of Load Increments for LS 5

Table 5.5 Total Load Steps for Different Load Step Sets

Load Step Set	Total Load Steps	Total Divisions
LS 1	22	21
LS 2	43	42
LS 3	64	63
LS 4	85	84
LS 5	106	105
LS 10	211	210
LS 15	316	315
LS 25	526	525
LS 50	1,051	1,050
LS 100	2,101	2,100

5.5.2 Simulation Results for Models Using Optimal Load Step Sizes

In the simulation results for conventional meshing models, Figure 5.17, showed that an increased mesh quality (a decreased maximum aspect ratio) has a decreasing influence of ΔW_{avg}. But, a reduced load step size (increased number of load steps) increased ΔW_{avg} values for all different sets of models. The effects of smaller load step size and finer mesh quality have opposite impacts on simulation result ΔW_{avg}. Similar trends were observed in the simulations using fan-out meshing strategy (Figure 5.18). Simulation results were converged to the magnitudes of 0.0914 (conventional) and 0.0913 (fan-out) $\times 10^6$ J/m^3, respectively, while a simulation set of model AR 4 (maximum aspect ratio of 4) and load step LS 100 (total load step number of 2,101) was used. With a close inspection of Figure 5.17 and Figure 5.18, the load step size presented greater impact on simulation results than mesh quality in this convergence study as illustrated in Figure 5.19.

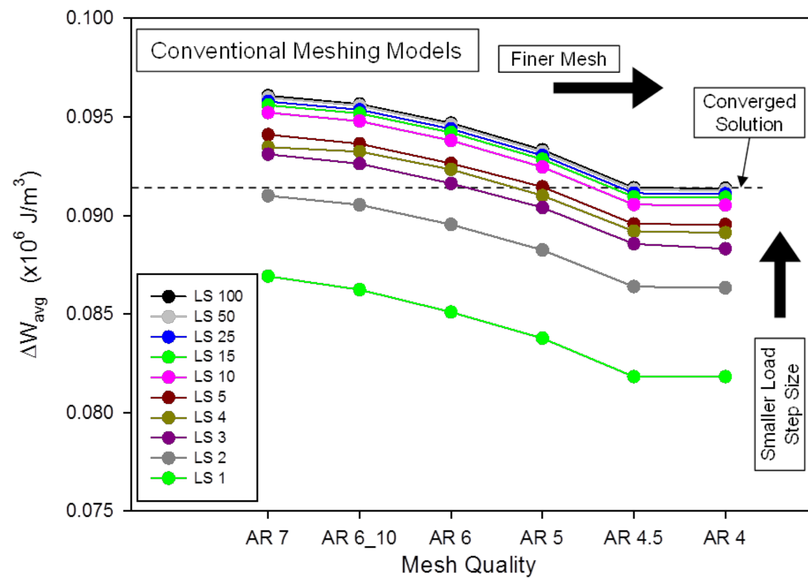

Figure 5.17 Effects of Mesh Quality and Load Step Size on Simulation Results for Conventional Meshing Strategy

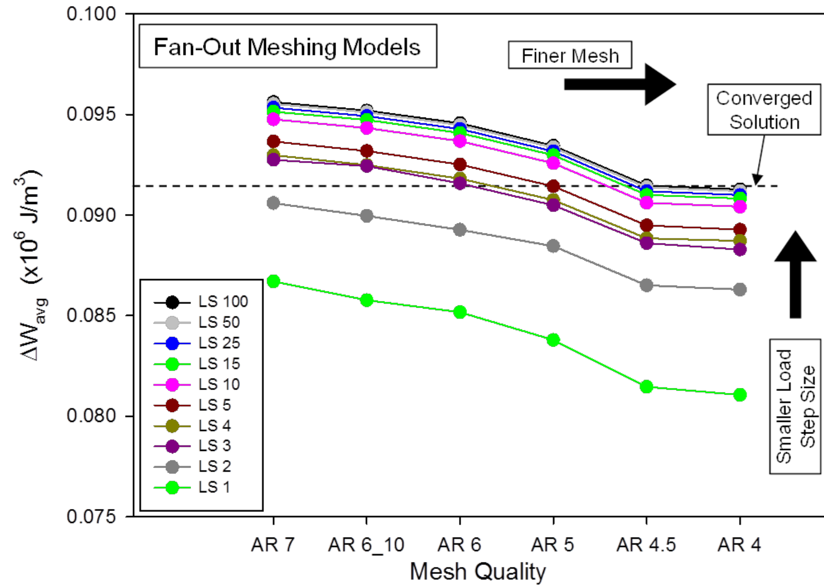

Figure 5.18 Effects of Mesh Quality and Load Step Size on Simulation Results for Fan-Out Meshing Strategy

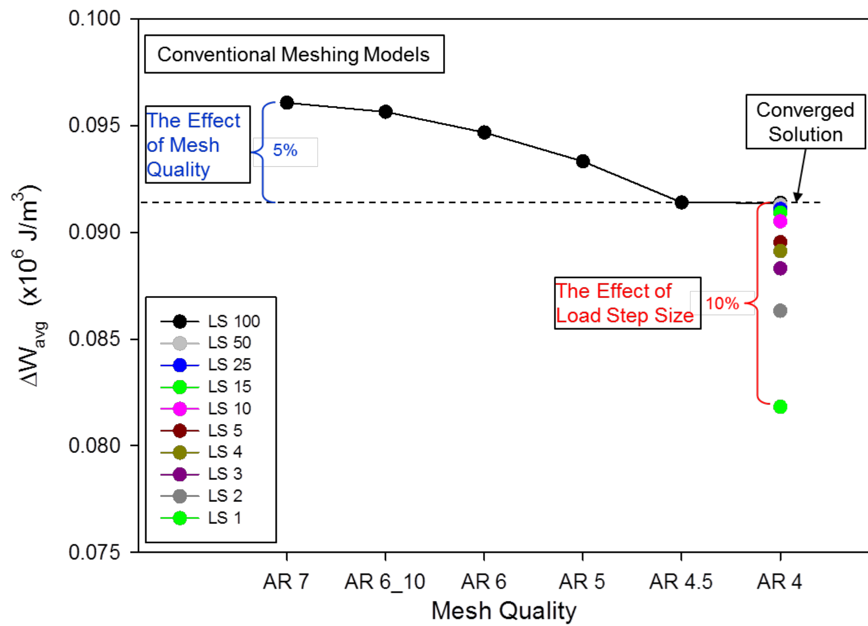

Figure 5.19 Comparisons of the Effects of Mesh Quality and Load Step Size on Simulation Results for Model AR 4

In Figure 5.20, the ΔW_{avg} values for AR 4 model were stabilized (errors < 3 %) after load step set (LS) greater than LS 5. However, normalized computational time also

dramatically increased as LS greater than LS 5. Thus, load step sets between LS 1 and LS 5 are more suitable using for package simulation as simulation efficiency concern.

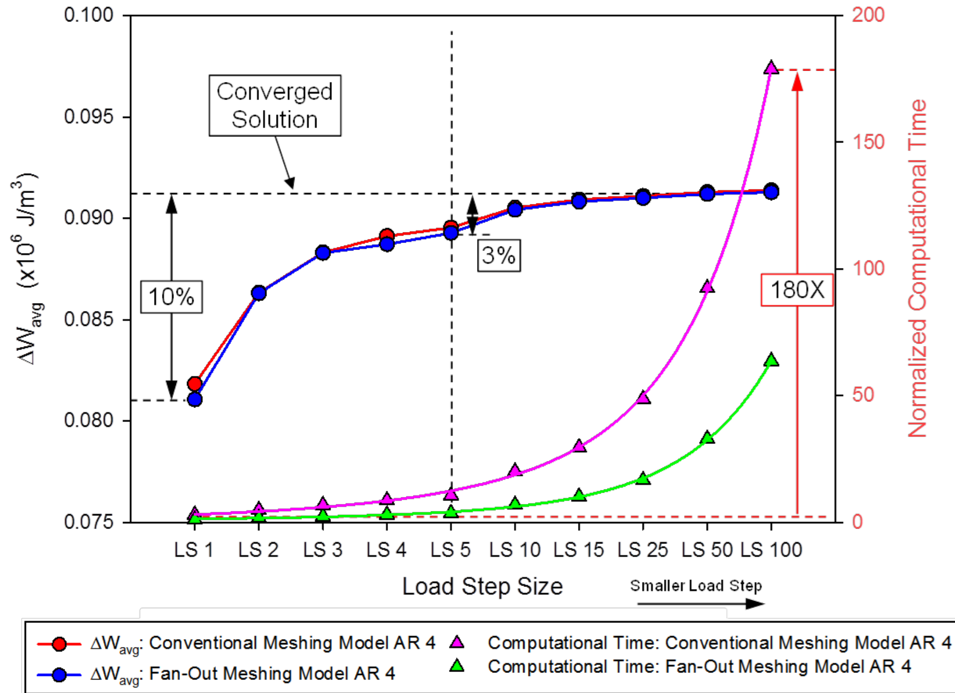

Figure 5.20 Comparisons of Simulation Result ΔW_{avg} Values and Normalized Computational Times for AR 4 Models Simulated with LS 100

Simulation results and normalized computational time for different AR models simulating with LS 100 (2101 load steps, the smallest load step size in this study) were compared in Figure 5.21. The errors of simulation results ΔW_{avg} were less than 5 % while the normalized computational time increased 47 times between finest meshing model (conventional AR 4) and the most efficient (fan-out AR 6_10) model.

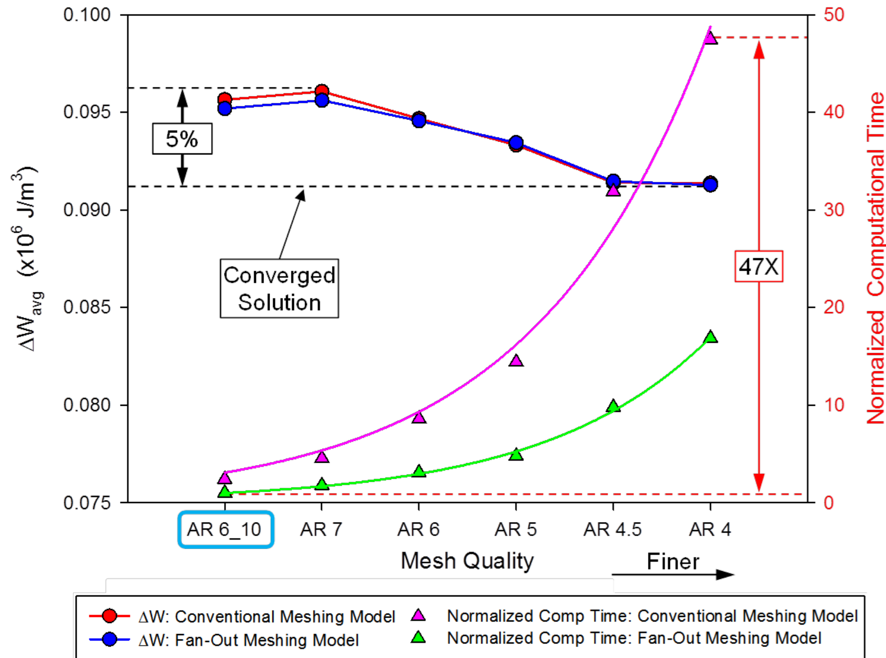

Figure 5.21 Comparisons of Simulation Result ΔW_{avg} Values and Normalized Computational Time for Different AR Models Simulating with LS 100

5.6 Optimized Analysis Strategy

As a pair of converged solutions can be found in the finest mesh quality model (AR 4) and the smallest load step size (LS 100) in Figure 5.17 and Figure 5.18, the best decision of the optimal model set to achieve the balance between accuracy and efficiency can be found by drawing a horizontal line (as combined in Figure 5.22) across the converged ΔW_{avg} values and finding the closest simulation set of FE model and load step size.

Model AR 6_10 having the smallest model size among all different AR models yields the preferable FE model size for building package size model. As circled in Figure 5.22 load step sets of LS 2 and LS 3 are the most closest to converged solution for conventional and fan-out AR 6_10 models resulting errors of 0.9% and 1.2%, respectively (Figure 5.23 and Table 5.6). Hence, simulation sets of model AR 6_10 and

load steps of LS 3 and LS 2 were chosen for the convergence study of package models. In the same computer resources, the converged simulation with conventional meshing leads to about 1,330X greater in computational time than simulation from an optimized simulation set (as listed in Table 5.6).

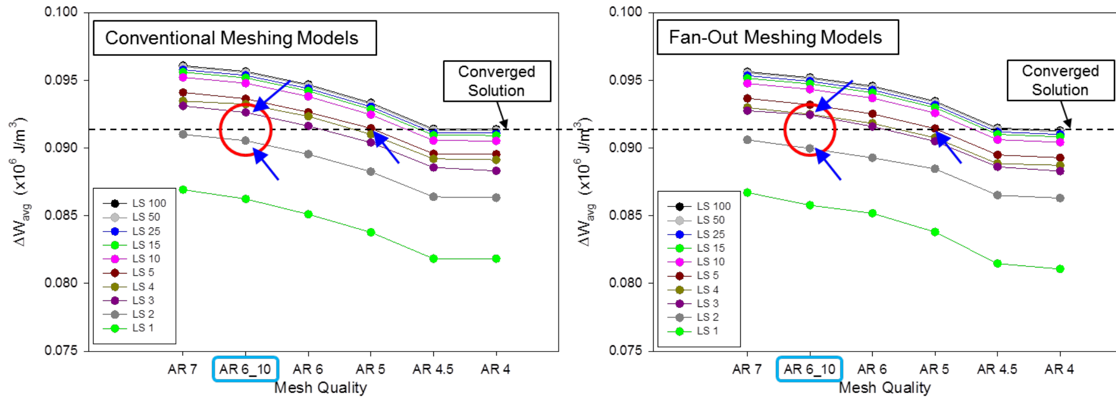

Figure 5.22 Strategy of Determination of Optimized Simulation Set

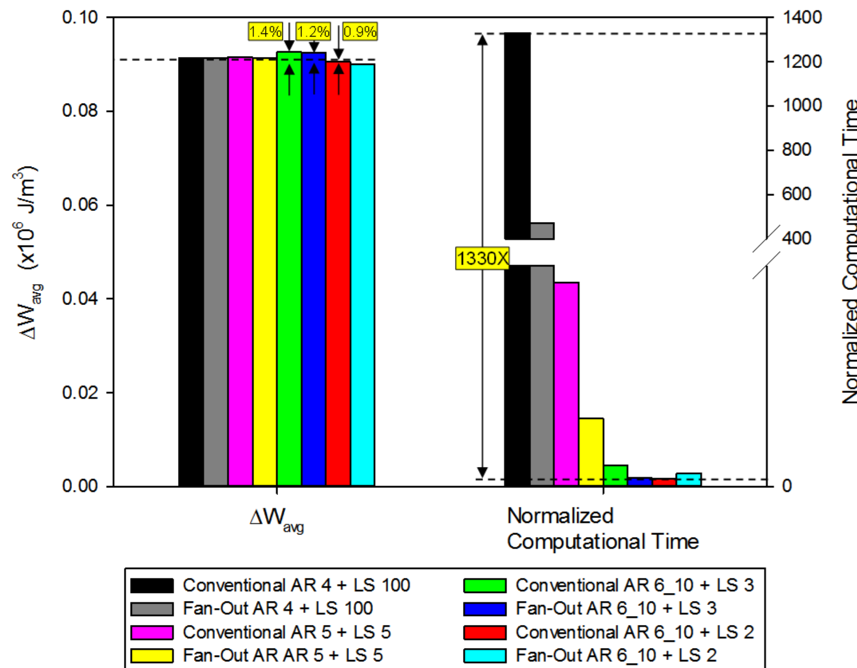

Figure 5.23 Comparisons of Simulation Result ΔW_{avg} Values and Normalized Computational Time for Different Simulation Sets

Table 5.6 Comparisons for Different Simulation Sets of Unit Model

Mesh Quality	Conventional AR 4	Conventional AR 5	Conventional AR 6_10	Conventional AR 6_10
Load Step	LS 100	LS 5	LS 3	LS 2
Model Size (Elements)	491,832	146,048	23,104	23,104
ΔW_{avg} ($\times 10^6$ J/m^3)	0.0914	0.0915	0.0926	0.0905
Error (%)	-	0	1.4	0.9
Normalized Comp Time	1330X	23X	2.4X	1.7X

Mesh Quality	Fan-Out AR 4	Fan-Out AR 5	Fan-Out AR 6_10	Fan-Out AR 6_10
Load Step	LS 100	LS 5	LS 3	LS 2
Model Size (Elements)	165,352	47,616	9,408	9,408
ΔW_{avg} ($\times 10^6$ J/m^3)	0.0913	0.0914	0.0924	0.08996
Error (%)	-	0	1.2	1.5
Normalized Comp Time	470X	7.7X	1X	0.7X

In order to verify the optimized simulation strategy, the history curves of volume-weighted averaging PLWK were evaluated. In Figure 5.24, it can be seen that history curves generating from the optimized models were always close to those two converged curves. These history curves of volume-weighted averaging PLWK verified that using optimal sets of low-density meshing model with selected load steps still can achieve a high quality solution as high-density meshing model with a large number of load steps does. Similar distributions of PLWK after five cycles for the converged and optimized simulation sets were presented in Figure 5.25 and yielded errors less than 2% as listed in Table 5.6.

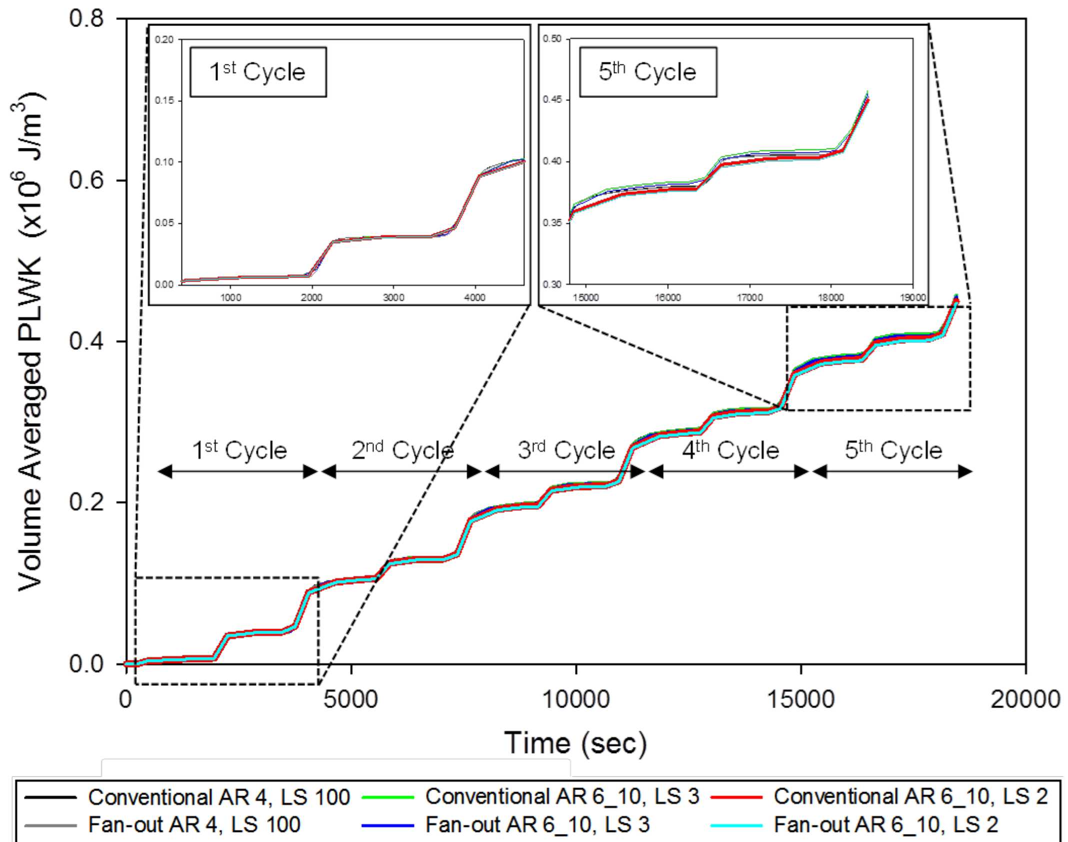

Figure 5.24 History Curves of Volume-Weighted Averaging PLWK for Different Simulation Sets

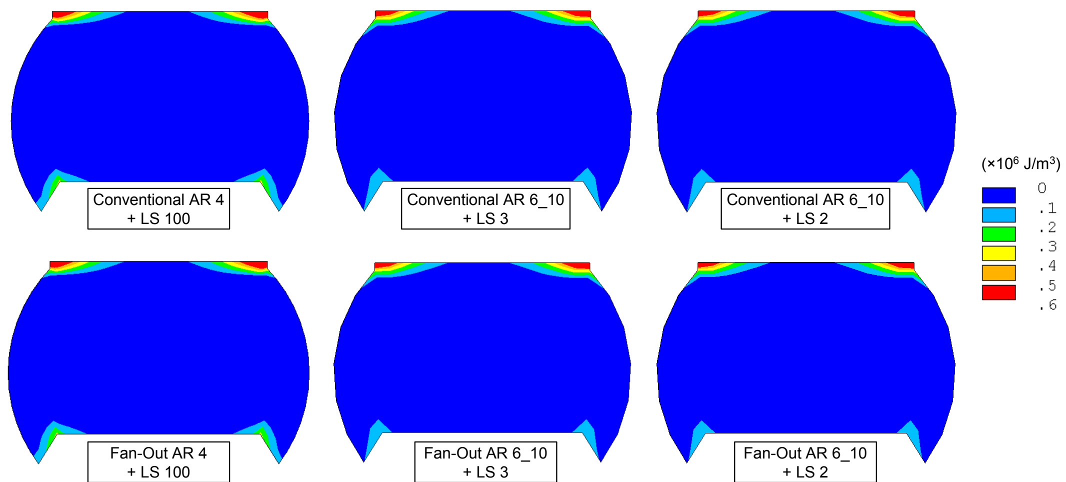

Figure 5.25 Distributions of PLWK after Five Cycles for Different Simulation Sets

5.7 Convergence Study on Multi-Joints Package Using Quarter 8 × 8 PBGA Package Assembly

As the convergence study of single joint unit model has been done, the study moved on the multi-joints package assembly. Considering the capability of the computer used for this study, a quarter 8 × 8 PBGA assembly with 25 solder joints (Figure 5.1) was used for multi-joints convergence study.

5.7.1 Selected Simulation Set for the Convergence Study of Multi-Joints Package Assembly

Utilizing the trends of the convergence study of unit model (Figure 5.22), the closest to converged solution can be found by using AR 5 model and load step LS 5. Several simulation sets of different mesh quality models and load steps were chosen, they were (1) AR 5 with LS 5 and (2) AR 6_10 with LS 2 and LS 3. In the convergence study of the unit model, the simulation results for the first simulation set had a negligible error compared to the converged solution (AR 4 + LS 100). Thus, package assembly simulation using this set was considered as the converged solution for multi-joints package assembly and the reference for comparisons.

5.7.2 Simulation Results for Multi-Joints Package Assembly Models

All critical regions were at the top side of solder joint G7 under the silicon die shadow for all simulation sets. Model sizes of AR 5 simulating converged solutions have increased to 3,651,20 and 1,190,400 elements for conventional and fan-out meshing models, respectively (summarized in Table 5.7), and also took most longest time for

simulations. Simulation results show that fan-out models simulated with optimal load step size yielded a close result comparing with the simulation using a high-density meshes and small load step size.

Table 5.7 Comparisons for Different Simulation Sets of Quarter 8 × 8 PBGA Assembly

Mesh Quality	Conventional AR 5	Conventional AR 6_10	Conventional AR 6_10
Load Step	LS 5	LS 3	LS 2
Model Size (Elements)	3,651,20	577,600	577,600
ΔW_{avg} ($\times 10^6$ J/m^3)	0.1365	0.1378	0.1351
Error (%)	0	1.7	0.2
Normalized Comp Time	64X	2.5X	1.6X

Mesh Quality	Fan-Out AR 5	Fan-Out AR 6_10	Fan-Out AR 6_10
Load Step	LS 5	LS 3	LS 2
Model Size (Elements)	1,190,400	235,200	235,200
ΔW_{avg} ($\times 10^6$ J/m^3)	0.1354	0.1352	0.1320
Error (%)	0	0.2	2.5
Normalized Comp Time	20X	1X	0.7X

Figure 5.26 showed the ΔW_{avg} values for the joints F6 to K10 locating along the diagonal direction of the package assembly. Differences for the joints at the same location were less than 3% compared to the converged solution (AR 5 + LS 5). In Figure 5.27, the simulation time were dramatically decreased while the optimal models were simulated. Thus, a balance between efficiency and accuracy was obtained and validated in multi-joints package assembly model by using the proposed strategy.

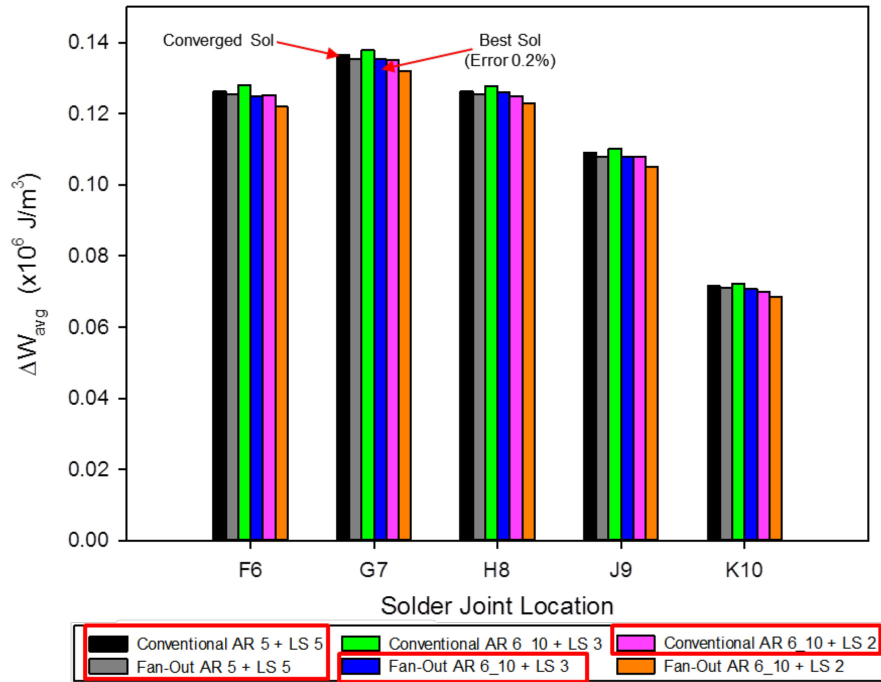

Figure 5.26 Variations of Simulation Results with Different Solder Joint Locations for Quarter 8 × 8 PBGA Assembly

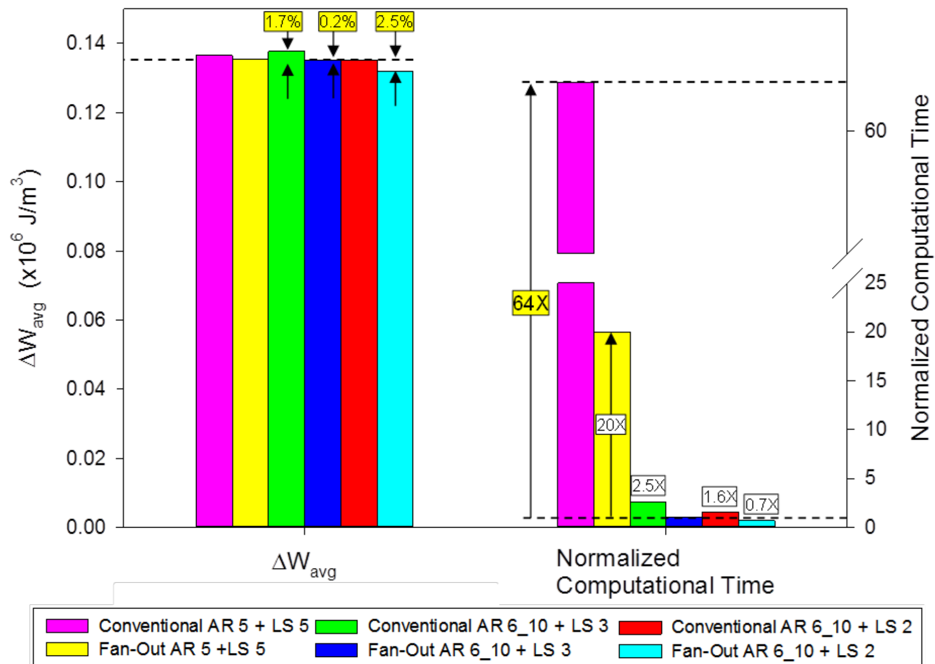

Figure 5.27 Comparisons of Simulation Result ΔW_{avg} Values for Critical Joints G7 and Normalized Computational Time for Different Simulation Sets

5.8 Simulations for Quarter 15 × 15 Package Assembly Model

Example quarter 15 × 15 package was modeled with AR 6_10 using two meshing strategies and simulated with the optimal load step sets LS 3 and LS 2. The model sizes were 2,065,644 and 850,845 elements for conventional and fan-out meshing strategies as shown in Figure 5.28. The distributions of vertical displacement contours for two different meshing strategies (plotted in Figure 5.29) have a very good agreement. And according to simulation results listed in

Table 5.8, the differences of vertical displacement at point P's were less than 0.05%, which states the responses of package level were well captured via all selected simulation sets.

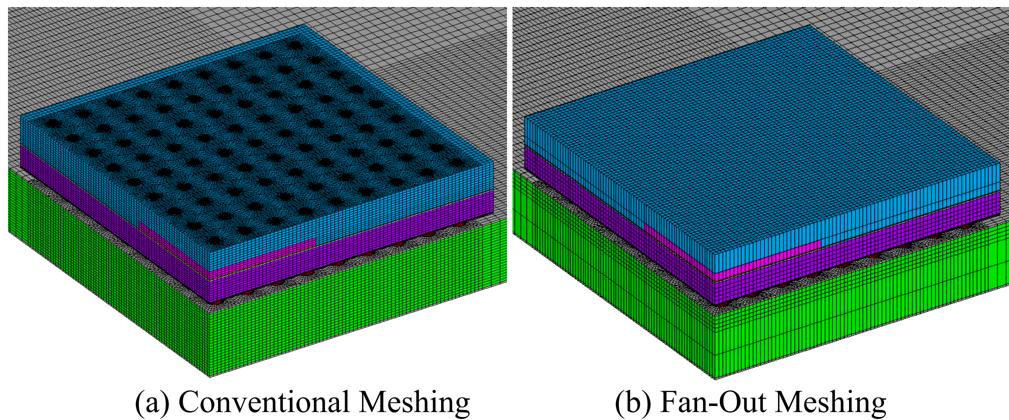

(a) Conventional Meshing (b) Fan-Out Meshing

Figure 5.28 Two Different Meshing Quarter 15 × 15 Package Assembly Models

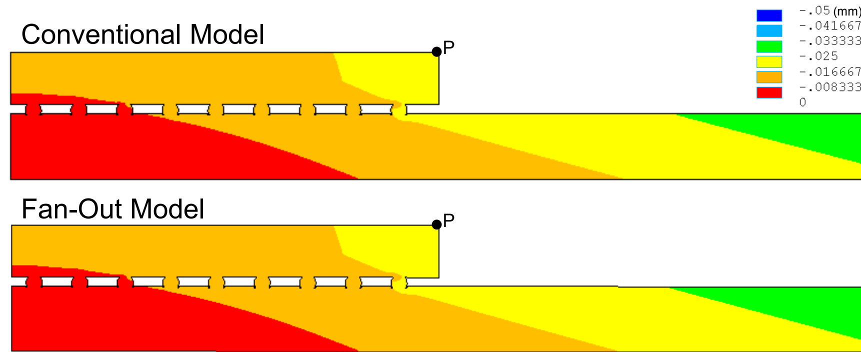

Figure 5.29 Vertical Displacements after Five Cycles for Different Meshing Models

Table 5.8 Comparisons for Different Simulation Sets of Quarter 15 × 15 PBGA Assembly

Mesh Quality	Conventional AR 6_10	Fan-Out AR 6_10	Conventional AR 6_10	Fan-Out AR 6_10
Load Step	LS 3	LS 3	LS 2	LS 2
Model Size (Elements)	2,065,644	850,845	2,065,644	850,845
ΔW_{avg} ($\times 10^6$ J/m^3)	0.1312	0.1282	0.1274	0.1256
Diff (%)	2.3	-	0.6	2
Vertical Displacement at Point P (mm)	-0.0215	-0.0215	-0.0215	-0.0215

In the detailed responses, the most critical regions were identified at the top sides of the solder joints M12 from all simulations. As the distributions of PLWK after five cycles plotted in Figure 5.30 and Figure 5.31, joints locating at the same location with different meshing strategies rendered similar distributions of PLWK contours and the potential critical regions were always located the top corners of solder joints.

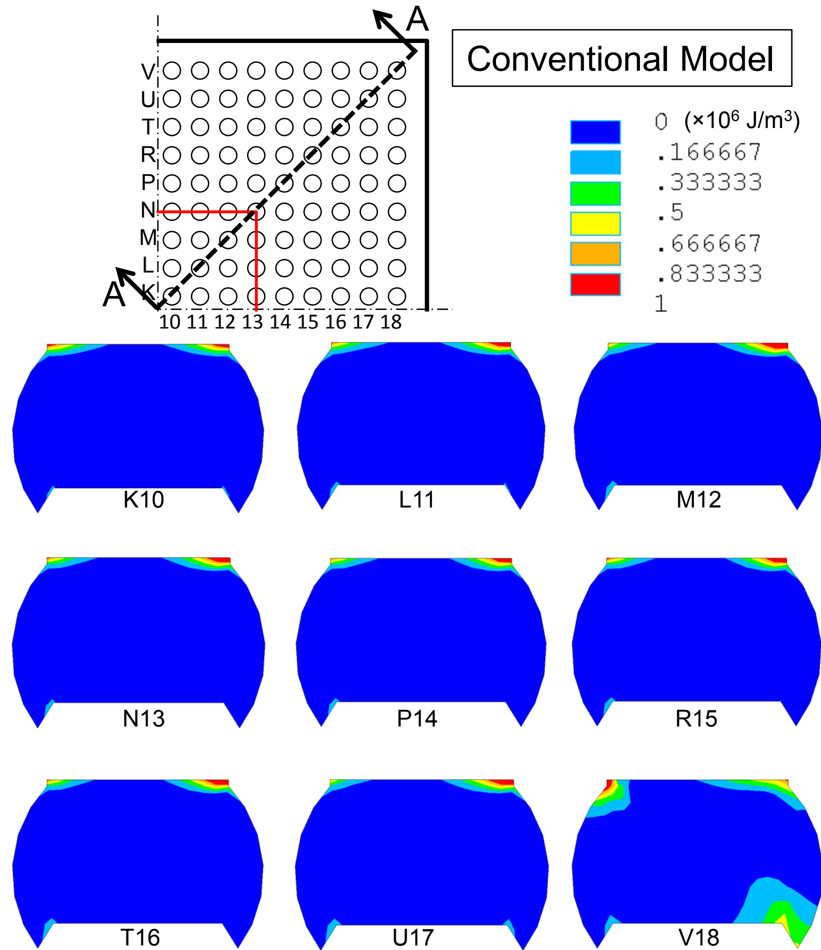

Figure 5.30 Distributions of PLWK after Five Cycles for Quarter 15 × 15 PBGA Assembly Model Using Conventional Meshing Strategy

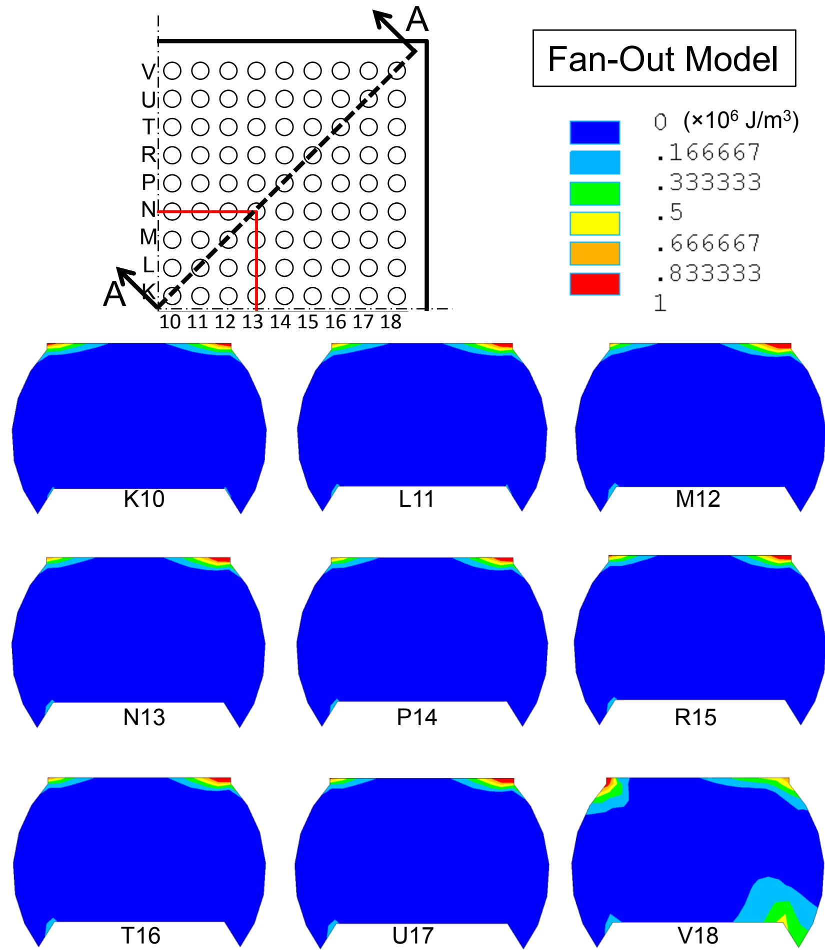

Figure 5.31 Distributions of PLWK after Five Cycles for Quarter 15 × 15 PBGA Assembly Model Using Fan-Out Meshing Strategy

Figure 5.32 showed ΔW_{avg} values for solder joints locating along the diagonal direction of package. It can be seen the differences for joints calculating from fan-out AR 6_10 + LS 3 and conventional AR 6_10 + LS 2 were always smaller than conventional AR 6_10 + LS 3.

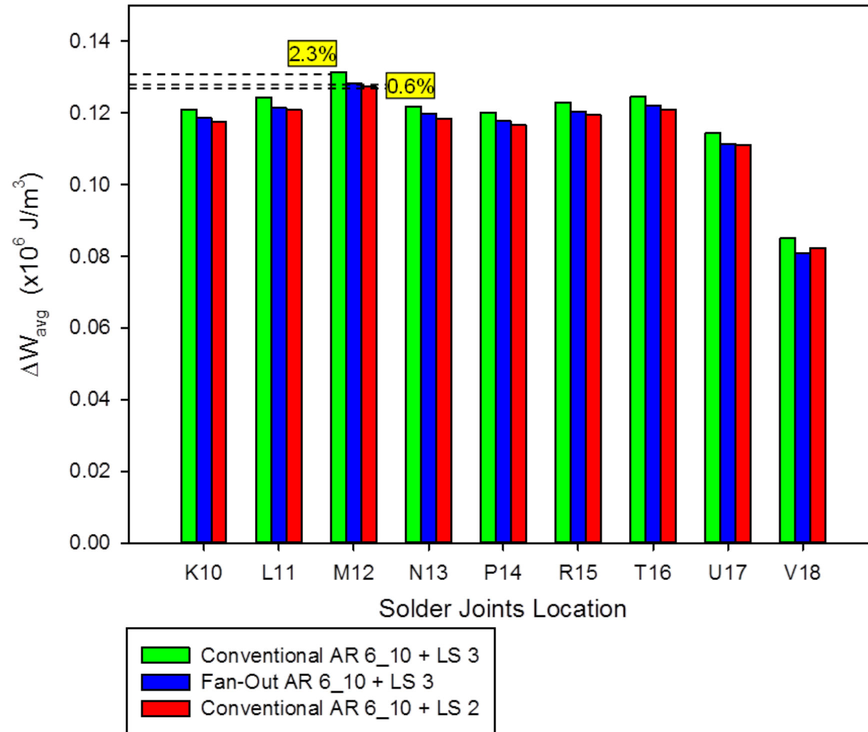

Figure 5.32 Variations of Simulation Results with Different Solder Joint Locations for Quarter 15 × 15 PBGA Assembly

Comparing with the simulation efficiency and accuracy of different approaches (Figure 5.33), the ratio of computational time was a factor of 3 (conventional : fan-out = 2.5:1) using same load step size while the difference of the simulation result was about 2.3%. The difference of ΔW_{avg} can be reduced to 0.6 % and only 0.75X time increased compared to fan-out simulation set while changing load step set to LS 2 for conventional meshing model.

In these convergence studies, an optimized simulation strategy was developed and realized the balance of accuracy and efficiency. Consistent simulation results verified the proposed methodology can work well in thermal-mechanical problem due to mismatch in CTE subjected to thermal cycling.

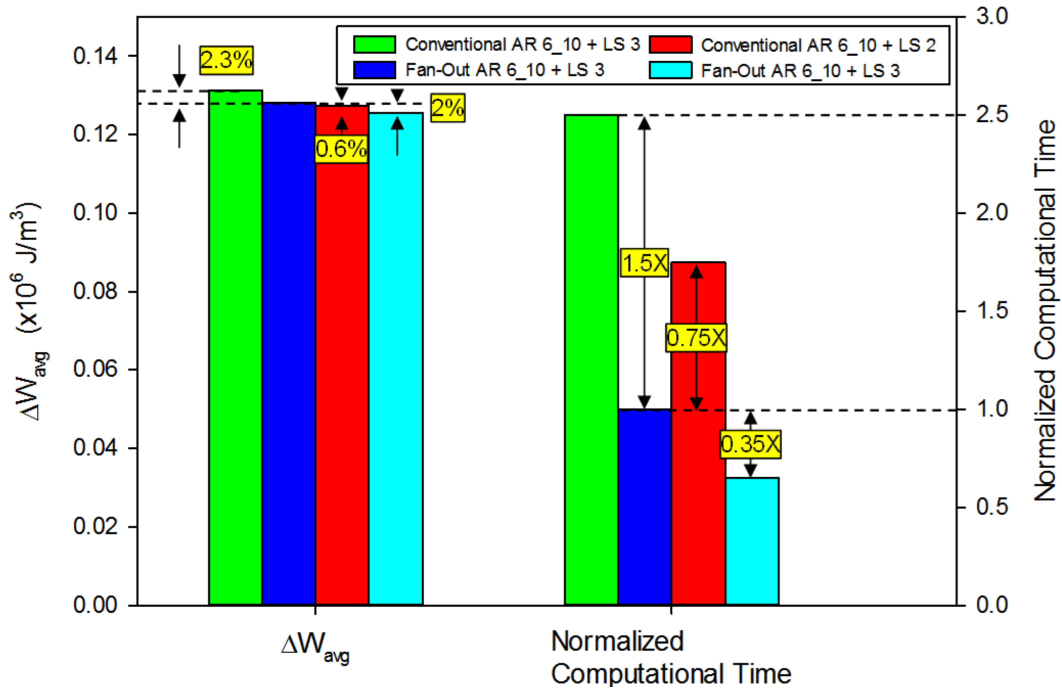

Figure 5.33 Comparisons of Simulation Result ΔW_{avg} Values for Critical Joints M12 and Normalized Computational Time for Different Simulation Sets

5.9 Flexibility on Design Change Using Fan-Out Meshing Strategy

In a design of package assembly, geometrical boundary edge of a component (such as silicon die) may not be aligned at the center or boundary edge of a unit model which increases the challenge of geometry partition and FE meshing, and prohibits minor dimension change of design.

Since regular rectangular element shapes were fanned out using the proposed meshing strategy, it has also increased the flexibility of FE meshing. An example of dimension change is illustrated in Figure 5.34. Dimensions of the die were changed from 2.8×2.8 mm^2 to 2.825×2.75 mm^2. In the improved meshing model, the transition region was at the top layer of the BT substrate. Therefore, elements above this transition region can be shifted to fit the actual boundaries without re-partitioning the geometrical model. Due to no extra elements were introduced, the simulation time was almost the

same as original design model. In design changed package, the simulation results (Table 5.9) have only 0.08% in difference, while the die size changed by 1%.

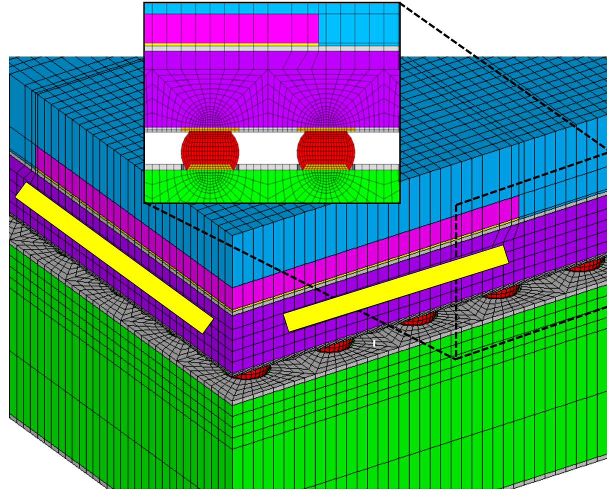

Figure 5.34 Detailed View of Design Change Package Model

Table 5.9 Effect of Design Change Package Model

Die Size (mm^2)	2.8 × 2.8	2.75 × 2.825
Mesh Quality	Fan-Out AR 6_10	Fan-Out AR 6_10
Load Step	LS 3	LS 3
No. of Elements	850,845	850,845
ΔW_{avg} ($\times 10^6$ J/m^3)	0.1282	0.1281
Diff (%)	-	0.08

5.10 Effect of Higher-Order Element

Two different order hexahedral elements are common use for analysis choice. They are [214]: (1) Linear hexahedron formulating with eight nodes and three degrees of freedom at each node. (2) Quadratic hexahedron defined by 20 nodes having three degrees of freedom per node. For bending-dominated problem, linear hexahedron suffers from shear locking [207] [206] [215], so that higher order quadratic hexahedron is a

better option. To determine the effect of element order on our study, package models (including quarter 8 × 8 and quarter 15 × 15 mm^2 packages) were analyzed using both linear and quadratic hexahedral elements. In addition, selective reduced integration (B-bar method) was used for two different order element models to avoid hourglass effort [28] [176]. Note that for 8 × 8 mm^2 package model, load step set LS 5 was used for calculating a converged solution.

Comparisons were listed in Table 5.10 and Table 5.11 for different models with different order hexahedral elements. The differences of simulation result ΔW_{avg} values were 1 % and 0.5 % for 8 × 8 and 15 × 15 mm^2 packages, respectively. This negligible phenomenon can be examined by the vertical displacement at of P (locating the top corner of mold compound as shown in Figure 5.29). The vertical displacements for 8 × 8 and 15 × 15 mm^2 package models were -0.0133 and -0.0214 mm, respectively, calculating via quadratic hexahedral models. Comparing with the dimensions of quarter packages (5.66 mm from center to corner for 8 × 8 mm^2 package and 10.61 mm for 15 × 15 mm^2 package), it can be seen bending is insignificant in our study. However, computational time for higher-order hexahedral element models increased 40 - 80% compared to linear hexahedral element models.

Table 5.10 Effect of Element Type on Quarter 8 × 8 mm^2 Package Model

Package Size	8 × 8	8 × 8
Element Type	8-Nodes Linear Hexahedron	20-Nodes Quadratic Hexahedron
Mesh Quality	Fan-Out AR 5	Fan-Out AR 5
Load Step	LS 5	LS 5
Model Size (Elements)	1,190,400	1,190,400
ΔW_{avg} ($\times 10^6$ J/m^3)	0.1354	0.1368
Diff (%)	-	1
Vertical Displacement at P (mm)	-0.0133	-0.0133
Normalized Comp Time	1X	1.8X

Table 5.11 Effect of Element Type on Quarter 15 × 15 mm^2 Package Model

Package Size	15 × 15	15 × 15
Element Type	8-Nodes Linear Hexahedron	20-Nodes Quadratic Hexahedron
Mesh Quality	Fan-Out AR 6_10	Fan-Out AR 6_10
Load Step	LS 3	LS 3
Model Size (Elements)	850,845	850,845
ΔW_{avg} ($\times 10^6$ J/m^3)	0.1283	0.1290
Diff (%)	-	0.5
Vertical Displacement at P (mm)	-0.0215	-0.0214
Normalized Comp Time	1X	1.4X

5.11 Effect of Element-Layers Used for Volume-Weighted Averaging ΔW_{avg} Calculation

As one element-layer crossing 10 μm thickness at the top of joints was used for calculating ΔW_{avg} in prior studies, another model having two element-layers across the same thickness was simulated (Figure 5.35). The simulation results of ΔW_{avg} values were compared in Figure 5.36. The difference of simulation results is less than 2 %, which means the effect of number of element layers used for volume-weighted averaging in a specific thickness is not significant. Thus, simulation result is not sensitive to the number of element layers crossing the specific thickness for evaluating accumulated strain energy density and similar conclusion has been reported in literature [99] [198] [176].

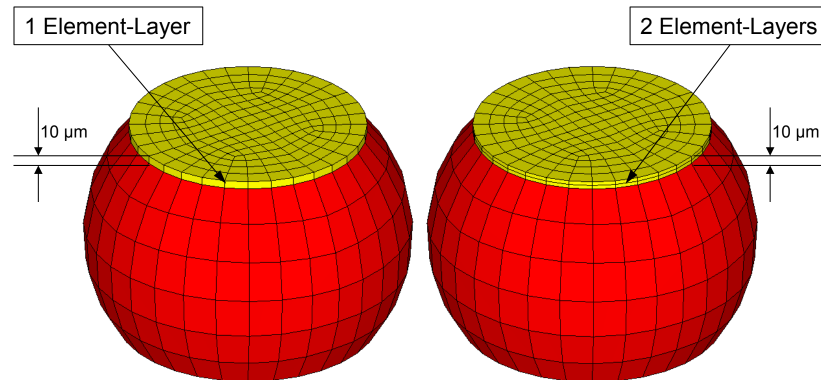

Figure 5.35 Element-Layer Crossing 10 μm Thickness

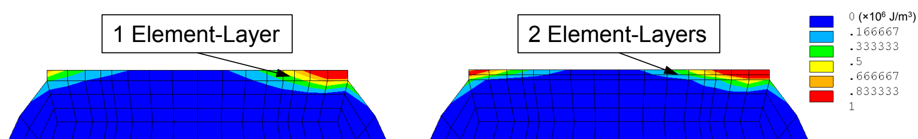

Figure 5.36 Simulation Results of PLWK Values for Models with Different Element Layers

5.12 Effect of Element-Layer for Components

The proposed fan-out meshing strategy used one element-layer for silicon die and mold compound above the silicon die, while another package model used two-layer element layer for the same region (Figure 5.37). The simulation results of ΔW_{avg} showed no difference for different element-layers models because this example model was not a large size package, induced the bending effect was not significant subjected to thermal expansion [129].

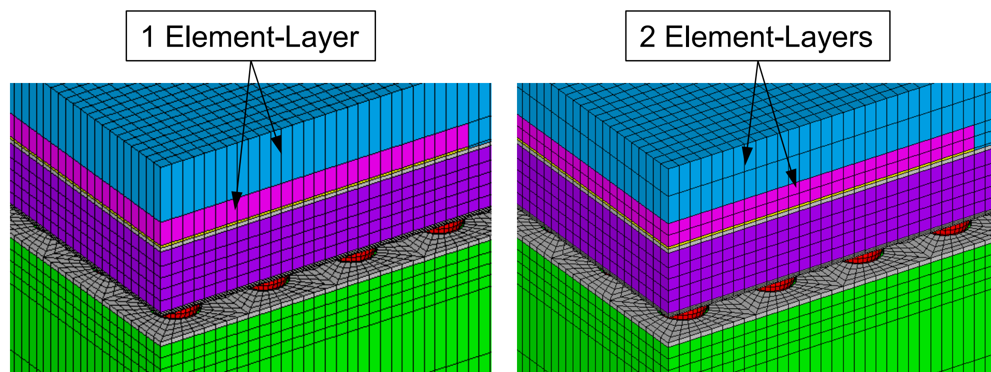

Figure 5.37 Different Element-Layers for Mold Compound and Silicon Die

5.13 Effect of PCB Model Size

The model size of PCB is another considerable factor to further improve simulation efficiency. A reduced PCB size model (Figure 5.38), its boundary edges equivalent to the package size, has been built and simulated. Simulation results of ΔW_{avg} values shown in Figure 5.39 resulted in a very good agreement but less computer resources/time were required while a smaller matrix was formed for a small PCB size model.

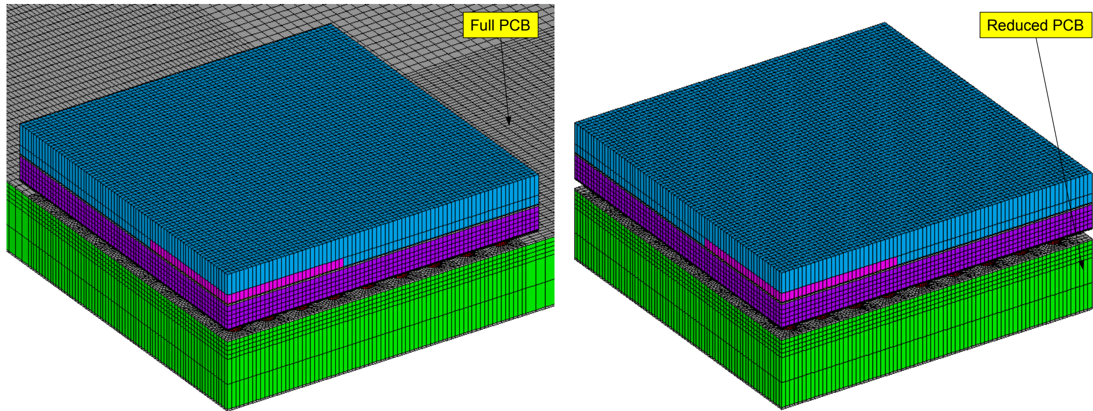

Figure 5.38 Different PCB Size Models

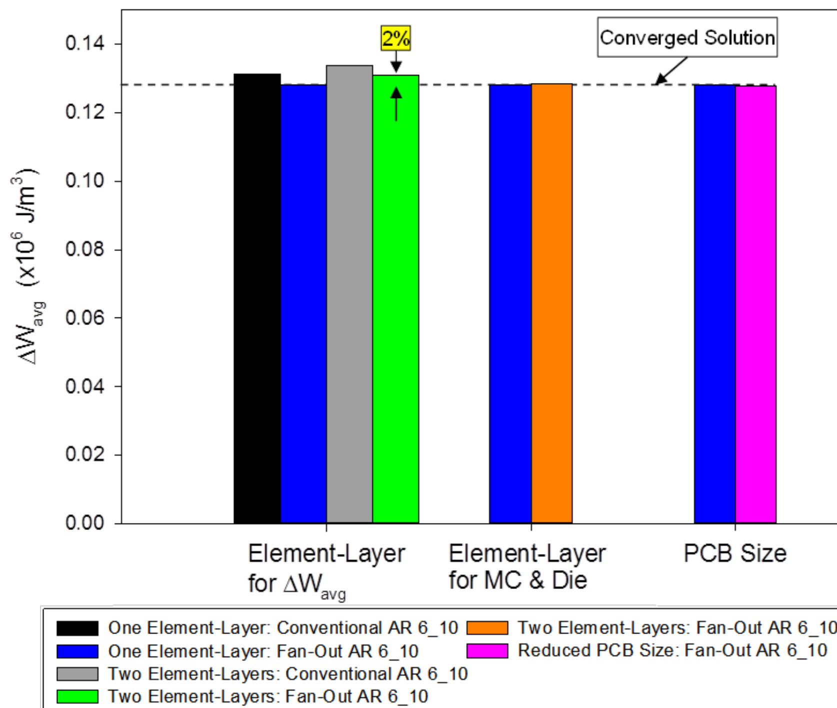

Figure 5.39 Comparisons of the Effects of Different Modeling Setups on Simulation Results

5.14 Effect of Initial Temperature Range

Temperature curves starting from temperature ramp-up and ramp-down (Figure 5.40) have intimal temperature changes of 100 and 65 °C, respectively. Simulation

results listed in Table 5.12 showed ΔW_{avg} values have no difference after five cycles for models simulating with these two different temperature curves.

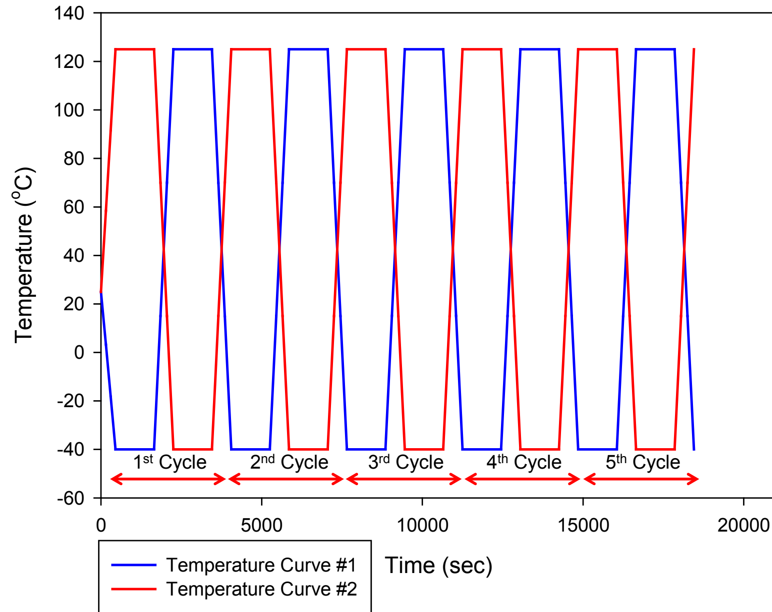

Figure 5.40 Two Different Thermal Cycling Curves

Table 5.12 Effect of Initial Temperature Change

Mesh Quality	Conventional AR 6_10	Fan-Out AR 6_10	Conventional AR 6_10	Fan-Out AR 6_10
Load Step	LS 3	LS 3	LS 3	LS 3
Temperature Curve	Curve #1	Curve #1	Curve #2	Curve #2
Initial Temperature Range (°C)	65	65	100	100
Model Size (Elements)	2,065,644	850,845	2,065,644	850,845
ΔW_{avg} ($\times 10^6$ J/m^3)	0.1312	0.1282	0.1313	0.1283
Diff (%)	2.3	-	2.3	-

5.15 Summary and Conclusions

In this study, the mesh continuity between high-density mesh and low-density mesh was realized by an improved fan-out meshing strategy utilizing a transition region

to transform circular mesh pattern to rectangular mesh pattern and also enlarge the element size. This fan-out meshing model reduced overall model size, mesh density, improved simulation efficiency, and kept solution quality. The flexibility of design change without re-partition was also realized by fan-out meshing strategy.

The convergence study of unit model predicted the trends of simulation results between mesh quality and load step size. Simulation results showed that load step size had greater influence than mesh quality (note that the mesh quality used for modeling in this study was in a range of fair to good meshing). Finer mesh quality performed opposite trend of simulation results with reducing load step size in the example models. It also revealed the choice of load step size is more crucial for solution quality. Similar to the convergence study of unit model, mesh quality and load step size performed opposite effects on convergence study of multiple-joints package assembly. An optimized analysis strategy was developed to determine the best corresponding mesh quality model and load step size to achieve the balance between accuracy and efficiency. Proposed strategy makes it possible to use a low-density meshing model with corresponding load step size to obtain a high quality result as using a high-density meshing model and load steps. This strategy was validated on the history curves for the volume-weighted averaging PLWK and ΔW_{avg} in the convergence studies of unit model and multiple-joints models.

Long term confusions of modeling have also been studied. Element-layers used for volume-weighted averaging energy accumulation have been proofed that it is not crucial once overall model was built with a good controlled mesh quality. The proposed optimized analysis strategy resolved the confusion of numbers of element-layers for

components (such as mold compound and silicon die). A negligible impact was performed between single and multiple element-layers used for such components. Simulation results showed that for the package assembly subjected to thermal expansion problem, PCB size has no effect on simulation results. The simulation results eventually converged to the same value after five cycles no matter the initial temperature change starting from ramp-down or ramp-up. Also, in this section, the use of higher-order element performed no significant change on simulation results but additional computational time were required due to the problem subjected to thermal cycling in this study is not a bending-dominated problem.

CHAPTER 6
IMPROVED FINITE ELEMENT MODELING STRATEGIES WITH MULTIPOINT CONSTRAINT FOR PBGA PACKAGES SUBJECTED TO THERMAL CYCLING

6.1 Introduction

The main purposes of electronic package are protecting fragile silicon chip and establishing interconnection from die to other components. Several design features for a package involve functionality, package size, heat dissipation, cost and etc. These requirements make the configuration of package even more complex and also increase the density of I/O counts in a limited space. PBGA technology utilizes the bottom side area of a package, where solder joints have been deployed in an area or perimeter array for supporting more I/O's in the same package size, make it become a popular option in electronic package area.

In an analysis of PBGA package assembly, the mesh connectivity for different components has become more challenge due to different geometric shapes (e.g. solder joint typically has a shape of sphere or cylinder and other components have a shape of block) and the complexity of component configuration. In addition, additional added materials (such as underfill or edge bonding are added to protect a packages from mechanical shock or vibration) also increase the level of difficulty of modeling. Conventional FE model using continuous meshing approach lacks of ability to make a regular shaped element model; thus, an improved modeling strategy is urgent needed.

Various FE modeling technologies (such as MPC, submodeling, and substructure) have been developed to model and simulate the problem more efficiently [164]. MPC, originally developed for simulating contact problem, is a solution for dealing with complex configuration of package assembly. The analysis, however, solving by MPC algorithms may require more computer resources due to the setup of contact and constraint relation and update of the contact relations. The accuracy and efficiency of MPC-based FE simulation for electronic package have not been evaluated completely in the literature [176] [191] [216]. Analyst uses this technique relied on their own knowledge and sometimes based on intuition; inappropriate setup of constraint relations may introduce numerical error resulting in inaccurate simulation result.

In this chapter, an improved MPC-based FE modeling strategy for PBGA was developed utilizing several different MPC setups. The proposed strategy reduces the difficulty of FE modeling, maximizes the efficiency, and also keeps solution consistency compared to continuous meshing modeling approaches.

In addition, the proposed strategy suggested a contacting elements ratio for different types of mesh patterns, and the location of MPC contact pair. The proposed approach works with different types of BGA array, including area and perimeter arrays, and achieves a good balance between simulation efficiency and accuracy.

6.2 Multi-Point Constraint

In a physical contacting analysis, interpenetration or penetration is not allowed in most cases. Multi-point constraint is a technique to establish a relation of contact compatibility to prevent interpenetration using extra elements (including master/target

and slave/contact elements) deployed along the contacting interfaces after the model was meshed with traditional elements. Three main MPC algorithms were developed for solving contact problem including [213] [217] [218]: Normal Lagrange, Penalty Augmentation, and Augmented Lagrange. The Normal Lagrange solves contact pressure as a DOF directly, so that there is no contact stiffness or penetration. The Penalty method introduces the penalty factor to eliminate the force generating proportional to the distance of penetration while a contact detection point has penetrated across the target surface. The augmented Lagrange method is similar to the penalty method using an internally calculated term to reduce sensitivity to contact stiffness of the penalty-based force calculation. The tradeoffs in generality, computational effort, and numerical accuracy have to be considered while choosing MPC algorithms.

Three major types of contact models for modeling a contact problem are: node-to-node, node-to-surface, and surface-to-surface models [179] [206] [207]. The node-to-node model is the simplest and faster method, but requires a prior knowledge of contacting surfaces and not suitable for the problem involving sliding or large rotations. The node-to-surface model is more robust for complex surfaces than node-to-node model because it does not need to know the exact location of contact. The surface-to-surface is a more general model for contact problem except some problems such as corner contact or snap-fit assemblies. Pre-understanding of contacting surfaces is not required, but surface-to-surface is the most computer resource intensive model.

Although the constraint equations eliminate some of DOF's of the contact and target elements, overall computational time is increased as forming constraint equations, contact detection, and updating constraint relations of large deformation analysis. In this

research, the use of MPC is limited to the use of tie constraints to bond/tie two contacting regions with incompatible meshes. MPC formulation using technique of nodal detection (normal direction from Master/Target surface) to detect potential penetration has the advantage of fewer detection points are required [219].

For building contact model, the node-to-surface contact model was used for the purpose of simulation efficiency. In the node-to-surface method [206] [207], the nodes on the master/target surface closest to each slave/contact node is calculated and used to determine the master nodes that are going to form the constraint. As an example shown in Figure 6.1, master/target nodes 202, 302, 303, and 203 are used to constrain slave/contact node A; nodes 204 and 304 are used to constrain node B; and node 402 is used to constrain node C.

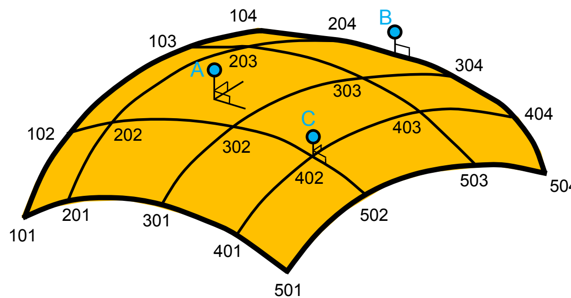

Figure 6.1 Node-to-Surface Method [206]

Since slave/contact surface cannot penetrate master/target surface but the inverse is not necessarily true (Figure 6.2), there are some general guidelines in proper setup master-slave (target-contact) relationships suggested by commercial FE software companies (e.g. ANSYS, ABAQUS etc.) [206] [207] [219]. Important guidelines were summarized as follows.

- The stiffer material side should be the master/target surface.
- The surface with the coarse mesh should be the master/target surface while fine mesh surface is slave/contact surface.
- Surface of higher order are slave/contact surface.

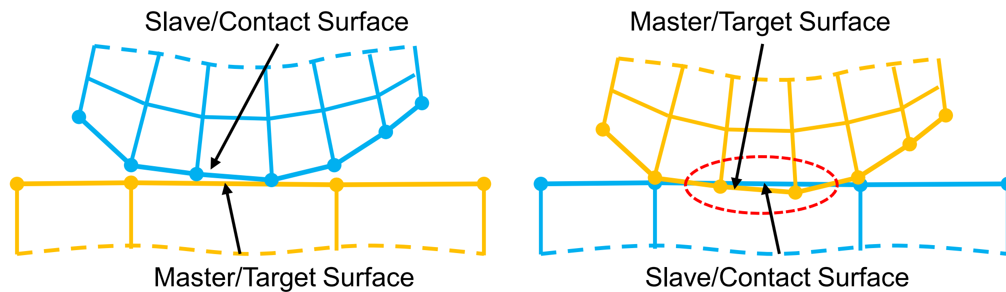

Figure 6.2 Two Different Master-Slave Relationships [219]

6.3 Finite Element Modeling and Simulation

Finite element analysis using highly nonlinear material and high-density meshing model is a computer-intensive task. Therefore, mesh generation is one of the most crucial steps in FE analysis since the decision made at this point has far-reaching effect on entire simulation.

Two most common used element types are the tetrahedral and hexahedral elements [25] [204]. Several robust algorithms have been developed to make it possible for auto-meshing via tetrahedral element on an arbitrary geometry. Unfortunately, literature [201] [202] [203] show that there are convergence and accuracy concerns about the application using tetrahedron in nonlinear material having plasticity behavior. Hexahedral (brick) element performs better accuracy over tetrahedral element in the problems related to plasticity, contact, and distortion [203], and less elements and

computer resources are required in a general problem while a model is meshed with hexahedral elements. Hexahedral element has becomes a more popular element type for the simulation encountering large deformation, contact, plasticity, etc. However, the mesh generation solver for fully auto-meshing via hexahedral element is still under developing; especially for algorithm of generating an all hex model with a reasonable element size [205].

Two types of mesh generation methods are widely used in FE area; they are free mesh and mapped mesh [199]. Compared to free mesh, mapped mesh has regular pattern, with obvious rows of elements, and can contain only hexahedron elements in a volume model to reduce overall mesh density. In this study, all FE models were meshed with hexahedron element using mapped approach for the purpose of obtaining high quality solution without time consuming calculation.

6.4 Example Model

An example model for a PBGA configuration composed of a chip (center red box in Figure 6.3) and an area array of 324 solder joints. Dimensions of the example package are listed in Table 6.1. The solder joint pitch in the model was 0.8 mm. Due to the symmetry of the example package, a one quarter model with symmetric boundary conditions was taken for demonstration. The material properties, loading condition, and fatigue model used in this chapter can be found in Chapter 4.2.

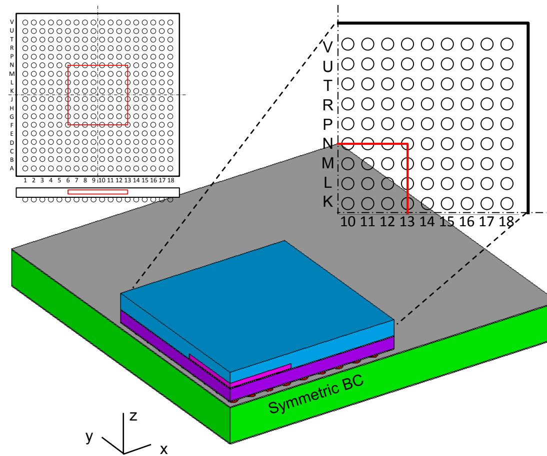

Figure 6.3 Example 15 × 15 PBGA Assembly

Table 6.1 Dimensions of Example 15 × 15 PBGA Assembly

Component	Dimensions (mm^2)
PCB	30 × 30
Solder Mask	30 × 30
BT Laminate	15 × 15
Die Attach	5.6 × 5.6
Silicon	5.6 × 5.6
Mold Compound	15 × 15

6.5 Continuous Meshing Modeling Strategies

Two continuous meshing modeling strategies can be found in the literature [28] [220] [221] [222] [223] [224]. The first modeling strategy is conventional meshing strategy as illustrated in Chapter 5.4.2. In meshes using this strategy, a circular mesh pattern can be observed in its top/bottom view as shown in Figure 6.4.

The second continuous meshing modeling strategy is the fan-out meshing strategy (Chapter 5.4.3 [189]), developed as follows: (1) a hemispherical mesh transition region was utilized to fan-out circular mesh pattern to rectangular pattern, (2) the controlled maximum aspect ratio of mesh was set to a factor of reasonable value for most partitions

of model, and (3) for tiny uninteresting partition, the factor of maximum aspect ratio was increased for a balance of geometrical fitting and element number size.

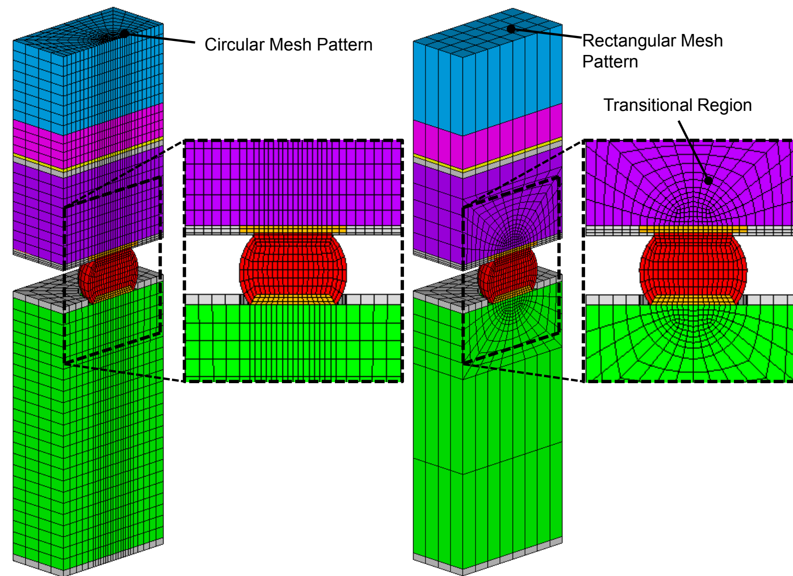

Figure 6.4 Conventional (Left) and Fan-Out (Right) Meshing Models

Relative to conventional approaches, the fan-out meshing strategy improves the accuracy of the simulations while simultaneously reducing the model size and simulation time by at least a factor of three. However, the thickness of transition region (equivalents to the height of solder joint is suggested for the purpose of generating a better quality of mesh) restricts the application of the package having a limited size of transition region (such as thin PCB/BT substrate).

6.6 MPC Methods in the Literature

Since geometry of solder joint in PBGA package has a shape of sphere, a circular mesh pattern (shown in Figure 6.5(a)) can be observed in its top/bottom view. The geometrical shape related to other component, however, mostly has a shape of

rectangular as shown in Figure 6.5(b). The incompatible in geometrical partitions resulting in incompatible mesh patterns increases the difficulty of achieving mesh continuity of the FE model.

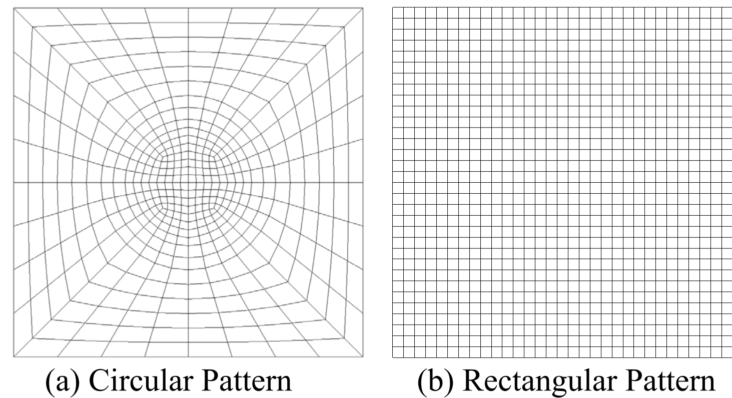

Figure 6.5 Different Mesh Patterns

Following common methodology of using MPC approach in the literature [28] [175] [176] [191] [225], the example model was meshed separately yielding two different mesh patterns as follows, (1) the solder joints, copper pads and solder mask were meshed using a fine mesh as the core region where a circular mesh pattern was presented as shown in Figure 6.6, and (2) the rest components of the package were meshed using a coarse mesh. Instead of circular mesh pattern, a more regular rectangular mesh pattern can be observed from the top/bottom view of MPC model. The mesh density was hugely reduced at the rectangular meshing region where low interest was taken. Then, MPC setup was added at the interface of these two different mesh patterns to establish constraint relation. Figure 6.6 showed the incompatible meshing patterns at the top of copper pad (orange) and the substrate (purple).

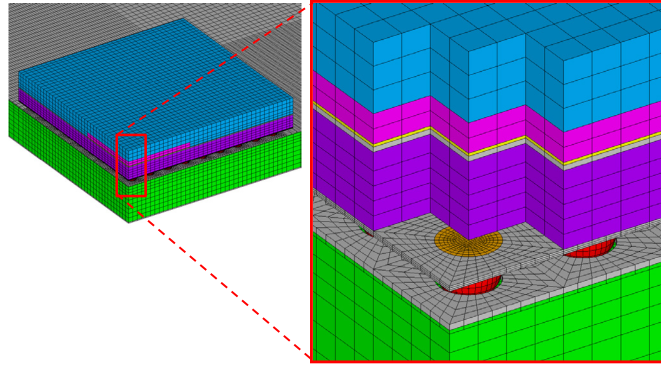

Figure 6.6 MPC FE Model

As the vertical displacement contours plotted in Figure 6.7, the overall distribution of vertical displacement for MPC model matched well with conventional (continuous meshing) model. In Figure 6.8, however, it can be seen that MPC model overestimate the PLWK over thermal cycles. It can be explained by the behavior of package assembly captured by coarse-mesh model was accurate, but the detailed response of displacement above the solder joint interpolating by MPC was lack of accuracy. Due to the inaccurate interpolation of the displacement, the ΔW_{avg} values were also greater than conventional model; this MPC setup introduced 24 - 42% differences of ΔW_{avg} values in our example as shown in Figure 6.9.

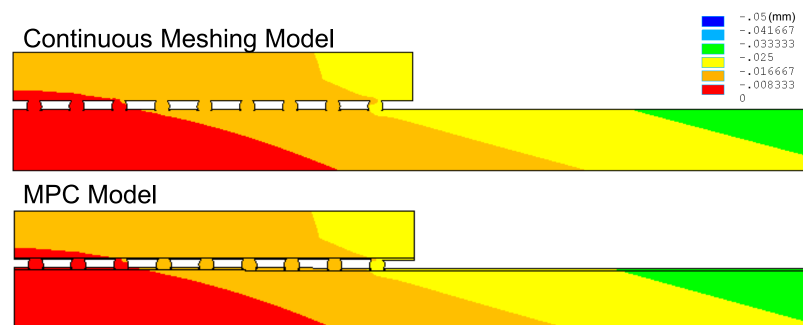

Figure 6.7 Comparison of Vertical Displacements after Five Cycles for Continuous Meshing Model and MPC Model

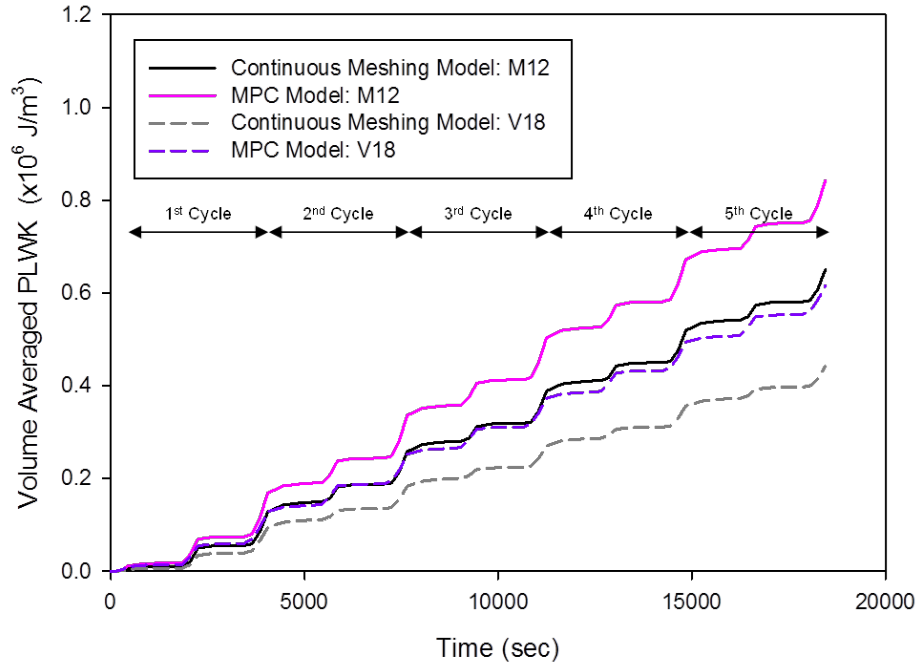

Figure 6.8 Comparison of History Curves of Volume-Weighted Averaging PLWK for Continuous Meshing Model and MPC Model

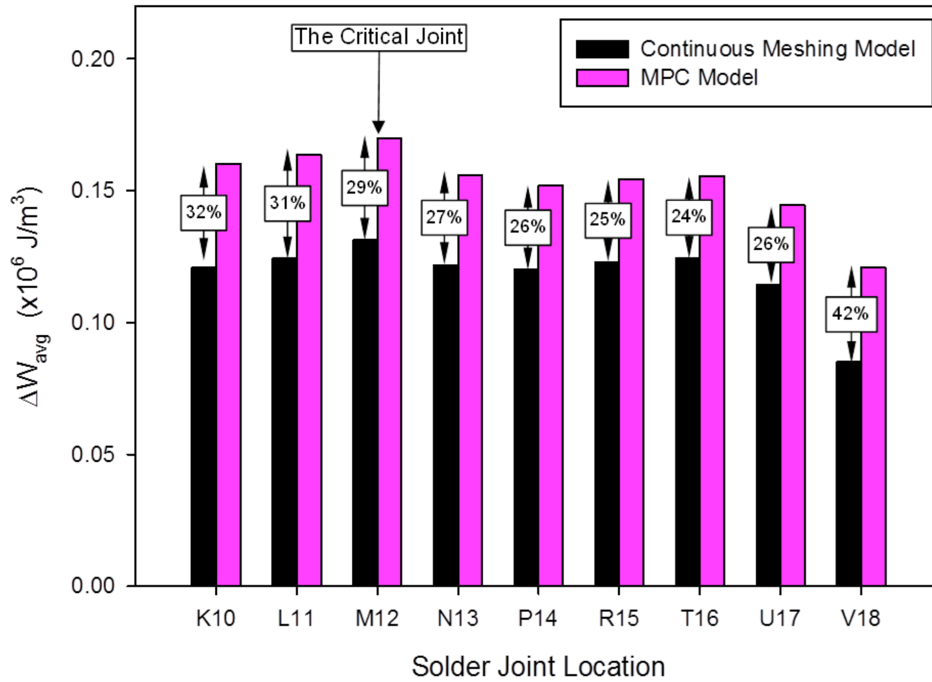

Figure 6.9 Comparison of ΔW_{avg} Values for Continuous Meshing Model and MPC Model

The MPC technique provides an effective approach for bonding two components together without considering mesh continuity. It improves modeling convenience using less geometric partitions, and reduces overall mesh density of the FE model. In addition, similar to continuous meshing model, the analysis using MPC calculates the responses for all solder joints of a package assembly in a simulation; unlike submodeling technique that an extra simulation (local simulation) is needed. Caution must be taken while using MPC to bond incompatible mesh pattern [28] [175] [191] [192] [193]. Bonding over coarse meshing with refine meshing may lose the accuracy of simulation. In this study, an improved metrology for finding the location of MPC contact pair and the effects of important factors of MPC setup was present.

6.7 The Use of MPCs with Compatible Meshes

Before we develop improved MPC modeling strategy for bonding general incompatible meshing surfaces, the effects of using MPC technique on bonding compatible meshing surfaces was studied first. The methodology used here is described as follows. After unit model was meshed, the mesh continuity between solder joint and copper pad was removed and then the contacting surfaces were bonded by MPC contact pairs as shown in Figure 6.10. Additional 1,058 elements for both different meshing models, listed in Table 6.2, contributing to MPC relations (containing master/target and slave/contact elements) were increased to provide sufficient DOF's constraints for tying solder joint and copper pad together. As simulation times listed in Table 6.2, it revealed that the MPC models calculated the same results but extra 12.5% computational time was taken compared to continuous meshing models. This solution validated the MPC contact

pair can be located at the interface of different types of material properties (linearity for copper and nonlinearity for solder) in a compatible meshing without losing accuracy.

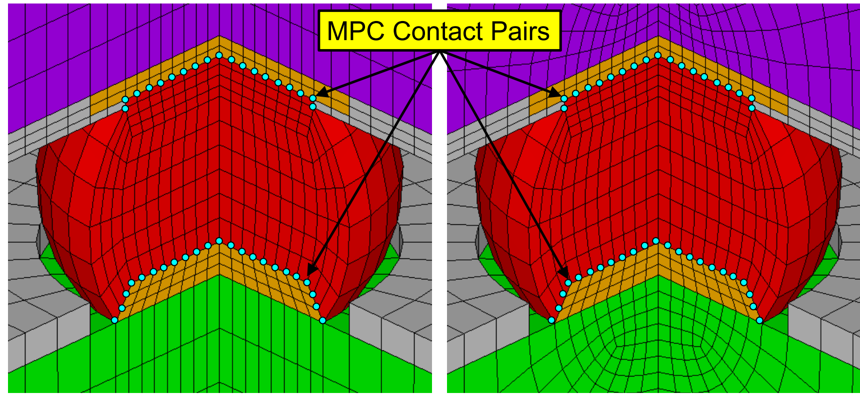

Figure 6.10 Cross-Sectional View of MPC

Table 6.2 Comparison of Results for Different Unit Models

Modeling Strategy	Conventional Model (Ref)	Fan-Out Model	MPC Model #1	MPC Model #2
	Continuous Meshing	Continuous Meshing	Conventional Model + MPC	Fan-Out Model + MPC
Model Size (Elements)	23,104	9,408	24,162	10,466
Elements for MPC	-	-	1,058	1,058
ΔW_{avg} ($\times 10^6$ J/m^3)	0.0926	0.0924	0.0925	0.0924
Diff (%)	0	0.2		0.2
Normalized Comp Time	1X	0.4X	1.3X	0.45X

After simulations, the displacement field remained continuous from PCB/BT substrate through copper pad and solder joint for the mesh compatible models. But, the simulation results of strains and stresses for MPC models present discontinuities at the interface where bonding by MPC approaches (as shown in Figure 6.11). Thus, the use of MPC should avoid locating at the interface between solder joint and copper pad while

using stress/strain based fatigue failure model. One improvement proposed by Syed [175] by placing MPC contact pairs several element-layers away from copper pads can prevent the discontinuities of stress and strain at interface of solder joint and copper pads. Although use MPC to connect compatible meshes is not a common option in analysis, this study reveals that the location of MPC is important; simulation result may not be continuous at the interface establishing by MPC technique.

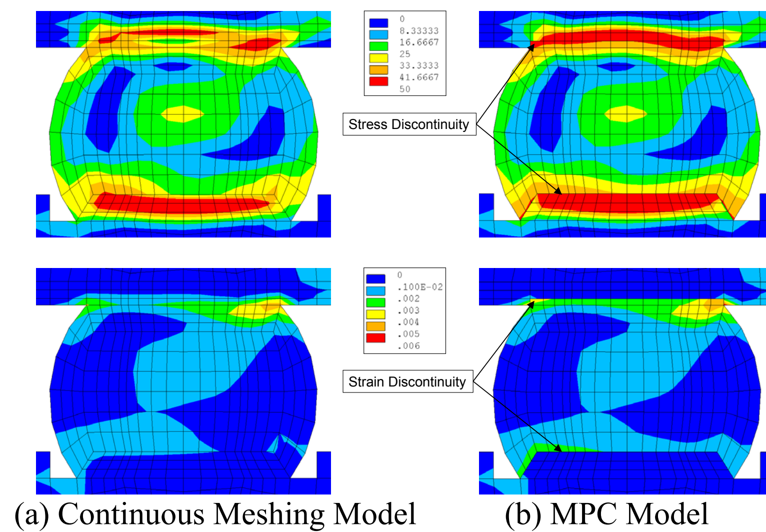

(a) Continuous Meshing Model (b) MPC Model

Figure 6.11 Simulation Results of Stress and Strain for Unit Model Using Different Modeling Strategies

6.8 The Use of the MPCs with Incompatible Meshes

Following studies focused on bonding incompatible mesh patterns, exploring the advantages of MPC technique, and developing new guide lines of analysis.

6.8.1 MPC Approach #1: MPC at the Interface between Two Different Materials

Following the common setup of MPC approach in the literature, the MPC contact pairs was deployed at interface of two contacting components which is the top and

bottom sides of copper pads (Figure 6.12) to bond copper pad and PCB/BT substrate together. Between the MPC contact pair, two different components have different material properties and mesh patterns. We named this approach as MPC approach #1 in this study. The advantage of this approach is that it is a very intuitive process to setup constraint relationship at the natural boundaries of two different components.

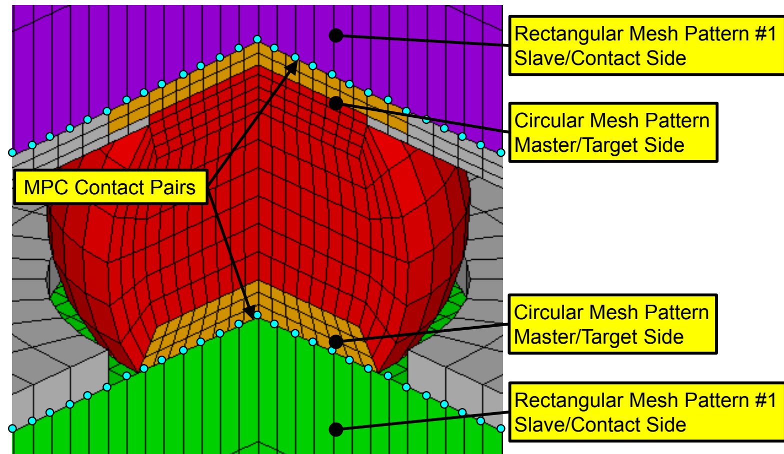

Figure 6.12 Cross-Sectional View of MPC Approach #1

Considering the different stiffness of two contacting surfaces, the stiffer material side was assigned as master/target side while slave/contact side was assigned to another material. A C/R ratio counting the ratio of contacting elements between two contacting surfaces is proposed as follow.

$$C/R = \frac{\text{Elements in Circular Mesh Pattern}}{\text{Elements in Rectangular Mesh Pattern}} \tag{6.1}$$

The circular mesh pattern and rectangular mesh pattern #1 (counting from solder joint side) belonging to different material properties were bonded by MPC contact pair

with five C/R ratios of 0.44, 0.78, 1.75, 7, and 28 as shown in Figure 6.13. Table 6.3 summarized the model sizes of different C/R ratios models. The smallest model size of MPC models was built by using C/R = 28 while C/R = 0.44 generated the largest MPC model.

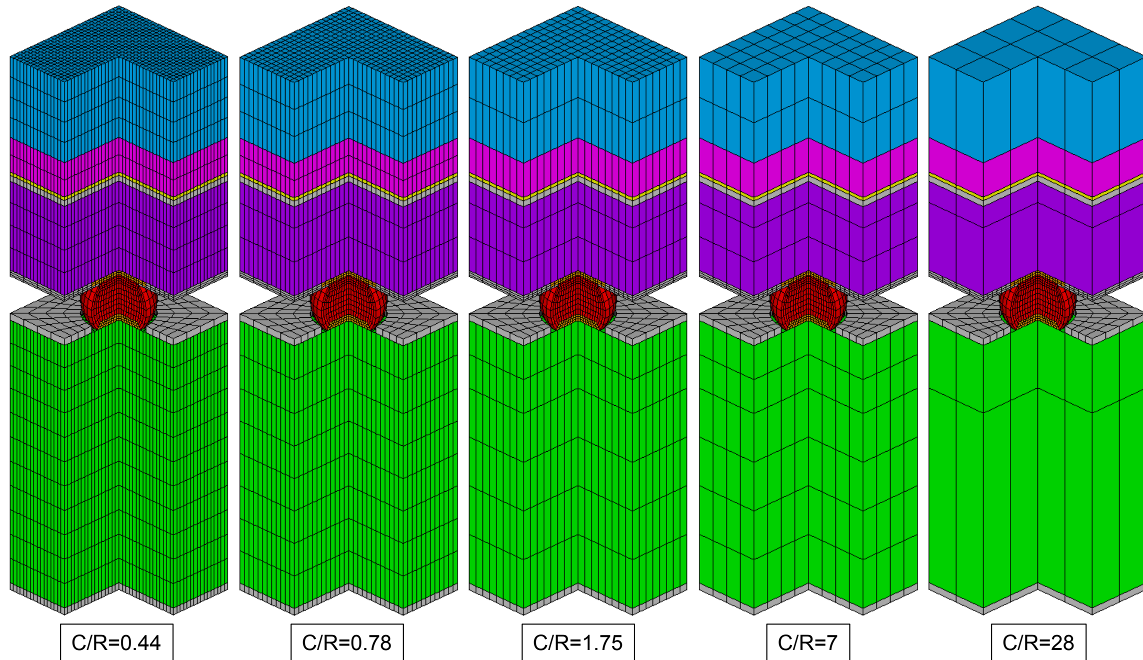

Figure 6.13 Unit Model Built Using MPC Approach #1 with Five Different C/R Ratios

Table 6.3 Comparison of Results for Unit Models Using MPC Approach #1

Modeling Strategy	Conventional	Fan-Out	MPC APP #1	MPC APP #1	MPC APP #1	MPC APP #1	MPC APP #1
C/R	Continuous Meshing	Continuous Meshing	0.44	0.78	1.75	7	28
Total Elements	23,104	9,408	31,874	17,314	9,538	6,242	5,314
Elements for MPC	-	-	2,946	2,018	1,346	930	818
Elements in Circular Pattern	N/A	N/A	448 (Master)	448 (Master)	448 (Master)	448 (Master)	448 (Master)
Elements in Rectangular Pattern			1,024 (Slave)	576 (Slave)	256 (Slave)	64 (Slave)	16 (Slave)
ΔW_{avg} ($\times 10^6$ J/m^3)	0.0926	0.0924	0.0979	0.1029	0.1003	0.0847	0.0678
Diff (%)	0	0	6	11.4	8.5	8.3	26.6

6.8.2 MPC Approach #2: MPC Locates within a Material

In MPC approach #2 of this study, the rectangular mesh pattern #1 was extended into the material-layer of BT substrate/PCB (Figure 6.14), which established a relation of MPC contact pair bonding elements of the same material property. Although, the MPC contact pair located within a material where no stiffness difference between two contacting sides, the setup of master/target and slave/contact sides still inherited from approach #1. Side closing to solder joint was assigned as master/target side. Different C/R ratios models building with approach #2 were plot in Figure 6.15. Comparing with a same C/R ratio models in Table 6.3 and Table 6.4, the model size of approach #2 was always greater than the model size of approach #1 due to two additional element-layers were extruded in approach #2. Note that the vertical height of the additional element-layer on one side of solder joint is 20 % height of the solder joint.

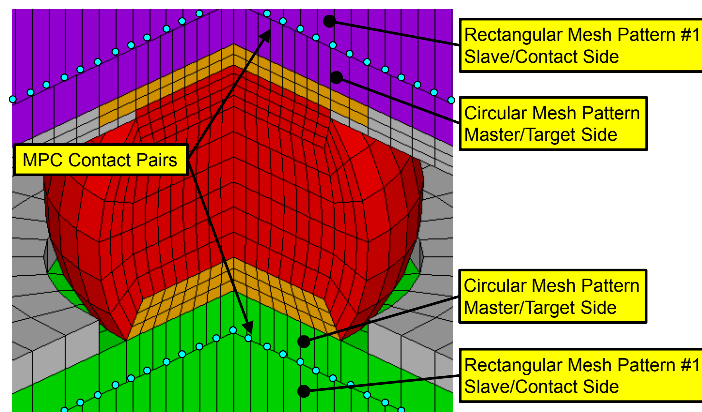

Figure 6.14 Cross-Sectional View of MPC Approach #2

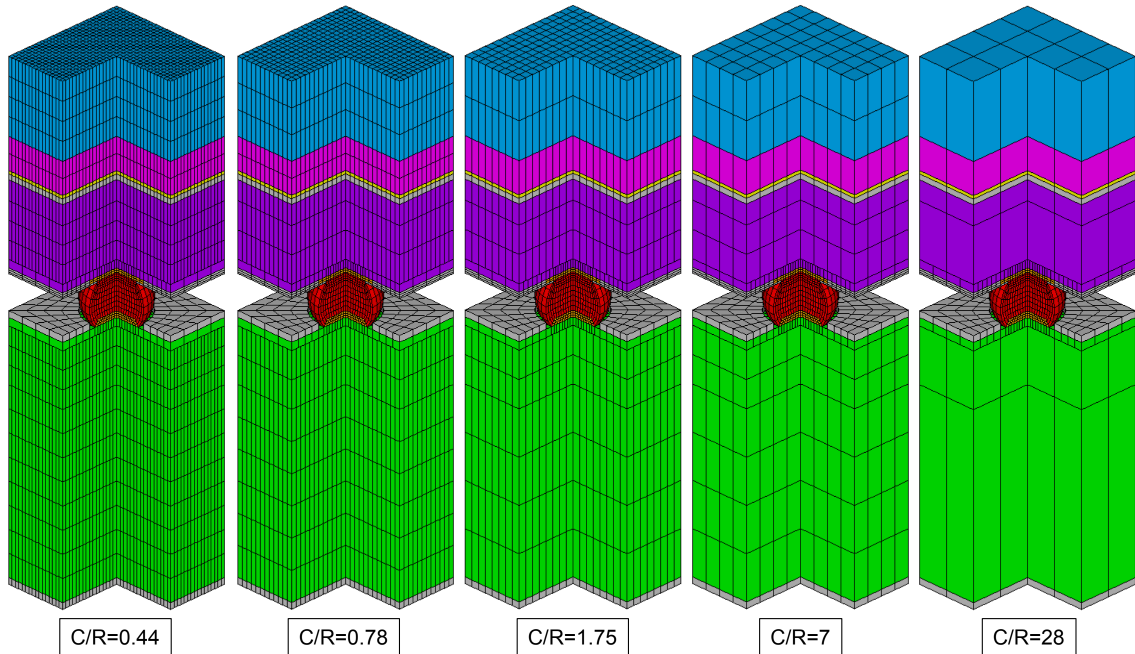

Figure 6.15 Unit Model Built Using MPC Approach #2 with Five Different C/R Ratios

Table 6.4 Comparison of Results for Unit Models Using MPC Approach #2

Modeling Strategy	Conventional	Fan-Out	MPC APP #2	MPC APP #2	MPC APP #2	MPC APP #2	MPC APP #2
C/R	Continuous Meshing	Continuous Meshing	0.44	0.78	1.75	7	28
Total Elements	23,104	9,408	32,706	18,146	10,370	7,074	6,146
Elements for MPC	-	-	2,978	2,050	1,378	962	850
Elements in Circular Pattern	N/A	N/A	448 (Master)	448 (Master)	448 (Master)	448 (Master)	448 (Master)
Elements in Rectangular Pattern			1,024 (Slave)	576 (Slave)	256 (Slave)	64 (Slave)	16 (Slave)
ΔW_{avg} ($\times 10^6$ J/m^3)	0.0926	0.0924	0.0924	0.0912	0.0895	0.0795	0.0654
Diff (%)	0	0	0.2	1.5	3.3	14.1	29.3

The locations of MPC contact pairs and model sizes for two approaches were compared in Figure 6.16 and Figure 6.17. The mesh density of rectangular mesh pattern side (slave/contact side) becomes lower/coarser while C/R ratio greater than 1.75; hence, model size decreased as C/R ratio increased. Note that the mesh pattern and number of elements for solder joint and copper pads of two approaches with different C/R ratios were all identical.

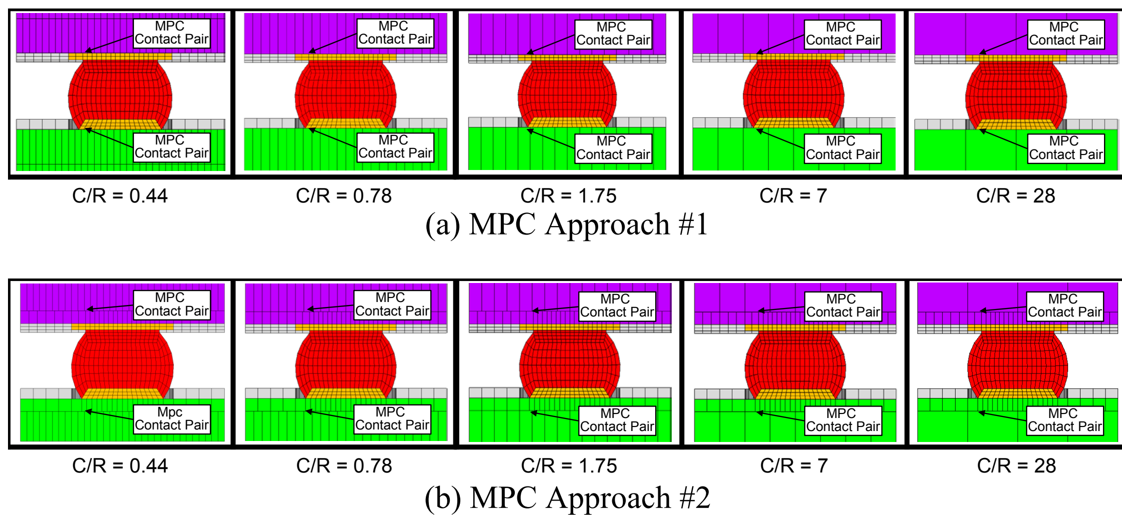

(a) MPC Approach #1

(b) MPC Approach #2

Figure 6.16 Comparison of Mesh Densities for MPC Approaches

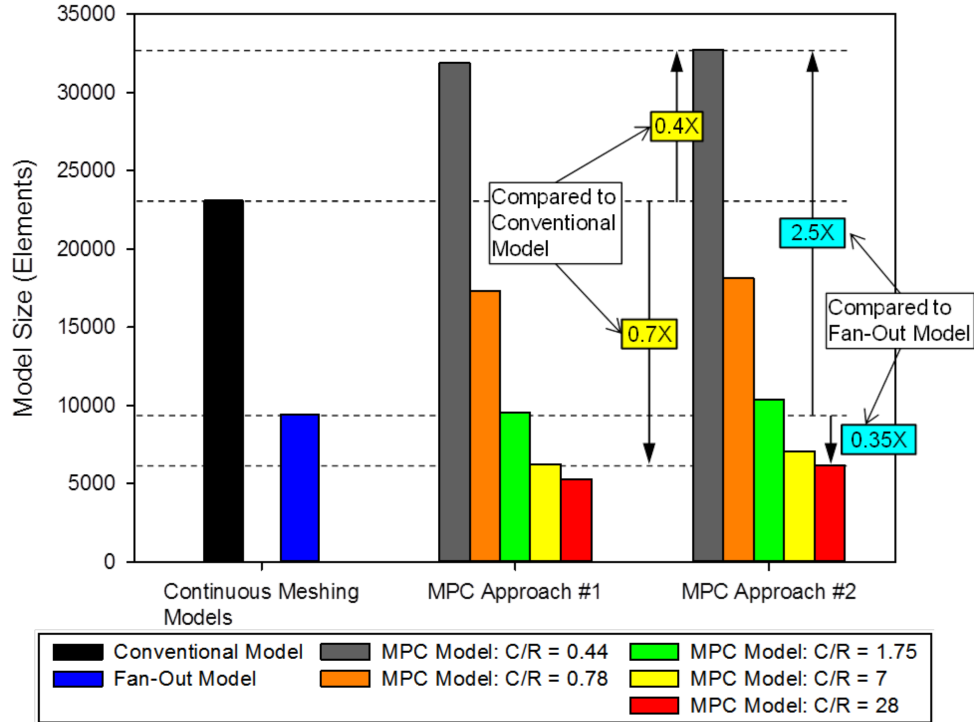

Figure 6.17 Comparisons of Model Sizes for Different C/R Ratios and MPC Approaches

6.8.3 Simulation Results for Models Using Different MPC Approaches

As simulation results listed in Table 6.3 and Table 6.4, C/R = 28 model yielded the poorest results while C/R = 0.44 model using approach #2 yielded a negligible difference (≤ 0.2%). In Figure 6.18, simulation results for approach #1 models presented a more deviation distribution than results for approach #2 models; even using a small C/R ratio of 0.44 still could not improve the solution quality. It can be explained by the improper interpolation of displacement field between contacting surfaces due to incompatible mesh patterns and mismatch in material properties (such as Young's modulus and CTE's).

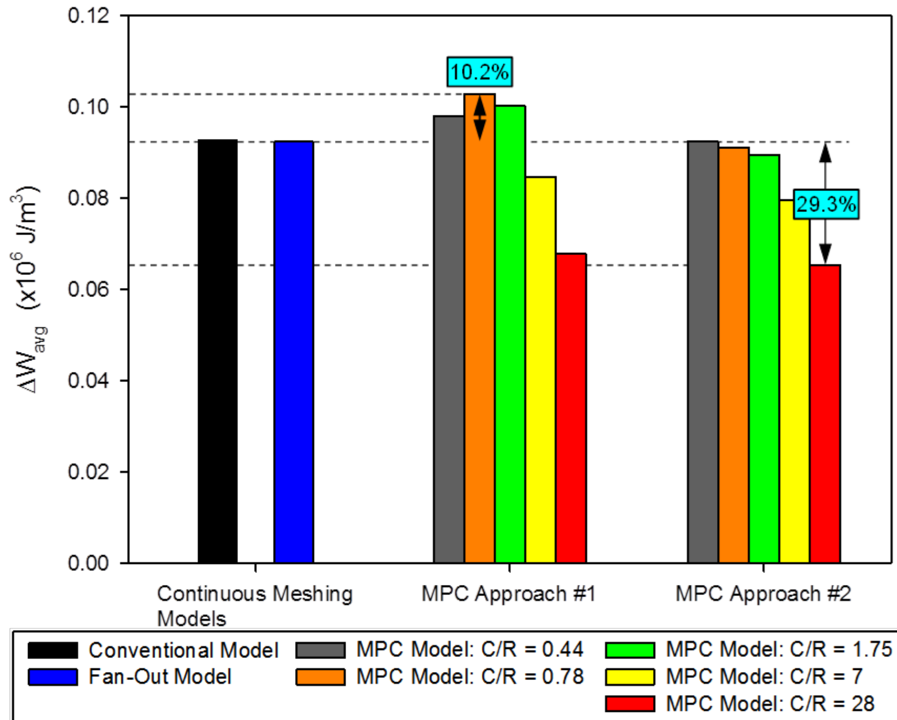

Figure 6.18 Comparisons of Simulation Results (ΔW_{avg}) for Models with Different C/R Ratios and MPC Approaches

As the differences of ΔW_{avg} values vs. C/R ratios for two approaches were compared in Figure 6.19, the differences have a very strong relation with the C/R ratios where they increased steeply after the C/R ratio greater than 2 concluding from the regression curve (red solid curve) plotted in Figure 6.19. Simulation results for approach #1 deviated from the C/R = 0.44 model and always performed a difference greater 5% in this unit model study. MPC approach #2 yielded a better solution quality for the models building with the C/R ratio bellowed a factor of 2 due to there is no material stiffness mismatch between contacting surfaces and mesh densities between two contacting surfaces were more closed. Thus, a fair to good solution quality can be expected utilizing MPC approach #2 with proposed C/R ratios less than 2. As a very high quality solution is concerned, the C/R ratio is suggested to less than a factor of 1.

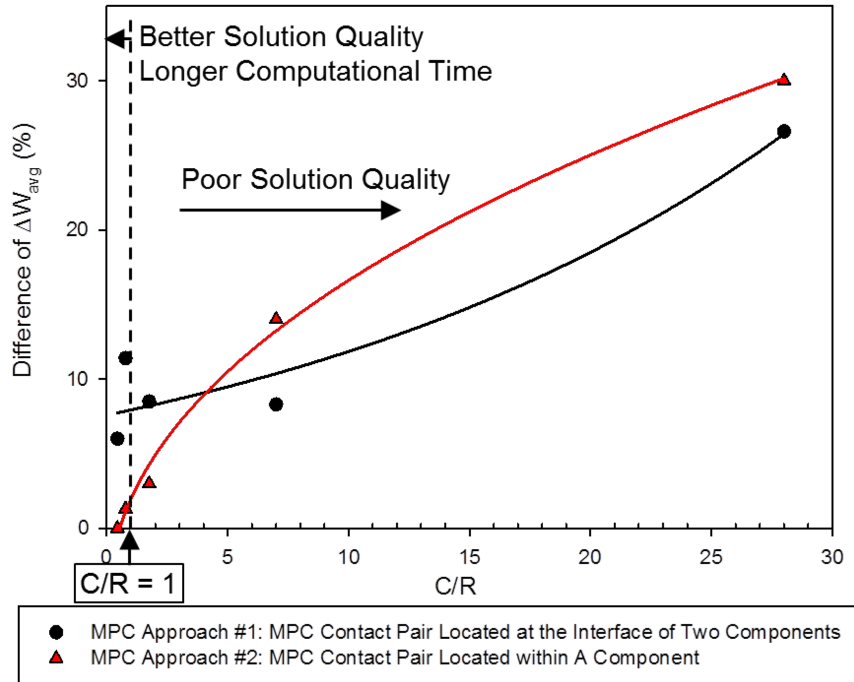

Figure 6.19 The Effects of C/R Ratio on the Percentage Error in ΔW_{avg} for Different MPC Approaches

The computational times for the approach #2 models were compared in Figure 6.20 and Table 6.5. Models of C/R = 0.44 and 0.78 took more time than conventional model while only C/R = 28 model took less time than fan-out model. The advantage of large C/R model is saving significant computational time, but the drawback is also obvious that it introduced great error as reported in literature [28].

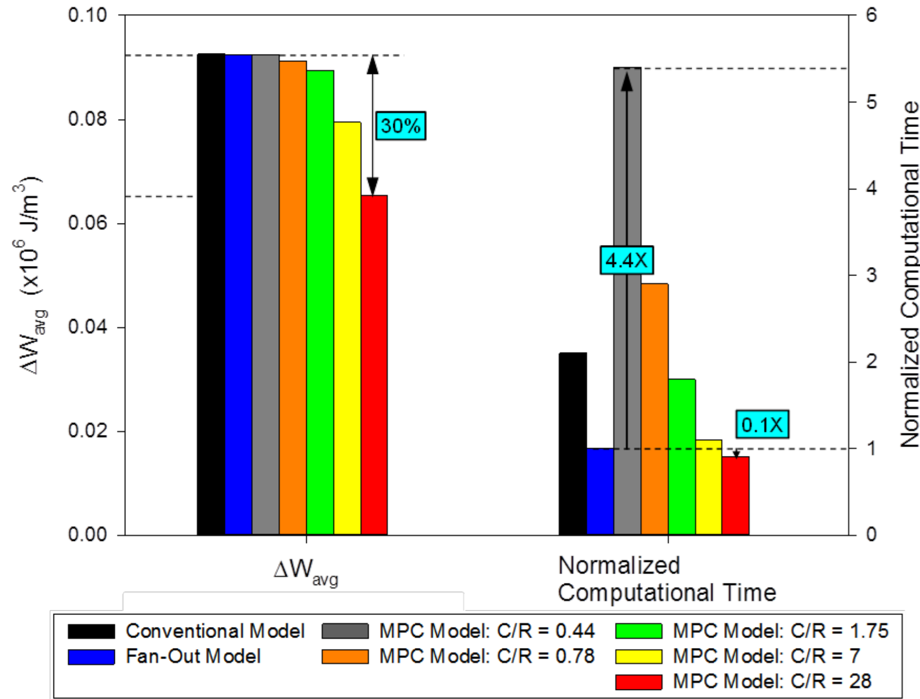

Figure 6.20 Comparisons of Simulation Results and Computational Times for the MPC Modeling Approaches

Table 6.5 Comparison of Results for Unit Models Using MPC Approach #2 with Different C/R Ratios

Modeling Strategy	Conventional Model	Fan-Out Model	MPC APP #2	MPC APP #2	MPC APP #2	MPC APP #2	MPC APP #2
C/R	Continuous Meshing	Continuous Meshing	0.44	0.78	1.75	7	28
Total Elements	23,104	9,408	32,706	18,146	10,370	7,074	6,146
ΔW_{avg} ($\times 10^6$ J/m^3)	0.0926	0.0924	0.0924	0.0912	0.0895	0.0795	0.0654
Diff (%)	0	0	0.2	1.5	3.3	14.1	29.3
Normalized Comp Time	2.1X	1X	5.4X	2.9X	1.8X	1.1X	0.9X

Proposed C/R ratio avoids counting complicated DOF's between the contacting surfaces and can predict solution quality and simulation efficiency well. MPC model saves the transitional region using in fan-out meshing model, relaxes modeling difficulty, and also reduces model size. Caution must be made that the location of MPC has great

influence on simulation result. An improvement method for reducing the error of C/R = 28 model was investigated in the next study.

6.9 Dependence of the Results on the Vertical Height of the Extruded Circular Mesh Pattern

In the convergence study of unit model, C/R = 28 model using MPC approach #2 performed the most efficient simulation but yielded the worst solution quality. An improvement method is by extending the vertical height of circular mesh pattern in PCB/BT substrate side [175]. Four different extending vertical heights (h) of 0.5, 0.75, 1, and 1.5 h_{sj} (solder joint height as shown in Figure 6.21) were tested.

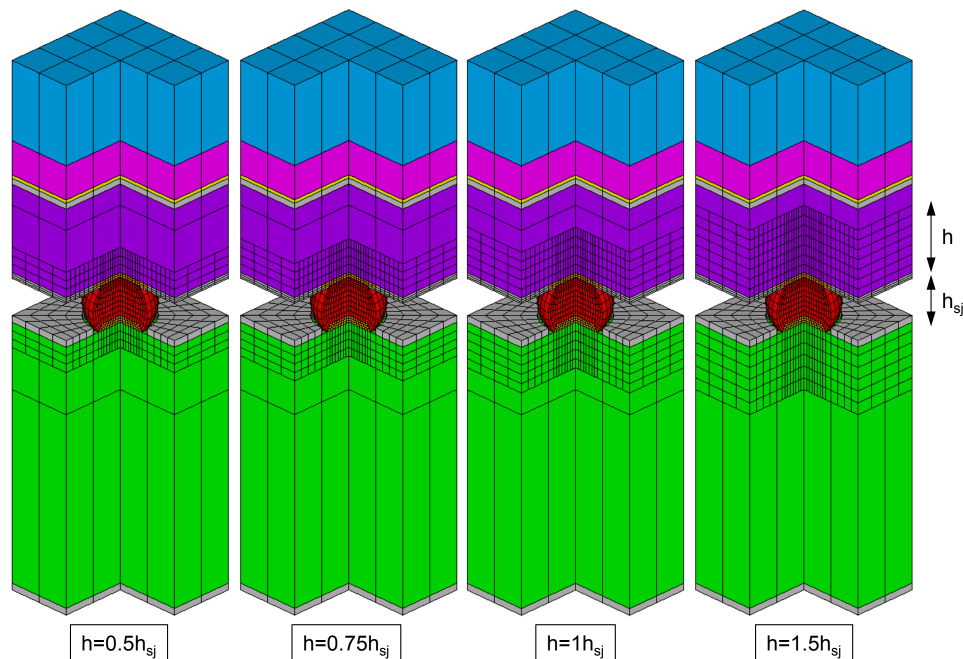

Figure 6.21 Four Different Vertical Heights for C/R = 28 Model

Simulation results for two different C/R ratio models were compared in Figure 6.22. It can be seen in yellow bars that the solutions for C/R = 7 models converged after h greater than 0.75 h_{sj}, even h = 0.5 h_{sj} still resulted in a fair difference. However, the converged solution for C/R = 28 model was obtained after h greater than h_{sj}. The model size of C/R = 7 model apparently was not suitable for package size modeling. Hence, model of C/R = 28 with h = 1.5 h_{sj} was chosen for comparisons of package size model with continuous meshing models.

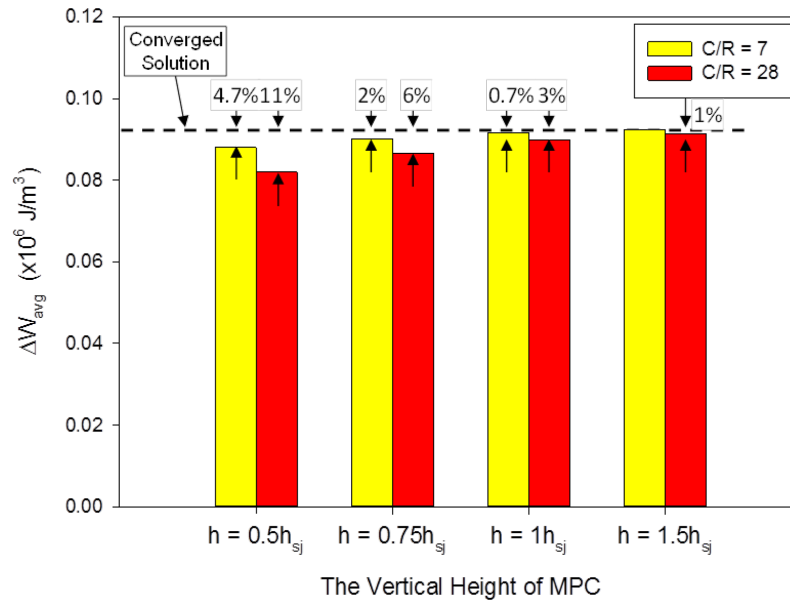

Figure 6.22 Comparisons of Simulation Results for Different Vertical Heights of the Extruded Circular Mesh Pattern

ΔW_{avg} values for solder joints locating at the diagonal direction of package assembly were compared in Figure 6.23. C/R = 28 model using h = 1.5 h_{sj} resulted in a fairly good agreement with continuous meshing models, but computational time was dramatically increased. Although MPC used for bonding different mesh density surfaces, element-saving on noninterest side still can't pay off the effects of increasing elements

extruding from high-density circular mesh side and the time for updating constraint relationships in a large mesh mismatch model. In the following study, instead of single-MPC was used on one side of solder joint, multiple-MPC contact pairs were introduced. Large mismatch in mesh density would avoid, and element density was layer-by-layer reduced using multiple MPC relations in-betweens.

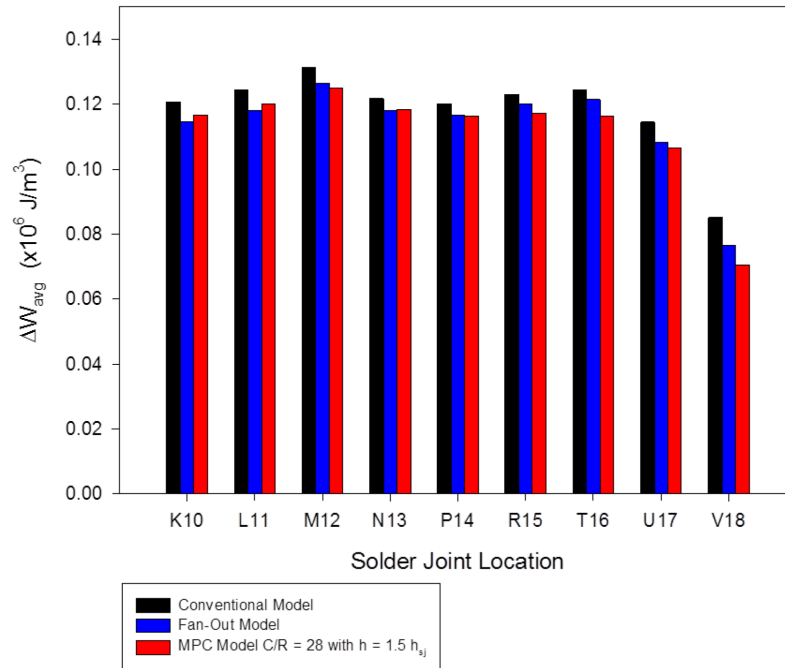

Figure 6.23 Dependence of the ΔW_{avg} Values on the Solder Joint Location for Different Modeling Approaches

6.10 The Use of Multiple MPC Contact Pair Layers (Unit Model)

In the previous study, two models building with C/R ratios of 0.44 and 0.78 resulted in better solutions; however, the model sizes of single-MPC unit models reached to 32,706 and 18,146 elements, respectively, which were still too many for a package simulation. In order to reduce mesh density, multiple-MPC contact pairs were used to reduce element numbers layer by layer. Following the methodology of MPC approach #2

in single-MPC study, master/target side was always assigned to the contacting side closed to solder joint side for each MPC contact pair.

Because the response of nonlinear solder material is sensitive to correct displacement interpolation, high-density mesh was preferred in the sensitive region for a correct interpolation of displacement field between two contacting surfaces. As a result, the C/R ratio of a factor of 0.44 was chosen for the MPC contact pair between the circular mesh pattern and rectangular mesh patter #1, as shown in Figure 6.24 (Only Shown the MPC Contact Pairs above the Solder Joint Side). For the MPC contact pair bonding similar rectangular mesh patterns, contacting elements ratio was increased to a factor of 4. Six MPC contact pairs in total were deployed within two materials; three contact pairs were located within BT substrate and another three pairs were within PCB. This multiple-MPC model was named as multiple-MPC model #1.

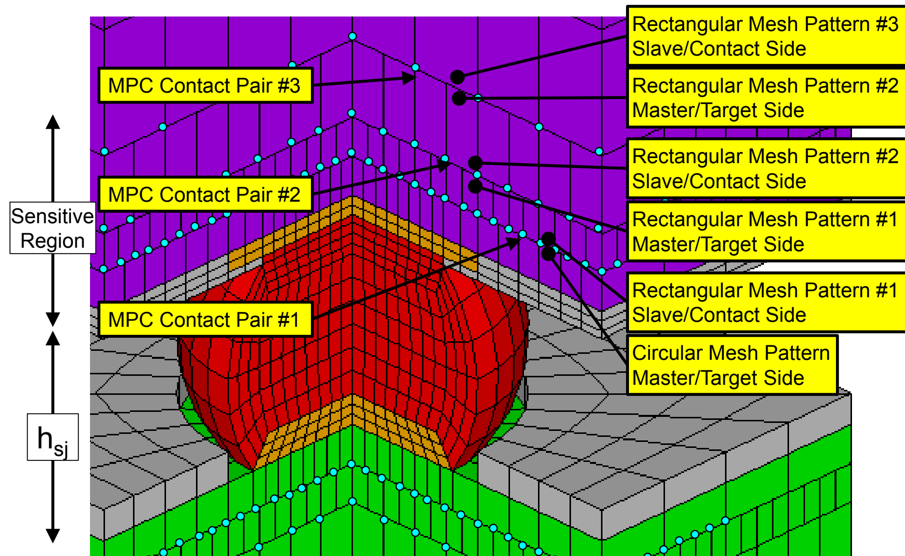

Figure 6.24 Cross-Sectional View of the Multiple-MPC Model #1

As listed in Table 6.6, the model size of multiple-MPC model #1 reduced to 14,726 elements, which was less than a half of the single-MPC model (32,705 elements). Simulation speed shown in Figure 6.25 also rendered an efficient simulation was achieved via multiple-MPC approach. In addition, the differences of ΔW_{avg} values for different unit models were less than 0.2%. Thus, multiple-MPC yielded a good solation quality and consumed a very close time as conventional model. In the following study, multiple-MPC approach would be applied on package assembly model; an further improvement on simulation efficiency for package model was developed.

Table 6.6 Simulation Results for Various Unit Models

Modeling Strategy	Conventional Model	Fan-Out Model	Single-MPC Model	Multiple-MPC Model #1
C/R	Continuous Meshing	Continuous Meshing	0.44	0.44
Total Elements	23,104	9,408	32,705	14,726
Elements for MPC	-	-	2,978	8,352
ΔW_{avg} ($\times 10^6$ J/m^3)	0.0926	0.0924	0.0924	0.0925
Diff (%)	0	0	0.2	0.2
Normalized Comp Time	2.4X	1X	5X	2.3X

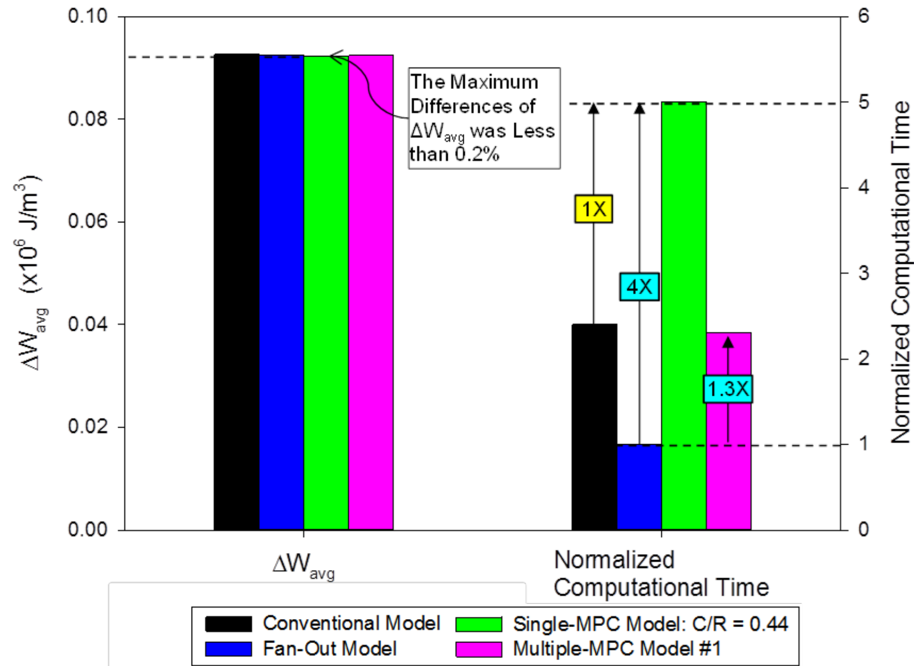

Figure 6.25 Comparisons of Simulation Results and Computational Times for Different Models

6.11 The Use of Multiple-MPC Contact Pairs (Full Assembly Quarter Model)

As multiple-MPC approach performed a better simulation speed and a high quality solution, another multiple-MPC model utilizing an increased C/R ratio as multiple-MPC model #2 was presented. New multiple-MPC model #2 used a larger C/R = 1.75 for bonding core region (including circular mesh pattern of solder joints, copper pads, part of BT and PCB as shown in Figure 6.26) and rectangular mesh pattern #1. The regions of rectangular mesh pattern were partitioned based on the boundaries of components, and contacting elements ratio within a material was a factor of 4. Unlike MPC model #1, array-copy operation of unit model is not used for MPC model #2. Core region was meshed with a fine mesh while coarser mesh used for the noninterest region. As true geometrical dimensions of components of a package assembly were taken into consideration, the dimensions of component may be needed to justify for the modeling

convenience while using continuous meshing approaches. The boundaries of silicon die, for example, were not aligned well at the center or edge of a unit model; then the dimensions of the die have to be scaled while using conventional modeling approach or array-copy model. This improved MPC modeling approach increases the modeling flexibility and takes the most advantage of MPC technique while FE modeling for different components can be separated.

Note that the vertical thickness of three MPC contact pairs on each side of multiple-MPC model #2 was controlled to less than a height of the solder joint, even though the thickness of PCB/BT substrate was greater than the height of solder joint in the example model.

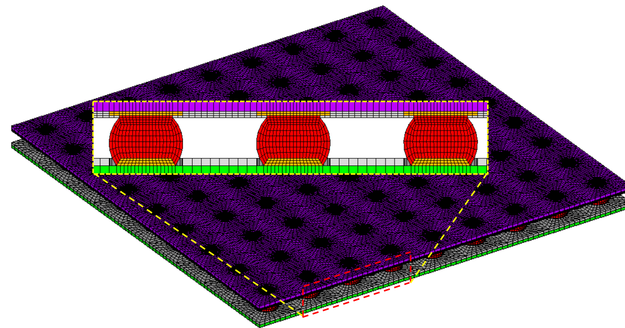

(a) Core/Interest Region of Multiple-MPC Model #2

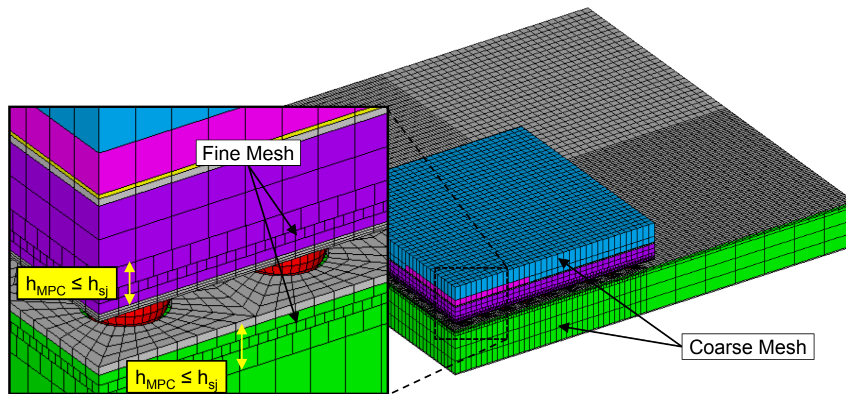

(b) Geometrical Partitions Based on Component Edges

Figure 6.26 Multiple-MPC Model #2

It can be seen from the top and side views of the package assemblies in Figure 6.27, multiple-MPC models presented lower mesh densities while the core region of all models shared the same fine mesh density. As a relaxed mesh density used on noninterest regions incorporated with fine mesh on interest region, model size was reduced to a reasonable range for saving more computer resources.

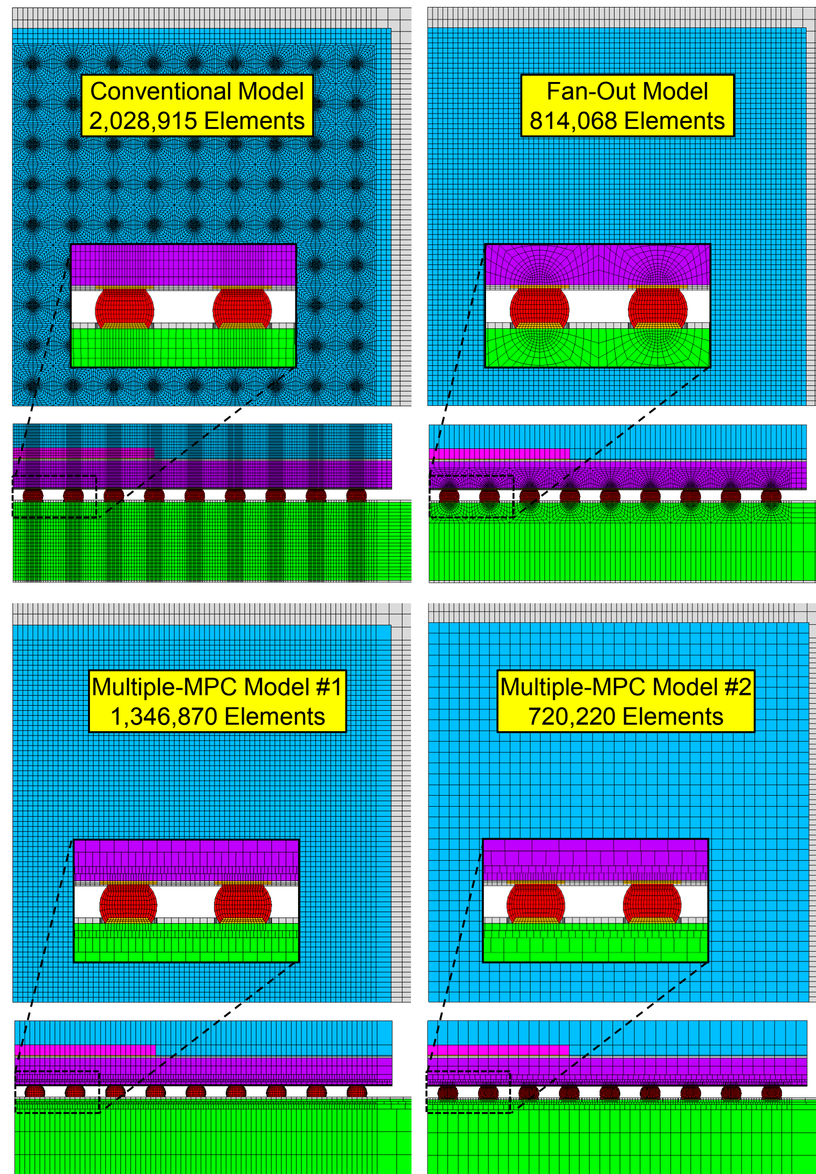

Figure 6.27 FE Models Built with Different Modeling Strategies

The simulation results for the solder joints locating along the diagonal of package assemblies were compared in Figure 6.28. Four different meshing models resulted in closed trend and magnitudes of ΔW_{avg} values; the maximum ΔW_{avg} value was founded at the top side of joint M12 for all models. Figure 6.29 and Table 6.7 compared the ΔW_{avg} values for joints M12 and computational times for different models. The maximum difference of simulation results for multi-MPC models was less than 3.5 % and also yielded in a good agreement compared to continuous meshing models. Multiple-MPC model #2 resulted in 0.64X and 0.1X computational time saving relative to conventional model and fan-out model, respectively. It stated the computational time can be reduced by adjusting the contacting element ratio of the multiple-MPC model.

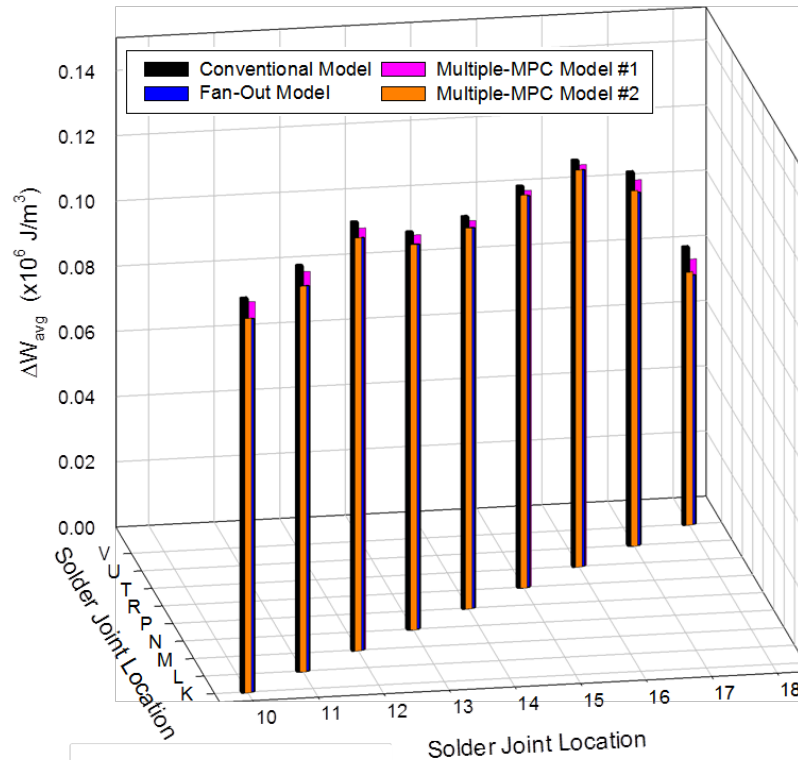

Figure 6.28 Dependence of the ΔW_{avg} Values on the Solder Joint Location for Different Modeling Approaches

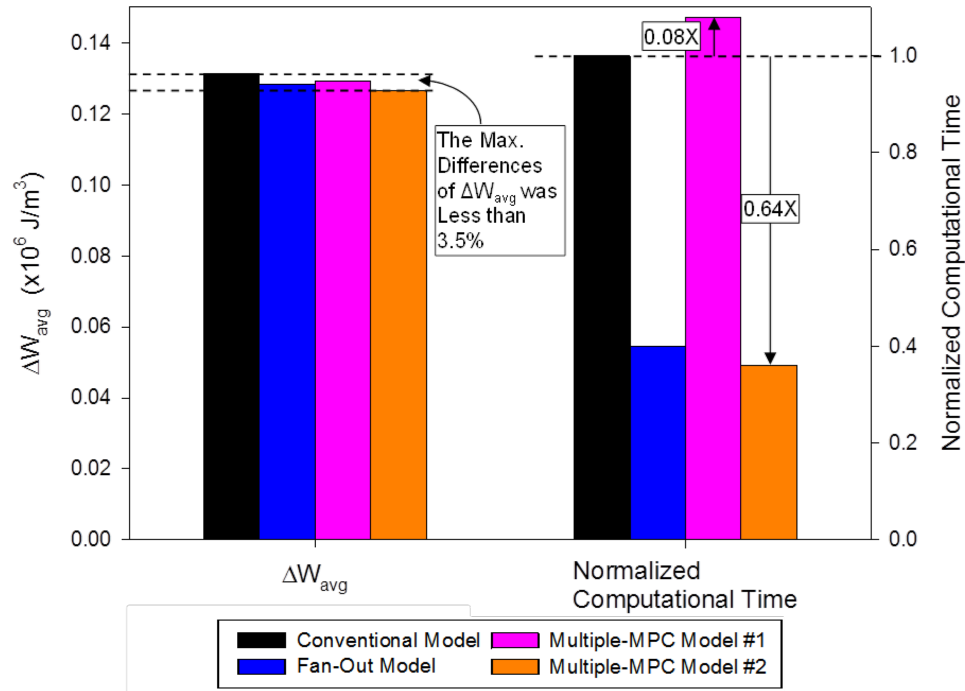

Figure 6.29 Simulation Results for Package Assembly Quarter Model with Different Modeling Strategies

Table 6.7 Summary of Comparisons for Multiple-MPC Package Assembly Quarter Models

Modeling Strategy	Conventional Model (Ref)	Fan-Out Model	Multi-MPC Model #1	Multi-MPC Model #2
C/R	Continuous Meshing	Continuous Meshing	0.44	1.75
Modeling Type	Array Copy	Array Copy	Array Copy	Array copy + Component Boundaries
No. of Elements	2,028,915	814,068	1,346,870	720,220
ΔW_{avg} ($\times 10^6$ J/m^3)	0.1313	0.1282	0.1293	0.1266
Diff (%)	0/2.3	2.4/0	1.5/0.8	3.5/1.2
Normalized Comp Time	1X	0.4X	1.08X	0.36X

The modeling flexibility, solution accuracy, and simulation efficiency have been achieved in multiple-MPC modeling approach. Another advantage of multiple-MPC

approach is the intuition of MPC setup. In this example, we always considered the contacting surface at the same side of copper pad, having stiffer material property, as the master/target side, even if using MPC approach #2 (the MPC within a material). It avoids assigning incorrectly master-slave relationship while only considers the element ratios between MPC contact pairs. One drawback of the multiple-MPC approach in this example is the simulation efficiency still has no significant improvement over the fan-out approach. Following study focused on the setups of master-slave (target-contact) relationship to investigate the effects of constraint setups.

6.12 Effect of Master-Slave Relationship on the Unit Model Results

In prior study, we considered the stiffer material side as master/target side to satisfy the assumption of contact algorithms, master/target can penetrates slave/contact surface. In order to study the effect of master-slave relationship on simulation result, the setup for contacting surfaces was exchanged; slave/contact side has been changed to at the same side of solder joint. MPC approach #3 (Figure 6.30) follows MPC approach #1, where MPC contact pair located at the interface between two different components, but the master-slave relationship setup has been updated. In a similar way, MPC approach #4 inherits MPC approach #2 with new contacting setup as shown in Figure 6.31.

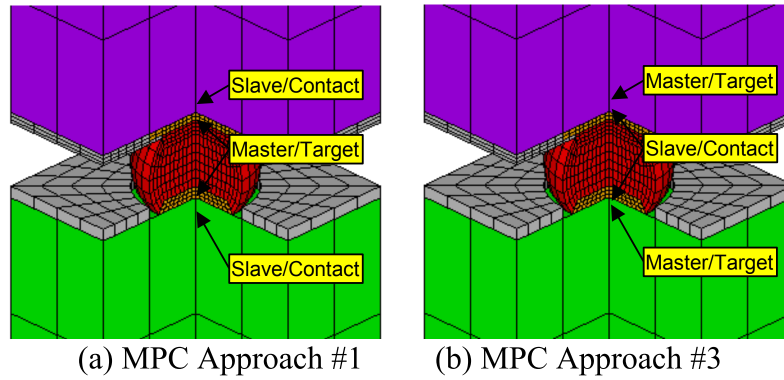

(a) MPC Approach #1 (b) MPC Approach #3

Figure 6.30 The Master-Slave Relationships
for MPC Approach #1 and MPC Approach #3

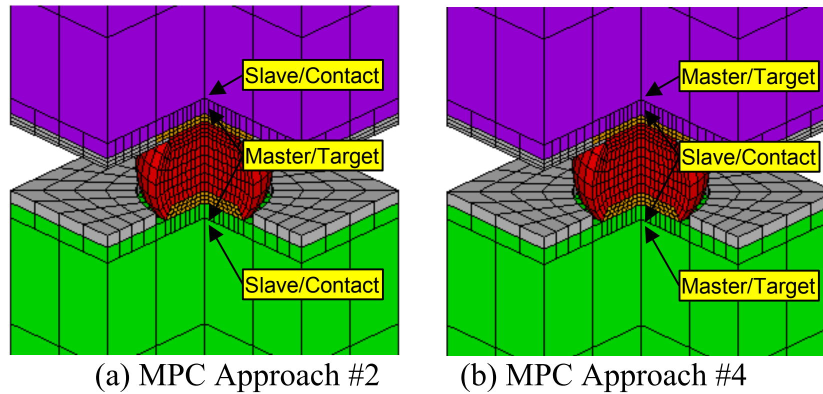

(a) MPC Approach #2 (b) MPC Approach #4

Figure 6.31 The Master-Slave Relationships
for MPC Approach #2 and MPC Approach #4

Figure 6.32 showed that no matter the setups of master-slave relationships, simulation results for MPC approaches #1 and #3 always resulted in poor solution qualities. The minimum difference of ΔW_{avg} was 6%, and it increased as C/R ratio increased due to both material stiffness and contacting mesh densities have significant effects on simulation results. MPC approach #3 may also introduces small penetration at the interface of two contacting material surfaces.

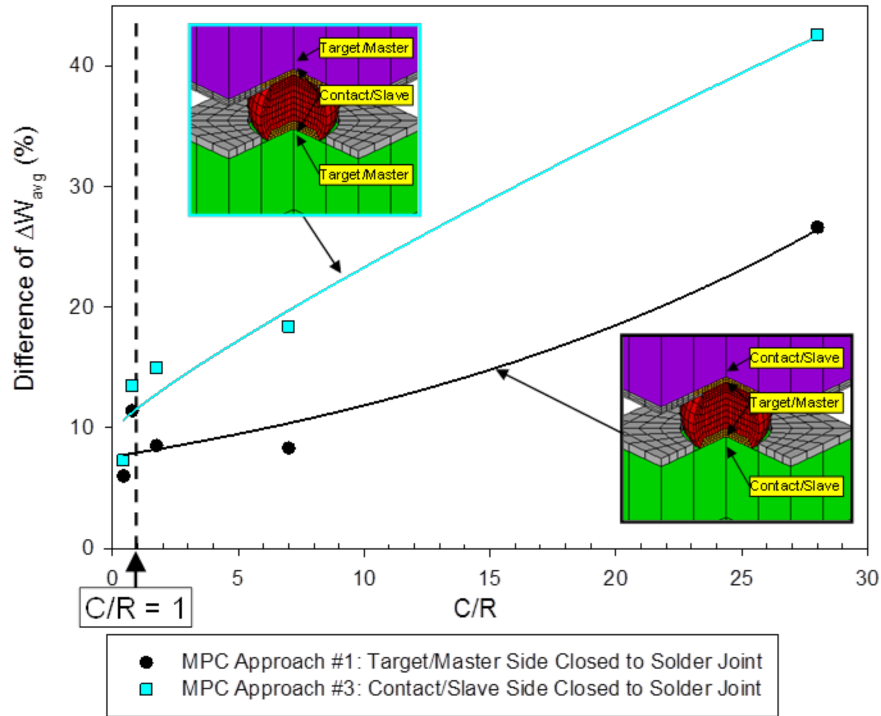

Figure 6.32 The Effects of C/R Ratio on the Percentage Error in ΔW_{avg} for MPC Approaches #1 and #3

MPC approach #4 yielded a better solution quality than approach #2 (Figure 6.33) since there is no material stiffness difference between MPC contact pair. As listed in Table 6.8, the difference of ΔW_{avg} for the C/R = 28 model is only 1.4 % compared to continuous meshing models while performed the fastest simulation time among all MPC approach #4 models. Thus, the setup of master-slave relationship less depends on mesh densities between MPC contact pair on this unit model study while considering high-density meshing side as slave/contact side and MPC contact pair locating within a material as MPC approach #2 were used.

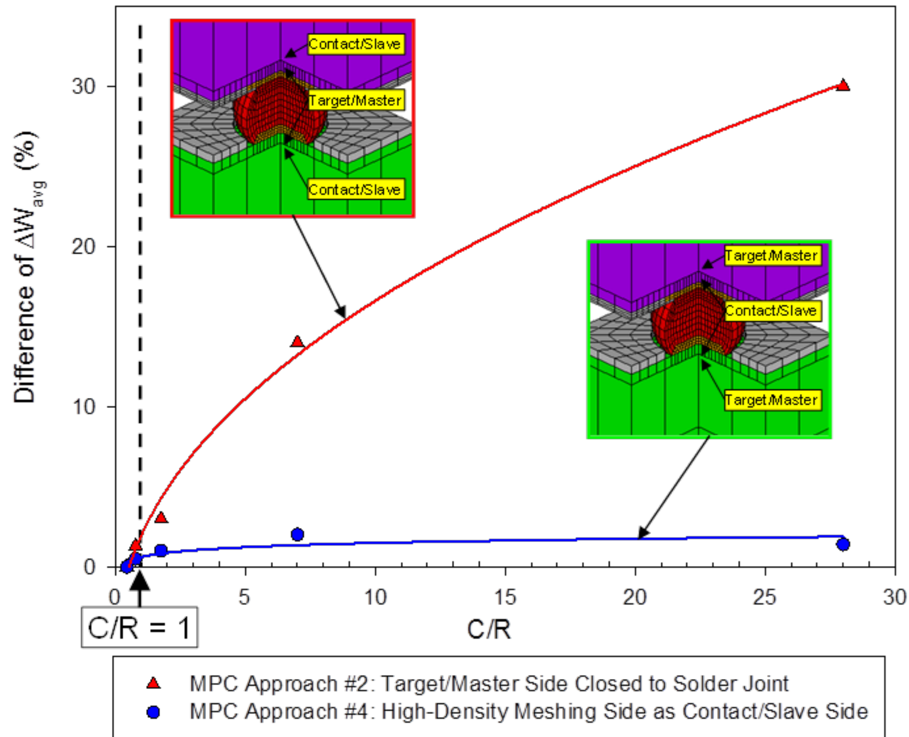

Figure 6.33 The Effects of C/R Ratio on the Percentage Error in ΔW_{avg} for MPC Approaches #2 and #4

Table 6.8 Summary of Results for the Unit Model Using MPC Approach #4 with Different C/R Ratios

Modeling Strategy	Conventional Model	Fan-Out Model	MPC APP #4	MPC APP #4	MPC APP #4	MPC APP #4	MPC APP #4
C/R	Continuous Meshing	Continuous Meshing	0.44	0.78	1.75	7	28
No. of Elements	23,104	9,408	32,706	18,146	10,370	7,074	6,146
ΔW_{avg} ($\times 10^6$ J/m^3)	0.0926	0.0924	0.0927	0.0929	0.0934	0.0942	0.0937
Diff (%)	0	0	0	0.5	1	2	1.4
Normalized Comp Time	2.1X	1X	5.4X	2.9X	1.8X	1.1X	0.9X

6.13 Effect of Master-Slave Relationship on Package Assembly Model

The promising effects for the unit model, modeling with C/R = 28 using MPC approach #4, on both efficiency and accuracy of simulation made it possible for an

economic package assembly analysis. As simulation results of package assembly models listed in Table 6.9, the model of approach #4 and C/R = 28 (named as MPC approach #4 model #1) resulted in a difference of 5.7 % of ΔW_{avg} at critical joint M12 comparing to continuous meshing package models. It is obviously greater than the expectation based on the unit model study. Hence, the effect of large mismatch in mesh density performed greater effects on package size simulation.

The improvement can be similar to the prior study of increasing the vertical height of the circular mesh pattern side from h = 0.25 h_{sj} to h = 0.5 h_{sj}. Another package model followed this approach, MPC approach #4 model #2, resulted in a reduced difference of 0.7 %. Due to the extended element-layers were extruded from the core side (high-density meshing region), the model size and simulation time increased as h increased; the efficiency was slightly lost but significantly improved simulation accuracy.

Table 6.9 Summary of Results for Different Proposed MPC-Based Quarter Package Assembly Models

Modeling Strategy	Conventional Model	Fan-Out Model	Multi-MPC Model #1	MPC APP #4 Model #1	MPC APP #4 Model #2	Multi-MPC APP #5
C/R	Continuous Meshing	Continuous Meshing	0.44	28	28	1.75
No. of Elements	2,028,915	814,068	1,346,870	511,785	647,037	656,042
ΔW_{avg} ($\times 10^6$ J/m^3)	0.1313	0.1282	0.1293	0.1355	0.1292	0.1255
Diff (%)	0	0	0.8	5.7	0.7	2.1
Normalized Comp Time	2.5X	1X	2.7X	0.7X	1.3X	0.8X

6.14 Effect of the Hybrid Use of Multiple-MPC and the Modified Master-Slave Relationship

An improved MPC modeling approach utilizing the hybrid use of multiple-MPC and modified master-slave relationship (named as MPC approach #5) was illustrated in Figure 6.34. Between the MPC considering updated master-slave relationship (MPC contact pair #2) and solder joint, another high-density element-layer where C/R = 1.75 forming MPC contact pair #1 was inserted for a better interpolation of the displacement field near solder array. Comparisons listed in Table 6.9 revealed the ΔW_{avg} and computational time for MPC approach #5 model were in between two MPC approach #4 models. Hence, this approach has the benefit of multiple-MPC model, keeps high quality solution, and also considering the updated master-slave relationship, great reductions of model size and simulation time.

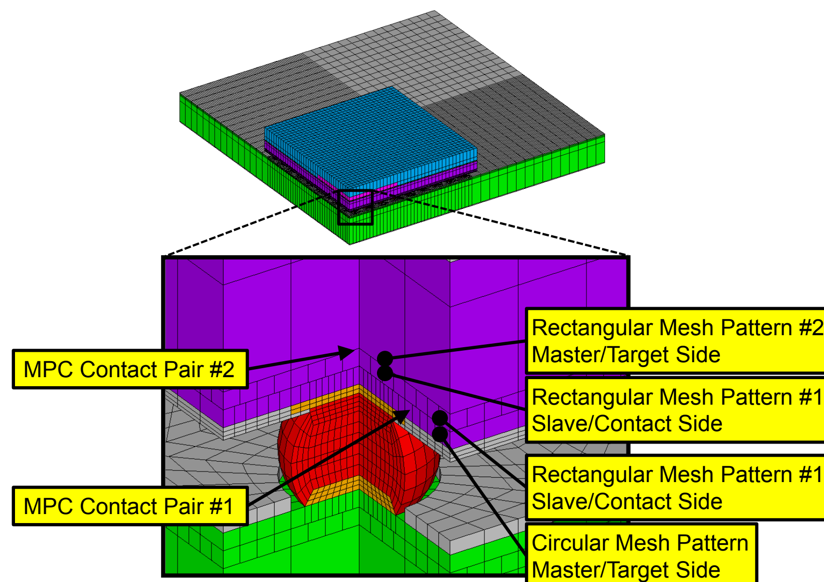

Figure 6.34 MPC Approach #5

6.15 Summary and Conclusions

Conventional MPC approaches used in literature may introduce impropriate MPC setup yielding in an inaccurate solution. Long term confusion of the location of MPC contact pair has been studied. Applied MPC directly at the interface of two different materials resulted in significant error comparing with continuous meshing model. The MPC locating within a material provides better solution quality due to no material property mismatch.

In this chapter, several different setups of MPC were studied and a flowchart for choosing best MPC-based approaches was summarized in Figure 6.35. It was found that solution quality is very sensitive to the proposed C/R ratio. High quality solution can be simulated by using C/R less than 1 while use MPC approach #2, considering close to solder joint side as master/target side . The C/R ratio between 1 and 2 achieves the balance of accuracy and efficiency of simulation. However, the use of single-MPC must be very careful about the setup of master-slave relationship. It is intuitive to consider copper pad as a stiffer material as the master/target side. The MPC approach #2 prevents the difference of material property, and the height of additional extruding element-layers can be easily controlled under a quarter height of solder joint. The solution quality for model using approach #2 can be significant improved while using C/R = 28 model by increasing the height of extruding element-layers to a one and half of solder joint height.

Multiple-MPC approach reduced mesh density layer-by-layer utilizing different contacting element ratios. It also avoids the confusion of MPC setups, only consider contacting side close to the stiffer material as master/target side. It has been proved the use of multiple-MPC approach can save great amount of simulation time comparing with

conventional model. Also, the span of multiple MPC contact pair can be limited to a small thickness within a component where no thick PCB/BT substrate was required.

The setup of master-slave relationship must consider the MPC location first. Simulation result showed no matter which master-slave relationship is, model of MPC locating at the interface between two different materials yields poor solution quality. MPC locating within a material, by contrast, has significant improvement while considering high mesh density side as slave/contact side. Although, large mismatch in mesh densities of contacting surfaces resulted in a difference of simulation results, increase extruding element-layers to a half of solder joint height can greatly reduce this difference.

The hybrid use of multiple-MPC and modified master-slave relationship as described in MPC approach #5 has the advantages of both approaches. Solution quality is easy to control by using dense element-layer in-between the MPC of modified master-slave relationship which reduces overall mesh density hugely. It was found to improve modeling flexibility, reduce difficulties with component connecting issues, and achieve a good balance between simulation costs and simulation accuracy.

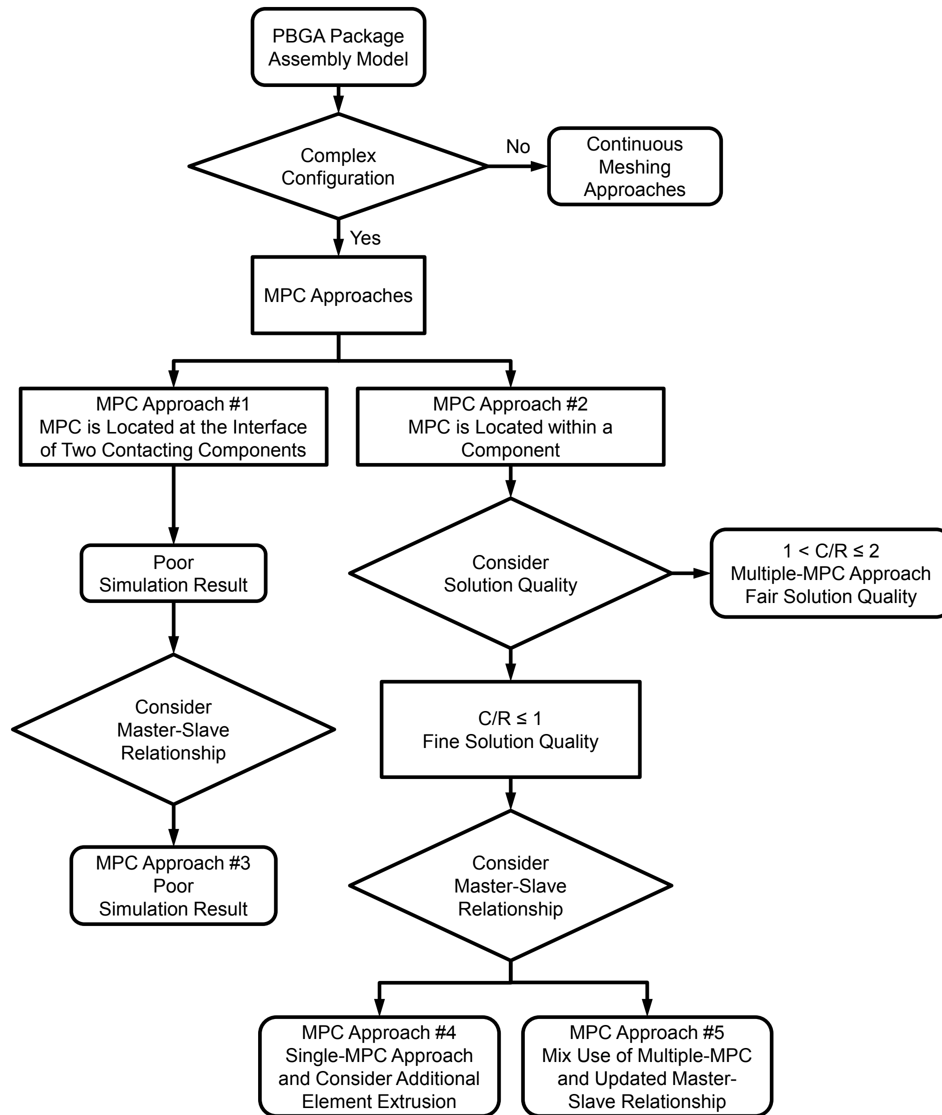

Figure 6.35 General Procedure for Choosing MPC-Based Approaches

CHAPTER 7
IMPROVED SUBMODELING FINITE ELEMENT SIMULATION STRATEGIES FOR PBGA PACKAGES SUBJECTED TO THERMAL CYCLING

7.1 Introduction

The development of electronic packaging tends to integrate high-density components and interconnections in a limited size assembly utilizing new designs, configurations, materials, and processes [226]. PBGA technology utilizes the bottom side area of a package, where solder joints have been deployed in an area or perimeter array for supporting more I/O's in the same package size, made it as a popular option in current electronic packaging area. The most commonly used pitches of solder joints for PBGA are 0.8, 1.0, and 1.27 mm which allow more interconnections over other packaging. However, a disadvantage of PBGA is solder joints may hide beneath another solder joint array after assembling to the PCB increases the difficulty of inspection and repair processes. These joints experience high stress/strain states subject to thermal-mechanical loading. Crack initials and propagates at the region of high accumulation of plastic strain/energy has arisen the reliability issue where any solder joint in area/perimeter array may failure during manufacture or in service.

The development of FEA allows people to better study the behaviors of solder joints of different configurations experiencing various loading conditions. Nonlinear FE problem, however, with a great number of nonlinear elements subjected to several loading cycles is still a hard task for one only have limited computer resources.

Assumptions and simplifications made for the FE model are not avoidable while consider a simulation involving 3D configuration of different components, high I/O counts, and nonlinear material properties.

Submodeling is a finite element based technique to study the local behavior which is relatively smaller than overall behavior of the entire model. Gustafsson et al. (Chapter 3.3.6) have summarized five commonly accepted FE models for studying the reliability of solder joint, which involve: (1) nonlinear slice model [165], (2) nonlinear global model with linear super elements [28], (3) linear global model with nonlinear submodel, (4) nonlinear global model and a nonlinear submodel, and (5) nonlinear global model with fine-meshing critical joint and a nonlinear local model. The first approach of nonlinear slice model utilizes only a diagonal slice of the assembly for analysis in order to reduce simulation costs. One of the drawbacks of this approach is the assumption of infinitely dimensions in the directions perpendicular (out-of-plane) to the slice planes. This results in an underestimation of the warpage of the package and overestimates the shear loading on the solder joints. The second approach is related to the technology of substructure which is not discussed in this paper. In the third approach, the global model is built using linear material properties only, whereas the local model includes nonlinear material properties. This assumption may have difficulty to identify the most critical joint using inelastic energy based failure criterion. The approaches (4) and (5) are most used in the literature; the difference is: refined meshes are used in the critical solder joints of the global model in the fifth method.

The FE problem involving path-dependent material property (such as Anand model) is sensitive to the load step size and the mesh quality [189]. The effects of these

factors, however, have not been studied completely in the literature [120] [184] [227] [228] [229] [230] [231]. Hence, the analysis solving by submodeling algorithms may not been dealt adequately in the stage of global model simulation for identifying the most critical joint. In additions, geometrical simplifications for global model using the assumptions of equivalent beam [181] [183] or volume equivalence [232] of solder joint may lack the ability to identify the critical joint correctly [184]. Thus, misinterpretation of the most critical joint may lead to underestimate or overestimate the magnitudes of inelastic strain or energy occurring failure mechanism.

In this chapter, the effects of mesh quality and load step size on the global and local models were presented. An improved minimum required vertical height of local model was developed. Then, the effects of geometrical simplification methods in the global model incorporating with Anand model and energy-based fatigue criteria were discussed. In additions, the effects of the hybrid use of different shapes of solder joints in a package model were studied. The proposed approaches achieve good reductions in computational times, better detailed modeling, and improved simulation accuracy.

7.2 Submodeling Technique

Submodeling is a FE technique used for obtaining more accurate and detailed solution in a specified small local region of the entire model (Figure 7.1). In submodeling, the behavior of the entire model, also called global model, is analyzed at first. A coarse mesh is preferred for global model by the reason of saving computational costs. Displacements calculated on the cut-boundary (the boundary of the local model which represents a cut through the global model) of the global model are interpolated and

applied as boundary conditions for local model. According to Saint-Venant's principle, the cut boundaries of the local model should far enough away from the stress concentration. Then, a local model meshed with a refined mesh is simulated with the interpolated boundary conditions. The steps required in a submodeling analysis are given as follows [207]:

- Create global model and obtain solution.
- Define cut boundaries and create local model.
- Select nodes on the cut boundaries and perform the interpolations of displacement and temperature fields along the cut boundaries.
- Output the cut boundary conditions.
- Resume the local model and read cut boundary condition files.
- Apply remaining loads (body loads or conditions along external boundaries).
- Obtain local model solution.
- Repeat the steps from cut boundary interpolation to local solution for each load step.

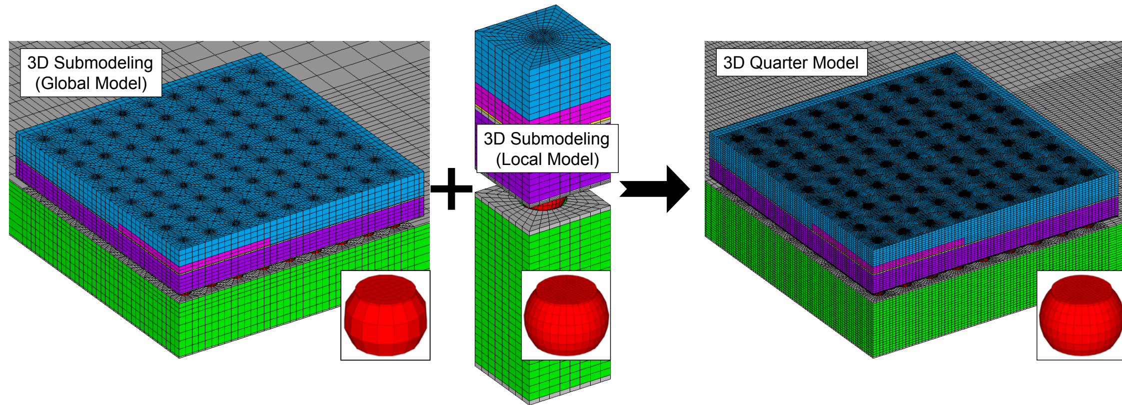

Figure 7.1 Scheme of Submodeling Technique

7.3 Finite Element Modeling and Simulations

Finite element based reliability predictions of fatigue life for solder joints undergoing accelerated thermal cycling testing are based on different types of constitutive equations (e.g. Anand model) describing the material behavior of solder, and failure criteria that describe the propagation of cracks. Simulation with highly nonlinear behavior and high-density mesh are computer-intensive slowing down overall computational time. Therefore, mesh generation is one of the most important steps in FE analysis since the decision made at this point has far-reaching effect on entire simulation. Two types of meshing generation methods are widely used in commercial FE packages including free and mapped meshing methods. Compared to free meshing, mapped meshing has regular pattern, with obvious rows of elements, and contains only hexahedron elements in a volume model. In this study, all FE models were meshed with hexahedron element using mapped meshing method for the purpose of obtaining high quality simulation results.

An example model for a PBGA configuration composed of a chip (center red box in Figure 7.2) and an area array of 100 solder joints is shown in Figure 7.2. Dimensions

of the example package are listed in Table 7.1. The solder joint pitch in the model was 0.8 mm. Due to the symmetry of the example package, a one quarter model with symmetric boundary conditions was taken for demonstration (Figure 7.3). Note that the PCB size for our example has been shown to have negligible influence on final results; thus, a reduced size of the PCB was used for an efficient analysis. The material properties, loading condition, and fatigue model used in this chapter can be found in Chapter 4.2.

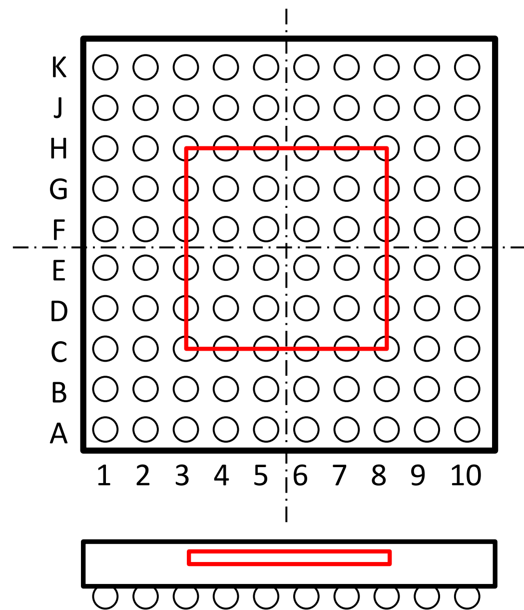

Figure 7.2 Engineering Drawing of Example 8 × 8 PBGA Package Assembly

Table 7.1 Dimensions of Example PBGA Assembly

Component	Dimensions (mm^2)
PCB	8 × 8
Solder Mask	8 × 8
BT Laminate	8 × 8
Die Attach	4 × 4
Silicon	4 × 4
Mold Compound	8 × 8

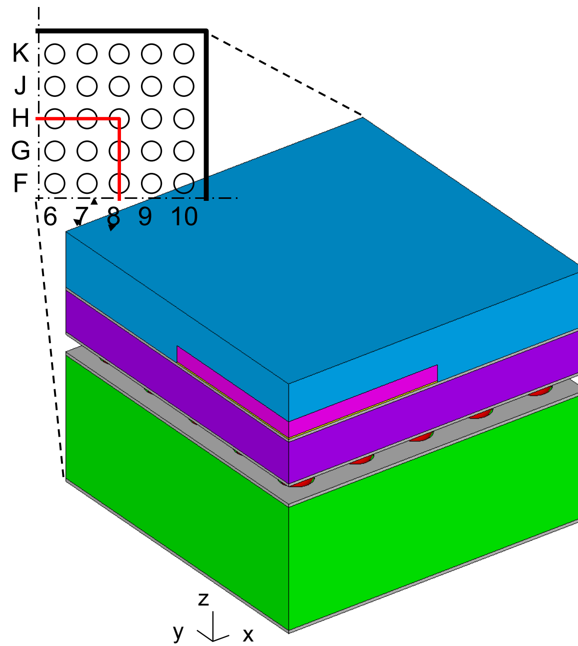

Figure 7.3 Quarter Assembly Model

The effects of the mesh quality and the load step size on simulation results have been studied by the convergence study of unit model and shown in Figure 7.4 (CHAPTER 5 and [189]). Restricted to the limited computer resources, it is not possible to build a quarter package assembly from the model set having converged solution (mesh quality of AR 4 and load steps of LS 100, each duration of a thermal cycle was divided evenly into 100 divisions). One option is choosing the model set having the closest to the converged solution for building the package assembly model as a reference; thus, the package model was built using mesh quality AR 5 model and simulated with load step LS 5 (each duration of a thermal cycle was divided evenly into five divisions; totally 106 load steps were used in five thermal cycles).

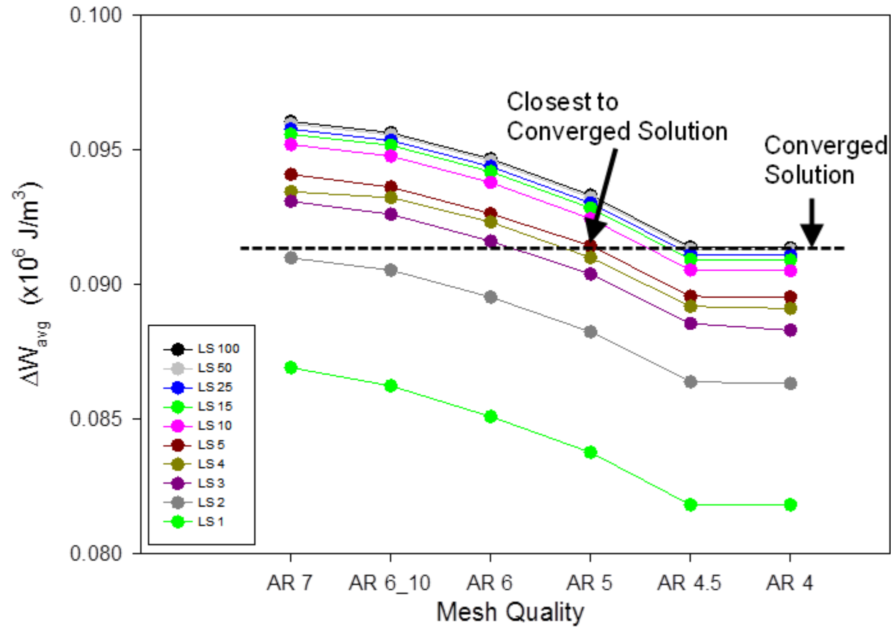

Figure 7.4 The Effects of Mesh Quality and Load Step Size on Simulation Results for Conventional Meshing Models

7.4 Effect of Mesh Quality

In our prior study, the simulation results were sensitive to mesh quality in a controlled load step size. The quarter assembly model (global model) was meshed using four different maximum aspect ratios of 5 (finest meshing), 10, 20, and 25 (coarsest meshing); and the total number of elements dramatically increased as the mesh quality increased as shown in Figure 7.5 and Table 7.2. It should be noted that the large aspect ratio elements were located at the thin regions (such as the regions of SMD and die attach); most regions of FE meshes were under a factor 4.

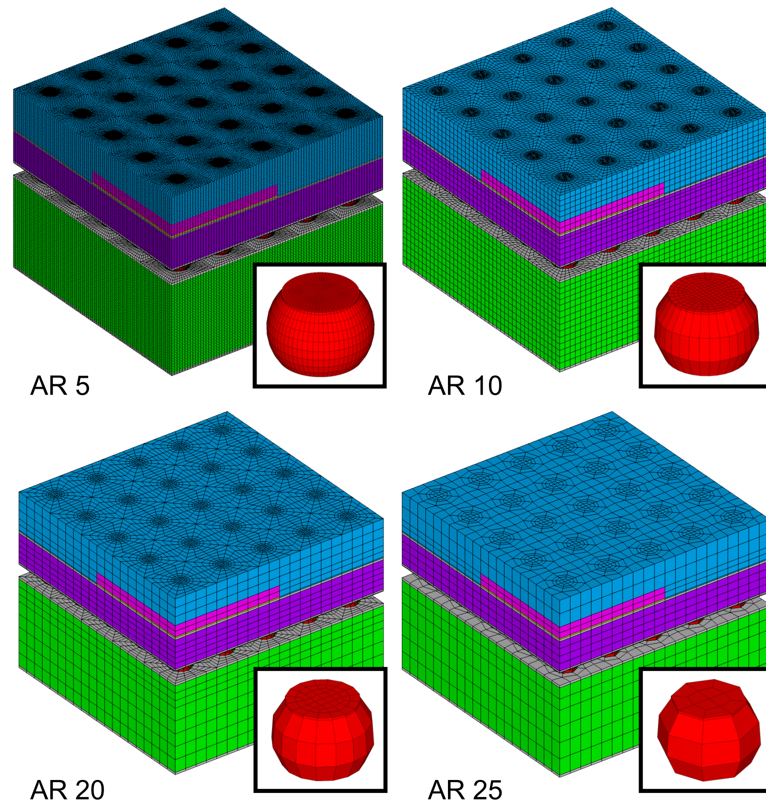

Figure 7.5 Global Models Meshed with Four Different Aspect Ratios

Table 7.2 Simulation Results for Global and Local Models

Mesh Quality	AR 5 (Finest)	AR 10 (Fair)	AR 20 (Coarse)	AR 25 (Coarsest)
Load Step	LS 5	LS 5	LS 5	LS 5
Global Model				
No. of Total Elements	3,651,200	311,200	76,800	21,600
No. of Nonlinear Elements	236,800	26,400	7,200	2,100
Sim. Result: The 5th ΔW_{avg} ($\times 10^6$ J/m^3)	0.1365	0.1523	0.1537	0.1616
Error (%)	-	11.6	12.6	18.4
Normalized Comp. Time	400X	16.7X	5.7X	1X

Local Model (Solder Joint G7)				
Sim. Result: The 5th ΔW_{avg} ($\times 10^6$ J/m^3)	0.1365	0.1332	0.1332	0.1340
Error (%)	-	2.4	2.4	1.8
Normalized Comp. Time	75X	3.9X	1.9X	1X

7.4.1 Simulation Results for Different Global Models

All different global models identified the joints G7 as the most critical joint, where large inelastic strain energy density accumulated at the top region of the joint (Figure 7.6). Simulation results listed in Table 7.2 showed the error of the ΔW_{avg} values increased as mesh quality decreased (max aspect ratio increased). However, the normalized computational time shown in Figure 7.7 indicated up to 400X saving while utilizing the coarsest mesh model AR 25.

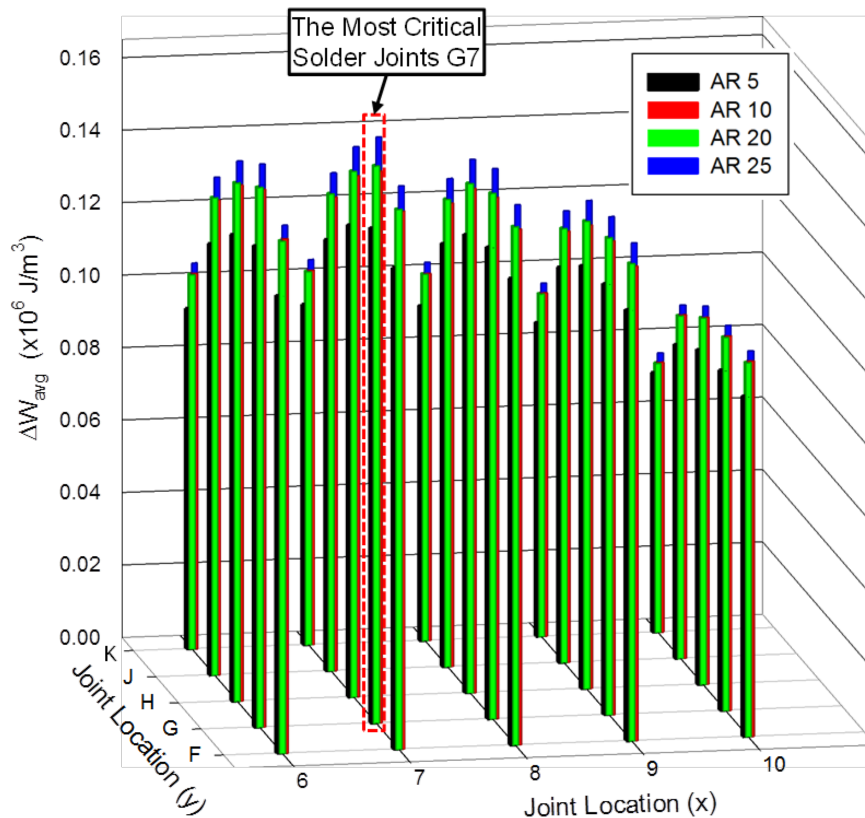

Figure 7.6 Simulation Results of ΔW_{avg} Values for Solder Joint Array of the Prepared Global Models

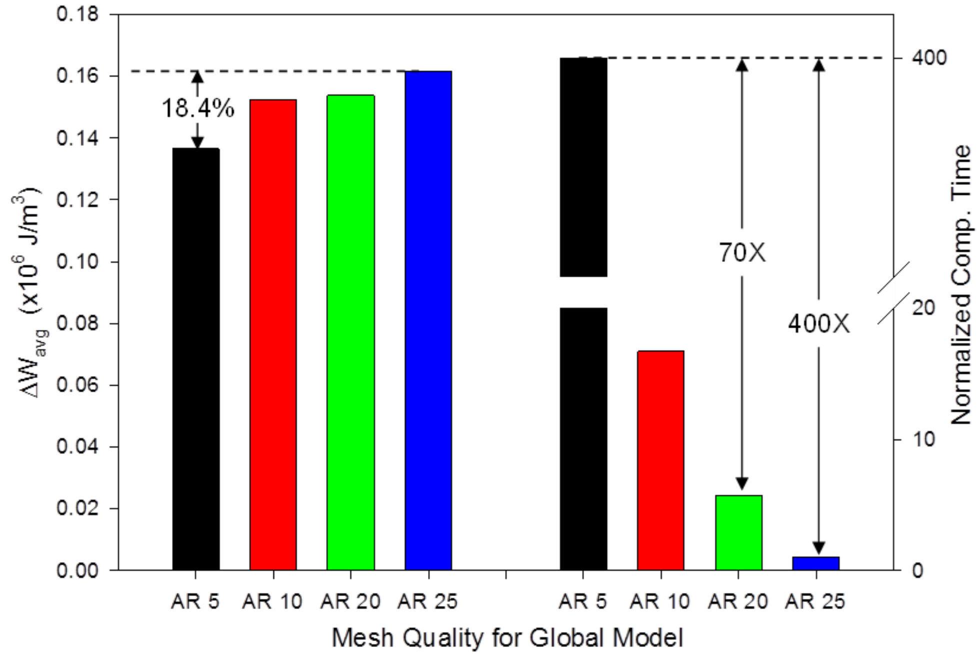

Figure 7.7 Comparisons of Simulation Results and Normalized Computational Time for the Prepared Global Models

Next, we examined the global responses of the prepared global models. The deflections at points P's, located at the far corner of the top face of mold compound along the diagonal direction, have very small differences after five cycles as shown in Figure 7.8. The maximum difference of vertical displacement, found at point P6, was only 0.75%. Also, the maximum difference of vertical displacements of point Q's, located at the top side of the critical joint, was less than 0.78% (Figure 7.9).

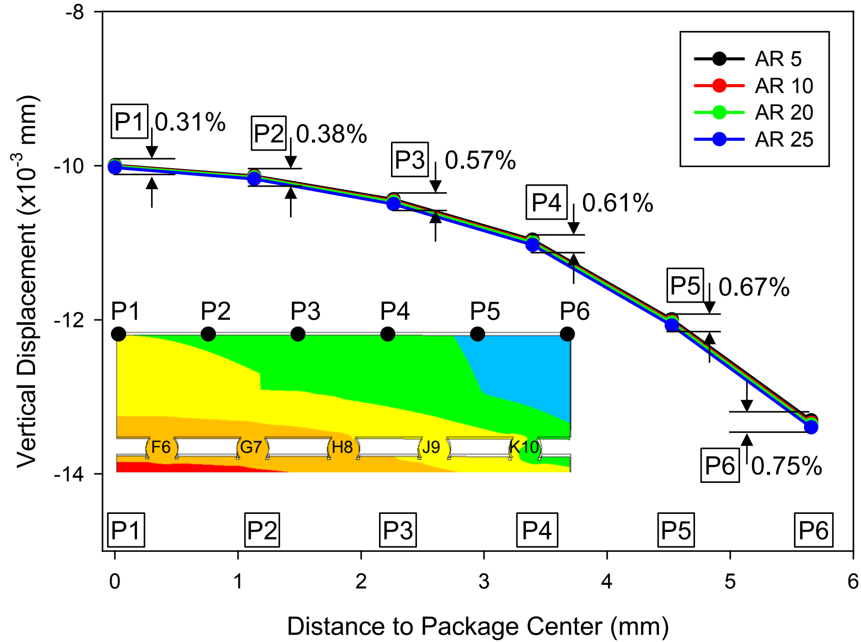

Figure 7.8 Vertical Displacements of Point P's for the Prepared Global Models

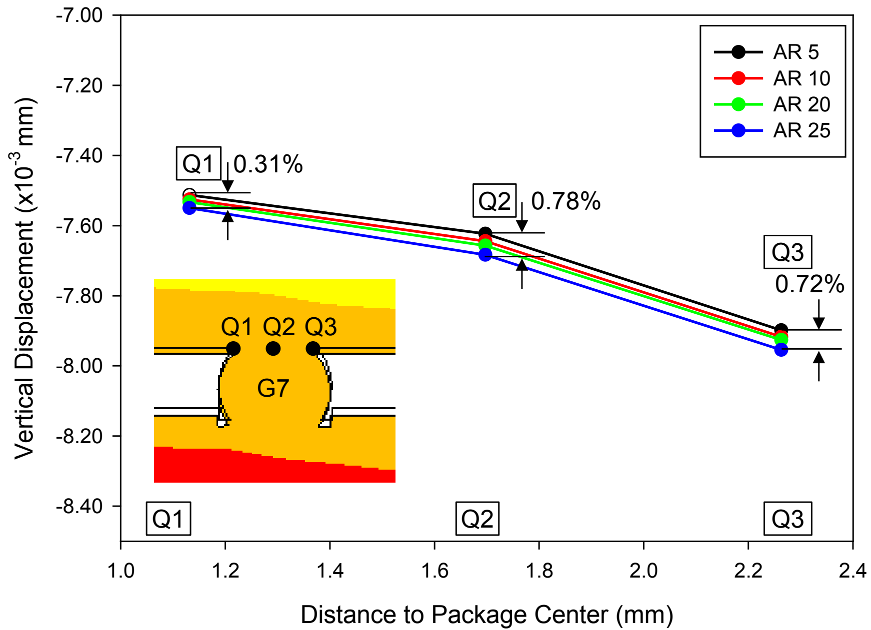

Figure 7.9 Vertical Displacements of Point Q's for the Prepared Global Models

However, as shown in Figure 7.10, coarse meshing models overestimated PLWK; larger portion of high PLWK can be observed in the global model AR 25. It also can be

seen in Figure 7.11, historic curves of volume-weighted averaging PLWK for coarser meshing models always higher than refined meshing model (AR 5). Thus, an error of the ΔW_{avg} value up to 18.4% can be expected. These phonemes yielded room for improvement by using submodeling technique; global models captured very close global responses compared to converged model, but the differences in local responses have negligible effects to the global responses.

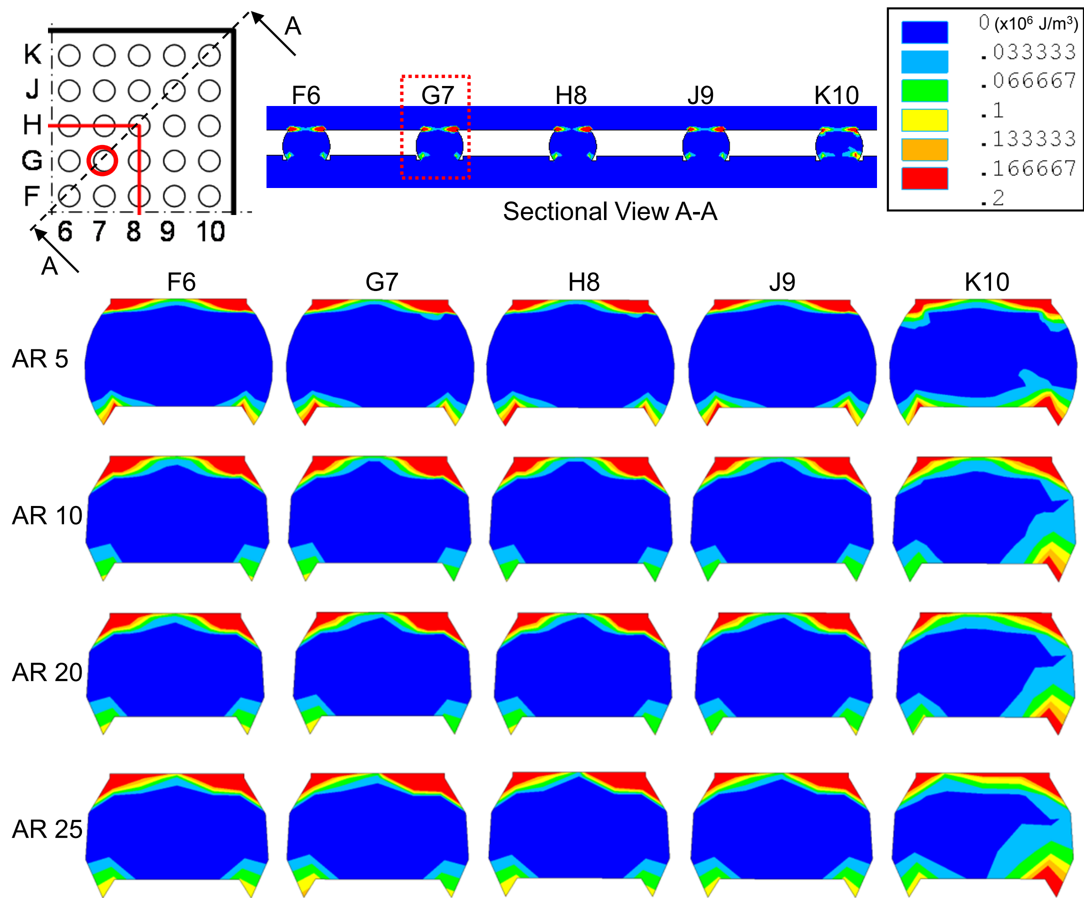

Figure 7.10 Contour Plots of PLWK after Five Cycles for the Prepared Global Models

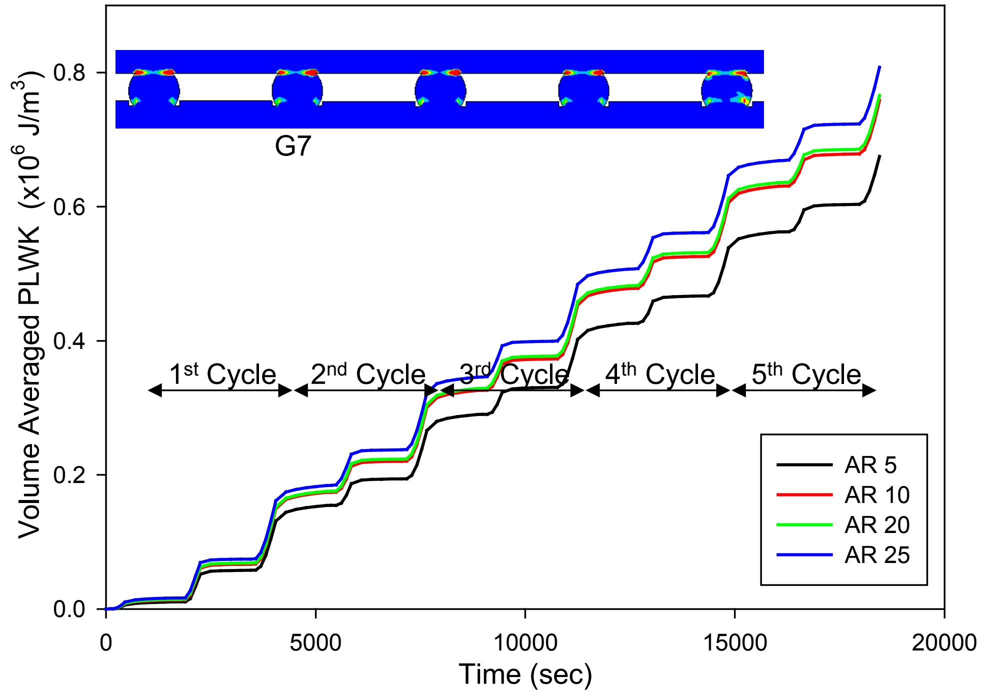

Figure 7.11 History Curves of Volume-Weighted Averaging PLWK for the Prepared Global Models

7.4.2 Simulation Results for Local Models

In the submodeling study, the cut-boundaries were defined along the perimeter sides of the unit model containing the critical joint G7. Then, the displacement fields of the cut-boundaries in accordance with the load steps were interpolated from three non-converged global models into the local models, meshed with the finest mesh quality AR 5 (maximum aspect ratio of 5). As shown in Figure 7.12 and Figure 7.13, the simulation results of volume averaged PLWK curves and ΔW_{avg} values have fair good agreements between different global-local model sets. In Figure 7.13, it can be observed that the overall computational time (combined global and local simulations) dramatically reduced and still kept high accurate results.

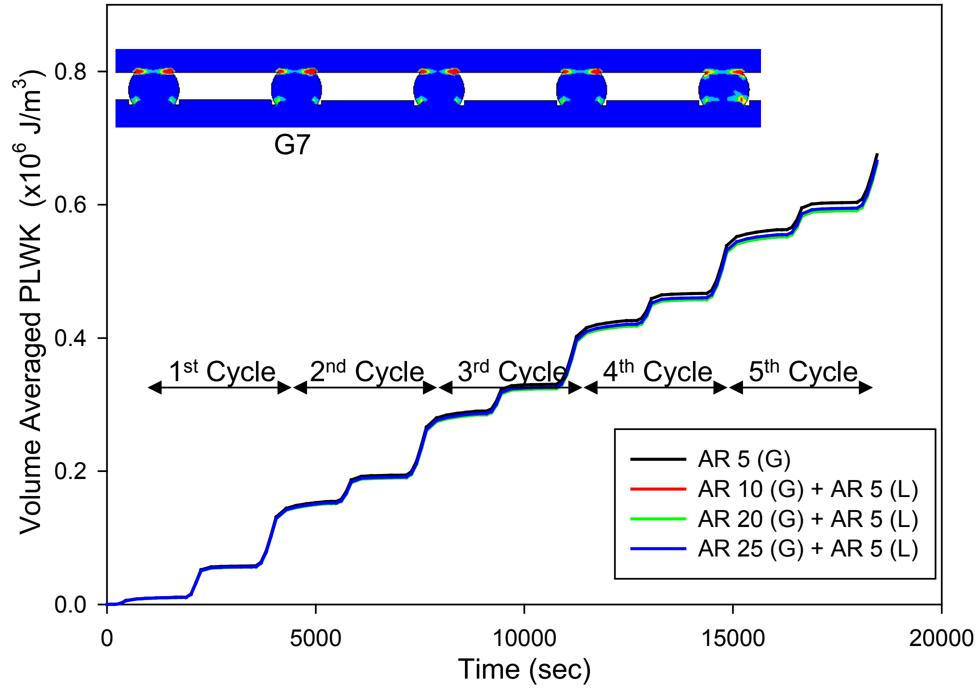

Figure 7.12 History Curves of Volume-Weighted Averaging PLWK for Local Models

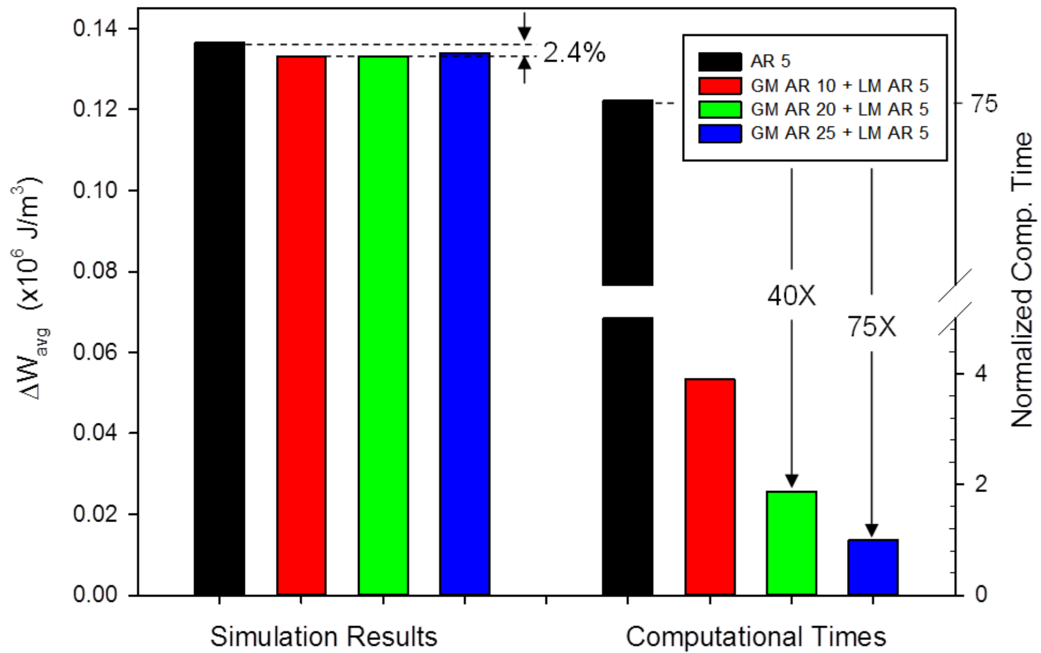

Figure 7.13 Simulation Results and Normalized Computational Time for Different Global-Local Model Sets

Here, the simulation times of the local models were greater than times for all non-converged global models. To improve the simulation efficiency, one can consider increasing the load step size, minimizing the volumetric size of the local model, and simplifying the geometric shape of solder joint in global model.

7.5 Effect of Load Step Size

Here, two load step sets (LS 5 and LS 2) were used as loading conditions for the global model meshing with AR 10. After the processes of interpolating simulation results of global models to local models (built with mesh quality of AR 5), Figure 7.14 showed the solution qualities for both global and local solutions were sensitive to load step sizes. As the convergence study of unit model (shown in Figure 7.4) indicated that the simulation using load step LS 2 yielded a poorer result than using LS 5 for AR 5 model, simulation set of local model AR 5 + load step LS 2 resulted in the same poor trend.

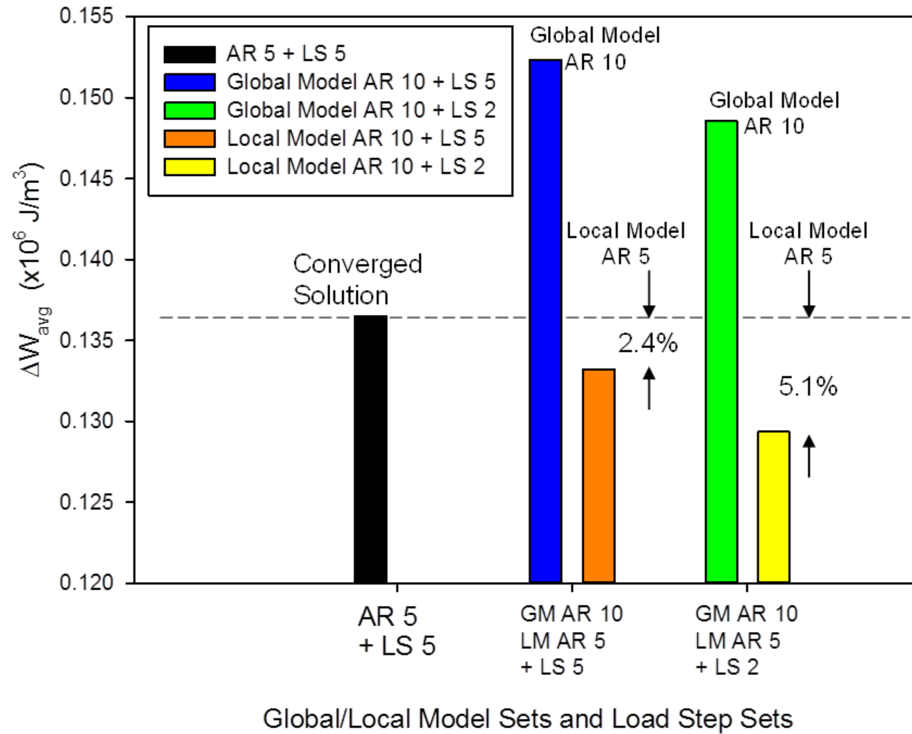

Figure 7.14 Simulation Results of ΔW_{avg} Values for Global-Local Model Sets Simulated with Different Load Step Sizes

7.6 Determine the Minimum Required Volumetric Size of Local Model

In the global-local simulation, the computational time for local model was greater than global model, especially for the global model built with rather coarse mesh (the max aspect ratio greater than 10). An approach to investigate the minimum required volumetric size of local model and still maintain the quality of solution is described as follow. Six different heights of vertical cut boundaries (h_{loc}) were examined here, they are 0h, 0.1h, 0.5h, 0.75h, 0.9h, and 1.0h where h is the height of solder joint as shown in Figure 7.15.

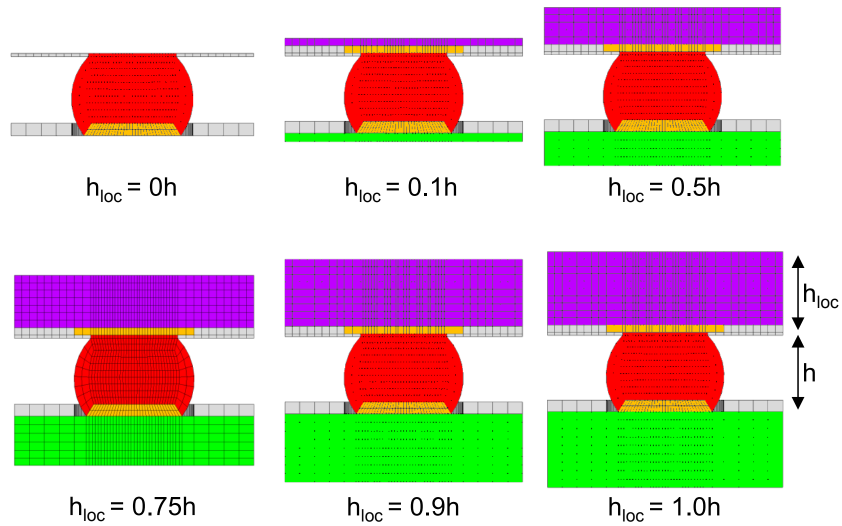

Figure 7.15 Six Different Heights for the Vertical Cut-Boundaries of Local Model

As shown in Figure 7.16, the local modes with different vertical height were simulated with three global models. Simulation results showed all solutions converged while $h_{loc} \geq 0.5$ h and resulted in good agreements (errors were less than 3%) with converged solution. Also, great reductions in computational times were presented as compared to the unit model with the full thickness of the package assembly. It is recommended that for the balance between efficiency and accuracy for local simulation, the minimum height of local model is suggested to equivalent to 0.5 h.

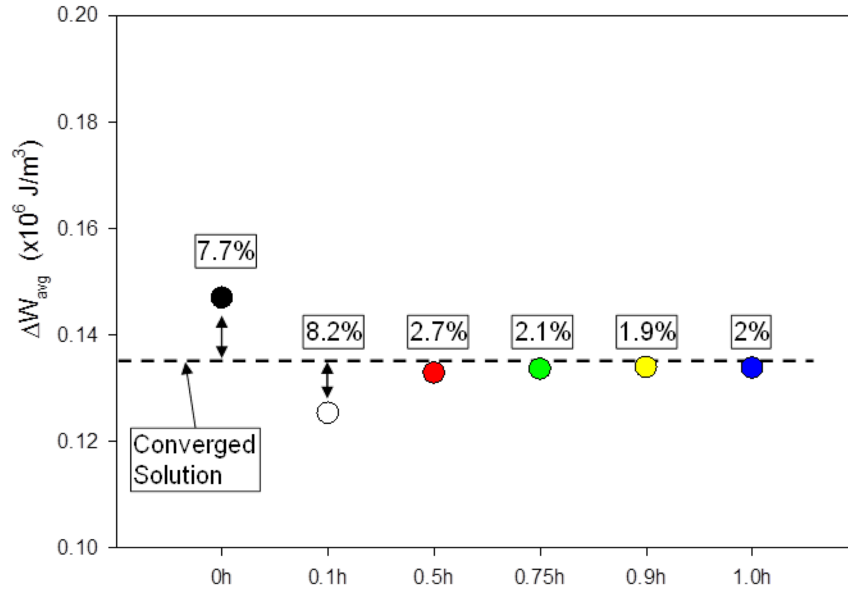

(a) Global Model AR10 + Local Model AR 5

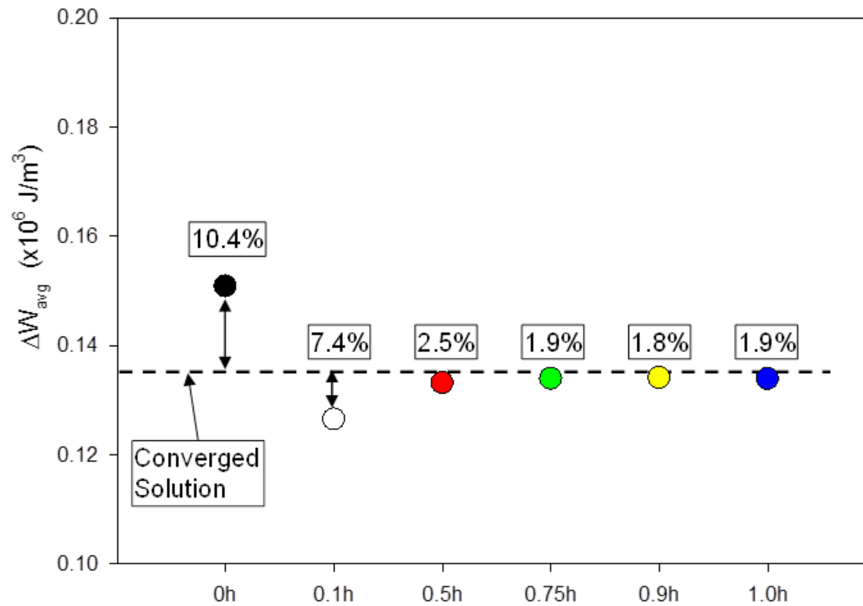

(b) Global Model AR20 + Local Model AR 5

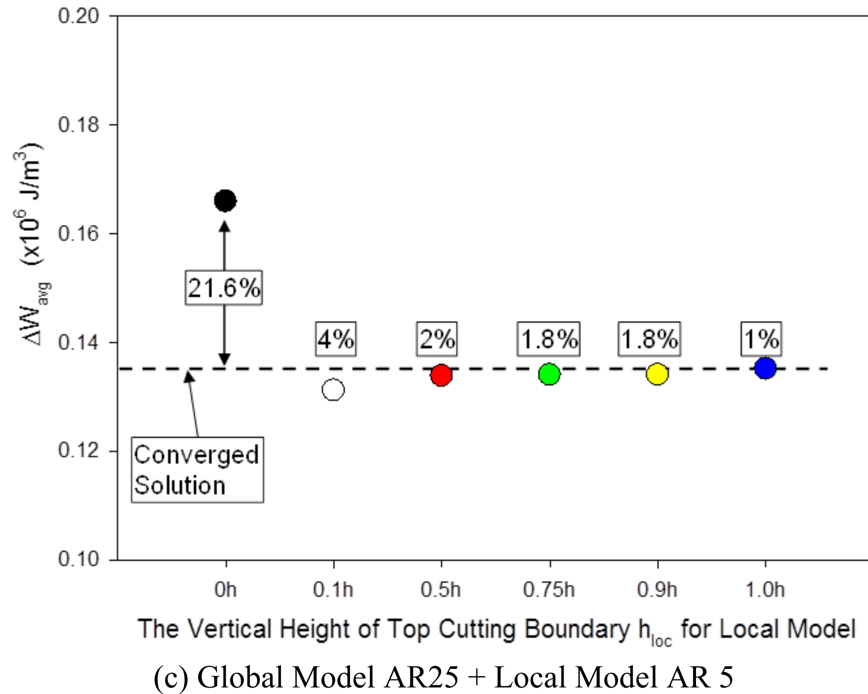

(c) Global Model AR25 + Local Model AR 5

Figure 7.16 Simulation Results of ΔW_{avg} Values for Local Models with Different Vertical Heights

7.7 Effect of Simplified Geometry Shapes for the Solder Joints in the Global Model

In the simplification of global model, the solder joints and copper pads were modified as beam, cylinder (Figure 7.17), or brick shapes (Figure 7.18) [99] [175] [232] [233]. Since the Anand model is not supported for beam element [207], this study focused on the geometrical simplification for solder joint with these two shapes.

After simplified global models were made, the mesh densities reduced dramatically and made simulations even more efficient. In the analyses of local models (AR 5 is the unit model built with the maximum aspect ratio 5 and AR 5* is a simplified model where its extruding vertical height h_{loc} = 0.5 h), it can be seen that although the simulation results for the simplified global models were diverged, the displacement interpolations at the cut boundaries were still accurate.

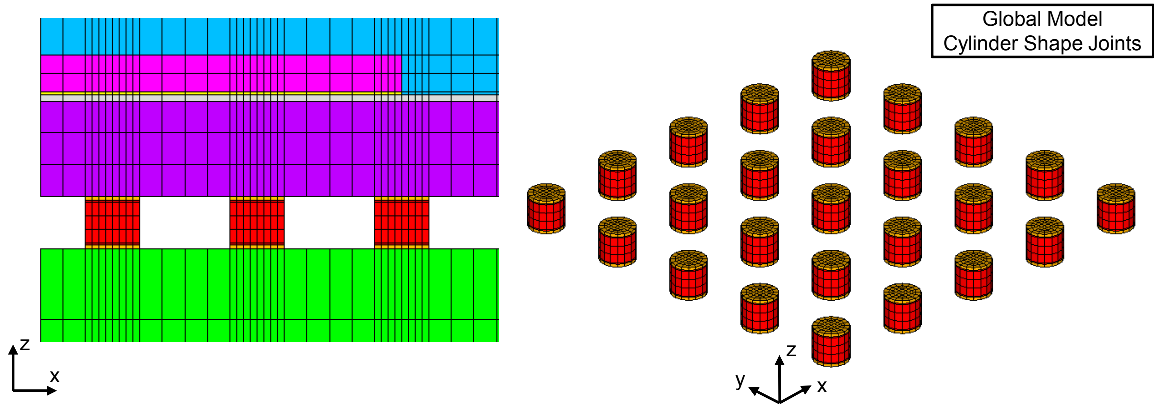

Figure 7.17 Simplified Geometry Shapes for Solder Joints in the Global Model, Cylinder Shape

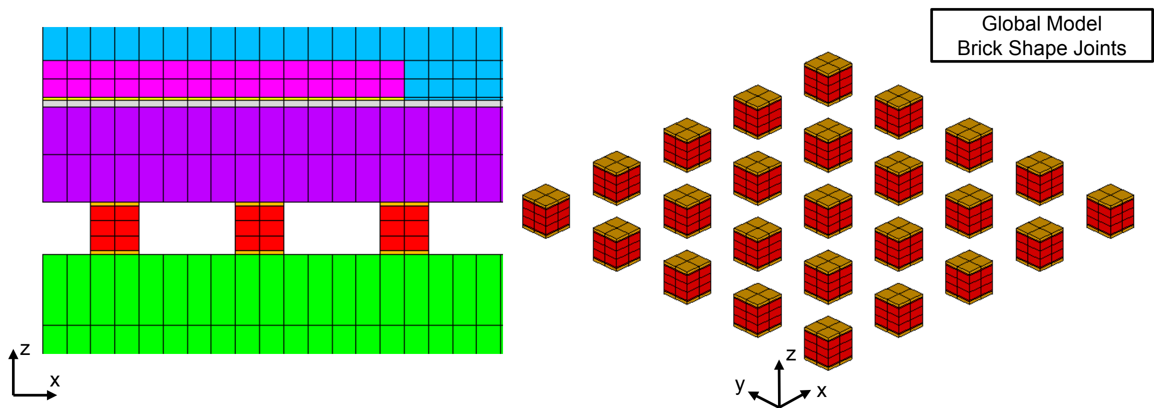

Figure 7.18 Simplified Geometry Shapes for Solder Joints in the Global Model, Brick Shape

The brick shape joint achieved mesh continuity without using other advanced FE techniques [193] and also reduced the difficulty of FE modeling due to the geometrical shapes of many other components in an electronic package assembly are typically in brick/rectangular shapes and provided more efficient simulation while coarse meshing model can be used. The contact areas, locating at the top side of the solder joints between solder joint and copper pad, for simplified global models and original global model shared the same area size and thickness. Thus, the volumes used for ΔW_{avg}

calculation of global models were identical. In the simulation results for global models, the magnitudes and distributions of PLWK (Figure 7.19 and Figure 7.20) were overestimated for the model with brick shape joints since brick shape joint has sharper corner (right angle, where stress concentration may occurred) compared to cylinder shape joint. Thus, caution must be taken while using simplified geometry shapes for the solder joints in the global model.

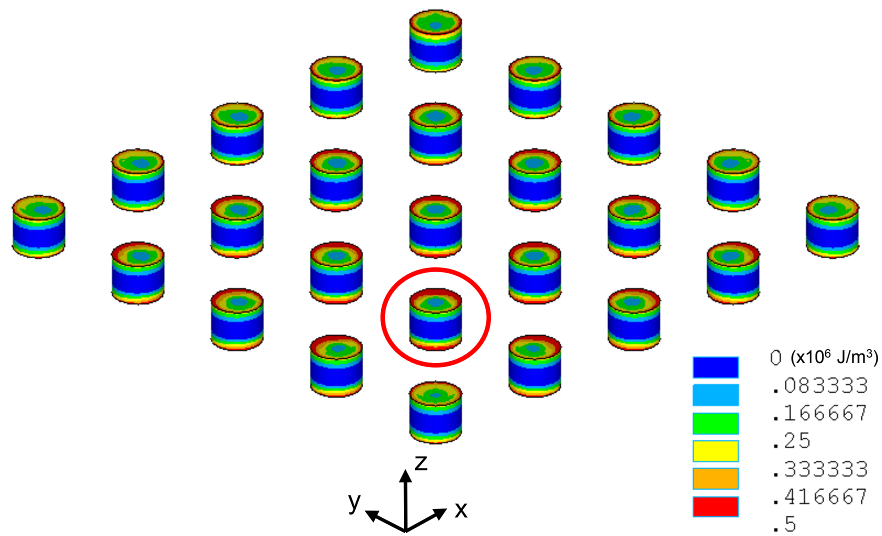

Figure 7.19 Contour Plot of PLWK after Five Cycles for Global Model with Cylinder Shape Joints

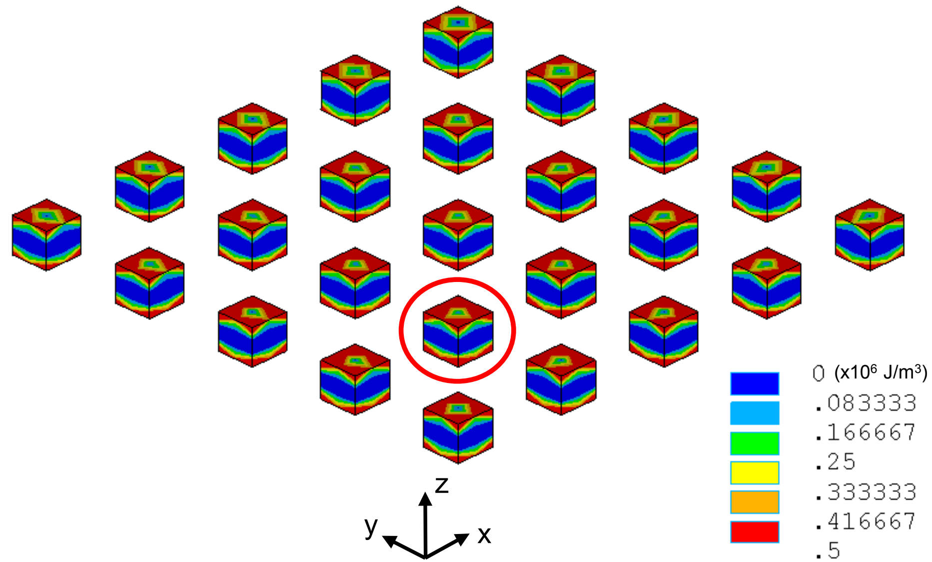

Figure 7.20 Contour Plot of PLWK after Five Cycles for Global Model with Brick Shape Joints

Simulation results for global models built with two different solder joint shapes were compared in Figure 7.21. It can be seen that although the simulation results for simplified global models diverged; the result for global model built with brick shape joint performed closer to converged solution than cylinder shape model. After local simulations, the simulation results for local models (AR 5*) were still in a very good agreement with converged solution. Note: AR 5^* model is a minimum local model whose vertical height $h_{loc} = 0.5$ h, where h is the height of the solder joint. Thus, we can see the displacement interpolations at the cut boundaries in this example were still accurate even use of a simplified global model and the minimum size local model.

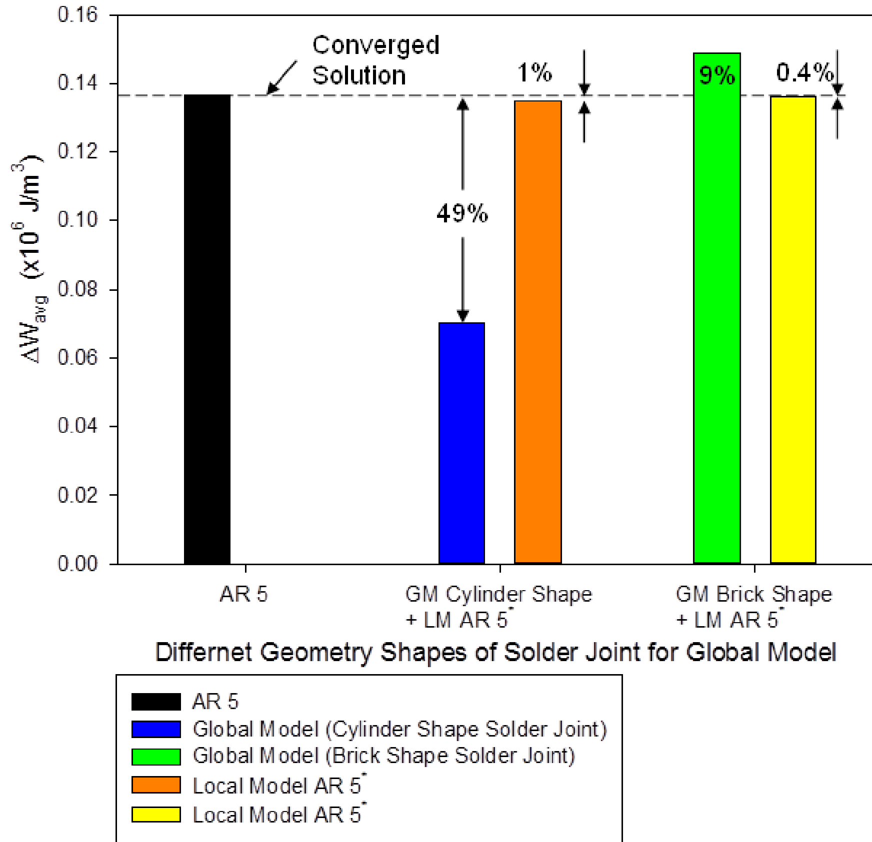

Figure 7.21 Comparisons of Simulation Results for Global Models Built with Different Shapes of Solder Joint

The FE model combining with the simplified global model (brick shape) and the minimum size local model (h_{loc} = 0.5 h) took less simulation time among all different models and saved 82X computational time compared to conventional model (Figure 7.22).

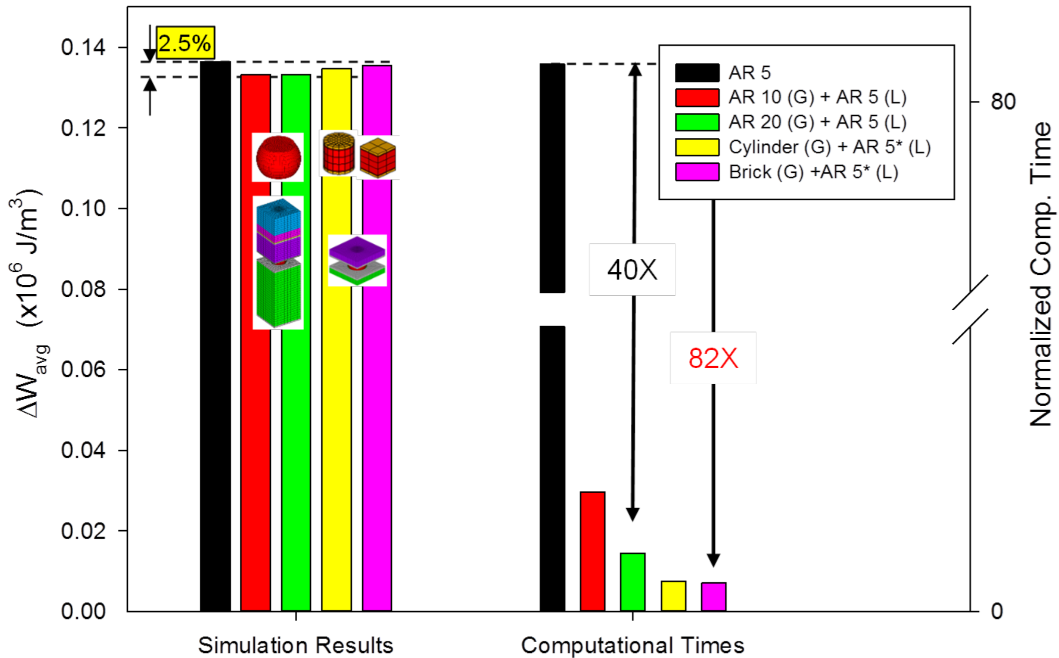

Figure 7.22 Comparisons of Simulation Results and Computational Time for Different Global-Local Model Sets

7.8 Effect of Hybrid Use Different Shapes of Solder Joint

It is worth mentioning that the mixture use of brick and cylinder shapes joints in a global model is not recommend due to the contour of high PLWK, greater than 0.5 $\times 10^6$ J/m^3 shown in Figure 7.19 and Figure 7.20, and the ΔW_{avg} calculated from brick shape model were greater than cylinder shape model (ΔW_{avg} = 0.1494 and 0.070 $\times 10^6$ J/m^3, respectively). For better understanding the influences of mixture use of brick and cylinder shapes joints, the diagonal solder joints of the area array building with brick shaped elements were replaced with cylinder shaped elements (Figure 7.23). As shown in Figure 7.24, the ΔW_{avg} calculated from the diagonal joints were always less than the other joints modeled in brick shape. Thus, misidentify the potential critical joint may occur in the stage of global model where mix use of different simplified shapes.

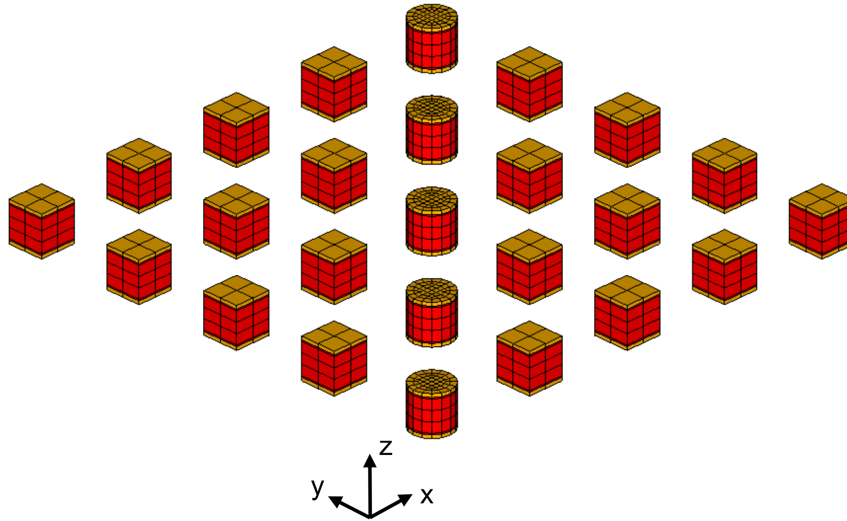

Figure 7.23 Hybrid Use of Brick and Cylinder Shapes Joints for Global Model

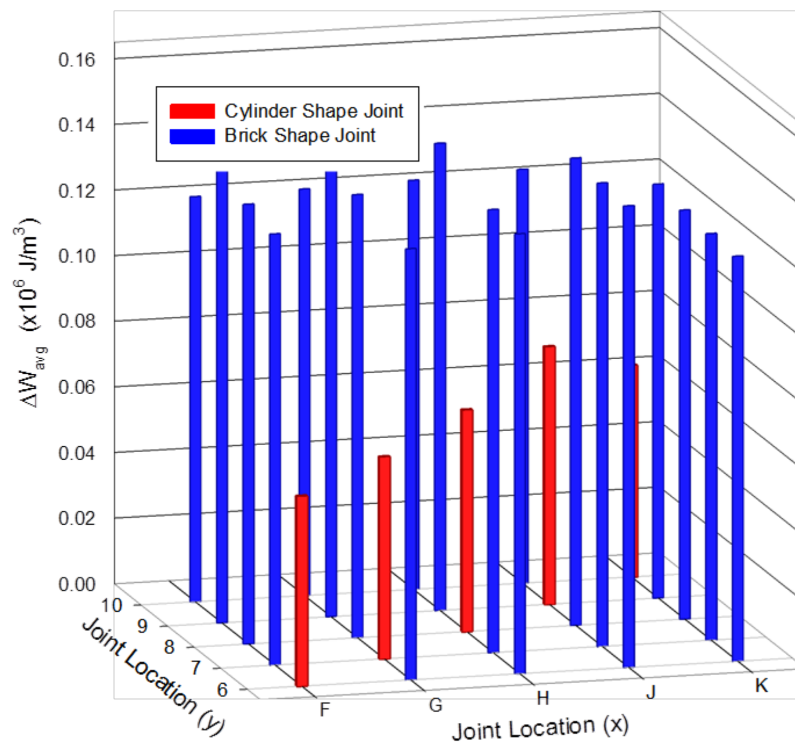

Figure 7.24 Simulation Results of ΔW_{avg} for Model of the Global Model with Mixture Joint Shapes

7.9 Summary and Conclusions

An improved submodeling based modeling strategy has shown that the accuracy of simulation results are sensitive to local model involving mesh quality, load step size, and the cut boundaries. Convergence study is suggested before using submodeling technique. In the geometric shape simplification, the minimum required height of vertical cut boundary (measured from the copper pad) is suggested to at least equivalent to a half height of solder joint for a better solution quality. Simplified brick shape provides modeling efficiency, but the high stress concentration may misidentify the most critical joint. In addition, hybrid use with different simplified shape joints in a model is not recommended. The proposed improved submodeling strategy reduces the overall computational time, results in 82X of overall computational time saving, and still maintains the accuracy of the solutions. The flowchart of approaches investigated of this chapter was provided in Figure 7.25.

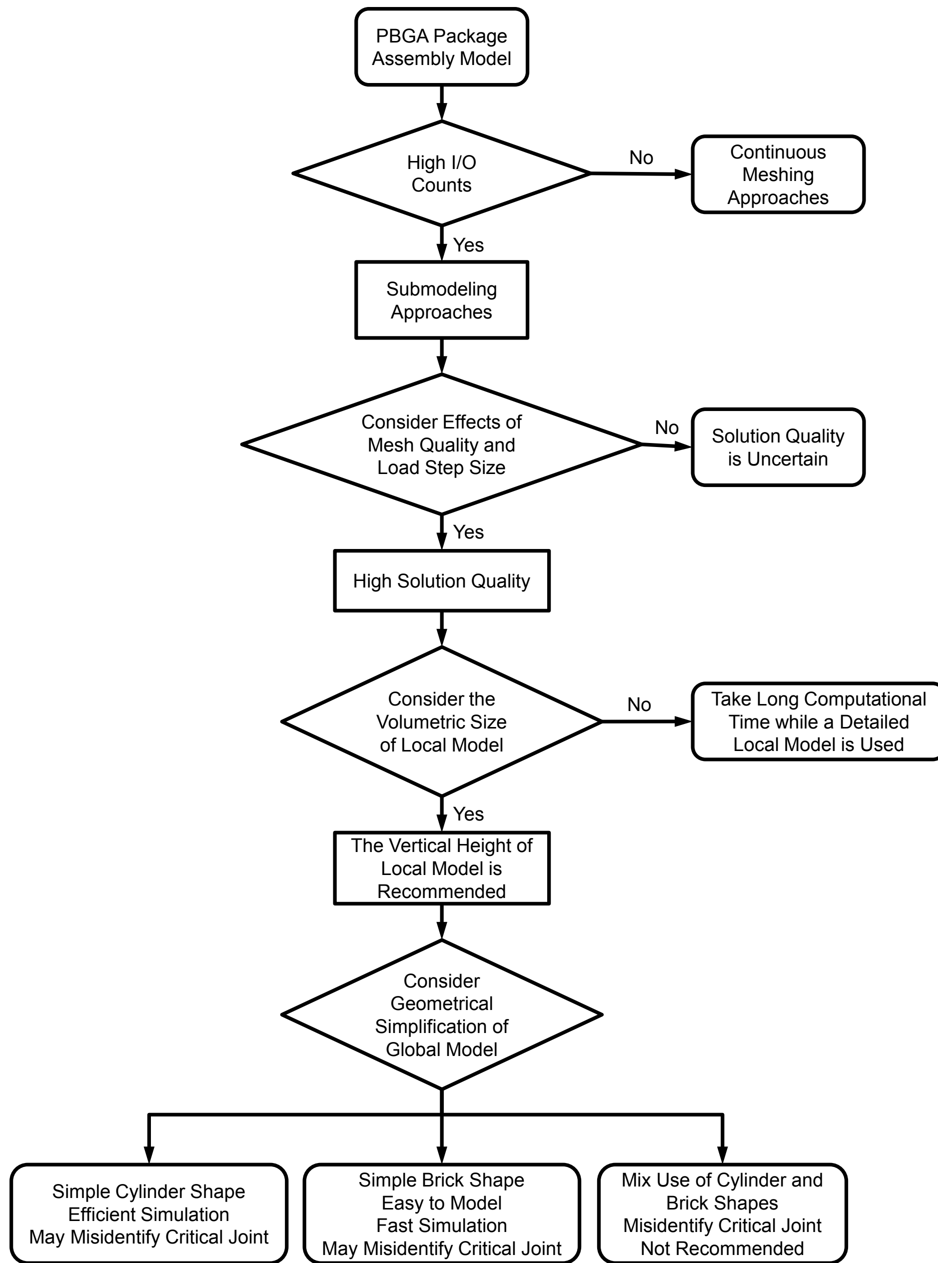

Figure 7.25 General Procedure for Choosing Submodeling Approaches

CHAPTER 8 SUMMARY AND CONCLUSIONS

8.1 Comparisons of Different Popular Finite Element Approaches in Electronic Packaging Area

Five most popular finite element modeling approaches, including 2D plane strain model, 3D slice model, 3D model, MPC model, and submodeling model, were compared in CHAPTER 4, especially in the areas of simulation accuracy and efficiency. The general assumptions used in the study included the use of viscoplastic material (Anand model, Chapter 2.1.2), energy-based fatigue model, cyclic loading condition, and no prior knowledge of the location of the most critical joint. Simulation results showed that 2D model performed the fastest simulation and yield a quick result over other models but sacrificing the accuracy. 3D-based approaches have their own advantages on capturing accurate responds caused by material behavior and package configuration. 3D slice model improved the solution quality over 2D slice model and still performed an efficient simulation. MPC, a powerful modeling technique requires no meshing continuity, simulated a large difference comparing with the 3D quarter model. Considering the common configurations of PBGA assemblies in the market, submodeling has its advantage on the balance between accuracy and efficiency. For more complex configurations, MPC, a powerful modeling technique requires no meshing continuity, provides more flexibility on modeling but accuracy may lose without appropriate treatments.

8.2 Improved Continuous Meshing Strategy

In CHAPTER 5, an improved meshing strategy utilizing the fan-out meshing approach has been proposed to reduce mesh density of a continuous meshing model and still keep simulation quality. This approach can be summarized as follows: (1) a hemispherical mesh transition region was utilized to fan-out circular mesh pattern to rectangular pattern, (2) the controlled maximum aspect ratio of mesh was set to a factor of reasonable value for most partitions of model, and (3) for tiny uninteresting partition, the factor of maximum aspect ratio was increased for a balance of geometrical fitting and element number size. This method allows for the mesh density to be increased in the solder joints while reducing the overall number of elements in the model.

8.2.1 Effects of the Mesh Density and the Load Step Size

The convergence study was studied to understand the effects of mesh quality and load step size on solution quality and simulation efficiency. An optimal analysis strategy was proposed using the relationship of mesh quality-load step size to determine the best model set for achieving the balance between simulation efficiency and accuracy. To calculate a reliable solution in an economic simulation was realized by this optimal approach by using low-density meshing model and fewer load steps; the proposed strategy avoided time-consuming tasks including modeling and calculating as shown in the literature.

8.2.2 Effect of the Number of Element-Layer across the Thickness of Solder Joint

In this dissertation, all the comparisons discussed above are based on the volume-weighted averaging response of 10 micron thick layer at the top side of the critical solder joint. One of the advantages of the volume-weighted averaging accumulation of inelastic strain energy density prevents the extreme simulated result in certain element that overestimates the effort of ΔW. Chapter 5.11 shows two different element-layer models for this 10 micron thickness of solder by changing the number of elements across the thickness. It is apparent that as long as the mesh quality for building entire model is high enough, the response values for different element-layer are not affected significantly. Thus, for a converged solution, one element across this thickness is possible while the entire model is built using the controlled maximum aspect ratio of element shape under a factor of 6.

8.2.3 Effect of Element Types

In Chapter 5.10, the effects of the use of two different orders of hexagonal element (8-node brick element with linear displacement and 20-node element with quadratic displacement) were presented. In the simulation of temperature cycle, there is no significant difference in the simulation result of ΔW_{avg} between two element types of models. However, the normalized computational time increased dramatically while using higher order element for modeling model and resulted in about 1.8 X in calculation time than 8-node element model due to increased number of nodes and degrees of freedom. For non-bending dominated problem, it is recommended to use 8-node element to achieve the balance of simulation efficiency and accuracy.

8.2.4 Effect of PCB Size

It has been shown in Chapter that the PCB outside the shadow of a package assembly has a negligible effect on simulation results in this dissertation. As a result, analyst can make a better use of the elements for detail modeling of interest region. In addition, as presented in Chapter 5.13, a converged solution for the problem of package size level can be simulated without additional assumptions.

8.3 Improved Discontinuous MPC Modeling Strategies

As mention earlier, MPC performs high flexibility on modeling as well as its solution quality is highly sensitive to the setup of MPC relationship. The proposed MPC approaches remedied the insufficient of general guidelines provided by software companies and improved solution quality without losing simulation efficiency.

8.3.1 Effect of the Location of the MPC Contact Pair

The proposed location of MPC contact pair states the MPC setup should avoid directly locating at the interface between two contacting surfaces. Instead of common understanding of the use of MPC, the MPC contact pair should locate within a material for preventing material property mismatch and minimizing the computational error. When the location of MPC is closed to the region of interest, cautions must be taken due to the use of MPC introduces stress/strain discontinuity between MPC contact pair. It is suggested that the location of MPC keeps at least one element-layer away from the interest region.

8.3.2 Multiple-MPC Modeling Approach

The idea of the proposed multiple-MPC approach (Chapter 6.10) matches well with the conventional MPC concepts, the side closed to the stiffer material (copper pad) is always considered as master side. Instead of using single-MPC, the proposed approach using multiple MPC contact pairs reduces mesh density layer by layer. This approach works well with two contacting material have significant difference in stiffness and is a very intuitive concept without considering comprehensive setup of master-slave relationship.

8.3.3 Effect of Master-Slave Relationship

The modified master-slave relationship considers the low mesh density side as master side and high mesh side as slave side. This approach improved the solution quality while considering the MPC contact pair located within a material. The solution quality can still be kept even large contacting elements ratio was used. For a better solution quality, it is recommended that the location of MPC at a distance of half height of solder joint away from the interest region. In contrast, simulation results showed the result accuracy did not improve when using the conventional MPC and considering the master-slave relationship.

Since both multiple-MPC and updated master-slave relationship approaches can reduce simulation time and model size, the mix of these two approaches results in better solution quality and simulation efficiency.

8.4 Improved Global-Local Modeling Strategies

In Chapters 7.4 and 7.5, the effects of mesh quality and load step size on the use of submodeling technique have been investigated. It is found that the solution quality is sensitive to the utilized mesh quality and load step size, and dominated by the local model. The simulation results showed the coarse-mesh global models can capture the global responses and identify the correct critical solder joints disregarding the load step size. Due to both global and local models share the same load steps, it is required to use a particular load step size (depends on the expected result accuracy) for global model and then the displacement information corresponding the load step was exported as additional boundary conditions for local model.

8.4.1 Effect of the Volumetric Size of Local Model

Since the local model is used for capturing the detail and accurate responses, local model is always built with high-density mesh. As a result, the simulation for local model takes longer time than for global model. The proposed minimized volumetric size of local model reduces the model size and still keeps the solution quality. The recommended vertical height of the local model is equal to twice height of the solder joint.

8.4.2 Effect of Simplified Geometry Shapes for the Solder Joints in the Global Model

Although the use of simplified geometry shapes, including cylinder and brick shapes, further reduces simulation time, these two simplified still can result in a

misidentification of the most critical joint at the simulation stage of global model. The parametric study of the simplified geometry shape for solder joint still under development; caution must be taken while use the simplified shape for modeling. The results in lower simulation results of ΔW_{avg} for cylinder shape joints.

8.4.3 Hybrid Use of Different Simplified Joint Shapes

The assumption of the hybrid use of different simplified joint shapes is using cylinder shape for modeling potential critical joints to obtain a better solution quality. However, simulation result showed the brick shape joint easily overestimates the ΔW; the cylinder shape joint experienced less impact while hybrid shape joints undergo thermal cycling. Thus, it is not recommended different shapes of solder joint in a package assembly modeling.

8.5 Conclusions

The main conclusions from this work are:

1. An improved modeling methodology for continuous meshing model utilizing fan-out meshing strategy was proposed to reduce model size, keep mesh quality of the model, and maintain solution quality.
2. The determination of optimal load step size for the thermal cycling problem developed from the convergence study of the unit model resolved the long term issue of the required load step number for the each duration of thermal loading curve.

3. The simplification of package model size can be realized by reducing the number of element-layers for uninterested region. Also, the use of 8 node brick element is sufficient for the solved problems in this study.
4. Proposed improved MPC-based analysis strategy reduced modeling difficulty and improved simulation efficiency. Detailed guidelines were proposed to allow analyst better understand the setup of MPC technique for the thermal cycling problems.
5. Proposed submodeling-based analysis strategy improved the solution quality, further reduce simulation costs, and ensure the correct identification of critical joint.
6. In this study, the simulation accuracy, efficiency and consistence have been achieved between each proposed modeling and analysis strategy.

REFERENCES

[1] Dally, J. W., Lall, P., and Suhling, J. C., *Mechanical Design of Electronic Systems*.: College House Enterprises, 2014.

[2] Yeh, L. T., “Review of Heat Transfer Technologies in Electronic Equipment,” *Journal of Electronic Packaging*, Vol. 117(4), pp. 333-339, 1995.

[3] Perkins, A. E. and Sitaraman, S. K., *Solder Joint Reliability Prediction for Multiple Environments*.: Springer US, 2009.

[4] Vianco, P. T., “Development of Alternatives to Lead-Bearing Solders,” *Proceedings of Surface Mount Technical Association International Conference*, 1993.

[5] Hwang, J. S., *Implementing Lead-Free Electronics*.: McGraw-Hill Education, 2004.

[6] Zhang, Q., Dasgupta, A., and Haswell, P., “Creep and High-Temperature Isothermal Fatigue of Pb-Free Solders,” *Proceedings of InterPACK*, 2003.

[7] Bradley, E., “Lead-free Solder Assembly: Impact and Opportunity,” *Proceedings of Electronic Components and Technology Conference*, pp. 41-47, 2003.

[8] NCMS, “Lead-Free Solder Project: Final Report,” *National Center for Manufacturing Sciences*, 1997.

[9] Lee, N. C., “Getting Ready for Lead Free Solders,” *Soldering and Surface Mount Technology*, Vol. 9(2), pp. 65-69, 1997.

[10] Abtew, M. and Selvaduray, G., “Lead-Free Solders in Microelectronics,” *Materials Science and Engineering*, Vol. 27(5-7), pp. 95-141, 2000.

[11] Kim, K. S., Huh, S. H., and Suganuma, K., “Effects of Intermetallic Compounds on Properties of Sn–Ag–Cu Lead-Free Soldered Joints,” *Journal of Alloys and Compounds*, Vol. 352(1-2), pp. 226-236, 2003.

[12] Yoon, J. W., Kim, S. W., and Jung, S. B., “IMC morphology, Interfacial Reaction and Joint Reliability of Pb-Free Sn–Ag–Cu Solder on Electrolytic Ni BGA Substrate,” *Journal of Alloys and Compounds*, Vol. 392(1-2), pp. 247-252, 2005.

[13] Yu, D. Q. and Wang, L., “The Growth and Roughness Evolution of Intermetallic Compounds of Sn–Ag–Cu/Cu Interface During Soldering Reaction,” *Journal of Alloys and Compounds*, Vol. 458(1-2), pp. 542-547, 2008.

[14] Wu, C. M. L., Yu, D. Q., Law , C. M. T., and Wang, L., “Properties of Lead-Free Solder Alloys with Rare Earth Element Additions,” *Materials Science and Engineering: R: Reports*, Vol. 44, pp. 1-44, 2004.

[15] Sona, M. and Prabhu, K. N., “Review on Microstructure Evolution in Sn–Ag–Cu Solders and Its Effect on Mechanical Integrity of Solder Joints,” *Journal of Materials Science: Materials in Electronics*, Vol. 24(9), pp. 3149-3169, 2013.

[16] Evans, R. W. and Wilshire, B., *Creep of Metals and Alloys*.: Institute of Metals, 1985.

[17] Engelmaier, W., “Surface Mount Solder Joint Reliability: Issues, Design, Testing, Prediction,” *Workshop Notes, Engelmaier Associates*, 1995.

[18] Engelmaier, W., "Solder Joints in Electronics: Design for Reliability," *Engelmaier Associates, L. C.*, 1997.

[19] ASTM E606, "Standard Test Method for Strain-Controlled Fatigue Testing," *ASTM International*, Vol. 03.01, 2012.

[20] Tummala, R. R., *Fundamentals of Microsystems Packaging*.: McGraw Hill, 2001.

[21] Suhir, E., "Accelerated Life Testing (ALT) in Microelectronics and Photonics: Its Role, Attributes, Challenges, Pitfalls, and Interaction with Qualification Tests," *Journal of Electronic Packaging*, Vol. 124(3), pp. 281-291, 2002.

[22] Lee, T. K., Bieler, T. R., Kim, C. U., and Ma, H., *Fundamentals of Lead-Free Solder Interconnect Technology: From Microstructures to Reliability*.: Springer, 2015.

[23] JESD22-A104E, "Temperature Cycling," *JEDEC*, 2014.

[24] JESD22-A106B, "Temperature Shock," *JEDEC*, 2016.

[25] Tamin, M. N. and Shaffiar, N. M., *Solder Joint Reliability Assessment: Finite Element Simulation Methodology*.: Springer International Publishing, 2014.

[26] Lee, W. W., Nguyen, L. T., and Selvaduray, G. S., "Solder Joint Fatigue Models: Review and Applicability to Chip Scale Packages," *Microelectronics Reliability*, Vol. 40(2), pp. 231-244, 2000.

[27] Chen, G., Zhao, X., and Wu, H., "A Critical Review of Constitutive Models for Solders in Electronic Packaging," *Advances in Mechanical Engineering*, Vol. 9(8), pp. 1-21, 2017.

[28] Fan, X., Pei, M., and Bhatti, P. K., "Effect of Finite Element Modeling Techniques on Solder Joint Fatigue Life Prediction of Flip-Chip BGA Packages," *Proceedings of Electronic Components and Technology Conference*, pp. 972-980, 2006.

[29] Pang, J. H. L., "Lead-Free Solder Materials: Design for Reliability," in *Micro- and Opto-Electronic Materials and Structures: Physics, Mechanics, Design, Reliability, Packaging*, Suhir, E., Lee, Y. C., and Wong, C. P., Eds.: Springer, 2007, ch. 12.

[30] Ridout, S. and Bailey, C., "Review of Methods to Predict Solder Joint Reliability under Thermo-Mechanical Cycling," *Fatigue & Fracture of Engineering Materials & Structures*, Vol. 30(5), pp. 400-412, 2006.

[31] Che, F. X. and Pang, J. H. L., "Thermal Fatigue Reliability Analysis for PBGA with Sn-3.8Ag-0.7Cu Solder Joints," *Proceedings of Electronics Packaging Technology Conference*, pp. 787-792, 2004.

[32] Zhang, Q. and Dasgupta, A., "Constitutive Properties and Durability of Selected Lead-free Solder," in *Lead-free Electronics*, Ganesan, S. and Pecht, M., Eds.: Wiley, 2006, ch. 6, pp. 237-381.

[33] Yao, Y., Long, X., and Keer, L. M., "A Review of Recent Research on the Mechanical Behavior of Lead-Free Solders," *Applied Mechanics Reviews*, Vol. 69(4), pp. 040802-1-15, 2017.

[34] Che, F. X., Pang, J. H. L., Zhu, W. H., Sun, W., and Sun, A. Y. S., "Modeling Constitutive Model Effect on Reliability of Lead-Free Solder Joints," *Proceedings of International Conference on Electronic Packaging Technology*, pp. 26-29, 2006.

[35] Yeo, A., Lee, C., and Pang, J. H. L., "Flip Chip Solder Joint Reliability Analysis

Using Viscoplastic and Elastic-Plastic-Creep Constitutive Models," *IEEE Transactions on Components and Packaging Technologies*, Vol. 29(2), pp. 355-363, 2006.

[36] Ramberg, W. and Osgood, W., "Description of Stress-Strain Curves by Three Parameters," *National Advisory Committee for Aeronautics*, pp. 1-27, 1943.

[37] Pang, J. H. L., Xiong, B. S., and Che, F. X., "Modeling Stress Strain Curves for Lead-Free 95.5Sn-3.8Ag-0.7Cu Solder," *Proceedings of The 5th International Conference on Thermal and Mechanical Simulation and Experiments in Microelectronics and Microsystems, EuroSimE2004*, pp. 449-453, 2004.

[38] Darveaux, R. and Banerji, K., "Constitutive Relations for Tin-Based Solder Joints," *IEEE Transactions on Components, Hybrids, and Manufacturing Technology*, Vol. 15(6), pp. 1013-1024, 1992.

[39] Qian, Z. and Liu, S., "On the Life Prediction and Accelerated Testing of Solder Joints," *The International Journal of Microcircuits and Electronic Packaging*, Vol. 22(4), pp. 288-304, 1999.

[40] Ohring, M., *Reliability and Failure of Electronic Materials and Devices*.: Academic Press, 1998.

[41] Lau, J. H., Ed., *Thermal Stress and Strain in Microelectronics Packaging*.: Van Nostrand Reinhold, 1993.

[42] Norton, F. H., *The Creep of Steel at High Temperatures*.: McGraw-Hill, 1929.

[43] Pang, J. H. L., Xiong, B. S., and Low, T. H., "Creep and Fatigue Characterization of Lead Free 95.5Sn-3.8Ag-0.7Cu Solder," *Proceedings of Electronic Components and Technology Conference*, pp. 1333-1337, 2004.

[44] Sitaraman, S. K. and Kacker, K., "Thermomechanical Reliability Prediction of Lead-Free Solder Interconnects," in *Lead-Free Solder Interconnect Reliability*, Shangguan, D., Ed.: ASM International, 2005, ch. 8, pp. 181-198.

[45] Zhang, Q., Dasgupta, A., and Haswell, P., "Partitioned Viscoplastic-Constitutive Properties of the Pb-Free Sn3.9Ag0.6Cu Solder," *Journal of Electronic Materials*, Vol. 33(11), pp. 1338–1349, 2004.

[46] Avery, D. H. and Backofen, W. A., "A Structural Basis for Superplasticity," *Transactions of the American Society of Metals*, Vol. 58, p. 551, 1965.

[47] Shine, M. C. and Fox, L. R., "Fatigue of Solder Joints in Surface Mount Devices," *Low Cycle Fatigue-ASTM*, Vol. 942, pp. 588-610, 1987.

[48] Song, H. G., Morris, J. W., and Hua, F., "The Creep Properties of Lead-Free Solder Joints," *The Journal of The Minerals, Metals & Materials Society*, Vol. 54(6), pp. 30-32, 2002.

[49] Wiese, S., Feustel, F., and Meusel, E., "Characterisation of Constitutive Behaviour of SnAg, SnAgCu and SnPb Solder in Flip Chip Joints," *Sensors and Actuators A: Physical*, Vol. 99(1-2), pp. 188-193, 2002.

[50] Wiese, S., Meusel, E., and Wolter, K. J., "Microstructural Dependence of Constitutive Properties of Eutectic SnAg and SnAgCu Solders," *Proceedings of Electronic Components and Technology Conference*, pp. 197-206, 2003.

[51] Vianco, P. T., "Fatigue and Creep of Lead-Free Solder Alloys: Fundamental

Properties," in *Lead-Free Solder Interconnect Reliability*, Shangguan, D., Ed.: ASM International, 2005, ch. 3, pp. 67-106.

[52] Garofalo, F., *Fundamentals of Creep and Creep-Rupture in Metals*.: McMillan, 1965.

[53] Shi, X. Q., Wang, Z. P., Yang, Q. J., and Pang, J. H. L., "Creep Behavior and Deformation Mechanism Map of Sn-Pb Eutectic Solder Alloy," *Journal of Engineering Materials and Technology*, Vol. 125, pp. 81-88, 2002.

[54] Knecht, S. and Fox, L. R., "Constitutive Relation and Creep-Fatigue Life Model for Eutectic Tin-Lead Solder," *IEEE Transactions on Components, Hybrids, and Manufacturing Technology*, Vol. 13(2), pp. 424-433, 1990.

[55] Wiese, S. and Wolter, K. J., "Microstructure and creep behaviour of eutectic SnAg and SnAgCu solders," *Microelectronics Reliability*, Vol. 44, pp. 1923-1931, 2004.

[56] Ashby, M. F. and Jones, D. R. H., *Engineering Materials 1: An Introduction to Properties, Applications and Design*, 4th Edition.: Elsevier, 2012.

[57] Xiao, Q. and Armstrong, W. D., "Tensile Creep and Microstructural Characterization of Bulk Sn3.9Ag0.6Cu Lead-Free Solder," *Journal of Electronic Materials*, Vol. 34(2), pp. 196-211, 2005.

[58] Mukherjee, S., Nuhi, M., Dasgupta, A., and Modarres, M., "Creep Constitutive Models Suitable for Solder Alloys in Electronic Assemblies," *Journal of Electronic Packaging*, Vol. 138(3), pp. 030801-1-13, 2016.

[59] Ma, H., "Constitutive Models of Creep for Lead-Free Solders," *Journal of Materials Science*, Vol. 44(14), pp. 3841-3851, 2009.

[60] Zhang, L., Han, J., He, C., and Guo, Y., "Reliability Behavior of Lead-Free Solder Joints in Electronic Components," *Journal of Materials Science: Materials in Electronics*, Vol. 24, pp. 172-190, 2013.

[61] Langdon, T. G. and Mohamed, F. A., "A New Type of Deformation Mechanism Map for High-temperature Creep," *Materials Science and Engineering*, Vol. 32, pp. 103-112, 1978.

[62] Wiese, S., Schubert, A., Walter, H., Dudek, R., Feustel, F., Meusel, E., and Michel, B., "Constitutive Behaviour of Lead-free Solders vs. Lead-containing Solders-Experiments on Bulk Specimens and Flip-Chip Joints," *Proceedings of Electronic Components and Technology Conference*, pp. 890-902, 2001.

[63] Hart, E. W., "Constitutive Relations for the Nonelastic Deformation of Metals," *Journal of Engineering Materials and Technology*, Vol. 98(3), pp. 193-202, 1976.

[64] Mei, Z. and Morris, J. W., "Characterization of Eutectic Sn-Bi Solder Joints," *Journal of Electronic Materials*, Vol. 21(6), pp. 599-607, 1992.

[65] Wiese, S., Roellig, M., Mueller, M., and Wolter, K. J., "The Effect of Downscaling the Dimensions of Solder Interconnects on Their Creep Properties," *Microelectronics Reliability*, Vol. 48, pp. 843-850, 2008.

[66] Clech, J., "Review and Analysis of Lead-Free Solder Material Properties," in *Lead-Free Electronics:iNEMI Projects Lead to Successful Manufacturing*, Bradley, E. et al., Eds.: Wiley, 2007, ch. 2, pp. 47-123.

[67] Frear, D. R., Jang, J. W., Lin, J. K., and Zhang, C., "Pb-Free Solders for Flip-Chip

Interconnects," *The Journal of The Minerals, Metals & Materials Society*, Vol. 53(6), pp. 28-33, 2001.

[68] Mavoori, H., Chin, J., Vaynman, S., Moran, B., Keer, L., and Fine, M., "Creep, Stress Relaxation, and Plastic Deformation in Sn-Ag and Sn-Zn Eutectic Solders," *Journal of Electronic Materials*, Vol. 26(7), pp. 783-790, 1997.

[69] Wiese, S. and Rzepka, S., "Time-Independent Elastic-Plastic Behaviour of Solder Materials," *Microelectronics Reliability*, Vol. 44, pp. 1893-1900, 2004.

[70] Zhang, Q., Dasgupta, A., and Haswell, P., "Viscoplastic Constitutive Properties and Energy-Partitioning Model of Lead-Free Sn3.9Ag0.6Cu Solder Alloy," *Proceedings of Electronic Components and Technology Conference*, pp. 1862-1868, 2003.

[71] Pang, J. H. L., Low, T. H., Xiong, B. S., and Che, F. X., "Design for Reliability (DFR) Methodology for Electronic Packaging Assemblies," *Proceedings of Electronic Components and Technology Conference*, pp. 470-478, 2003.

[72] Amagai, M., Watanabe, M., Omiya, M., Kishimoto, K., and Shibuya, T., "Mechanical Characterization of Sn-Ag-Based Lead-Free Solders," *Microelectronics Reliability*, Vol. 42, pp. 951-966, 2002.

[73] Stephens, J. J. and Frear, D. R., "Time-Dependent Deformation Behavior of Near-Eutectic 60Sn-40Pb Solder," *Metallurgical and Materials Transactions*, Vol. 30(5), pp. 1301-1313, 1999.

[74] Darveaux, R., Banerji, K., Mawer, A., and Dody, G., "Reliability of Plastic Ball Grid Array Assembly," in *Ball Grid Array Technology*, Lau, J. L., Ed.: McGraw-Hill, 1995, pp. 379-442.

[75] Hong, B. Z., "Thermal Fatigue Analysis of a CBGA Package with Lead-Free Solder Fillets," *Proceedings of ITherm Conference*, pp. 205-211, 1998.

[76] Vianco, P. T., Rejent, J. A., and Kilgo, A. C., "Creep Behavior of the Ternary 95.5Sn-3.9Ag-0.6Cu Solder-Part I: As-Cast Condition," *Journal of Electronic Materials*, Vol. 33(11), pp. 1389-1400, 2004.

[77] Schuber, A., Dudek, R., Auerswald, E., Gollhardt, A., Michel, B., and Reicbl, H., "Fatigue Life Models for SnAgCu and SnPb Solder Joints Evaluated by Experiments and Simulation," *Proceedings of Electronic Components and Technology Conference*, pp. 603-610, 2003.

[78] Pang, J. H. L., *Lead Free Solder Mechanics and Reliability.*: Springer, 2012.

[79] Pang, J. H. L., Chong, D. Y. R., and Low, T. H., "Thermal Cycling Analysis of Flip-Chip Solder Joint Reliability," *IEEE Transactions on Components and Packaging Technologies*, Vol. 24(4), pp. 705 - 712, 2001.

[80] Pang, J. H. L., Seetoh, C. W., and Wang, Z. P., "CBGA Solder Joint Reliability Evaluation Based on Elastic-Plastic-Creep Analysis," *Journal of Electronic Packaging*, Vol. 122(3), pp. 255-261, 2000.

[81] Dowling, N. E., *Mechanics Behavior of Materials: Engineering Methods for Deformation, Fracture, and Fatigue.*: Prentice-Hall International Editions, 1993.

[82] McDowell, D. L., Miller, M. P., and Brooks, D. C., "A Unified Creep-Plasticity Theory for Solder Alloys," *Fatigue of Electronic Materials*, pp. 42-59, 1994.

[83] Basaran, C., Zhao, Y., Tang, H., and Gomez, J., "A Damage-Mechanics-Based Constitutive Model for Solder Joints," *Journal of Electronic Packaging*, Vol. 127(3), pp. 208-214, 2005.

[84] Anand, L., "Constitutive Equations for Hot Working of Metals," *International Journal of Plasticity*, Vol. 1(3), pp. 213-231, 1985.

[85] Bodner, S. R. and Partom, Y., "Constitutive Equations for Elastic-Viscoplastic Strain-Hardening Materials," *Journal of Applied Mechanics*, Vol. 42(2), pp. 385-389, 1975.

[86] Chaboche, J. L., "Constitutive Equations for Cyclic Plasticity and Cyclic Viscoplasticity," *International Journal of Plasticity*, Vol. 5(3), pp. 247-302, 1989.

[87] Wang, G. Z., Cheng, Z. N., Becker, K., and Wilde, J., "Applying Anand Model to Represent the Viscoplastic Deformation Behavior of Solder Alloys," *Journal of Electronic Packaging*, Vol. 123(3), pp. 247-253, 2001.

[88] Brown, S. B., Kim, K. H., and Anand, L., "An Internal Variable Constitutive Model for Hot Working of Metals," *International Journal of Plasticity*, Vol. 5(2), pp. 95-130, 1989.

[89] Motalab, M., Cai, Z., Suhling, J. C., and Lall, P., "Determination of Anand Constants for SAC Solders Using Stress-Strain or Creep Data," *Proceedings of ITherm*, pp. 910-923, 20112.

[90] Basit, M., Ahmed, S., Motalab, M., Roberts, J. C., Suhling, J. C., and Lall, P., "The Anand Parameters for SAC Solders after Extreme Aging," *Proceedings of ITherm Conference*, pp. 440-447, 2016.

[91] Chen, X., Chen, G., and Sakane, M., "Prediction of Stress-Strain Relationship with an Improved Anand Constitutive Modelfor Lead-Free Solder Sn-3.5Ag," *IEEE Transactions on Components and Packaging Technologies*, Vol. 28, pp. 111-116, 2005.

[92] Bai, N., Chen, X., and Gao, H., "Simulation of Uniaxial Tensile Properties for Lead-Free Solders with Modified Anand Model," *Materials and Design*, Vol. 30, pp. 122-128, 2009.

[93] Cheng, Z. N., Wang, G. Z., Chen, L., Wilde, J., and Becker, K., "Viscoplastic Anand Model for Solder Alloys and Its Application," *Soldering & Surface Mount Technology*, Vol. 12(2), pp. 31-36, 2000.

[94] Bhate, D., Chan, D., Subbarayan, G., Chiu, T. C., Gupta, V., and Edwards, D. R., "Constitutive Behavior of Sn3.8Ag0.7Cu and Sn1.0Ag0.5Cu Alloys at Creep and Low Strain Rate Regimes," *IEEE Transactions on Components and Packaging Technologies*, Vol. 31(3), pp. 622-633, 2008.

[95] Rodgers, B., Flood, B., Punch, J., and Waldron, F., "Experimental Determination and Finite Element Model Validation of the Anand Viscoplasticity Model Constants for SnAgCu," *Proceedings of 6th International Conference on Thermal, Mechanial and Multi-Physics Simulation and Experiments in Micro-Electronics and Micro-Systems*, pp. 490-496, 2005.

[96] Wang, Q., Liang, L., Chen, X., Weng, X., Liu, Y., Irving, S., and Luk, T., "Experimental Determination and Modification of Anand Model Constants for Pb-

Free Material 95.5Sn4.0Ag0.5Cu," *Proceedings of 2007 International Conference on Thermal, Mechanical and Multi-Physics Simulation Experiments in Microelectronics and Micro-Systems. EuroSime 2007*, 2007.

[97] Reinikainen, T. O., Marjamaki, P., and Kivilahti, J. K., "Deformation Characteristics and Microstructural Evolution of SnAgCu Solder Joints," *Proceedings of 6th International Conference on Thermal, Mechanial and Multi-Physics Simulation and Experiments in Micro-Electronics and Micro-Systems*, pp. 91-98, 2005.

[98] Pei, M. and Qu, J., "Constitutive Modeling of Lead-Free Solders," *Proceedings of International Symposium on Advanced Packaging Materials: Processes, Properties and Interfaces*, pp. 45-49, 2005.

[99] Che, F. X. and Pang, J. H. L., "Fatigue Reliability Analysis of Sn–Ag–Cu Solder Joints Subject to Thermal Cycling," *IEEE Transactions on Device and Materials Reliability*, Vol. 13(1), pp. 36-49, 2013.

[100] Chen, X., Chen, G., and Sakane, M., "Modified Anand Constitutive Model for Lead-Free Solder Sn-3.5Ag," *Proceedings of ITherm*, pp. 447-452, 2005.

[101] Msolli, S., Dalverny, O., Alexis, J., and Karama, M., "Effects of the Unified Viscoplastic Formulation and Temperature Terms on the Thermomechanical Behavior of Soldering Materials," *Key Engineering Materials*, Vol. 498, pp. 219-226, 2012.

[102] Chaboche, J. L., "A Review of Some Plasticity and Viscoplasticity Constitutive Theories," *International Journal of Plasticity*, Vol. 24(10), pp. 1642-1693, 2008.

[103] Frear, D. R., Jones, W. B., and Kinsman, K. R., *Solder Mechanics: A State of the Art Assessment*.: Warrendale Pa.: Minerals, Metals & Materials Society, 1991.

[104] Hall, P. M., "Creep and Stress Relaxation in Solder Joints," in *Solder Joint Reliability Theory and Applications*, Lau, J. H., Ed.: Springer US, 1991, ch. 10.

[105] Manson, S. S., *Thermal Stress and Low-Cycle Fatigue*.: McGraw-Hill, 1996.

[106] Coffin, L. F., *A Study of the Effects of Cyclic Thermal Stresses on a Ductile Metal*.: Schenectady, New York: Knolls Atomic Power Laboratory, 1953.

[107] Pang, J. H. L., Tan, T. I., and Sitarama, S. K., "Thermo-Mechanical Analysis of Solder Joint Fatigue and Creep in a Flip Chip on Board Package Subjected to Temperature Cycling Loading," *Proceedings of Electronic Components and Technology Conference*, pp. 878-883, 1998.

[108] Yang, Q. D., Shim, D. J., and Spearing, S. M., "A Cohesive Zone Model for Low Cycle Fatigue Life Prediction of Solder Joints," *Microelectronic Engineering*, Vol. 75, pp. 85-95, 2004.

[109] Kilinski, T. J., Lesniak, J. R., and Sandor, B. I., "Modern Approaches to Fatigue Life Prediction of SMT Solder Joints," in *Solder Joint Reliability: Theory and Applications*, Lau, J. H., Ed.: Springer Science & Business Media, 2013, ch. 13.

[110] Stephens, R. I., Fatemi, A., Stephens, R. R., and Fuchs, H. O., *Metal Fatigue in Engineering*, 2nd Edition.: John Wiley & Sons, 2000.

[111] Coffin, L. F., "Fatigue at High Temperature-Prediction and Interpretation," *Proceedings of The Institution of Mechanical Engineers*, Vol. 188, pp. 109-127,

1974.

[112] Solomon, H. D., "Predicting Thermal and Mechanical Fatigue Lives from Isothermal Low Cycle Data," in *Solder Joint Reliability: Theory and Applications*, Lau, J. H., Ed.: Van Nostrano Reinhold, 1991, ch. 14, pp. 406-454.

[113] Shi, X. Q., Pang, J. H. L., Zhou, W., and Wang, Z. P., "A Modified Energy-Based Low Cycle Fatigue Model for Eutectic Solder Alloy," *Scripta Materialia*, Vol. 41(3), pp. 289-296, 1999.

[114] Engelmaier, W., "Fatigue Life of Leadless Chip Carrier Solder Joints During Power Cycling," *IEEE Transactions on Components, Hybrids, and Manufacturing Technology*, Vol. 6(3), pp. 232-237, 1983.

[115] Chauhan, P., Osterman, M., Lee, S. W. R., and Pecht, M., "Critical Review of the Engelmaier Model for Solder Joint Creep Fatigue Reliability," *IEEE Transactions on Components and Packaging Technologies*, Vol. 32(3), pp. 693-700, 2009.

[116] Knecht, S. and Les, F., "Integrated Matrix Creep: Application to Accelerated Testing and Lifetime Prediction," in *Solder Joint Reliability: Theory and Applications*, Lau, J. H., Ed.: Springer, 1991, pp. 508-544.

[117] Syed, A. R., "Creep Crack Growth Prediction of Solder Joints During Temperature Cycling - An Engineering Approach," *Journal of Electronic Packaging*, Vol. 117(2), pp. 116-122, 1995.

[118] Syed, A. R., "Factors Affecting Creep-Fatigue Interaction in Eutectic Sn/Pb Solder Joints," *Proceedings of InterPACK '97*, pp. 1535-1542, 1997.

[119] Syed, A. R., "Thermal Fatigue Reliability Enhancement of Plastic Ball Grid Array (PBGA) Packages," *Proceedings of Electronic Components and Technology Conference*, pp. 1211-1216, 1996.

[120] Syed, A. R., "Accumulated Creep Strain and Energy Density Based Thermal Fatigue Life Prediction Models for SnAgCu Solder Joints," *Proceedings of Electronic Components and Technology Confelrence*, pp. 737-746, 2004.

[121] Dasgupta, A., Oyan, C., Barker, D., and Pecht, M., "Solder Creep-Fatigue Analysis by an Energy-Partitioning Approach," *Journal of Electronic Packaging*, Vol. 114(2), pp. 152-160.

[122] Morrow, J., "Cyclic Plastic Strain Energy and Fatigue of Metals," *American Society for Testing and Materials*, pp. 45-87, 1965.

[123] Solomon, H. D. and Tolksdorf, E. D., "Energy Approach to the Fatigue of 60/40 Solder. Part 1: Influence of Temperature and Cycle Frequency," *Journal of Electronic Packaging*, Vol. 117(2), pp. 130-135, 1995.

[124] Akay, H. U., Paydar, N. H., and Bilgic, A., "Fatigue Life Predictions for Thermally Loaded Solder Joints Using a Volume-Weighted Averaging Technique," *Journal of Electronic Packaging*, Vol. 119(4), pp. 228-235, 1997.

[125] Paydar, N., Tong, Y., and Akay , H. U., "A Finite Element Study of Factors Affecting Fatigue Life of Solder Joints," *Journal of Electronic Packaging*, Vol. 116(4), pp. 265-273, 1994.

[126] Pao, Y. H., "A Fracture Mechanics Approach to Thermal Fatigue Life Prediction of Solder Joints," *IEEE Transactions on Components, Hybrids, and Manufacturing*

Technology, Vol. 15(4), pp. 559-570, 1992.

[127] Darveaux, R., "Effect of Simulation Methodology on Solder Joint Crack Growth Correlation and Fatigue Life Prediction," *Proceedings of Electronic Components and Technology Conference*, pp. 147-154, 2000.

[128] Darveaux, R., "Effect of Simulation Methodology on Solder Joint Crack Growth Correlation and Fatigue Life Prediction," *Journal of Electronic Packaging*, Vol. 124(3), pp. 147-154, 2002.

[129] Pang, J. H. L. and Chong, D. Y. R., "Flip Chip on Board Solder Joint Reliability Analysis Using 2-D and 3-D FEA Models," *IEEE Transactions on Advanced Packaging*, Vol. 24(4), pp. 499-506, 2001.

[130] Chong, D. Y. R., Kapoor, R., and Sun, A. Y. S., "Reliability Assessment of a High Performance Flip-Chip BGA Package (organic substrate based) using Finite Element Analysis," *Proceedings of Electronic Components and Technology Conference*, pp. 207-213, 2003.

[131] Li, C. Y., Subrahmanyan, R., Wilcox, J. R., and Stone, D., "A Damage Integral Methodology for Thermal and Mechanical Fatigue of Solder Joints," in *Solder Joint Reliability: Theory and Applications*, Lau, J. H., Ed.: Van Nostrand Reinhold, 1991, ch. 12, pp. 361-383.

[132] Solomon, H. D., "Low Cycle Fatigue of 60/40 Solder Plastic Strain Limited vs. Displacement Limited Testing," *Proceedings of ASM's 3d Electronic Packaging: Materials and Processes*, pp. 29-47, 1985.

[133] Guo, Z., Sprecher, A. F., Kim, M., and Conrad, H., "Monotonic Properties and Low-Cycle Fatigue of Several Soft Solder Alloy Systems," *Proceedings of Materials Developments in Microelectronic Packaging: Performance and Reliability*, pp. 155-162, 1991.

[134] Guo, Z. and Conrad, H., "Fatigue Crack Growth Rate in 63Sn37Pb Solder Joints," *Journal of Electronic Packaging*, Vol. 115, pp. 159-164, 1993.

[135] Satoh, R., Arakawa, K., Harada, M., and Matsui, K., "Thermal Fatigue Life of Pb-Sn Alloy Interconnections," *IEEE Transactions on Components, Hybrids, and Manufacturing Technology*, Vol. 14, pp. 224-232, 1991.

[136] Chow, C. L., Yang, F., and Fang, H. E., "Damage Mechanics Characterization on the Fatigue Behaviour of a Solder Joint Material," *Journal of Mechanical Engineering Science*, Vol. 215(8), pp. 883-892, 2001.

[137] Stolkarts, V., Moran, B., and Keer, L. M., "Constitutive and Damage Model for Solders," *Proceedings of Electronic Components and Technology Conference*, pp. 379-385, 1998.

[138] Stolkarts, V., Keer, L. M., and Fine, M. E., "Damage Evolution Governed by Microcrack Nucleation with Application to the Fatigue of 63Sn-37Pb Solder," *Journal of the Mechanics and Physics of Solids*, Vol. 47, pp. 2451-2468, 1999.

[139] Stolkarts, V., Keer, L. M., and Fine, M. E., "Constitutive and Cyclic Damage Model of 63Sn-37Pb Solder," *Journal of Electronic Packaging*, Vol. 123, pp. 351-355, 2001.

[140] Abdul-Baqi, A., Schreurs, P. J. G., and Geers, M. G. D., "Fatigue Damage

Modeling in Solder Interconnects Using a Cohesive Zone Approach," *International Journal of Solids and Structures*, Vol. 42, pp. 927-942, 2005.

[141] Chaboche, J. L., Feyel, F., and Monerie, Y., "Interface Debonding Models: A Viscous Regularization with a Limited Rate Dependency," *International Journal of Solids and Structures*, Vol. 38(18), pp. 3127-3160, 2001.

[142] Kanchanomai, C., Miyashita, Y., and Mutoh, Y., "Low Cycle Fatigue Behavior and Mechanisms of a Eutectic Sn-Pb Solder 63Sn/37Pb," *International Journal of Fatigue*, Vol. 24, pp. 671-683, 2002.

[143] Rust, W., *Non-Linear Finite Element Analysis in Structural Mechanics*.: Springer International Publishing, 2015.

[144] Bhatti, M. A., *Fundamental Finite Element Analysis and Applications: with Mathematica and Matlab Computations*.: Wiley, 2005.

[145] Bhatti, M. A., *Advanced Topics in Finite Element Analysis of Structures: with Mathematica and Matlab Computations*.: Wiley, 2006.

[146] Kim, N. H., *Introduction to Nonlinear Finite Element Analysis*.: Springer, 2015.

[147] Dauksher, W., "Design for Reliability—Finite Element Modeling of Lead-Free Solder Interconnects," in *Lead-Free Solder Interconnect Reliability*, Shangguan, D., Ed.: ASM International, 2005, ch. 9, pp. 199-225.

[148] Dudek, R., Döring, R., and Michel, B., "Reliability Prediction of Area Array Solder Joints," *Journal of Electronic Packaging*, Vol. 125(4), pp. 562-568, 2003.

[149] Yeh, C. P., Zhou, W. X., and Wyatt, K., "Parametric Finite Element Analysis of Flip Chip Reliability," *International Journal of Microcircuits and Electronic Packaging*, Vol. 19(2), pp. 120-127, 1996.

[150] Michaelides, S. and Sitaraman, S. K., "Die Cracking and Reliable Die Design for Flip-Chip Assemblies," *IEEE Transactions on Advanced Packaging*, Vol. 22(4), pp. 602-613, 1999.

[151] Park, J. E., Jasiuk, I., and Zubelewicz, A., "Stresses and Fracture at the Chip/Underfill Interface in Flip-Chip Assemblies," *Journal of Electronic Packaging*, Vol. 125(1), pp. 44-52, 2003.

[152] Akay, H. U., Liu, Y., and Rassaian, M., "Simplification of Finite Element Models for Thermal Fatigue Life Prediction of PBGA Packages," *Journal of Electronic Packaging*, Vol. 125(3), pp. 347-353, 2003.

[153] Michaelides, S. and Sitaraman, S. K., "Effect of Material and Geometry Parameters on the Thermo-Mechanical Reliability of Flip-Chip Assemblies," *Proceedings of ITherm Conference*, pp. 193-200, 1998.

[154] Sarihan, V., "Temperature Dependent Viscoplastic Simulation of Controlled Collapse Solder Joint Under Thermal Cycling," *Journal of Electronic Packaging*, Vol. 115, pp. 16-21, 1993.

[155] Sarihan, V., "Energy Based Methodology for Damage and Life Prediction of Solder Joints Under Thermal Cycling," *IEEE Transactions on Components, Packaging, and Manufacturing Technology: Part B*, Vol. 17(4), pp. 626-631, 1994.

[156] Feustel, F., Wiese, S., and Meusel, E., "Time-Dependent Material Modeling for Finite Element Analyses of Flip Chips," *Proceedings of Electronic Components*

and Technology Conference, pp. 1548-1553, 2000.

[157] Yan, C., Qin, Q. H., and Mai, Y. W., "Nonlinear Analysis of Plastic Ball Grid Array Solder Joints," *Journal of Materials Science: Materials in Electronics*, Vol. 12(11), pp. 667-673, 2001.

[158] Sylvester, M. F., Banks, D. R., Sylvester, M. F., and Kern, R. W., "Thermal Cycling Effects on Eutectic Flip-Chip Die on Organic Packages," *Proceedings of International Conference on High-Density Interconnect and Systems Packaging*, pp. 438-443, 2000.

[159] Rzepka, S., Korhonen, M. A., Meusel, E., and Li, C. Y., "The Effect of Underfill and Underfill Delamination on the Thermal Stress in Flip-Chip Solder Joints," *Journal of Electronic Packaging*, Vol. 120(4), pp. 342-348, 1998.

[160] Chen, L., Zhang, Q., Wang, G., Xie, X., and Cheng, Z., "The Effects of Underfill and Its Material Models on Thermomechanical Behaviors of a Flip Chip Package," *IEEE Transactions on Advanced Packaging*, Vol. 24, pp. 17-24, 2001.

[161] Chiang, K. N., Liu, Z. N., and Peng, C. T., "Parametric Reliability Analysis of No-Underfill Flip Chip Package," *IEEE Transactions on Components and Packaging Technologies*, Vol. 24(4), pp. 635-640, 2001.

[162] Amagai, M. and Nakao, M., "Ball Grid Array (BGA) Packages with the Copper Core Solder Balls," *Proceedings of Electronic Components and Technology Conference*, pp. 692-701, 1998.

[163] He, A., Osborn, T., Allen, S. A. B., and Kohl, P. A., "All-Copper Chip-to-Substrate Interconnects Part II. Modeling and Design," *Journal of The Electrochemical Society*, Vol. 155(4), pp. D314-D322, 2008.

[164] Gustafsson, G., Guven, I., Kradinov, V., and Madenci, E., "Finite Element Modeling of BGA Packages for Life Prediction," *Proceedings of Electronic Components and Technology Conference*, pp. 1059-1063, 2000.

[165] Dauksher, W. and Lau, J., "A Finite-Element-Based Solder-Joint Fatigue-Life Prediction Methodology for Sn–Ag–Cu Ball-Grid-Array Package," *IEEE Transactions on Device and Materials Reliability*, Vol. 9(2), 2009.

[166] Hsieh, M. C., Lee, C. C., and Hung, L. C., "Comprehensive Thermo-Mechanical Stress Analysesand Underfill Selection of Large Die Flip ChipBall Grid Array," *IEEE Transactions on Components, Packaging and Manufacturing Technology*, Vol. 3(7), pp. 1155 - 1162, 2013.

[167] Zhong, Z. and Yip, P. K., "Finite Element Analysis of a Three-Dimensional Package," *Soldering & Surface Mount Technology*, Vol. 15(1), pp. 21-25, 2003.

[168] Chong, D. Y. R., Goh, K. Y., Kapoor, R., and Sun, A. Y. S., "Reliability Analyses for New Improved High Performance Flip Chip BGA Packages," *Proceedings of Electronics Packaging Technology Conference*, pp. 695-700, 2003.

[169] Yeo, A., Lee, C., and Pang, J. H. L., "Flip Chip Solder Joint Fatigue Life Model Investigation," *Proceedings of Electronics Packaging Technology Conference*, pp. 107-114, 2002.

[170] Zahn, B. A., "Impact of Ball Via Configurations on Solder Joint Reliability in Tape-Based, Chip-Scale Packages," *Proceedings of Electronic Components and*

Technology Conference, pp. 1475-1483, 2002.

[171] Yeo, A., Lee, C., and Pang, J. H. L., "Flip Chip Solder Joint Fatigue Analysis Using 2D and 3D FE Models," *Proceedings of Thermal and Mechanical Simulation and Experiments in Microelectronics and Microsystems*, pp. 549-553, 2004.

[172] Zahn, B. A., "Finite Element Based Solder Joint Fatigue Life Predictions for a Same Die Stacked Chip Scale Ball Grid Array Package," *Proceedings of Electronics Manufacturing Technology Symposium*, pp. 274-284, 2002.

[173] Zhu, W. H., Stoeckl, S., Pape, H., and Gan, S. L., "Comparative Study on Solder Joint Reliability Using Different FE-Models," *Proceedings of Electronics Packaging Technology Conference*, pp. 687-694, 2003.

[174] Yao, Q. and Qu, J., "Three-Dimensional versus Two-Dimensional Finite Element Modeling of Flip-Chip Packages," *Journal of Electronic Packaging*, Vol. 121(3), pp. 196-201, 1999.

[175] Syed, A. R., "Predicting Solder Joint Reliability for Thermal, Power, & Bend Cycle within 25% Accuracy," *Proceedings of Electronic Components and Technology Conference*, pp. 255-263, 2001.

[176] Syed, A. R., "Updated Life Prediction Models for Solder Joints with Removal of Modeling Assumptions and Effect of Constitutive Equations," *Proceedings of The 7th International Conference on Thermal, Mechanical and Multiphysics Simulation and Experiments in Micro-Electronics and Micro-Systems, EuroSime2006*, pp. 1-9, 2006.

[177] Riebling, J., "Finite Element Modeling of Ball Grid Array Components," *Master's Thesis, State University of New York at Binghamton*, 1996.

[178] Madenci, E., Guven, I., and Kilic, B., *Fatigue Life Prediction of Solder Joints in Electronic Packages with Ansys*.: Springer US, 2003.

[179] Madenci, E. and Guven, I., *The Finite Element Method and Applications in Engineering Using ANSYS*, 2nd Edition.: Springer US, 2015.

[180] Fei, L., Liang, L., and Liu, Y., "An Improved Substructure Method for Prediction of Solder Joint Reliability in Thermal Cycle," *Proceedings of International Conference on Electronic Packaging Technology & High Density Packaging*, pp. 311-316, 2009.

[181] Cheng, H. C., Chiang, K. N., and Lee, M. H., "An Effective Approach for Three-Dimensional Finite Element Analysis of Ball Grid Array Typed Packages," *Journal of Electronic Packaging*, Vol. 120(2), pp. 129-134, 1998.

[182] Ju, T. H., Chan, Y. W., Hareb, S. A., and Lee, Y. C., "An Integrated Model for Ball Grid Array Solder Joint Reliability," *Proceedings of ASME International Mechanical Engineering Congress and Exposition*, pp. 83-89, 1995.

[183] Chan, Y. W., Ju, T. H., Hareb, S. A., and Lee, Y. C., "Reliability Modeling for Ball Grid Array Assembly with a Large Number of Warpage Affected Solder Joints," *Journal of Electronic Packaging*, Vol. 124(3), pp. 246-253, 2002.

[184] Zhang, T., Rahman, S., Choi, K. K., Cho, K., Baker, P., Shakil, M., and Heitkamp, D., "A Global-Local Approach for Mechanical Deformation and Fatigue Durability

of Microelectronic Packaging Systems," *Journal of Electronic Packaging*, Vol. 129, pp. 179-189, 2007.

[185] Chen, C., Suhling, J. C., and Lall, P., "Comparison of FEA Modeling Techniques for Plastic Ball Grid Array Assemblies," *Proceedings of ITherm*, pp. 1195-1206, 2018.

[186] Che, F. X. and Pang, J. H. L., "Solder Joint Reliability Assessment: Finite Element Simulation Methodology Fatigue Reliability Analysis of Sn–Ag–Cu Solder Joints Subject to Thermal Cycling," *IEEE Transactions on Device and Materials Reliability*, Vol. 13(1), pp. 36-49, 2013.

[187] Zahn, B. A., "Solder Joint Fatigue Life Model Methodology for 63Sn37Pb and 95.5Sn4Ag0.5Cu Materials," *Proceedings of Electronic Components and Technology Conference*, pp. 83-94, 2003.

[188] Motalab, M., Basit, M., Suhling, J. C., Bozack, M. J., and Lall, P., "Creep Test Method for Determination of Anand Parameters for Lead Free Solders and Their Variation with Aging," *Proceedings of ITherm Conference*, pp. 127-142, 2014.

[189] Chen, C., Suhling, J. C., and Lall, P., "Improved Meshing Strategy for Finite Element Modeling of PBGA Thermal Cycling," *Proceedings of ITherm*, pp. 448-455, 2016.

[190] Pang, J. H. L., Tan, T. I., Lim, G. Y., and Wong, C. L., "Thermal Stress Analysis of Direct Chip Attach Electronic Packaging Assembly," *Proceedings of Electronic Packaging Technology Conference*, pp. 170-176, 2016.

[191] Chow, S. G., Lin, Y., Ouyang, E., and Ahn, B., "A Finite Element Analysis of Board Level Temperature Cycling Reliability of Embedded Wafer Level BGA (eWLB) Package," *Proceedings of Electronic Components and Technology Conference*, pp. 1448-1454, 2012.

[192] Syed, A. R., Sharon, G., and Darveaux, R., "Factors Affecting Pb-free Flip Chip Bump Reliability Modeling for Life Prediction," *Proceedings of Electronic Components and Technology Conference*, pp. 1715-1725, 2012.

[193] Chen, C., Suhling, J. C., and Lall, P., "Improved Finite Element Modeling Strategies with Multipoint Constraints for BGA Packages Subjected to Thermal Cycling," *Proceedings of ITherm*, pp. 1456-1465, 2017.

[194] Chen, C., Suhling, J. C., and Lall, P., "Improved Submodeling Finite Element Simulation Strategies for BGA Packages Subjected to Thermal Cycling," *Proceedings of ITherm*, pp. 1146-1154, 2018.

[195] Lu, D. and Wong, C. P., Eds., *Materials for Advanced Packaging*, 2nd Edition.: Springer International Publishing, 2009.

[196] Koric, S. and Thomas, B. G., "Thermo-Mechanical Models of Steel Solidification Based on Two Elastic Visco-Plastic Constitutive Laws," *Journal of Materials Processing Technology*, Vol. 197(1-3), pp. 408-418, 2008.

[197] Okura, J. H., Shetty, S., Ramakrishnan, B., Dasgupta, A., Caers, J. F. J. M., and Reinikainen, T., "Guidelines to Select Underfills for Flip Chip on Board Assemblies and Compliant Interposers for Chip Scale Package Assemblies," *Microelectronics Reliability*, Vol. 40(7), pp. 1173-1180, 2000.

[198] Yang, Q. J., Shi, X. Q., Wang, Z. P., and Shi, Z. F., “Finite-Element Analysis of a PBGA Assembly Under Isothermal/Mechanical Twisting Loading,” *Finite Elements in Analysis and Design*, Vol. 39(9), pp. 819-833, 2003.

[199] Ho-Le, K., “Finite Element Mesh Generation Methods: A Review and Classification,” *Computer-Aided Design*, Vol. 20(1), pp. 27-38, 1988.

[200] Wang, E., Nelson, T., and Rauch, R., “Back to Elements - Tetrahedra vs. Hexahedra,” *Proceedings of International ANSYS Conference*, 2004.

[201] Benzley, S. E., Perry, E., Merkley, K., Clark, B., and Sjaardema, G., “A Comparison of All Hexagonal and All Tetrahedral Finite Element Meshes for Elastic and Elasto-plastic Analysis,” *Proceedings of 4th International Meshing Roundtable*, pp. 179-191, 1995.

[202] Cifuentes, A. O. and Kalbag, A., “A Performance Study of Tetrahedral and Hexahedral Elements in 3-D Finite Element Structural Analysis,” *Finite Elements in Analysis and Design*, Vol. 12(3-4), pp. 313-318, 1992.

[203] Nielsen, C. V., Zhang, W., Alves, L. M., Bay, N., and Martins, P., *Modeling of Thermo-Electro-Mechanical Manufacturing Processes: Applications in Metal Forming and Resistance Welding*.: Springer-Verlag London, 2013.

[204] Banabic, D., Bunge, H. J., Pöhlandt, K., and Tekkaya, A. E., *Formability of Metallic Materials: Plastic Anisotropy, Formability Testing, Forming Limits*.: Springer-Verlag Berlin Heidelberg, 2000.

[205] Weill, J. C., “Towards an Automatic and Reliable Hexahedral Meshing,” *Proceedings of Fifth Workshop on Grid Generation for Numerical Computations*, pp. 1-63, 2016.

[206] ABAQUS, “Abaqus Documentation,” *Dassault Systèmes*, 2014.

[207] ANSYS, “ANSYS Documentation,” *ANSYS Inc.*, 2012.

[208] MSC, *Linear Static Analysis User's Guide*.: MSC Software, 2012.

[209] Owen, S. J., Canann, S. A., and Saigal, S., “Pyramid Elements for Maintaining Tetrahedra to Hexahedra Conformability,” *ASME Trends in Unstructured Mesh Generation*, Vol. 220, pp. 123-129, 1997.

[210] Lo, D. S. H., *Finite Element Mesh Generation*.: CRC Press, 2017.

[211] Larson, M. G. and Bengzon, F., *The Finite Element Method: Theory, Implementation, and Applications*.: Springer, 2013.

[212] Kythe, P. and Wei, D., *An Introduction to Linear and Nonlinear Finite Element Analysis: A Computational Approach*.: Birkhäuser Basel, 2004.

[213] Liu, G. R. and Quek, S. S., *The Finite Element Method: A Practical Course*.: Butterworth-Heinemann, 2003.

[214] Rao, S. S., *The Finite Element Method in Engineering*, 4th Edition.: Butterworth-Heinemann, 2005.

[215] Sun, E. Q., “Shear Locking and Hourglassing in MSC Nastran, ABAQUS, and ANSYS,” *Proceedings of MSC Software Corporation’s 2006 Americas Virtual Product Development Conference: Evolution to Enterprise Simulatio*, pp. 17-19, 2006.

[216] Darveaux, R., "Thermal Cycle Fatigue Life Prediction for Flip Chip Solder Joints," *Proceedings of Electronic Components and Technology Conference* , pp. 703-711, 2014.

[217] Felippa, A. (1998) Introduction to Finite Element. [Online]. http://www.colorado.edu/engineering/CAS/courses.d/IFEM.d/Home.html

[218] Liu, S. and Liu, Y., *Modeling and Simulation for Microelectronic Packaging Assembly: Manufacturing, Reliability and Testing*.: John Wiley & Sons (Asia), 2011.

[219] ANSYS, "Advanced Contact," *ANSYS Training Manual*, 2005.

[220] Fan, X. J., Varia, B., and Han, Q., "Design and Optimization of Thermo-Mechanical Reliability in Wafer Level Packaging," *Microelectronics Reliability*, Vol. 50(4), pp. 536-546, 2010.

[221] Zhang, L., Han, J., Guo, Y., and He, C., "Anand Model and FEM Analysis of SnAgCuZn Lead-Free Solder Joints in Wafer Level Chip Scale Packaging Devices," *Microelectronics Reliability*, Vol. 54, pp. 281-286, 2014.

[222] Chiu, T. C., Lin, J. J., Yang, H. C., and Gupta, V., "Reliability Model for Bridging Failure of Pb-Free Ball Grid Array Solder Joints under Compressive Load," *Microelectronics Reliability*, Vol. 50(12), pp. 2037-2050, 2010.

[223] Lau, C. S., Abdullah, M. Z., and Ani, F. C., "Computational Fluid Dynamic and Thermal Analysis for BGA Assembly During Forced Convection Reflow Soldering Process," *Soldering & Surface Mount Technology*, Vol. 24(2), pp. 77-91, 2012.

[224] Ladani, L. J. and Dasgupta, A., "Damage Initiation and Propagation in Voided Joints: Modeling and Experiment," *Journal of Electronic Packaging*, Vol. 130(1), pp. 011008-1-11, 2008.

[225] Yu, D., Lee, H., and Park, S., "Reliability Assessment of Preloaded Solder Joint Under Thermal Cycling," *Journal of Electronic Packaging*, Vol. 134(4), 2012.

[226] Elshabini, A., Wang, G., and Barlow, F., "Future Trends in Electronic Packaging," *Proceedings of Smart Structures and Materials 2006: Smart Electronics, MEMS, BioMEMS, and Nanotechnology*, pp. 61720Z-1-8, 2006.

[227] Zahn, B. A., "Comprehensive Solder Fatigue and Thermal Characterization of a Silicon Based Multi-Chip Module Package Utilizing Finite Element Analysis Methodologies," *Proceedings of The 9th International ANSYS Conference and Exhibition*, 2000.

[228] Pierce, D. M., Sheppard, S. D., Vianco, P. T., Regent, J. A., and Grazier, J. M., "Fatigue Life Prediction Methodology for Lead-Free Solder Alloy Interconnects: Development and Validation," *Proceedings of the IPC/JEDEC Global Conference on Lead Free Reliability & Reliability Testing for RoHS Lead Free Electronics*, pp. 1-20, 2007.

[229] Lau, C. S., Abdullah, M. Z., Mujeebu, M. A., and Yusop, N. M., "Finite Element Analysis on the Effect of Solder Joint Geometry for the Reliability of Ball Grid Array Assembly with Flexible and Rigid PCBs," *Journal of Engineering Science and Technology*, Vol. 9(1), pp. 47-63, 2014.

[230] Rodgers, B., Punch, J., Jarvis, J., Myllykoski, P., and Reinikainen, T., "Finite

Element Modeling of a BGA Package Subjected to Thermal and Power Cycling," *Proceedings of ITherm Conference*, pp. 993-1000, 2002.

[231] Huijun, J. W., Hoe, C., and Hua, W. E., "Modeling Solder Joint Reliability of BGA Packages Subject to Drop Impact Loading Using Submodeling," *Proceedings of ABAQUS Users' Conference*, pp. 1-11, 2002.

[232] Mukai, M., Kawakami, T., Takahashi, K., Kishimoto, K., and Shibuya, T., "Thermal Fatigue Life of Solder Bumps in BGA," *JSME International Journal. Series A, Solid Mechanics and Material Engineering*, Vol. 41(2), pp. 260-266, 1998.

[233] Syed, A. R., Kim, S., and Lin, W., "Building Accuracies in Finite Element Models for Life Prediction of Solder Joints," *Proceedings of Electronics Packaging Technology Conference*, 2007.